Universidade do Minho
Escola de Engenharia

Inês Varela Gomes

Biomechanical performance of magnesium stents obtained by ultrasonic-microcasting. Numerical modeling and material experimental characterization.

outubro de 2022

Biomechanical performance of magnesium stents obtained by ultrasonic-microcasting. Numerical modeling and material experimental characterization.

Inês Varela Gomes

UMinho | 2022


REPÚBLICA PORTUGUESA
CIÊNCIA, TECNOLOGIA E ENSINO SUPERIOR
FCT Fundação para a Ciência e a Tecnologia
NORTE2020
CENTRO 2020
ALENTEJO 2020
POCH
PORTUGAL 2020
UNIÃO EUROPEIA
Fundo Social Europeu

Universidade do Minho
Escola de Engenharia

Inês Varela Gomes

Biomechanical performance of magnesium stents obtained by ultrasonic-microcasting. Numerical modeling and material experimental characterization.

Tese de Doutoramento
Programa Doutoral Em Líderes Para Indústrias Tecnológicas

Trabalho efetuado sob a orientação do
Professor Doutor Hélder de Jesus Fernandes Puga
Professor Doutor José Luís de Carvalho Martins Alves

outubro de 2022

DIREITOS DE AUTOR E CONDIÇÕES DE UTILIZAÇÃO DO TRABALHO POR TERCEIROS

ACKNOWLEDGMENTS

I was told that pursuing a PhD was a lonely path. In my case, I was lucky enough to share this unique experience with the most encouraging people and count on the support of institutions, allowing me to succeed.

To my supervisor, Professor Hélder Puga, my research mentor for the last years, since my MSc thesis, back in 2016. I express my deep gratitude for pushing me further and for always believing in my potential, even in the moments I did not. His knowledge and friendship were essential for developing this work, but, most of all, I could not ask for a better example of commitment and resilience. I will take that for life.

To my co-supervisor, Professor Luís Alves, for sharing his knowledge and experience. His guidance and help were of utmost importance for this work. This work would certainly be poorer without his contribution.

To Fundação para a Ciência e a Tecnologia (FCT) for funding this work through the PhD grant PD/BD/140094/2018, in the context of MIT Portugal Program.

My special thanks to Professor Fabrizio D'Errico, from Politecnico di Milano, for sharing his expertise in the magnesium alloys processing field, which has deeply contributed to the merit of this work. Also, to Professor Jan Bohlen, from Helmholtz-Zentrum Hereon, with whom I had the pleasure to work on extrusion processing.

To Hydrumedical, S.A. and, especially to Doctor Alexandre Barros, Doctor Sara Neves and Dr. Margarida Pacheco, for the opportunity of working together in the study of magnesium alloys' corrosion behavior.

To the Department of Mechanical Engineering of the University of Minho, my second home. A special word to the technical workers for their unceasing support and goodwill and to Doctor Alexandra Alves, who was available to share his knowledge whenever I asked.

My deep thanks to my "Partners in Lab", mainly to Diogo and Grilo, for their companionship. Their unwearying support and tireless enthusiasm made this journey easier. Also, to Muhrat for his sincere friendship, advice, and help to pursue this work. His experience sharing contributed greatly to this work.

To Martim, Maria do Carmo, Gastão and Maria Vitória, my faithful friends for all hours and the best company on the long nights.

To my brother Rui and my sister-in-law Isabel, for all the scientific support and constant willingness to help. They are, undoubtedly, the biggest fans of this work.

My deepest gratitude and love to Paulo, my partner in every single aspect of my life. Your constant support helped me fight for this work even in the darkest moments. For me, you are the perfect description of loving and cherishing, and there is no way I could have a better person beside me.

Finally, to THE best. My parents, my leading examples. My biggest fans, but also my most demanding critics. I would never be capable of thanking you for all that you have been for me. If I could be a small fraction of what you are, what a wonderful person I would be. I love you.

O meu sincero agradecimento a todos.

STATEMENT OF INTEGRITY

I hereby declare having conducted this academic work with integrity. I confirm that I have not used plagiarism or any form of undue use of information or falsification of results along the process leading to its elaboration.

I further declare that I have fully acknowledged the Code of Ethical Conduct of the University of Minho.

RESUMO

O desejo constante de superação impulsiona a evolução num mundo moderno onde a mudança ocorre a uma velocidade estonteante. Os desafios tecnológicos e sociais são cada vez mais ambiciosos, o que se traduz na necessidade de soluções extraordinárias, uma situação transversal a todas as áreas do conhecimento. Tomando a área da manufatura e materiais como exemplo, tal torna-se evidente. Aplicações no âmbito das áreas aeroespacial, biomédica e ambiental encabeçam os interesses e prioridades das comunidades científica e industrial, o que é justificado pelo impacto que qualquer avanço nesses domínios poderá significar para a sociedade.

Neste sentido, existe uma necessidade de materiais e processos que possibilitem obter o desempenho requerido para aplicação em cenários de grande exigência, como os referidos.

O magnésio e as suas ligas são considerados fortes candidatos para aplicação nas áreas em questão, especialmente para o fabrico de *stents* biodegradáveis, dada a sua excelente biocompatibilidade. Não obstante, a sua baixa conformabilidade à temperatura ambiente, a elevada reatividade e fácil ignição durante o e rápida degradação sob condições fisiológicas dificulta a sua aplicação alargada.

O presente estudo focou-se na investigação do potencial da aplicação de tratamento por ultrassons no processo de fundição da liga de magnésio AZ91D-Ca, com o objetivo de melhorar as propriedades do material através da modificação da sua microestrutura. O tratamento foi aplicado em dois momentos distintos: (i) no banho metálico, de forma a promover a sua desgaseificação e (ii) durante o vazamento e solidificação do material, de modo a promover a afinação e modificação da microestrutura. A degradação do material e consequente efeito nas propriedades mecânicas foi investigada através da realização de testes dinâmicos de imersão em *Earle's Balanced Salt Solution*. As curvas de tensão-deformação resultantes dos ensaios de tração do material imerso até 7 dias foram utilizadas como dados de entrada do modelo numérico desenvolvido com o objetivo de simular o processo de colocação do *stent* e otimizar a sua geometria. Os resultados obtidos demonstraram que o tratamento por ultrassom pode modificar significativamente a microestrutura da liga de magnésio AZ91D-Ca, melhorando as suas propriedades mecânicas e de resistência à corrosão, o que, de acordo com os dados obtidos através da simulação numérica, se mostrou determinante no desempenho do *stent.*

Palavras-chave: Ligas de Magnésio; Fundição; Tratamento por Ultrassons; Análise de Elementos Finitos; *Stent*

ABSTRACT

In the modern world, change happens at lightning speed, and the eagerness for great deeds drives evolution. The technological and societal goals are increasingly ambitious, translating into the need for outstanding and complex solutions: this is a transversal and unquestionable truth to all the knowledge areas. Considering the manufacturing and materials area example, this becomes crystal clear. The aerospace, biomedical, and environmental-related applications have been leading the interests and priorities of both research and industrial communities, which is motivated by the potential impact any advance in this area can have in society.

In this sense, there is a need for materials and processes that can offer the properties required for application in such demanding scenarios.

Magnesium and its alloys are considered strong candidates for these applications, especially biodegradable stents manufacturing, because of their excellent biocompatibility. Nonetheless, some issues, such as poor formability at room temperature, high reactivity and easy ignition during the melting process and loss of mechanical strength motivated by fast degradation under physiological conditions, hinder their widespread.

This study investigated the potential of applying ultrasound treatment to the casting process of AZ91D-Ca alloys, aiming at improving the material's properties by tailoring their microstructure. Ultrasonic vibration was applied in two moments: (i) to the magnesium melt to promote its degassing and (ii) during the pouring and subsequent solidification to induce microstructural refinement and modification. Dynamic immersion tests in Earle's Balanced Salt Solution were carried out to assess the degradation behavior of the material and its effect on the mechanical properties. Uniaxial tensile tests were performed on the material after immersion for up to seven days, and the strain-stress curves were used as input data for a numerical model developed to simulate the stent deployment procedure and optimize the device's design.

It has been demonstrated that ultrasound treatment could significantly modify the microstructure of AZ91D-Ca alloys, improving their mechanical and corrosion properties. Furthermore, the material's enhanced properties have been demonstrated to play a significant role in the stent performance assessed through numerical simulation, stressing the potential of this technique for manufacturing magnesium-based biomedical devices.

Keywords: Magnesium alloys; Casting; Ultrasound Treatment; Finite Element Analysis; Stent

TABLE OF CONTENTS

LIST OF FIGURES

CHAPTER 1

CHAPTER 2

CHAPTER 3

CHAPTER 4

CHAPTER 5

LIST OF TABLES

CHAPTER 2

CHAPTER 3

CHAPTER 4

CHAPTER 5

CHAPTER 6

LIST OF ABBREVIATIONS

BDS - Biodegradable Stent

BMS - Bare-Metal Stent

CAD - Computer-Aided Design

COBYLA - Constrained Optimization BY Linear Approximation

CVD - Cardiovascular Diseases

DES - Drug-Eluting Stents

EBSS - Earle's Balanced Salt Solution

EDS - Energy-Dispersive X-ray Spectroscopy

FEA - Finite Element Analysis

FEM - Finite Element Method

GP-Zone - Guinier-Preston Zone

HE - Hyperelastic Model

ISR - In-Stent Restenosis

LE - Linear Elastic Model

MMM - Multi-frequency, Multimode, Modulated

OE - Open-ended Balloon

OM - Optical Microscopy

PCI - Percutaneous Coronary Intervention

PTCA - Percutaneous Transluminal Coronary Angioplasty

RE - Rare Earth

RO - Research Objective

SEM - Scanning Electron Microscopy

ST - Stent Thrombosis

TE - Taper-ended Balloon

US - Ultrasound

XPS - X-ray Photoelectron Spectroscopy

XRD - X-Ray Diffraction

LIST OF SYMBOLS

Latin Symbols

Symbol	Description	Unit
A	Surface are	m^2
C_y	Hardening rate	[-]
C_{ij}	Mooney-Rivlin parameters	[-]
C	Right Cauchy-Green tensor	[-]
C^{el}	Fourth-order stiffness tensor	[-]
d	Grain size	μm
E	Young modulus	Pa
	Green-Lagrange strain tensor	[-]
F	Deformation gradient	[-]
f	Fraction of intermetallics	%
$\overline{I}_1, \overline{I}_2, \overline{I}_3$	Isochoric Strain invariants of the Cauchy-Green strain tensor	[-]
J_{el}	Elastic Jacobian	[-]
k	Isothermal rate constant	[-]
	Bulk modulus	Pa
L	Length	m
m	Mass	kg
n	Avrami exponent	[-]
p	Pressure	Pa
r	Radius	m
	Normal polar coordinate	[-]
t	Time	s
	Thickness	m
u	Displacement	m
v	Poisson's coefficient	[-]
Y_o	Initial flow stress	Pa
Y_{sat}	Saturation flow stress	Pa

W	Strain energy density	J/m^3
z	Third cylindrical coordinete	[-]

Greek symbols

Symbol	Description	Unit
α	Planes	[-]
β		
γ		
δ	Kronecker delta	[-]
$\bar{\varepsilon}^p$	Equivalent plastic strain	[-]
θ	Azimuthal angle	rad
λ	Lamé parameters	[-]
μ		
π	Second-order Piola-Kirchhoff stress tensor	Pa
ρ	Density	kg/m^3
σ_y	Plastic flow stress	Pa
σ_o	Friction stress	Pa

CHAPTER 1 – INTRODUCTION

A PhD applicant is expected to do research on a selected topic and contribute new information to the area as part of the doctoral program. Moreover, it must be a priority to build the research so that the outcome can answer a recognized issue or address a previously acknowledged lack, contributing to improving the society to which one belongs and linking technical potential with human needs.

To demonstrate the candidate's suitability to be considered for a Doctor of Philosophy degree, this document describes the knowledge produced in the field of magnesium alloy processing and the numerical simulation of magnesium stents to be manufactured via ultrasonic microcasting.

1.1. CORONARY ARTERY DISEASE – THE 21ST-CENTURY HEALTH CHALLENGE

In recent years, the incidence of cardiovascular diseases (CVD) has increased and is now the leading cause of sudden and unexpected death worldwide. According to World Health Organization data [1], around 16 million people died of CVD and strokes in 2019, representing nearly 27% of all global deaths. In particular, ischaemic heart disease has seen the most significant increase in fatalities since 2000, rising by more than 2 million deaths to 8.9 million deaths in 2019. In fact, during the last 15 years, these illnesses have remained the major cause of mortality worldwide [2]. Moreover, it is estimated that CVD are responsible for the highest component of healthcare expenses, spending around €192 billion annually in Europe, of which approximately one-third is allocated to direct treatment costs, with the remainder

associated with informal care costs and productivity losses [3]. This value in the United States of America may exceed USD 200 billion annually [4].

Nearly all occurrences of coronary artery disease and peripheral arterial disease are caused by atherosclerosis [5]. This disease is associated with a chronic systemic inflammatory process that affects the wall of coronary, carotid and aorta arteries and other peripheral vessels, compromising their elasticity [6]. As a result of the deposition of lipids, macrophages, lymphocytes and fibrous tissue inside the intima, the walls of the blood vessel become thicker and stiffer, limiting the lumen and, subsequently, the blood flow to the organs. These phenomena result in ischaemic events that may lead to death. In addition, the plaque may rupture, resulting in the development of a blood clot that might precipitate a heart attack [7]. The described process is shown in Figure 1.1.

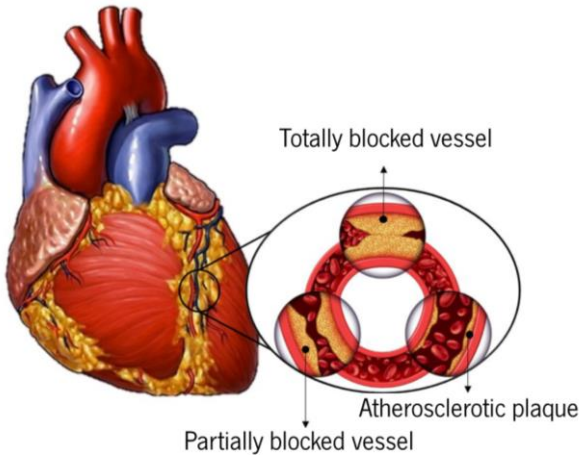

Figure 1.1 – Atherosclerosis progression (adapted from [8]).

Several approaches have been developed over the last several decades to treat patients with this illness, improving their quality of life and decreasing the likelihood of fatal occurrences such as blood vessel blockage. One example is percutaneous transluminal coronary balloon angioplasty (PTCA), in which a balloon is guided through a wire to the stenosis site and is inflated to compress it, relieving the blockage and restoring normal blood flow to the heart [9]. This procedure was a breakthrough in the percutaneous coronary intervention (PCI) paradigm, which has previously undergone four significant revolutions [10], as seen in Figure 1.2, where the main drawbacks associated with each one are also shown.

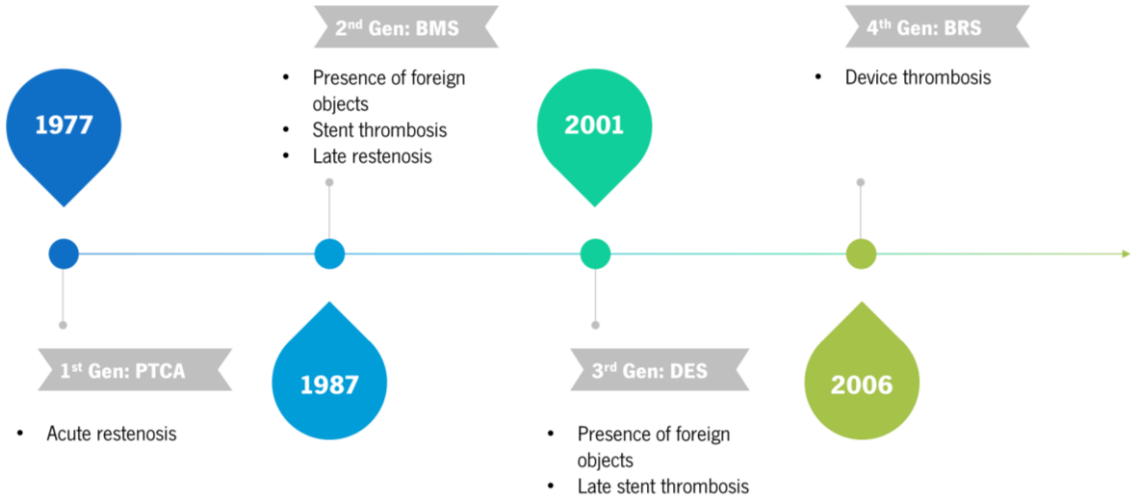

Figure 1.2 – Evolution of PCI over time.

The first PTCA with a balloon catheter was successfully performed in 1977 by Andreas Grüntzig [11]. In 1985, he had completed 2623 interventions with a success rate higher than 90%. This treatment, however, results in plaque compression and/or even fracture, which commonly precipitates adverse outcomes such as acute artery closure and restenosis. Towards this scenario of potential deathly consequences, the enthusiasm about PTCA dampened, and coronary stent implantation emerged as a promising alternative [10]. In the stenting procedure, a catheter system is used to place a stent in the narrowed area of the blood vessel, followed by balloon inflation to expand it. As the stent deforms plastically, the scaffolding effect remains, assuring the reopening of the artery even after the balloon and the catheter system have been removed [12,13]. In Figure 1.3, the stent deployment process is illustrated.

Self- or balloon-expandable metallic materials, including 316L stainless steel, cobalt-chromium alloys, and nitinol, were often used in the initial generation of stents. Although the application of the bare-metal stents (BMS) was initially pointed to as the solution for the problems presented by balloon angioplasty, the clinical outcomes demonstrated the occurrence of adverse events, including in-stent restenosis (ISR), neointimal hyperplasia, permanent physical irritation, chronic inflammatory local reactions, and stent thrombosis (ST) [14]. Since the stent stays in the body after the patient has healed, the immune system is stimulated to respond to this foreign material. Multiple autopsies revealed that the process after stent deployment is analogous to wound healing and platelet adhesion, minor luminal thrombus formation, fibrin deposition, and local inflammatory cellular infiltrate could be observed [15,16].

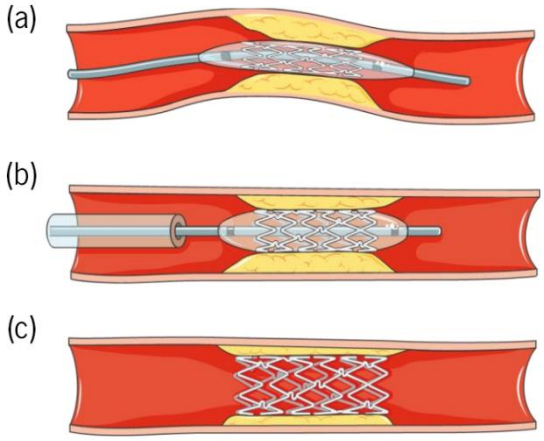

Figure 1.3 – Stent deployment process: (a) catheter system placement of the crimped stent in the stenosed artery; (b) balloon inflation and subsequent stent expansion; (c) balloon deflation and catheter withdrawal.

The development of drug-eluting stents (DES) arose from the attempt to mitigate ISR and vascular inflammation events and so improve the effectiveness of stenting therapy. These stents were coated with antiproliferative or immunosuppressive pharmacologic agents, such as paclitaxel and sirolimus, embedded within a durable bioabsorbable polymer, and released locally over time, thereby reducing the proliferation of smooth muscle cells and, consequently, the formation of neointima [17,18].

Although the initial controlled trials had shown positive results regarding the application of DES, late adverse events were reported in posterior clinical studies [19–22]. The main concerns were motivated by the suboptimal biocompatibility of the polymers used, which was the origin of a greater propensity for late and very late ST and local drug toxicity [23]. Indeed, it was suggested that a connection could exist between the presence of durable polymers and chronic vessel wall inflammation with delayed hypersensitivity reactions, arterial healing, and complete stent strut re-endothelialization promoted by the inhibition of endothelial cell proliferation, stent malapposition, and accelerated neo-atherosclerosis [23]. Moreover, the dimensions of the stent made it challenging to pass through the blood vessels, particularly convoluted and tiny ones [17]. Despite these adverse effects, the ISR rate fell from about 20-40% with BMS to 6-8% with the first generation of DES [23]. Even though the implantation of DES suffered a significant reduction by 2007, clinicians began to prescribe dual antiplatelet therapy for periods superior to one year after the procedure to avoid late ST.

To overcome the drawbacks presented by the first generation of DES, a second one was developed, characterized by thinner struts combined with more biocompatible polymers and new cell-cycle inhibitors such as everolimus and zotarolimus. These modifications permitted the design of novel DES with enhanced flexibility, better drug deliverability, shorter release time, and improved re-endothelialization

[24]. The third generation of DES with a three-layered polymer was then released, which granted enhanced deliverability and suppression of the initial inflammatory response [25]. Such adjustments increased the effectiveness of stenting treatments; yet, it was difficult to satisfy all medical needs and eliminate the shortcomings in these devices up to that point. In fact, despite the frequency of ST having fallen to <1.00% at a mean follow-up of 21.7 months with the most common DES, such a potentially deadly complication is still a substantial downside [26], compounded by the much greater cost compared to BMS. In addition, target lesion revascularization, the prevention of late lumen expansion, and the absence of reactive vasomotion remained unaddressed when both BMS and DES generations remained in the body and were battled as foreign bodies [10,27].

The most recent development in stent technology, biodegradable stents (BDS), is being touted as the way to reduce the aforementioned adverse effects, marking the fourth revolution in interventional cardiology [28]. BDS play a temporary scaffolding role while the vessel wall heals and reorganizes itself. During this time, the stent dissolves, and the organism absorbs the resultant products until the device is eliminated. This way, it is possible for the vessel to restore the vasoreactivity with the potential of vessel remodeling, as stated by Hu *et al.* [10], citing Waksman *et al.* [29]. Different materials have already been used in manufacturing metallic and polymeric BDS. Whilst the most popular polymeric stents include those made of polymers synthesized from lactic acid, glycolic and caprolactone families, such as poly-L-lactic acid (PLLA), poly (lactide-co-glycolide) (PLGA), poly-glycolic acid (PGA), poly (D, L-lactide/glycolide) copolymer (PDLA), poly-D, L-lactide (PDLLA) and poly e-caprolactone (PCL), the metallic options are focused mainly on iron, magnesium and zinc-based alloys [10].

Magnesium is one of the most prominent metallic elements utilized in biodegradable biomedical device production because of its favorable properties, mainly when alloyed. These materials exhibit outstanding features, including excellent biocompatibility [30,31] and a high strength-to-weight ratio [32]. In addition, the magnesium cations that occur from material breakdown under physiological circumstances may be harmlessly and effectively eliminated in the urine [33], and they do not pose any carcinogenic risk [34]. Furthermore, magnesium alloys present excellent castability [35], even better than their aluminium and copper counterparts, and high machinability, so complex designs can be obtained with dimensional accuracy [36].

Despite the indisputable advantages of magnesium and its alloys, their application in the biomedical field, particularly in stent manufacturing, is still challenging, primarily due to their high corrosion rate and poor mechanical strength, which compromise the support provided to the blood vessel. Additionally, coronary

stents are frequently obtained from laser cutting of micro-tubes, which may be found unfeasible for magnesium alloys through conventional processes [37]. Indeed, due to their hexagonal close-packed structure, magnesium and its alloys present limited plasticity and formability at room temperature, requiring the micro-tubes to be produced at high temperatures to activate different slip systems and deliver a homogenous material flow with enhanced formability. However, multiple sequential steps of hot and cold working would be required [38], making obtaining micro-tubes with uniform thickness and high-quality precision impracticable.

These drawbacks significantly restrict the widespread use of magnesium and its alloys in the stents industry. Nonetheless, these constraints provide a window of opportunity and incentive to seek and study innovative strategies for overcoming the known material and manufacturing process-related obstacles.

The *Leaders for Technical Industries – Engineering Design and Advanced Manufacturing* doctoral program proposes a systematic approach to assessing such engineering challenges by training human resources for integration into competitive engineering design and manufacturing scenarios while fostering knowledge through research in relevant areas for disruptive innovation. In this regard, the pursuit of cutting-edge technologies study and the search for new techniques and methodologies to improve understanding in a specific area are driven by the program and are, thus, present in this work. A comprehensive study on the manufacturing process's impact, in particular, the application of ultrasound treatment to a magnesium alloy melt or during its solidification on microstructural, mechanical and corrosion properties, was carried out. Additionally, the effect of the material's properties on the functional performance of a coronary stent during its deployment and in-service time is assessed through finite element analysis (FEA).

1.2. STATEMENT OF THE PROBLEM

The symbiosis between engineering, technology, and health professionals frames the future of healthcare. The increasing complexity of our everyday challenges demands a comprehensive approach by a multidisciplinary team in order to identify the most appropriate and beneficial answer. The manufacturing of biodegradable magnesium alloys through ultrasonic-microcasting is currently under development as part of a team project – *UMTechnology* - carried out in the Foundry Lab at the University of Minho, comprising three main tasks, each associated with a PhD project, namely (i) *Development of a new technique for manufacturing biodegradable magnesium stents (Finished)*, (ii) *Biomechanical performance of magnesium stents obtained by ultrasonic-microcasting. Numerical modeling and material experimental characterization* (**this work**) and (iii) Numerical and *in vitro* study of blood flow to optimize biodegradable

magnesium stents manufactured by micro-casting (*ongoing*). The development of the *UMTechnology* project allowed, therefore, to address the mechanical engineering issues associated with the development of biodegradable magnesium stents, from defining a manufacturing route to the evaluation by finite element analysis (FEA) of their structural, degradation and hydrodynamic performance under physiological-simulated conditions, including the optimization of material properties through ultrasound treatment.

Aiming to surpass the already listed shortcomings of the current manufacturing technology, a micro-casting technique resorting to ceramic moldings was suggested by V. Lopes [39] to produce biodegradable magnesium stents. This fabrication route presents unique advantages compared to the conventional ones, namely:

Time and cost effectiveness	Investment casting makes it feasible to achieve near net-shape components, resulting in a shorter production chain with reduced related costs.
Versatility	Casting procedures enable the production of stents in various sizes and geometries [40] that cannot be produced using laser cutting or other traditional techniques (*e.g.* strut cross-section variation).
Material modification to create customized microstructural and mechanical qualities	Using chemical and/or physical procedures, such as microalloying and ultrasonic treatment, may alter the microstructure and performance of a material.
Improved corrosion resistance	Laser cutting causes thermal damage such as heat-affected zone, microcracks, and tensile residual stress, adversely affecting corrosion processes *in vivo* and increasing corrosion rates [41]. Casting procedures, on the other hand, provide a smooth surface, which helps reduce the material's deterioration.

This manufacturing technique represents a breakthrough in stent production, although its potential has not yet been completely exploited. Specifically, it is unclear whether processing techniques of magnesium alloys can modify the material's structure and thereby change its mechanical and corrosion properties to fit the application requirements. In this regard, the ultrasound treatment of magnesium alloys is a potential technique for refining their microstructure, which is anticipated to influence their mechanical

performance and corrosion resistance significantly. The acoustic energy delivered to the molten metal or solidifying material may refine the grain and intermetallic compounds, enhancing its mechanical properties. Furthermore, the ultrasonic degassing effect helps reduce porosity, which is seriously detrimental to mechanical strength.

Notwithstanding the already pointed advantages of such a methodology, casting magnesium alloys is still challenging due to the material's high reactivity and flammability. In fact, using a protective atmosphere of SF_6 gas is the most common approach to melt magnesium, making the process harmful to the environment as this is the most potent greenhouse gas known. Considering the increasingly restrictive environmental policies and the reasoned concerns about climate change, it must be a global goal to reduce the impact of every human activity, in which manufacturing processes are included, for a more sustainable economy, industry and society. In this sense, alternatives for magnesium casting are also explored in this work.

This research studies the effect of ultrasound treatment on the microstructural and mechanical properties of AZ91D-xCa (x = 1, 1.5, wt.%) in an attempt to determine the optimal processing conditions to meet the performance requirements of a coronary stent. In order to assess the functional performance of coronary stents, numerical simulations of their deployment are conducted using experimental data from the material's characterization as input to the numerical model.

1.3. RESEARCH OBJECTIVES

Magnesium and its alloys are a subject that is gaining a great deal of attention in a variety of fields, including the aeronautical, aerospace, and car industries, as well as the biomedical field. In 2021, in the ScienceDirect database, magnesium and its alloys were the topic of almost 26,000 publications. In addition, a substantial rise in the number of publications on biodegradable magnesium alloys has been seen since 2005, demonstrating their importance.

Several works have been published in this context, focusing on magnesium alloys' microstructure, mechanical properties and corrosion [42]. The exploration of processing procedures to optimize the magnesium alloy's characteristics for use in stents is limited and mostly focused on severe plastic deformation and chemical methods. In addition, even though FEA has been extensively used to model the functional performance of stents, there is still potential to research how material properties affect numerical outcomes.

Hence, it is expected that this work explores the effect of the ultrasound treatment of a magnesium alloy on its microstructural, corrosion and mechanical properties aiming to optimize the functionality of a biodegradable stent assessed through FEA. To accomplish that, a set of multidisciplinary research objectives (**RO**) was established:

RO1: Provide a characterization of the magnesium alloy AZ91D-xCa (x = 1, 1.5, wt.%) obtained through ultrasound-assisted casting by developing a comprehensive study of the effect of the ultrasound treatment processing conditions on the microstructural, corrosion, and mechanical properties.

RO2: Investigate the influence of the ultrasound treatment of the material on their downstream processing (*e.g.,* heat treatment and severe plastic deformation).

RO3: Characterize the corrosion behavior of the AZ91D-xCa (x = 1, 1.5, wt.%) processed under different conditions when subjected to physiological-inspired conditions.

RO4: Develop a numerical model capable of simulating the stent functional performance using the data collected from the material's characterization resultant from the above points.

As stated in the previous sections, magnesium and its alloys are undoubtedly part of the near future of several industries. Nonetheless, challenges concerning their processing and performance must be addressed to allow the magnesium-based components and products to be widespread. By accomplishing the presented RO, this work may contribute to developing knowledge under the scope of magnesium alloy processing, shedding light on their potential.

1.4. THESIS STRUCTURE

This document consists of six chapters, of which three are dedicated to presenting the research work developed to accomplish the objectives defined in the previous section. These chapters are presented in a research paper format comprising the methodology followed, the results obtained, their discussion, and the key conclusions. Following is a brief description of each chapter to give the reader an overview of the work presented herein.

In **Chapter 1**, the setting of the subject and the impetus for the investigation are described. The issue description, research aims, and major contributions of this thesis to scientific knowledge within the domain of magnesium alloy processing and FEA for stent functional performance evaluation are specified.

Chapter 2 is subdivided into two sections focused on the state of the art of (i) processing of magnesium alloys and (ii) application of FEA for stent functional performance assessment. A systematic review of the

application of ultrasound treatment for refining and modifying the microstructure of magnesium alloys was conducted, allowing for discussion of the approaches and results reported in the literature. In the scope of stent behavior simulation, the strategies adopted concerning the simulated system composition, the constitutive material modeling, and the boundary conditions definition are detailed and discussed.

The results concerning the ultrasound treatment's effect on the outcomes of the heat treatment process are presented and discussed in **Chapter 3**. Solution treatment is performed under different temperature and time conditions to assess the influence of the as-cast microstructure on the intermetallics' dissolution kinetics. Furthermore, solution-treated samples are subjected to artificial aging to investigate the material's precipitation behavior. The mechanical properties of the samples are assessed through hardness measurements and uniaxial tensile testing of the material in the as-cast, solutionized, and peak-age conditions.

Considering the relevance of the magnesium-based wires in the biomedical industry, namely for coiled stent manufacturing, billets obtained through conventional gravity casting and ultrasound-assisted casting were extruded to assess this processing route's influence on the corrosion behavior of the extruded material. In this sense, **Chapter 4** details the study of the wires' degradation when subjected to a continuous flow of Earle's Balanced Salt Solution (EBSS) for up to 7 days and compares the results obtained by the two materials considering the corrosion mechanisms involved, the degradation rate and the corrosion products formed. The loss of mechanical strength due to the material deterioration is assessed through uniaxial tensile testing of wires immersed for 48 h to 7 days. The material data is then used as input for the numerical modeling of the stent performance, considering the decrease in the mechanical properties in **Chapter 5**. Additionally, three other case studies concerning the application of FEA to predict the influence of the (i) modeling strategy of the deployment procedure, (ii) material properties, and (iii) stent geometry on the stenting procedure are presented.

Finally, the concluding remarks are briefly presented in **Chapter 6**, as well as the main scientific outputs of this work

1.5. CONTRIBUTION OF THE WORK

The extensive application of magnesium and its alloys depends on advances in safe handling, enhancement of mechanical properties, and increased corrosion resistance. In fact, a shift in the industry paradigms is being driven by the climate emergency and, more recently, by the world society context, characterized by high uncertainty concerning energy availability.

In this regard, the development of the current study, despite its emphasis on enhancing the material performance for use in the production of stents, has yielded findings applicable to other applications, notably structural ones.

The experimental work has proved that melting magnesium alloys without a protective atmosphere is feasible if alloyed with elements such as calcium - AZ91D-xCa (x = 1, 1.5, wt.%) -, opening a new window of opportunities for industrial usage.

The effect of the application of ultrasound treatment under different conditions on the casted products was assessed through microstructural and mechanical characterization. The potential of this processing technique for microstructure refinement and modification was demonstrated. Furthermore, the influence of the ultrasound treatment on the downstream processing of the cast products through heat treatment and extrusion was comprehensively investigated.

The degradation behavior of the AZ91D-xCa (x = 1, 1.5, wt.%) under physiological-inspired conditions was studied through a dynamic immersion test of the wires obtained from non- and ultrasound-treated casted billets in EBSS. This approach produced in-depth knowledge about the influence of the microstructure on the corrosion behavior of the magnesium alloy. Additionally, the degradation of the mechanical properties due to exposure to the corrosive medium was assessed through tensile testing. The acquired material data was then employed as an input in the FEA of the stent's functional performance, allowing for predicting the device's failure caused by a loss of mechanical strength.

CHAPTER REFERENCES

[1] A. Timmis, P. Vardas, N. Townsend, A. Torbica, H. Katus, D. de Smedt, C.P. Gale, A.P. Maggioni, S.E. Petersen, R. Huculeci, D. Kazakiewicz, V. de Benito Rubio, B. Ignatiuk, Z. Raisi-Estabragh, A. Pawlak, E. Karagiannidis, R. Treskes, D. Gaita, J.F. Beltrame, A. McConnachie, I. Bardinet, I. Graham, M. Flather, P. Elliott, E.A. Mossialos, F. Weidinger, S. Achenbach, European Society of Cardiology: Cardiovascular Disease Statistics 2021, European Heart Journal 43 (2022) 716–799. https://doi.org/10.1093/eurheartj/ehab892.

[2] World Health Organization, The top 10 causes of death, 2022.000Z, https://www.who.int/news-room/fact-sheets/detail/the-top-10-causes-of-death, accessed 19 September 2022.655Z.

[3] A. Timmis, N. Townsend, C.P. Gale, R. Grobbee, N. Maniadakis, M. Flather, European Society of Cardiology: cardiovascular disease statistics 2017, European heart journal 39 (2018) 508–579.

[4] D.K. Arnett, R.S. Blumenthal, M.A. Albert, A.B. Buroker, Z.D. Goldberger, E.J. Hahn, C.D. Himmelfarb, A. Khera, D. Lloyd-Jones, J.W. McEvoy, E.D. Michos, M.D. Miedema, D. Muñoz, S.C. Smith, S.S. Virani, K.A. Williams, J. Yeboah, B. Ziaeian, 2019 ACC/AHA Guideline on the Primary Prevention of Cardiovascular Disease: A Report of the American College of Cardiology/American Heart Association Task Force on Clinical Practice Guidelines, Circulation 140 (2019) e596-e646. https://doi.org/10.1161/CIR.0000000000000678.

[5] L. Badimon, T. Padró, G. Vilahur, Atherosclerosis, platelets and thrombosis in acute ischaemic heart disease, European heart journal. Acute cardiovascular care 1 (2012) 60–74. https://doi.org/10.1177/2048872612441582.

[6] M.A. Peña-Duque, J.L. Romero-Ibarra, M.B.A. Gaxiola-Macías, E.A. Arias-Sánchez, Coronary Atherosclerosis and Interventional Cardiology, Archives of medical research 46 (2015) 372–378. https://doi.org/10.1016/j.arcmed.2015.06.005.

[7] J. Groner, A. Goepferich, M. Breunig, Atherosclerosis: Conventional intake of cardiovascular drugs versus delivery using nanotechnology - A new chance for causative therapy?, Journal of controlled release official journal of the Controlled Release Society 333 (2021) 536–559. https://doi.org/10.1016/j.jconrel.2021.03.034.

[8] I. V. Gomes, Biomechanical Optimization and Design for Manufacturing of Magnesium Alloy Stents Produced by Ultrasonic-Microcasting. MSc Thesis, 2017.

[9] Talia F. Malik, Vijai S. Tivakaran, Percutaneous Transluminal Coronary Angioplasty, in: T.F. Malik, V.S. Tivakaran (Eds.), StatPearls [Internet], StatPearls Publishing, 2022.

[10] T. Hu, C. Yang, S. Lin, Q. Yu, G. Wang, Biodegradable stents for coronary artery disease treatment: Recent advances and future perspectives, Materials science & engineering. C, Materials for biological applications 91 (2018) 163–178. https://doi.org/10.1016/j.msec.2018.04.100.

[11] A. Gruntzig, Transluminal dilatation of coronary-artery stenosis, Lancet (London, England) 1 (1978) 263. https://doi.org/10.1016/s0140-6736(78)90500-7.

[12] J. Bukala, P. Kwiatkowski, J. Malachowski, Numerical analysis of crimping and inflation process of balloon-expandable coronary stent using implicit solution, International journal for numerical methods in biomedical engineering 33 (2017). https://doi.org/10.1002/cnm.2890.

[13] H. Bahreinizad, M. S. Bani, A. Khosravi, A. Karimi, A numerical study on the application of the functionally graded bioabsorbable materials in the stent design, Artery Research 24 (2018) 1–8. https://doi.org/10.1016/j.artres.2018.09.001.

[14] A. Curcio, D. Torella, C. Indolfi, Mechanisms of smooth muscle cell proliferation and endothelial regeneration after vascular injury and stenting: approach to therapy, Circulation journal official journal of the Japanese Circulation Society 75 (2011) 1287–1296. https://doi.org/10.1253/circj.cj-11-0366.

[15] A.K. Mitra, D.K. Agrawal, In stent restenosis: bane of the stent era, Journal of clinical pathology 59 (2006) 232–239. https://doi.org/10.1136/jcp.2005.025742.

[16] R. Virmani, A. Farb, Pathology of in-stent restenosis, Current opinion in lipidology 10 (1999) 499–506. https://doi.org/10.1097/00041433-199912000-00004.

[17] J. Wang, H. Luo, Percutaneous Coronary Intervention: A Concise Historical Review, The Cardiologist 1 (2017) 1–9.

[18] D.-H. Lee, J. M. Torre Hernandez, The Newest Generation of Drug-eluting Stents and Beyond, European cardiology 13 (2018) 54–59. https://doi.org/10.15420/ecr.2018:8:2.

[19] E. Camenzind, P.G. Steg, W. Wijns, Stent thrombosis late after implantation of first-generation drug-eluting stents: a cause for concern, Circulation 115 (2007) 1440-55; discussion 1455. https://doi.org/10.1161/CIRCULATIONAHA.106.666800.

[20] P.A. Gurbel, D.E. Kandzari, Stent thrombosis associated with first-generation drug-eluting stents: issues with antiplatelet therapy, Netherlands heart journal monthly journal of the Netherlands Society of Cardiology and the Netherlands Heart Foundation 15 (2007) 148–150. https://doi.org/10.1007/BF03085971.

[21] T. Tada, R.A. Byrne, I. Simunovic, L.A. King, S. Cassese, M. Joner, M. Fusaro, S. Schneider, S. Schulz, T. Ibrahim, I. Ott, S. Massberg, K.-L. Laugwitz, A. Kastrati, Risk of stent thrombosis among bare-metal stents, first-generation drug-eluting stents, and second-generation drug-eluting stents: results from a registry of 18,334 patients, JACC. Cardiovascular interventions 6 (2013) 1267–1274. https://doi.org/10.1016/j.jcin.2013.06.015.

[22] K. Yamaji, L. Räber, T. Zanchin, E. Spitzer, C. Zanchin, T. Pilgrim, S. Stortecky, A. Moschovitis, M. Billinger, C. Schönenberger, F. Eberli, P. Jüni, T.F. Lüscher, D. Heg, S. Windecker, Ten-year clinical outcomes of first-generation drug-eluting stents: the Sirolimus-Eluting vs. Paclitaxel-Eluting Stents for Coronary Revascularization (SIRTAX) VERY LATE trial, European heart journal 37 (2016) 3386–3395. https://doi.org/10.1093/eurheartj/ehw343.

[23] A. Ernst, J. Bulum, New-Generations-Of-Drug-Eluting-Stents-A-Brief-Review, European Medical Journal Interventional Cardiology 1 (2014).

[24] J. Foerst, M. Vorpahl, M. Engelhardt, T. Koehler, K. Tiroch, R. Wessely, Evolution of Coronary Stents: From Bare-Metal Stents to Fully Biodegradable, Drug-Eluting Stents, Comb Prod Ther 3 (2013) 9–24. https://doi.org/10.1007/s13556-013-0005-7.

[25] M.F. Brancati, F. Burzotta, C. Trani, O. Leonzi, C. Cuccia, F. Crea, Coronary stents and vascular response to implantation: literature review, Pragmatic and observational research 8 (2017) 137–148. https://doi.org/10.2147/POR.S132439.

[26] N. Korei, A. Solouk, M. Haghbin Nazarpak, A. Nouri, A review on design characteristics and fabrication methods of metallic cardiovascular stents, Materials Today Communications 31 (2022) 103467. https://doi.org/10.1016/j.mtcomm.2022.103467.

[27] Y. Sotomi, Y. Onuma, C. Collet, E. Tenekecioglu, R. Virmani, N.S. Kleiman, P.W. Serruys, Bioresorbable Scaffold: The Emerging Reality and Future Directions, Circulation Research 120 (2014) 1341–1352. https://doi.org/10.1161/CIRCRESAHA.117.310275.

[28] R. Erbel, C. Di Mario, J. Bartunek, J. Bonnier, B. de Bruyne, F.R. Eberli, P. Erne, M. Haude, B. Heublein, M. Horrigan, C. Ilsley, D. Böse, J. Koolen, T.F. Lüscher, N. Weissman, R. Waksman, Temporary scaffolding of coronary arteries with bioabsorbable magnesium stents: a prospective, non-randomised multicentre trial, Lancet (London, England) 369 (2007) 1869–1875. https://doi.org/10.1016/S0140-6736(07)60853-8.

[29] R. Waksman, Update on Bioabsorbable Stents: From Bench to Clinical, Journal of Interventional Cardiology 19 (2006) 414–421. https://doi.org/10.1111/j.1540-8183.2006.00187.x.

[30] J. Wang, J. Xu, W. Liu, Y. Li, L. Qin, Biodegradable Magnesium (Mg) Implantation Does Not Impose Related Metabolic Disorders in Rats with Chronic Renal Failure, Scientific reports 6 (2016) 26341. https://doi.org/10.1038/srep26341.

[31] J. Dong, T. Lin, H. Shao, H. Wang, X. Wang, K. Song, Q. Li, Advances in degradation behavior of biomedical magnesium alloys: A review, Journal of Alloys and Compounds 908 (2022) 164600. https://doi.org/10.1016/j.jallcom.2022.164600.

[32] S.V.S. Prasad, S.B. Prasad, K. Verma, R.K. Mishra, V. Kumar, S. Singh, The role and significance of Magnesium in modern day research-A review, Journal of Magnesium and Alloys 10 (2022) 1–61. https://doi.org/10.1016/j.jma.2021.05.012.

[33] N.E.L. Saris, E. Mervaala, H. Karppanen, J.A. Khawaja, A. Lewenstam, Magnesium: an update on physiological, clinical and analytical aspects, Clinica Chimica Acta 294 (2000) 1–26. https://doi.org/10.1016/S0009-8981(99)00258-2.

[34] M. Moravej, D. Mantovani, Biodegradable metals for cardiovascular stent application: interests and new opportunities, International journal of molecular sciences 12 (2011) 4250–4270. https://doi.org/10.3390/ijms12074250.

[35] A.A. Luo, Magnesium casting technology for structural applications, Journal of Magnesium and Alloys 1 (2013) 2–22. https://doi.org/10.1016/j.jma.2013.02.002.

[36] B. Jahani, K. Meester, X. Wang, A. Brooks, Biodegradable Magnesium-Based Alloys for Bone Repair Applications: Prospects and Challenges, Biomedical Sciences Instrumentation 56 (2020) 292–304.

[37] V.C. Shunmugasamy, E. Khalid, B. Mansoor, Friction stir extrusion of ultra-thin wall biodegradable magnesium alloy tubes — Microstructure and corrosion response, Materials Today Communications 26 (2021) 102129. https://doi.org/10.1016/j.mtcomm.2021.102129.

[38] J. Wang, Y. Zhou, Z. Yang, S. Zhu, L. Wang, S. Guan, Processing and properties of magnesium alloy micro-tubes for biodegradable vascular stents, Materials science & engineering. C, Materials for biological applications 90 (2018) 504–513. https://doi.org/10.1016/j.msec.2018.05.005.

[39] V.Lopes, Development of a New Technique for Manufacturing Biodegradable Magnesium Stents. PhD, Guimarães, 2022.

[40] X.-Z. Yue, K. Kitazono, X.-J. Yue, B.-Y. Hur, Effect of fluidity on the manufacturing of open cell magnesium alloy foams, Journal of Magnesium and Alloys 4 (2016) 1–7. https://doi.org/10.1016/j.jma.2015.11.007.

[41] M.P. Sealy, Y.B. Guo, J.F. Liu, C. Li, Pulsed Laser Cutting of Magnesium-Calcium for Biodegradable Stents, Procedia CIRP 42 (2016) 67–72. https://doi.org/10.1016/j.procir.2016.02.190.

[42] J. Song, J. Chen, X. Xiong, X. Peng, D. Chen, F. Pan, Research advances of magnesium and magnesium alloys worldwide in 2021, Journal of Magnesium and Alloys 10 (2022) 863–898. https://doi.org/10.1016/j.jma.2022.04.001.

CHAPTER 2 – LITERATURE REVIEW

The development of magnesium-based biomedical devices is a promising research area that presents exciting challenges regarding material processing design and manufacturing.

Although some magnesium alloy stents have previously been introduced to the market, there is still an opportunity to improve the overall devices' performance concerning their mechanical and corrosion-related properties [1].

In this regard, aluminum-containing magnesium alloys provide superior corrosion resistance and enhanced mechanical properties, making them an attractive alternative for stent manufacturing. However, the optimal stent has not yet been developed, and material processing and design optimization will undoubtedly play a role in its development.

This chapter aims to review the literature published in the scope of the main pillars of this research work, namely the ultrasound treatment of magnesium-aluminum alloys and finite element modeling of stents, beginning by highlighting magnesium's contribution to the biodegradable device's domain. Following a methodology for systematic review, the ultrasound-based treatment techniques for magnesium alloys are described and briefly explored. The current state of the art regarding using FEA for stent performance simulation is discussed in light of the stent expansion technique and design optimization methodologies.

2.1. BIODEGRADABLE STENTS – MAGNESIUM AND ITS ALLOYS AS A PROMISING SOLUTION

The third revolution in stent technology, BDS era, aims to eliminate the difficulties associated with earlier generations [2]. This approach involves the development of stents composed of materials dissolved or absorbed by the organism over a period during which the stent offers support for the vessel wall, keeping it open while the remodeling process continues. When the degrading process is completed, it is anticipated that the vessel wall will be healed and, therefore, the restoration of vasoreactivity with the potential of vessel remodeling and the restoration of normal vascular contractility are possible. Also, the restenosis risk is lower than with BMS [3].

These biodegradable devices are intended to provide a scaffolding effect for about 6 to 12 months. Afterward, the vessel expectedly returns to a more natural and healed condition [4]. Thus, the ideal BDS verifies the following principles: (1) the stent rate degradation is such that it matches both the artery healing and remodeling processes, therefore providing enough scaffolding support throughout this period, and (2) the products that result from the degradation process are not harmful to the organism [2]. The progression of the biodegradable stent's breakdown process and loss of mechanical integrity is shown in Figure 2.1.

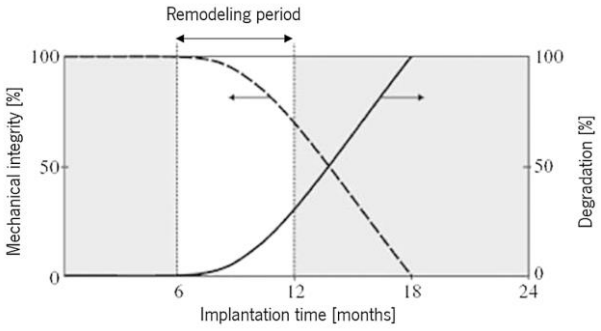

Figure 2.1 – Idealized progress of degradation (solid line) and loss of mechanical integrity (dashed line) of a biodegradable stent (adapted from [5]).

Manufacturing a magnesium scaffold with suitable radial strength for an adequate period without overly thick struts and capable of acting as a drug-delivery platform whose degradation does not produce an unacceptable inflammatory response is a great challenge [5]. Indeed, device makers have offered many stent models over the last few years, but most have failed [6].

Magnesium alloys have superior corrosion resistance and mechanical properties compared to pure magnesium. Hence their use provides significant benefits compared to magnesium alone. Young's modulus and yield strength of these materials are significantly lower than those of stainless steel or nickel-titanium alloys, so stents manufactured in magnesium alloys must have thicker structures to ensure the

scaffolding effect. On the other hand, thicker struts are also associated with higher risks of adverse events such as ISR [7–9].

The first magnesium stent was built in AE21 alloy (Mg-Al-Mn), and its degradation took about one month. Despite so, these preliminary findings were positive since they demonstrated biocompatibility, a minimal inflammatory response, and hypothrombogenicity. Then, BIOTRONIK created and introduced the Lekton Magic version of the device. This innovative stent was manufactured in WE43 magnesium alloy (Mg-Y-Zr-RE) using laser technology and could remain in the organism for about 1 to 3 months. The efficacy of these devices was assessed in a clinical trial whose results revealed that significant vessel recoil caused by early radial strength loss and neointimal proliferation occurred when the biodegradable stent was used [10]. These findings led to a new iteration in which a stent with a modified strut cross-section and cell design was developed. In addition, a refined WE43 magnesium alloy was employed since it exhibited lower degradation rates and improved collapse pressure than the previous model (1.5 bar *vs.* 0.8 bar). Later, antiproliferative drug coatings were applied, resulting in the DREAMS-1G, the first drug-eluting absorbable metal scaffold.

Currently, the second-generation DREAMS is commercialized as Magmaris, a magnesium alloy stent with excellent radial support, longer scaffolding time, and degradation time superior to 12 months. This device provided more flexibility, a more uniform vessel covering, and increased resistance to crushing. A coating elutes sirolimus for more than 3 months, and tantalum radiopaque edge markers were added to enhance the X-ray visibility. Magmaris received CE certification as the first bioresorbable drug-eluting metal scaffold and the third drug-eluting scaffold device after the two-prior polymer-based Absorb BVS and DeSolve [11]. Figure 2.2 illustrates the progress of resorbable magnesium stents and their properties.

As a method to delay the corrosion rate, the alteration of the stent's shape and/or manufacturing process has been suggested [12], and innovative structural design and microstructure modification have been created in recent years. The advancement of the magnesium stents given by BIOTRONIK is one example.

Alternatively, magnesium alloys' chemical composition might be modified to circumvent the abovementioned drawbacks. Mao *et al.* [13] reported a magnesium alloy with the composition Mg-2.2Nd-0.1Zn-0.4Zr wt.%, named JDBM-2, which is suggested to be promising once it combines the benefits of standard medical stainless steel and polymer. Moreover, JDBM-2 provides a highly homogeneous degradation mechanism and long-term structural and mechanical durability. However, incorporating Rare Earth (RE) elements has considerable downsides, the most notable of which is the high cost and environmental effect [14].

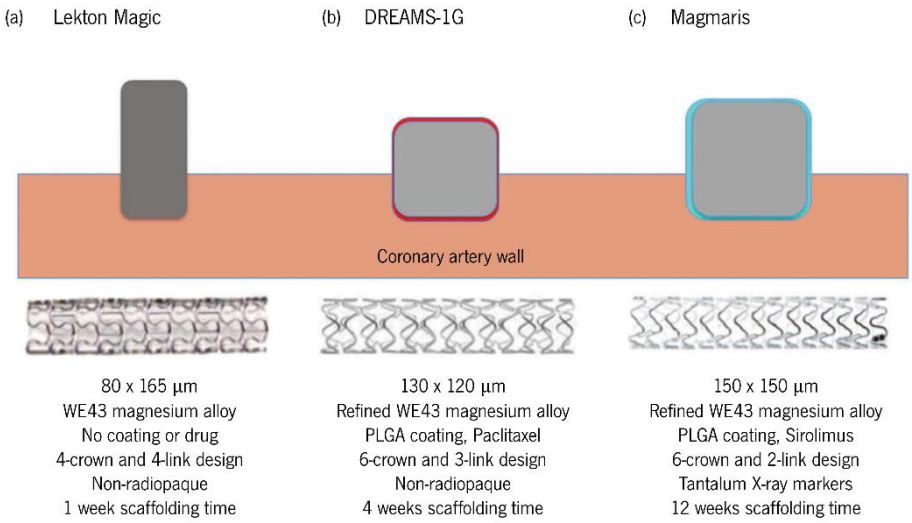

Figure 2.2 – Evolution of magnesium resorbable stents: (a) Lekton Magic, (b) DREAMS-1G, and (c) Magmaris (adapted from [11]).

Consequently, even though the application of such materials represents a breakthrough in this field and a promising alternative to traditional medical stainless steel and polymer for clinical applications, the development of an efficient, cost-effective, and environmentally friendly approach is still lacking.

2.2. MAGNESIUM ALLOYS PROCESSING – THE ULTRASOUND TREATMENT AS THE ROUTE FOR OPTIMAL MECHANICAL PROPERTIES

In recent years, there has been an increase in interest in magnesium and its alloys, particularly for structural applications in the automotive, railway, and aerospace sectors [15–17]. Such popularity stems from an engaging combination of comprehensive properties: low density, high strength-to-weight ratio, excellent machinability, and good castability [18–20]. Moreover, magnesium is pointed to as the best green material of the 21st century, which yields an increasing interest in studying it comprehensively [21].

Despite the desirable characteristics of this material, demanding requirements are imposed on the quality of the products, which emphasizes the need for ongoing development of metal processing technologies [22]. Among other problems in the magnesium casting process, it is common to obtain heterogeneous and coarse dendritic morphology due to its high susceptibility to solidification defects, which is seriously detrimental to magnesium mechanical properties [23].

Several authors have pointed out the microstructure refinement of cast parts as a route for overcoming the material defects enhancing magnesium alloys' mechanical performance [19–24]. Moreover, casting processes that may provide a refined and homogeneous microstructure can be of great value since there is a growing desire for cost-effective procedures capable of enhancing subsequent manufacturing

processes [25]. The grain refinement of aluminum-free magnesium alloys can be easily achieved by adding elements such as zirconium, and some works have already been carried out using additions between 0.2-1.0 wt.% to promote heterogeneous nucleation [26–30]. However, this approach does not produce satisfactory results in magnesium-aluminum alloys owing to the development of stable intermetallic phases between aluminum and zirconium, such as Al_3Zr, which are ineffective as magnesium grain nucleants [31–33]. Likewise, refining elements like carbon, calcium, and strontium may also be added. Nonetheless, the formation of intermediate compounds causes environmental issues [34], hot tearing [35], and reduced ambient temperature properties [36]; therefore, the findings have not been encouraging [37].

The matrix microstructure modification by a physical process may overcome the limitation of chemical refinement methods as it may be applied regardless of the alloy composition and without changing it [20]. In the physical path to grain refining, an external field such as electromagnetic or mechanical stirring/vibration, pulse electric current, or intensive shearing using twin screws, among others, is introduced into the molten material during its solidification [37]. However, some obstacles were discovered in the use of several of these strategies. The application of the mechanical stirring technique is associated with the formation of unpredictable microstructures and phases due to the high temperature of the melt that usually compromises the stirrer's integrity [38]. On the other side, in the electric current pulse technology, the electric pulse needs to be directly passed through the melt, which may result in its contamination, while a pulsed magnetic field requires an extremely high current which can result in undesirable splashing at the top surface of the melt [39,40].

In this context, ultrasound treatment has delivered promising results in refining magnesium-aluminum alloys [41,42], which explains why the number of studies on this subject has increased over the last several years.

Compared to other grain processing methods, this technology offers substantial benefits for industrial applications, including high grain-refining efficiency, simplicity of operation, and low cost, while needing simple equipment that can be easily framed in the industrial environment. Moreover, conversely to what is verified in aluminum alloys' melts, titanium sonotrode, which provides excellent dimensional stability and high efficiency in transmitting the ultrasonic vibration, is very stable and almost insoluble in magnesium alloys, preventing melt contamination [43,44]. Another advantage of ultrasonication is that melt poisoning by oxidation is significantly diminished during irradiation, given that the melt surface is not severely disturbed.

The ultrasonic energy may be delivered isothermally or continuously via an immersed sonotrode into the melt. A non-contact approach may be preferred depending on the melting point and chemical reactivity of the sonotrode material [41]. Microstructure modification mechanisms depend on which treatment is applied, so differences between results are expected. Indeed, the outcomes are conditioned by several factors, including the temperature at which the treatment is applied, its duration, and the ultrasound power deployed.

In this way, ultrasound application for grain refinement of magnesium-aluminum alloys has experienced an interest rise promoted by the potential of these materials for high-tech applications. Although scarcely explored, the refinement of magnesium-based alloys may constitute an interesting route for improving the overall performance of biomedical devices, given that microstructure features are deeply associated with mechanical and corrosion-related properties.

2.2.1. ULTRASOUND TREATMENT CONDITIONS

There are two approaches to grain refining using ultrasound treatment: isothermal or continuous application of ultrasonic vibration to the melt during solidification. Concerning this issue, the research does not indicate a clear preference for one of these techniques over the other, indicating that either may help enhance the microstructure of the materials.

The definition of the ultrasound treatment parameters, such as ultrasound power, processing time, and temperature at which treatment is performed, are key factors that researchers have comprehensively investigated to find the optimal procedure, as presented in Table 2.1 andTable 2.2. The intended application mainly determines the material selection. Still, a tendency to AZ91 (Mg-Al-Zn) trend might be seen in this respect. Such a preference is justified by the popularity of this material for structural applications, despite its high susceptibility to solidification defects, low strength, and low ductility at room temperature [41,45]. Once these drawbacks may be overcome through grain refinement, this alloy becomes a promising candidate for studying ultrasound treatment effects [19].

Table 2.1 – Treatment conditions used in studies of continuous application of ultrasonic treatment during material solidification.

Ref.	Alloy	US Power [W]	US Temperature [°C]	US Duration [s]	OBS.
[20]	AZ31; AZ80; AZ91	NA*	From 725 - 750	420	(a) The melt was homogenized at 725 °C - 750 °C after what it was ultrasonicated.
[24]	AZ91	NA*	From 615 to 580; From 615 to 595; From 595 to 590	NA*	(a) Before the ultrasound treatment, the melt was superheated up to 720 °C, and the furnace was turned off. (b) A thermocouple was inserted near the middle of the melt to acquire the temperature during solidification
[43]	AZ31	1700 W/cm^2	From 730 to 680	180	(a) The material was melted at 730 °C, following which it was removed from the furnace for ultrasonication 680 °C.
[46]	AZ91D	NA*	From 615 to 580	NA*	(a) Before the ultrasound treatment, the melt was superheated up to 720 °C, and the furnace was turned off. (b) A thermocouple was inserted near the middle of the melt to acquire the temperature during solidification.
[47]	AZ31; AJ62; AZ91	1400 W/cm^2	From 680	180	(a) Ultrasound treatment was applied at 680 °C for 180 s after the crucible had been withdrawn from the furnace.
[48]	AZ91	300; 500; 700	From 730	NA*	(a) The melt was poured at 730 °C to a sand mold after what it was ultrasonicated.
[49]	Mg-8Li-3Al	50; 110; 170; 210; 260	NA*	90	(a) The melt was poured into a stainless-steel mold preheated to 600 °C in a preserving heat furnace.
[50]	AZ91D	400	From 680 to 608	NA*	(a) The melt was kept at 700 °C for 15 min for homogenization. The molten alloy was then allowed to cool to 680 °C before pouring.
[51]	AZ80	600	From 650 to 571	NA*	(a) The alloy was heated up to 720 °C and kept at that temperature for 15 min for homogenization after what the furnace was turned off. (b) After ultrasonication, the crucible was withdrawn from the furnace.

NA* - Not Available; NA – Not Applicable

Table 2.2 – Treatment conditions used in studies of the isothermal application of ultrasonic treatment to the melt.

Ref.	Alloy	US Power [W]	US Temperature [°C]	US Duration [s]	Pouring Temperature [°C]	OBS.
[41]	AZ91	400, 600, 800, 1000	680	100	The melt solidified inside the crucible	(a) The melt was modified with C_2Cl_6 at 745 °C and purified with Ar_2 at 720 °C before the ultrasonication. (b) A thermocouple was inserted near the middle of the melt to acquire the temperature during solidification.
[17]	AZ91E	NA*	740	60; 120; 180; 240	720	-
[22]	AZ91	120, 240, 360	700	300	700	-
[23]	AS41	4300 W/cm^2	605; 620	30; 60; 90	605; 620	(a) The material was melted at 700 °C
[52]	AM60; AZ91	500; 1000	650	180; 300; 600	650	-
[45]	AZ91	350	700	1200	720	(a) Ultrasound treatment was applied at 700 °C, after which the melt was heated up to 720 °C
[53]	AZ80	230; 600; 950; 1400	650	NA*	The melt solidified inside the crucible	(a) The melt was kept at 650 °C for 600 s before ultrasonication. (b) After ultrasonication, the melt was water-quenched immediately.
[54]	AZ80	1200 (Single); 600 + 600 (Dual)	650	300	650	-

NA* - Not Available; NA – Not Applicable

In the casting process, magnesium's high reactivity is a concern when melting it, given its tendency to oxidize and burn if no protection against oxidation is used. This behavior is caused by the formation of a loose permeable oxide coating that allows oxygen passage, supporting burning below the oxide at the surface and severely compromising the sanity of the piece due to oxide inclusions [55]. To prevent it, most authors resort to a protective atmosphere composed of CO_2 and SF_6 as their presence promotes the formation of the $MgFe_2$, a compound that blocks the pores of MgO film and makes it more protective against oxidation reactions [56]. An argon atmosphere may also help prevent magnesium alloys from igniting, constituting a less environmentally harmful option. Moreover, combined with calcium microalloying, which has been shown to increase the material's ignition temperature [57,58], this approach may ease the magnesium alloys' handling and processing while offering an eco-friendly manufacturing route.

Concerning the ultrasound treatment, the temperature at which ultrasonic vibration is applied is significantly related to the effect the treatment is intended to promote. Ultrasound processing at temperatures near *liquidus* temperature favors cavitation-enhanced nucleation but inhibits the action of cavitation-induced dendrites fragmentation, which may be detrimental to grain refinement results [59]. On the other hand, the application of ultrasonic vibration to solidifying material is often limited to a temperature range to promote an action during specific solidification phases, namely α-Mg nucleation or intermetallics formation. Regardless of the temperature playing a critical role in the treatment outcomes, the ultrasonic power is a parameter that can also profoundly influence the results of material ultrasonication, despite the type of treatment applied. In this context, different power values were reported in the literature, ranging from 50 W [49] to 1000 W [60], which led to a different material response to the treatment. Considering the approach adopted for the material ultrasonication, no relation appears between the type of ultrasound treatment – isothermal or continuous - and the range of ultrasonic power values applied.

The influence of the acoustic frequency applied was also a matter of study, although most authors had chosen values between 19 and 20 kHz. Chen *et al.* [52] followed a different approach and investigated the influence of the frequency used in the melt treatment of AM60 (Mg-Al-Zn) and AZ91 alloys by comparing the results obtained using 15 kHz and 20 kHz. Such an increase was associated with a shorter period for the growth of the cavitation bubbles in the melt, which became smaller and thus may exhibit a more robust ability for degassing fine cavities on tiny particle surfaces, producing finer microstructure. An original proposal was explored by Ning *et al.* [54], who studied the effect of applying dual-frequency

ultrasonic treatment to an AZ80 magnesium alloy melt and explained the experimental results in light of the numerical ones obtained through simulation of the cavitation phenomenon.

2.2.2. Microstructural and Mechanical Characterization

Microstructural characterization is perhaps the preferred approach to assess the effect of ultrasound treatment. The description of the material's microstructure, namely the grain size and sphericity measurement, is addressed in most articles devoted to the topic. Most research focuses on the effect of ultrasound treatment on the morphology and size of α-Mg. Table 2.3 displays the few known findings addressing the alteration of β-$Mg_{17}Al_{12}$ and Al_8Mn_5 intermetallic phases when the metal molten is treated by ultrasound. Khosro Aghayani and Niroumand [19] and Yang *et al.* [49] have previously identified a lack of research on this topic, which must be addressed given that the morphology of intermetallics might influence the mechanical and corrosion behavior of magnesium alloys [61,62].

In the non-treated condition, the α-Mg phase usually presents coarse and non-uniform dendritic morphology, which is reported to be changed to a finer and more globular one after ultrasound treatment by most authors. Nevertheless, Nie *et al.* [45] and Yang *et al.* [60] have not observed significant changes in the matrix structure. This situation is suggested to be promoted by the large gap between the treating temperature and melting point of the material, which makes it difficult the survival of the newly formed particles that remelt during the interval from the cessation of ultrasonication and pouring of the melt [60]. Moreover, the final grain size depends on the nucleation process and the growth setting. Nie *et al.* [35] showed that a slow latent heat extraction due to a high mold temperature might impair the ultrasound treatment's refining impact.

Table 2.3 – Summary of microstructural analysis results reported in the literature.

Ref.	Type	Microstructural Analysis			
		Phase composition		Grain size [μm]	
		Non-treated	US-treated	Non-treated	US-treated
[41]	Isothermal Treatment	Equiaxed grains of **α-Mg** phase with dot-like particles distributed in the grains.	There was no evident change in the **α-Mg** phase between non- and ultrasound-treated samples. The phase composition remained the same when the applied ultrasonic power was increased. However, intermetallic phases' size, percentage, and distribution altered significantly. **Eutectic phase**: when 600 W of ultrasonic power was applied, the area % of the lamellar eutectic phase grew to its maximum level. A further increase in ultrasonic power resulted in a progressive reduction in the percentage of area. **β-$Mg_{17}Al_{12}$**: when ultrasonic power increased, the fraction of **β-$Mg_{17}Al_{12}$** surface area decreased. **Al_8Mn_5**: the average area of Al_8Mn_5 particles decreases as the ultrasonic power rises to 600 W and then quickly increases as the ultrasonic power rises to 1000 W.	NA*	
[17]	Isothermal Treatment	**α-Mg** phase: coarse-grained structure with a combination of equiaxed and elongated grains. **β-$Mg_{17}Al_{12}$**: large continuous network precipitated along grain boundaries. Mn-Al: blocky and needle-like shapes are not homogeneously distributed through the matrix since large clusters could be observed.	**α-Mg** phase: the grain size was finer than the untreated sample when sonicated for 60 s. However, the microstructure presented a semi-equiaxed structure composed of elongated and equiaxed grains. Additional sonication to 120 s improved the grain size and morphology even further, and the microstructure evolved to a more equiaxed state with a reduced number of elongated grains. Sonicating for 180 seconds, the microstructure became completely equiaxed with a significant decrease in the grain size. Increasing the ultrasound treatment time from 180 to 240 s did not significantly influence the grain size and morphology. **Intermetallic phase**: as the sonication time increased, the **β-$Mg_{17}Al_{12}$** networks became more refined. The ultrasound treatment effectively reduced the overall length of the eutectic networks and improved their distribution. Upon sonicating the alloy for 120 s, the **Mn-Al intermetallics** became more homogeneously distributed throughout the alloy matrix with minimal signs of agglomeration.	202	144 (60 s); 109 (120 s); 50 (180 s, 240 s)

Table 2.3 – Summary of microstructural analysis results reported in the literature (cont.).

Ref.	Type	Microstructural Analysis			
		Phase composition		Grain size [μm]	
		Non-treated	US-treated	Non-treated	US-treated
[20]	Continuous Treatment	Dendritic structure with long arms of **α-Mg** phase.	Non-dendritic fine grains of **α-Mg** phase. A gradual increase in the grain size was observed with increasing distance from the ultrasound radiator.	NA*	
[22]	Isothermal Treatment	**α-Mg** phase: coarse and non-uniform dendritic microstructure. **β-$Mg_{17}Al_{12}$**: continuous network at the grain boundaries. **Mg_2Si**: angular particles dispersed in the matrix. **MgFeAl(Si)**: relatively spherical phase dispersed in the matrix.	**α-Mg phase**: finer and equiaxed dendrites. The grain size decreased, and the grain uniformity increased as the ultrasound power increased. Although the grains were still dendritic, they exhibited fewer branches and shorter arms at higher ultrasonic power, leading to higher sphericity. **β-$Mg_{17}Al_{12}$**: smaller and more fragmented particles. The sphericity of the particles, their uniformity, and distribution were enhanced. Higher ultrasonic power led to better results. **Mg_2Si**: globular and finer particles. The results revealed a decreasing trend for **Mg_2Si** particle size and an increasing trend for their sphericity by increasing the ultrasonic power. The application of 360 W has produced the most refined particles with all **Mg_2Si** particles. **MgFeAl(Si)**: smaller and rounder particles. The increase in ultrasonic power led to better results; however, since these particles are intrinsically round, the effect of ultrasonic treatment was not as significant as on the other intermetallic phases.	280	180 (120 W, 240 W); 125 (360 W)
[23]	Isothermal Treatment	Coarse dendrites with long arms of **α-Mg** throughout the samples demonstrate the dendrite growth mode.	Equiaxed grains of the primary **α-Mg** phase were found along with a network of **β-$Mg_{17}Al_{12}$** intermetallic phase. **Mg_2Si** phase in the Chinese script structure is segregated along the grain boundary. The microstructure obtained after ultrasonication at 605 °C was finer and more globular than the material ultrasonicated at 620 °C. The increase in ultrasound treatment duration led to finer grains, regardless of the processing temperature.	375 (605 °C); 330 (620 °C)	605 °C: ≈ 175 (30 s); ≈ 125 (60 s); ≈ 92 (90 s); 620 °C: ≈ 240 (30 s); ≈ 147 (60 s, 90 s)

Table 2.3 – Summary of microstructural analysis results reported in the literature (cont.).

Ref.	Type	Microstructural Analysis			
		Phase composition		Grain size [μm]	
		Non-treated	US-treated	Non-treated	US-treated
[24]	Continuous Treatment	Coarse dendrites of **α-Mg** phase throughout the sample, demonstrating the normal dendrite growth mode.	The temperature at which the ultrasonic vibration was applied significantly changed the morphology and size of the **α-Mg** phase. **From 615 ºC to 595 ºC** Fine uniform grains of **α-Mg** **From 595 ºC to 590 ºC and from 590 ºC to 580 ºC** Dendritic grains of **α-Mg**. The microstructure of US-treated samples in the temperature range of 590 °C - 580 °C was coarser than that of samples treated at 595 °C to 590 °C but slightly more refined than that without ultrasonic vibration.	500	NA*
[43]	Continuous Treatment	Coarse equiaxed dendritic structure throughout the ingot.	Refined equiaxed grain structure only below the ultrasound radiating face when the sonotrode was deeply immersed in the melt. No noticeable refinement occurred adjacent to the cylindrical face of the sonotrode near the melt surface. When the sonotrode was positioned just touching the solidifying melt, an equiaxed grain structure was obtained at the central region of the sample.	2000	107 (5 mm below the ultrasound radiating face)
[46]	Continuous Treatment	Coarse dendrites of the **α-Mg** phase throughout the samples demonstrate normal dendrite growth.	Refined grains of **α-Mg** phase. The grain morphology is significantly different since it was modified from developed dendrites to non-dendrites grains.	900	195
[47]	Continuous Treatment	NA*	Finer grains of **α-Mg**	NA*	NA*

Table 2.3 – Summary of microstructural analysis results reported in the literature (cont.).

Ref.	Type	Microstructural Analysis			
		Phase composition		Grain size [μm]	
		Non-treated	US-treated	Non-treated	US-treated
[48]	Continuous Treatment	Coarse dendrites of **α-Mg** throughout the samples demonstrate the dendrite growth mode.	The dendritic structure was fragmented, and a more globular phase formed. A gradual decrease in grain size was noticed as the ultrasonic power increased. Although the grain size decreased slightly at 300 W of ultrasonic power, the grain morphology was still coarse. When the ultrasonic power increased to 700 W, the **α-Mg** grains became finer and globular.	202	195 (300 W); 152 (500 W); 146 (700W)
[52]	Isothermal Treatment	Large dendritic grains of **α-Mg** phase.	Fine and more homogeneous microstructure. Tiny particles from the melt were noticed dispersed in the **β-$Mg_{17}Al_{12}$** phase. The grains became finer when the frequency increased from 15 kHz to 20 kHz.	AZ91: 205; AM60: 200	**AZ91**: 125 (600 s, 20 kHz); **AM60**: 90 (600 s, 20 kHz)
[45]	Isothermal Treatment	Microstructure composed of primary **α-Mg** and eutectic phase **β-$Mg_{17}Al_{12}$**. **β-$Mg_{17}Al_{12}$**: plates located mainly at grain boundaries.	**α-Mg phase**: no relevant changes were noticed. **β-$Mg_{17}Al_{12}$**: finer and oriented lamellar phase along the grain boundaries.	NA*	
[49]	Continuous Treatment	Coarse rosette structure of **α-Mg** phase surrounded by **β-$Mg_{17}Al_{12}$** intermetallic phase.	The morphology of the **α-Mg** phase was changed to a finely near-globular structure. The increase of ultrasonic power up to 170 W improved the refining effect remarkedly. Nevertheless, when the ultrasonic power was 260 W, the microstructure got coarser. For 170 W of ultrasonic power, the longer the treatment, the finer the **α-Mg** phase.	≈ 140	US Time = 90 s: ≈ 90 (50 W); ≈ 92 (110 W); ≈ 40 (170 W); ≈ 60 (210 W); ≈ 70 (260 W); US Power = 170 W: ≈ 80 (60 s); ≈ 40 (90 s); ≈ 35 (130 s)

Table 2.3 – Summary of microstructural analysis results reported in the literature (cont.).

Ref.	Type	Microstructural Analysis			
		Phase composition		Grain size [μm]	
		Non-treated	US-treated	Non-treated	US-treated
[53]	Isothermal Treatment	Coarse dendrites with long arms of **α-Mg** throughout the samples demonstrate the dendrite growth mode.	The dendritic phase of the **α-Mg** phase was broken into a near globular one, and the grain size reduced remarkedly as the ultrasonic power increased to 600 W. However, the grain became coarser when the ultrasonic power was 950 W or 1400 W.	387	147 (600 W, 15 s)
[50]	Continuous Treatment	NA*	Finer grain structure and more homogeneous **α-Mg** matrix compared with the untreated samples. Uniform dispersion of the intermetallic phase **β-$Mg_{17}Al_{12}$** along the grain boundaries.	120	64
[51]	Continuous Treatment	**α-Mg** phase: coarse dendritic structure, demonstrating a dendrite growth mode. **β-$Mg_{17}Al_{12}$**: coarse reticular **β-$Mg_{17}Al_{12}$**phase distributed along **α-Mg** boundaries.	**α-Mg phase**: refined equiaxial grains. **β-$Mg_{17}Al_{12}$**: the phase was broken into small fragments and became discontinuous. The number of **β-$Mg_{17}Al_{12}$** particles along the **α-Mg** grain boundaries decreased.	NA*	NA*
[54]	Isothermal Treatment	**α-Mg** phase: dendritic microstructure with developed secondary dendrite arms. **β-$Mg_{17}Al_{12}$**: continuous network along the grain boundaries.	**SUT 20 kHz**: the grains were refined, and the secondary dendrite arms were shortened remarkably. The intermetallic phase was fragmented, and its average area decreased. **SUT 15 kHz**: the secondary dendrite arm almost disappeared, and the roundness was increased. A significant amount of a point-like second phase appeared. **DUT**: the grains became finer and spherical. The second phase distribution was more dispersed and exhibited the shape of a point and short strip. The intermetallic phase average area decreases to its minimum.	174	123 (SUT 20 kHz); 99 (SUT 15 kHz); 80 (DUT)

SUT – Single-frequency ultrasonic treatment; DUT – Double-frequency ultrasonic treatment; OM – Optical Microscopy; SEM – Scanning Electron Microscopy; EPMA - Electron Probe Micro Analyzer; NA* – Not Available

Another interesting finding was shared by Qian et al. [43], who reported that the microstructural refinement was observed almost exclusively below the ultrasound radiating face. The grain refinement effect became less significant in other directions, and the grain size increased progressively with increasing distance to the radiating face. Despite the large cool surface and the melt surface disturbance caused by transverse motion, there was no apparent grain refinement in the vicinity of the cylindrical face of the sonotrode near the melt surface. In this way, the authors demonstrated that the immersion depth of the sonotrode into the melt has no considerable impact on the effect of grain refining. Zhang *et al.* [20] discovered that, although the impact of cavitation diminishes away from the radiator, the whole ingots exhibited refined microstructure, suggesting that sufficient nuclei have been transported and distributed in the bulk melt through acoustic streaming. The fragmentation of the β-$Mg_{17}Al_{12}$ continuous network and its more uniform distribution along α-Mg grain boundaries were the most significant changes concerning the effect of ultrasound treatment on the morphology of this phase [17,41,50,51]. Nie *et al.* [45] also documented a shift from coarse plates to fine and oriented lamellar morphology.

The effect of ultrasonic power on the microstructure of the material was explored in the works of Gao *et al.* [48], Khosro Aghayani and Niroumand [22], Yao *et al.* [49], and Yang *et al.* [60]. Most results showed that the increase in ultrasonic power led to a decrease in grain size, which is explained by the associated intensification of the cavitation phenomenon. However, according to Shao *et al.* [53], there is a threshold value over which the thermal effect compromises the grain refinement ability. The resulting drop in the melt's cooling rate may accelerate grain growth, hence diminishing the effect of ultrasound treatment on grain refining.

Regarding the duration of the treatment, Chen *et al.* [59], Patel *et al.* [23], and Emadi *et al.* [17] stated that longer treatments result in smaller grains.

The Hall-Petch relation [63] describes the relationship between the microstructure of a material and its mechanical properties:

$$\sigma_y = \sigma_0 + k_y d^{-1/2} \tag{2.1}$$

where σ_y is the plastic flow stress [MPa], σ_0 is the friction stress of mobile dislocations [MPa], k_y defines the characteristic constant that depends on the number of impurities and alloying elements [MPa·nm$^{1/2}$], and d is the grain size [nm]. In this sense, it is expected that the grain refinement effect of ultrasound may be reflected in enhancing the mechanical performance of the treated material, namely in its tensile properties (Table 2.4).

Table 2.4 – Summary of mechanical properties reported in the literature.

Ref.	Type	Mechanical Properties							
		Yield Strength [MPa]		Tensile Strength [MPa]		Elongation		Hardness [HV]	
		Non-treated	US-treated	Non-treated	US-treated	Non-treated	US-treated	Non-treated	US-treated
[41]	Isothermal Treatment	NA*							
[17]	Isothermal Treatment	95	111	138	161	1.35	2.2	NA*	NA*
[20]	Continuous Treatment	NA*							
[22]	Isothermal Treatment	NA*							
[23]	Isothermal Treatment	NA*							
[24]	Continuous Treatment	NA*							
[43]	Continuous Treatment	NA*							
[46]	Continuous Treatment	81	94	288	376	14.9	22%	NA*	NA*
[47]	Continuous Treatment	NA*	NA*	NA*	NA*	NA*	NA*	NA*	NA*
[48]	Continuous Treatment	NA*	NA*	145	162 (300 W); 166 (500 W); 195 (700 W)	2.3%	4% (300 W); 4,5% (500 W) 5.2% (700 W)	NA*	NA*

Table 2.4 – Summary of mechanical properties reported in the literature (cont.).

Ref.	Type	Mechanical Properties							
		Yield Strength [MPa]		Tensile Strength [MPa]		Elongation		Hardness [HV]	
		Non-treated	US-treated	Non-treated	US-treated	Non-treated	US-treated	Non-treated	US-treated
[52]	Isothermal Treatment	NA*	NA*	AZ91: 170; AM60: 183	AZ91: 156 (1000 W, 20 kHz, 600 s); AM60: 175 (1000 W, 20 kHz, 600 s)	AZ91: 3.7 %; AM60: 5.6 %	AZ91: 2.5 % (1000 W, 20 kHz, 600 s); AM60: 5.4 (1000 W, 20 kHz, 600 s)	AZ91: 72; AM60: 64	AZ91: 80 (1000 W, 20 kHz, 600 s); AM60: 64 (1000 W, 20 kHz, 600 s)
[45]	Isothermal Treatment	No significant difference was noticed	No significant difference was noticed	120	160	2%	4%	NA*	NA*
[49]	Continuous Treatment	NA*	NA*	170	184 (170 W, 90 s)	14%	18.50 % (170 W, 90 s)	NA*	NA*
[53]	Isothermal Treatment	NA*							
[50]	Continuous Treatment	NA*	NA*	160	225	1.4%	3.5%	65	78
[51]	Continuous Treatment	87	107	118	170	2.1%	5.4%	NA*	NA*
[54]	Isothermal Treatment	110	119 (SUT 20 kHz); 125 (SUT 15 kHz); 146 (DUT)	145	155 (SUT 20 kHz); 174 (SUT 15 kHz); 193 (DUT)	NA*	NA*	NA*	NA*

A network of the brittle β-$Mg_{17}Al_{12}$ phase resulted in poor mechanical characteristics in non-treated samples, specifically low ultimate tensile strength and elongation. It was hypothesized that refining this phase would significantly enhance these properties [22]. Nie *et al.* [45] performed a solution heat treatment for dissolving β-$Mg_{17}Al_{12}$ and compared its mechanical performance to an ultrasound-treated sample to corroborate this theory. The identical results obtained by both samples confirmed that the reduction of β-$Mg_{17}Al_{12}$ continuity was behind the enhancement of the material's mechanical behavior. Besides, the refinement of grains suppresses deformation by twinning and promotes deformation by sliding, leading to enhanced ductility [46,48]. The same authors also suggested that the absence of significant change in the yield properties of the ultrasonicated material was due to its weak effect on refining the α-Mg phase. This assumption agrees with the results presented by other authors [17,51,54], who achieved finer microstructures and improved yield strength.

2.2.3. MECHANISMS BEHIND ULTRASONIC REFINEMENT ABILITY

Ultrasound's widespread use in material processing stems from its remarkable ability to modify the different phases and tailor the microstructure of light alloys. Indeed, the control of the material solidification is crucial for improving the mechanical performance, cast quality, and downstream processability of such alloys [64]. Despite that, the mechanisms that explain the ultrasound refining effect are still the focus of several investigations, and a comprehensive explanation has not been formulated yet.

The material microstructure is complex and multiphase, consisting of primary grains and intermetallic and eutectic compounds. In this sense, the design of refining procedures is of tremendous scientific and technological importance, but it requires an in-depth understanding of the material behavior during its solidification [20].

Cavitation and acoustic streaming are frequently pointed to as the main mechanisms behind the efficacy of ultrasound treatment regarding microstructure refinement. The cavitation phenomenon promotes a set of effects that may be associated with a more refined microstructure, namely: (1) formation of localized high-pressure points in the molten melt, which, according to the Clausius-Clapeyron equation, increases its melting point, resulting in significant localized undercooling and intensified nucleation; (2) development of pressure pulses during the compression period of the acoustic wave as a result of the collapse of cavitation bubbles, promoting the rupture of large grains and dendritic arms as well as the disintegration of inoculation substrates clusters; (3) vaporization of the melt at the surface of the bubbles during the expansion period of the acoustic wave, promoting the decrease of the temperature at the interface where

solid particles start nucleating; upon the collapse of the bubbles, the newly formed particles are dispersed into the melt; and (4) increase of impurities and solid particles wettability, favoring heterogeneous nucleation. Furthermore, acoustic streaming, a liquid flow promoted by the acoustic pressure gradient, plays an essential role in developing mechanical forces that fragment the dendrite arms and disintegrate the particle's agglomerates. Additionally, it is beneficial for melt stirring [65].

The discussion of the mechanisms that underlie the ultrasound's ability to refine the material's microstructure is reported by most of the works. A summary of the proposed mechanisms is in Table 2.5.

Table 2.5 – Ultrasound treatment mechanisms proposed in the literature.

Ultrasound Treatment Mechanisms	References
Increase of impurities wettability/ Heterogeneous nucleation	[17,42,45–47,50,52,53,66–68]
Promotion of the recently formed nuclei survival through increased cooling rate due to (i) metal chill effect of the ultrasound horn and (ii) streaming effect, which promotes the melt stirring and, thus, its faster cooling.	[46,48,68]
Increase in phases melting point promoted by the pressure pulse caused by cavitation	[41,47,66,67]
Cavitation through undercooling verified at the melt/bubble interface leads to local nucleation of the solid phase.	[48,52,66,67]
Dispersion of the recently formed nuclei in the melt, enhancing heterogeneous nucleation.	[19,41,42,48,51,52,66]
Disintegration and distribution of the agglomerated nucleant particles	[53,66]
Local melting of thinner parts and sharp edges leading to their spheroidization	[22]
Fragmentation of the intermetallic phases	[50,51]
Hard and soft impingement	[22]
Decrease of solute enrichment at the solidification front due to high-speed flow originated by the collapse of cavitation bubbles	[51]
Increase of cavitation area and initial cavitation nucleus	[53]
Fragmentation of the dendrites under the action of pressure waves promoted by cavitation bubbles collapse	[50,51]
Mn-Al particles' nucleation from the oxide followed by them acting as nucleant for α-Mg	[17]

Although the vast importance of cavitation and acoustic streaming in modifying the microstructure is well-accepted, the investigation of other contributions from nucleation, particle fragmentation, and coarsening is still scarce [20].

The temperature during cooling at which the different phases are formed defines how ultrasound treatment may modify the materials' microstructure [22]. In this sense, the processing temperature is a key parameter that may be selected to activate a particular mechanism or effect on a specific phase.

Indeed, Patel *et al.* [23] applied ultrasonic vibration isothermally to AS41 (Mg-Al-Si) melt at 605 °C and 620 °C and observed variations in the microstructure of the material. Above *the liquidus* temperature, ultrasonication promoted the formation of equiaxed grains, whereas, below the liquidus temperature, globular grains were obtained. Towards these results, the authors proposed different mechanisms for the refining effect of ultrasound treatment according to the processing temperature. The application of ultrasonic vibration above the *liquidus* temperature is suggested to promote cavitation and therefore (i) enhance heterogeneous nucleation through the increase of melting point of the phases, (ii) improve the wettability of impurities and inclusions that become active in the solidification stage, and (iii) induce endothermic vaporization of liquid at the formed bubbles. At lower processing temperatures, the authors hypothesized that the refining effect was caused by the fragmentation of dendrites caused by the implosion of cavitation bubbles, followed by the formation of globular grains from fragmented dendrite arms. In addition to the distinct mechanisms that act at different temperatures, the survival of the newly formed nuclei is deeply dependent on this parameter. In this regard, Nie *et al.* [45] found that although ultrasound treatment had improved impurities' wettability and favored heterogeneous nucleation, no significant refinement of the α-Mg phase was observed. According to the authors, the remelting of the newly formed nuclei may be the reason for such results since the melt was elevated to a pouring temperature of 720 °C after ultrasonication.

Khosro Aghayani and Niroumand [22] reported an opposite conclusion, which showed the action of ultrasonic cavitation on cleaning poorly wetted surfaces as the fundamental mechanism underlying the attainment of a considerably finer microstructure. Additionally, they stated that cavitation and streaming phenomena played a critical role in the disintegration and distribution of agglomerated nucleant particles. The increased active nuclei led to earlier hard and soft impingement of the grains and, thereby, to the microstructure refinement.

Concerning intermetallic phases, the effect of ultrasonication is debated regarding mainly β-$Mg_{17}Al_{12}$ morphology. The β-$Mg_{17}Al_{12}$ phase has a formation point of 460 °C [69], which is far below the *liquidus*

temperature of magnesium alloys. Consequently, it is not expected that the pressure pulses may trigger such a high undercooling, so acoustic streaming is suggested to be the dominant mechanism behind this phase refinement. In this regard, Yang *et al.* [60] indicated that the acoustic stream promotes the decrease of aluminum boundary segregation and, hence, the decrease of aluminum concentration at the grain boundaries. According to the lever rule, such an event leads to a decrease in β-$Mg_{17}Al_{12}$ formation. Another interpretation was proposed by Khosro Aghayani and Niroumand [22]. They hypothesized that the increased grain boundaries of α-Mg and the more uniform chemical composition of the melt were the mechanisms behind the precipitation of β-$Mg_{17}Al_{12}$ phase at more locations, decreasing its continuity and size. Puga *et al.* [50] suggested fragmentation of the β-$Mg_{17}Al_{12}$ phase under acoustic streaming as a promoter of intermetallic refinement, which is likely to happen once the authors applied the ultrasonic vibration to the mold during the material solidification.

The dynamic of Al_8Mn_5 phase formation under ultrasonic vibration was described by Yang *et al.* [60], who applied ultrasonic vibration isothermally at 680 °C, about 20 °C above the melting temperature of that phase. The authors suggested that the rapid pressure pulses induced by cavitation might enhance the Al_8Mn_5 phase's melting point, resulting in significant local undercooling. Thus, the Al_8Mn_5 nuclei were formed and uniformly distributed through acoustic streaming, leading to a refined intermetallic phase. A similar explanation was proposed by Khosro Aghayani and Niroumand [22] for the refinement of Mg_2Si and MnFeAl(Si) intermetallic phases when subjected to ultrasound treatment. The same authors also reported the local melting of thinner parts and sharper edges of these phases due to temperature increase during half-period compression of cavitation bubbles. Such a phenomenon increased the number of growing intermetallics and promoted spheroidization.

Table 2.6 present a summary of the objectives of the main articles in this scope and their key findings to provide the reader with an overview of studies' evolution in this field.

Table 2.6 – Summary of the key findings reported in recent years.

Ref.	Key Findings
[41]	The microstructure of AZ91 alloy consisted of α-Mg phase, dot-like Al8Mn5 phase in matrix, black nodular β-$Mg_{17}Al_{12}$ phase, and netted shape eutectic structure at grain boundaries. The grain size of α-Mg grains did not decrease significantly, and the average area of Al_8Mn_5 particles decreased to the minimum when the applied ultrasonic power was increased to 600 W. Further power increase caused an inversion in such a tendency. The microstructure modifications were mainly associated with acoustic cavitation. The area percentage of β-$Mg_{17}Al_{12}$ decreased gradually with increasing the applied ultrasonic power. The fraction change is mainly attributed to the acoustic streaming by reducing the boundary segregation of aluminum.
[17]	The ultrasound treatment successfully refined the grains of the alloy. The application of ultrasound vibration for 180 s led to a significant decrease in the grain size (nearly 75 %) compared to the non-treated condition. This outcome was attributed to the cavitation-related cleaning and distribution of fine oxides as substrates for heterogeneous nucleation. The area fraction and average size of the deleterious β-$Mg_{17}Al_{12}$ eutectics were decreased. This was thought to be a side effect of the refined grains that resulted from ultrasound treatment. Sonication of the melt resulted in increased area fraction, improved distribution, and spheroidization of the Mn-Al intermetallics. This outcome was believed to directly affect ultrasound treatment through improved nucleation and cavitation-induced undercooling of the melt. The sonication process enhanced the mechanical properties of the alloy. The tensile and yield strengths of the alloy increased by 17%, and the ductility by 63%. Finer grain size, decreased β-$Mg_{17}Al_{12}$ volume fraction, and improved Mn-Al intermetallics distribution were thought to have contributed to this outcome.
[20]	Ultrasonication during the solidification of Mg-alloys AZ31, AZ91, and AJ62 showed extensive grain refinement. The refinement effect was more intense near the radiator, where the grain size was smaller. The grain size increased gradually as the distance increased. A direct correlation between the average grain size and the solute growth restriction factor was observed in the alloys indicating that strong fluid flow under ultrasonication does not diminish the growth restriction effect of solute. Grain refinement under ultrasonication was attributed to enhanced nucleation, indicating an increase in the number and potency of nucleating agents. At the same time, the eutectic and intermetallic modification was suggested to be a growth-related phenomenon caused by coarsening and spheroidization under the strong fluid flow from cavitation.

Table 2.6 – Summary of the key findings reported in recent years.

Ref.	Key Findings
[22]	Applying ultrasonic vibration to the melt before casting significantly affected the size and sphericity of α-Mg dendrites and the size, continuity, sphericity, and distribution of intermetallic particles formed during the cooling and solidification of the alloy. The increase in the ultrasonic power provided smaller, more rounded, and better-distributed grains and intermetallic particles. The microstructural effects were primarily associated with the cavitation and streaming phenomena during ultrasound treatment in the melt. The ultrasound treatment significantly enhanced the tensile strength of the AZ91 alloy. Such an effect was suggested to be a consequence of the discontinuity and refinement of β-$Mg_{17}Al_{12}$ particles in these samples.
[23]	In the ultrasonicated AS41 alloy, a nearly non-dendritic and refined microstructure was obtained instead of the non-uniform dendritic structure of the non-treated samples. Equiaxed grains formed when the ultrasonication was applied above the *liquidus* temperature, while globular grains were obtained when the material was ultrasonicated below the liquidus temperature. The average grain size decreased with an increase in the treatment time. After the ultrasound treatment, the β-$Mg_{17}Al_{12}$ and Mg_2Si intermetallic phases were well-distributed along the grain boundaries.
[24]	The decrease in the temperature at which the ultrasound treatment is performed leads to the reduction of the nucleation temperature and promotes the increase of the undercooling for nucleation. The application of ultrasonication at temperatures from 615 °C to 580 °C and from 615 °C to 595 °C developed an undercooling smaller than the other tested conditions. The difference between them was approximately 2 °C. The coarse dendrites formed with ultrasonic vibrations at temperatures below the *liquidus* temperature, while the finer microstructures were provided by ultrasonication during the nucleation stage. The grain refinement mechanism was discussed based on an analysis of the solidification behavior under ultrasonic vibration. The authors suggested that a combination of enhanced heterogeneous nucleation and dendrite multiplication led to the grain refinement obtained.
[43]	Ultrasonic refinement occurred almost exclusively below the radiating face. No refining effect was observed adjacent to the cylindrical face of the sonotrode immersed in the melt, despite providing a large chill surface and disturbing the melt surface through transverse motion. The immersion depth of the sonotrode in the melt has no noticeable impact on the resulting ultrasonic refinement. The finest grain size resulting from ultrasonication occurred immediately below the radiating face, and the grain size increased progressively with increasing distance from the radiating face towards the crucible walls. Ultrasonic refinement is symmetrical about the principal ultrasound propagation direction. The grain size along the principal propagation direction is progressively smaller than in other directions at the same distance from the radiating face.

Table 2.6 – Summary of the key findings reported in recent years.

Ref.	Key Findings
[47]	On average, the grain density of the ultrasonicated material increased by a factor of 8 x 103 compared to the non-treated one. According to the authors, such a significant increase in grain density is associated with a dramatic rise in active nucleants. In addition to the increase of the grain density, the presence of uniform equiaxed grains suggests that the grain refinement achieved is more likely due to enhanced nucleation than dendrite fragmentation.
[48]	The increase in the ultrasonic power used in the treatment of the material during its solidification led to an increase in both nucleation and cooling rates. This way, the refinement of the AZ91 microstructure was promoted. The coarse dendritic microstructure of the non-treated material was gradually transformed into a more globular and finer one as the ultrasonic power increased.
[52]	Ultrasound treatment of the melt is a new approach for magnesium and magnesium alloy casting. The fundamental basis is the generation of cavitation bubbles during ultrasonic treatment of the melt, which induces dispersion and degassing action. The application of ultrasonic vibration promoted the eutectic phase's refinement, the oxide films' disruption, and the reduction of the inclusion of particle size. Ultrasound treatment had a grain refining effect on cast magnesium and AZ91 and AM60 magnesium alloys, but no improvement was observed regarding their mechanical properties. The effects of grain refinement increased with increasing acoustic frequency, power, and treatment time. The results of grain refinement gradually faded with increased settling time of the melts after ultrasound treatment.
[45]	The effect of ultrasonic vibration and solution heat treatment on microstructures and tensile properties of AZ91 alloy was experimentally investigated. Ultrasonic vibration substantially affected the sphericity and distribution of the β-$Mg_{17}Al_{12}$ phase formed during the cooling and solidification of the alloy. The solution heat treatment dissolved the β-$Mg_{17}Al_{12}$ in both alloys with and without ultrasonic vibration. AZ91 samples subjected to ultrasonic vibration exhibited improved tensile properties compared to non-treated ones. The effect of solution heat treatment on the morphology of β-$Mg_{17}Al_{12}$ in the alloy can improve the tensile properties. Such results suggest that the β-$Mg_{17}Al_{12}$ phase precipitation at grain boundaries may be detrimental to the mechanical performance of AZ91 alloy.
[49]	Mg-8Li-3Al alloy microstructure was composed of α and β phases. α-Mg was modified from a coarse rosette-like structure to a finely globular one through ultrasound treatment. A finely rounded structure was obtained, especially when the power was 170 W. This effect became better as the duration of the treatment increased. An improvement of 9.5% and 45.7% were achieved in the tensile strength and elongation, respectively, when ultrasound treatment was applied at 170 W for 90 s.

Table 2.6 – Summary of the key findings reported in recent years.

Ref.	Key Findings
[53]	Ultrasound treatment of the melt refined the microstructure of the AZ80 alloy. The authors suggested that such an effect was due to both cavitation and streaming phenomena. The increase of ultrasonic power from 0 W to 600 W led to a significant decrease in the grain size, but such a tendency changed when the power increased further. The optimal ultrasonic power for the ultrasonic grain refinement of the AZ80 alloy was 600 W.
[50]	The application of high-intensity acoustic vibration promoted a uniform dispersion of the β-$Mg_{17}Al_{12}$ intermetallic phase and reduced porosity. Both tensile strength and strain were increased by 40.7 % and 150 %, respectively, when the material was processed through ultrasound vibration applied to the mold. Ultrasound treatment in the AZ91D samples suggested improving static mechanical properties without compromising the dynamic mechanical properties of these alloys.
[51]	The microstructure of AZ80 alloy was remarkably improved after ultrasound melt treatment. The primary α-Mg phase was changed from coarse dendrites to refined equiaxed grains, and the continuous brittle β-$Mg_{17}Al_{12}$ phase at α-Mg boundaries was refined and became discontinuous. Ultrasound treatment decreased the segregation of aluminum at the grain boundaries, and more aluminum dissolved into the α-Mg matrix. The tensile properties of AZ80 alloy with ultrasound treatment were significantly improved compared to those of the non-treated alloy. Such achievement was mainly related to the nearly equiaxed microstructure and dispersed β-$Mg_{17}Al_{12}$ phase at the grain boundaries.
[54]	The effect of refinement of ultrasonic is better than conventional casting. The 15 kHz SUT refinement is higher than 20 kHz, and the 15 + 20 kHz DUT refinement grants the best results. The samples treated under DUT exhibited the highest tensile strength, followed by 15 kHz SUT and 20 kHz SUT. Numerical studies performed by the authors showed that the cavitation area gradually increased with the initial cavitation nucleus radius. In the range of initial cavitation radius, the cavitation area produced by 15 kHzSUT was approximately twice that of SUT 20 kHz; After applying DUT, changing the spatial distribution of the cavitation area and increasing of cavitation area were caused by nonlinear superposition, and the cavitation area was more significant than the sum of the two SUT cavitation areas, which justifies the improved results

The refinement of magnesium alloys is a hot topic that brings together the interest of both academic and industrial researchers. Indeed, the results obtained mainly at the laboratory scale may be interpreted with optimism regarding its scale-up to the industrial environment. This way, research might be conducted to fully comprehend this processing approach's prospective outcomes and untapped capabilities. The study of the influence of ultrasonication on the material's microstructure may bring vital information to clarify the latter's role in mechanical behavior and shed light on different deformation mechanisms. Such knowledge is of great value in improving the downstream processability of magnesium alloys. Also, ultrasound treatment's role in these alloys' corrosion behavior is yet to be discussed. Comprehensive knowledge of the effect of ultrasonication on the overall performance of magnesium alloys can open a

broad new range of possible applications from which biomedical devices can be suggested as one of the most promising ones.

2.3. THE ROLE OF FINITE ELEMENT ANALYSIS IN THE STENT DESIGN

Since more than a decade ago, FEA has been used in the development process of medical device design. The finite element method (FEM) is a numerical approach that computes reactions across a discrete number of points – nodes – over the domain of interest, allowing the solution of boundary value problems. Its application in the biomedical device's design may provide critical information about the device's performance in virtual conditions that represent its real application which is then used for further optimization of the product. Before investing in costly prototype and bench testing equipment, FEA is a quick technique to collect device performance data, accelerating the development time and decreasing bench testing iterations [70].

2.3.1. STENT DEPLOYMENT PROCEDURE – THE SYSTEM ELEMENTS CONSIDERED IN THE NUMERICAL MODEL

One of the pioneering works involving the application of FEM in the prediction of stent behavior was presented by Whitcher *et al.* [71]. In this approach, the author studied the fatigue behavior of a nitinol stent, which was modeled as elastic-plastic despite its superelastic properties. This formulation does not provide a complete constitutive model for nitinol alloys, but it is revealed to be satisfactory predictive of the laboratory behavior for load cases at isothermal conditions and monotonic load cases. In this study, only the preload, which corresponded to the artery reaction on the stent, and the pulsatile radial forces resultant from systole and diastole were considered. The results showed that the peak tensile stresses were opposite the contact area. These values were used to develop the Goodman diagram for fatigue analysis, and the numerical model effectively predicted the experimental fatigue test. Although original, this study had significant shortcomings, namely the simplistic material constitutive modeling of nitinol and the neglect of the remaining elements of the system, i.e., the artery and the atherosclerotic plaque.

Following this example, more research has been performed to study the stent behavior in multiple scenarios, from the crimping process through the deployment procedure. Different authors have proposed several simulation strategies, reflecting different levels of complexity and accuracy. An overview of the developed works in FEA of stenting procedure allows noticing that several methods were adopted regarding the simulated system, the material formulation, and the boundary conditions, enabling the comparison of the obtained results in each approach.

According to Auricchio et al. [72], even though the need for accurate and better biomechanical studies focusing on the stenting method has previously been acknowledged, there was a severe lack of research in this field for a considerable amount of time. Indeed, in the same study, the authors highlighted some of the limitations of the previous research, namely (1) the omission of some of the elements involved in the stenting procedure, such as the plaque and the artery, (2) the simplification of the material models, which have different and quite complex constitutive models, and (3) the lack of a fully three-dimensional approach to the problem. In order to reach these results, the research team performed a study whose main goal was to investigate the revascularization of a stenotic artery through the deployment of a stent by building a three-dimensional model of the complete system. The authors used a straight artery segment and an atherosclerotic plaque modeled with a symmetric parabolic longitudinal profile, considering stenosis of 53 %. Due to the lack of accessible experimental data, both the artery and the plaque were considered homogeneous isotropic materials, using polynomial strain energy to model their behavior. The stent's inelastic behavior was described as resorting to a von Mises-Hill plasticity model with isotropic hardening. The presence of the balloon was represented by the application of a linear pressure increasing from zero to 1.30 MPa in the inner surface of the stent, promoting its expansion, and a first study considering the stent's free expansion was carried out. The results showed that the stent's expansion was not uniform, with the distal ends opening more than the central region of the device, in a positive dogboning characteristics behavior. This situation may lead to vessel damage and must, thus, be avoided. To address this issue, the authors inserted distal struts into the stent, resulting in a more uniform expansion profile. In this regard, the modified stent was simulated considering the plaque and artery. The results obtained regarding foreshortening, metal-artery ratio, and elastic recoil were very close to those relative to the original device and reported in the literature.

Even after the authors had presented their approach considering all the elements involved in the stenting procedure, the option of using only the stent to simulate the deployment procedure continued to be adopted in several studies [73–78]. Nonetheless, this study constituted a substantial advancement in the area of stent research, and it also provided several ideas for further research, such as evaluating the balloon's presence and the artery's composite structure. Moreover, this study presents one of the first strategies of stent geometry optimization, which, although based on the try-and-error method, has been proven effective in reducing the dogboning metric.

2.3.2. STRATEGIES FOR INFLATION BALLOON MODELING

The inclusion of the balloon in the stenting deployment numerical model as the promoter of the stent expansion was later proposed by Chua *et al.* [79]. In this approach, the authors used a cylinder to represent the balloon, modeled by a hyperelastic two-parameter Mooney-Rivlin law, and a Palmaz-Schatz-inspired stent geometry. When the inner surface of the balloon was exposed to increasing pressure, the stent expanded radially until failure stress was attained. The focus of this study was to analyze the stress distribution over the stent structure and its foreshortening. The results showed that the highest stress values were found in the corners of the stent cells, in their middle or bridging struts, as they are pulled apart from the remaining cells to assume a rhomboid shape. The stent exhibited a foreshortening of around 5 %. Although this work has brought a novelty by considering the presence of the balloon, it was still possible to identify some gaps that motivated further investigations, such as the absence of both the blood vessel and the atherosclerotic plaque, the neglection of the crimping phase previous to the stent deployment and the lack of experimental work to validate the numerical model. To overcome some of the limitations identified in this work, the same authors developed a complete model which included all the elements involved in the stenting process, i.e., the stent, the balloon, the artery, and the atherosclerotic plaque [80]. The authors concluded that the maximum stress location did not change despite both the artery and the plaque and remained at the cell's corners. Regarding the blood vessel, the maximum von Mises stress occurred near the symmetry edge of the plaque, indicating the risk of plaque rupture. Another important conclusion drawn from this study was that the presence of the plaque and the artery led to the need for increasing the applied pressure to reach the same diameter, as can be observed in Figure 2.3.

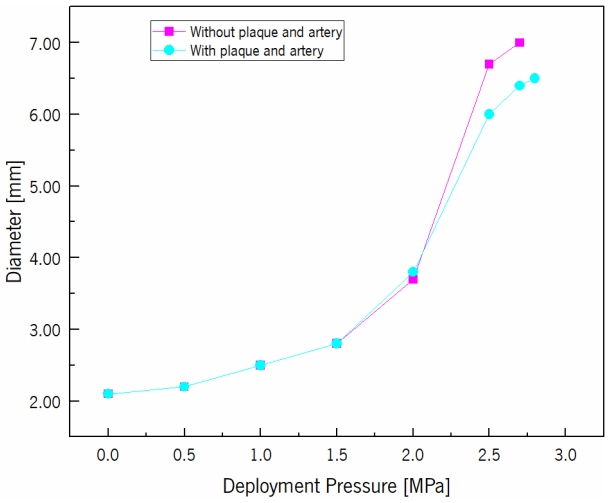

Figure 2.3 – Evolution of stent diameter with the deployment pressure obtained by Chua et al. [80].

As a result of including the balloon in the numerical simulation model, important questions have arisen concerning its geometry and constitutive material modeling. Various strategies, ranging from adopting a

basic cylinder to the actual fold-shaped balloon, were explored, and numerous studies were conducted to determine the effect of the balloon modeling technique on stent performance.

Polymeric materials are commonly used for balloon fabrication, and cylindrical models cannot accurately model their properties since they do not represent the initial phase of balloon expansion, which corresponds to its unfolding. To overcome such limitation, Liang *et al.* [81] developed an innovative approach to simplify the deployment procedure by using a stress-strain curve divided into two segments: the first one, with a lower slope, represented the phase of the folded balloon deploying to its original diameter, characterized by significant deformations under low pressures, and the second one, with higher slope, corresponding to its elastic expansion.

Other attempts were presented by several authors, such as Gervaso *et al.* [82], who tested three different modeling solutions that could be adopted to study stent-free expansion and stent expansion inside an artery: (i) uniform pressure imposed on the internal surface of the stent; (ii) rigid cylindrical surface expanded with displacement control, and (iii) deflated polymeric deformable balloon. The three scenarios are presented in Figure 2.4. The initial deflated configuration of the balloon was obtained by running a pre-analysis in which a negative pressure of 0.01 MPa was applied to the inner surface of the cylindrical balloon, resulting in a folded-like shape. When the presence of the artery was considered, i.e., in the scenario of confined expansion, a pressure of 0.013 MPa was imposed on the internal surface of the artery to mimic the physiological conditions associated with blood pressure. This study concluded that when the load was applied directly on the inner surface of the stent in a free-expansion scenario, the stent presented a barrel-shaped configuration during all the expansion phases. Otherwise, when the cylindrical balloon promotes the stent expansion under the same conditions, it maintains its cylindrical shape according to the linear displacement imposed on the inner cylinder—adopting the deflated balloon led to the stent expanding from its ends, exhibiting the typical dogboning shape. The models in which the presence of a balloon, cylindrical or deflated, was considered presented a similar stress distribution, while the stent model showed the most uniform distribution.

Moreover, when the deflated balloon was used, the stress values were notably lower than those of the remaining scenarios. All the studies presented comparable results concerning the maximum value of von Mises stress and the foreshortening parameter. Towards such a fact, the three models can be used interchangeably. The spatial stress distribution presented some differences, which may be related to the different deformed shapes reached at the expansion's end.

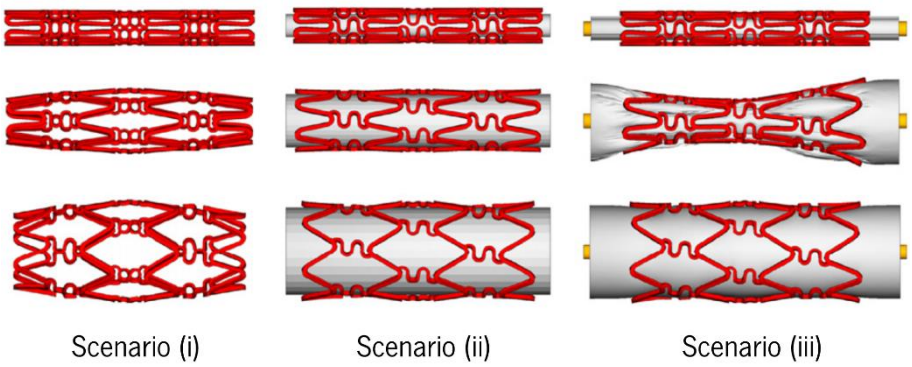

Figure 2.4 – Stent expansion modeling scenarios used by Gervaso et al. [82] and De Beule et al. [83] (adapted from [83]).

Considering the stent's confined expansion scenario, the increasing pressure caused artery wall strains to rise. In contrast, once the nominal diameter was attained in the deflated balloon model, the transmission of the pressure rise to the vessel was quite restricted. Although this study has brought an interesting approach and essential conclusions regarding how the balloon modeling may impact the results obtained, it presents a limitation regarding the artery-related outcomes due to adopting a linear isotropic material model.

In a similar study, De Beule *et al.* [83] explored the impact of the balloon folding on the stent expanded configuration, investigating the same three scenarios as Gervaso *et al.* [82] but with a different model of the folded balloon obtained via micro-CT based image reconstruction. The results obtained in the three studied conditions regarding the final stent configuration agreed with those of Gervaso *et al.* [82]. According to the authors' analysis, the radial displacement-driven cylindrical balloon expansion method provides useful and relatively accurate information regarding the final stent shape and the stresses and strains the device is subjected to when the nominal diameter is reached. In light of these findings, this method is considered the optimal choice since it represents a less computationally expensive model when compared to the folded balloon one. To further optimize the transient expansion of a new design, however, a model that is in good agreement with both qualitative and quantitative manufacturer's data and experiments is required. According to the obtained results, adopting a folded balloon is a very promising expansion strategy because it enables examining the balloon length, balloon-folding pattern, and stent positioning on stent performance. As the stent's deployment pattern and ultimately expanded configuration did not match the actual ones, disregarding the balloon's existence by directly applying radial pressure to the inner surface of the stent does not seem to be a viable design choice. Migliavacca *et al.* [84] had already drawn the same conclusion after comparing the expansion profile obtained numerically with those provided experimentally using the optical extensometer.

A different route was followed by Martin *et al.* [85], who also developed a study focused on finding an optimum strategy for modeling the configuration of the balloon. For that, the authors used three increasingly sophisticated models of a semi-compliant balloon: Balloon A, for which the tri-folded configuration and its attachment to the catheter were neglected, Balloon B, which presented a tri-folded configuration but did not consider the attachment to the catheter, and Balloon C, which exhibited both characteristics (see Figure 2.5).

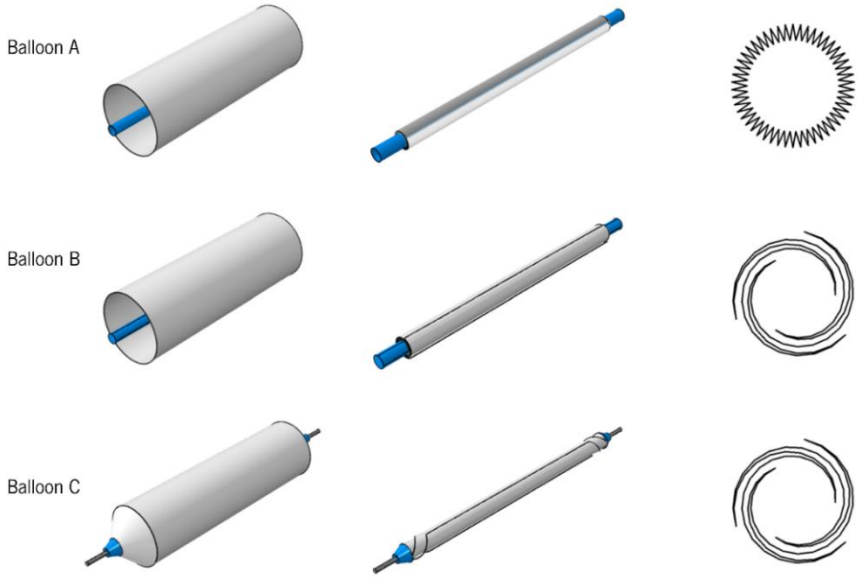

Figure 2.5 – Configuration of Balloon A, Balloon B, and Balloon C before deflation/folding (left) and following deflation/folding (middle) and cross-sectional profiles of the deflated/folded configuration of the angioplasty balloon models (right) [85].

Free expansion and expansion inside a stenotic vessel were considered for each arrangement. In both scenarios, it was reasonable to conclude that the folded shape of the balloon had an important effect on the pressure-diameter behavior of the stent, which became noticeable since the cylindrical shape of Balloon A was achieved at a lower expanding pressure compared to Balloon B and C. Consequently, the ultimate diameter of the stent following deflation of Balloon A was the greatest, followed by Balloon B and Balloon C. Regarding the influence of considering or not the bounding to the catheter, it was concluded that it did not present a significant impact on the results, since Balloon B and Balloon C showed similar behavior. Furthermore, no substantial differences were found between the predicted radial recoil of each balloon model, although some differences were noticed in foreshortening, mainly between Balloon C and the other two. The dogboning result highlighted that the balloon's configuration influenced the stent's transient behavior since its maximum occurred at different inflating pressures for each model. At the same time, there were significant disparities in its magnitude, with Balloon B exhibiting the highest value

of all the models evaluated. As previously suggested by De Beule *et al.* [83], the authors recommended that the idealized balloon model be used in studies in which the transient behavior of the stent and the magnitude of the stresses are not of critical importance, such as the exploratory studies performed on the scope of stent design. However, in the process latter stages, a realistic model must be used to accurately assess the impact of the behavior of the stent on the atherosclerotic plaque.

In addition to the balloon's representation and geometry, constitutive modeling is crucial. Although other laws may be used to model the material behavior, the most common ones are the isotropic linear elastic and the hyperelastic models, which are chosen mostly according to the adopted balloon shape. Indeed, the association of hyperelastic models with cylindrical balloons and linear elastic ones with folded configurations are the most common options.

A resume of both geometry and material models used in balloon modeling is presented in Table 2.7.

Table 2.7 – Resume table of balloon modeling strategies regarding both geometry and material model.

Ref.	Geometry	Material Model
[77,79,80,86–92]	Cylindrical Balloon	Hyperelastic – Mooney-Rivlin
[93,94]	Cylindrical Balloon	Linear Elastic
[95–98]	Folded Balloon	Linear Elastic

2.3.3. Artery modeling approaches

As balloon modeling demonstrates, artery modeling presents significant geometry and material behavior challenges. The stent-vessel interactions are important since they are a controlling factor of in-stent restenosis [99,100].

Most studies [77,87,90,101] have treated an artery as a single-layer tissue, neglecting that the blood vessel is composed of three layers with different behavior among them, influencing the system's overall response to the stenting procedure. This assumption is inconsistent with the state of knowledge regarding the characterization of arterial wall layers, which suggests that the fibre-reinforced structure of intima, media and adventitia layers must be considered in modeling the deformation of the blood vessels [102]. Recent research has delved further into modeling the three-layered artery, and many methodologies have been provided to analyze the stress created in the blood vessel. However, in a study developed by Schiavone and Zhao [103], the results suggested that using a homogeneous artery did not provide significant differences in expansion behavior (see Figure 2.6). Concerning the stress induced on the artery wall, the authors found that both models showed similar maximum stress magnitudes but with different

distribution. In the case of the single-layer model, the highest stresses are localized at the ends of the plaque, while for the layered model, such values are distributed along with the whole plaque. Moreover, since various material characteristics were applied to each layer, stress discontinuities were detectable between them. Nonetheless, the authors noted that the layered nature of the artery must be recognized.

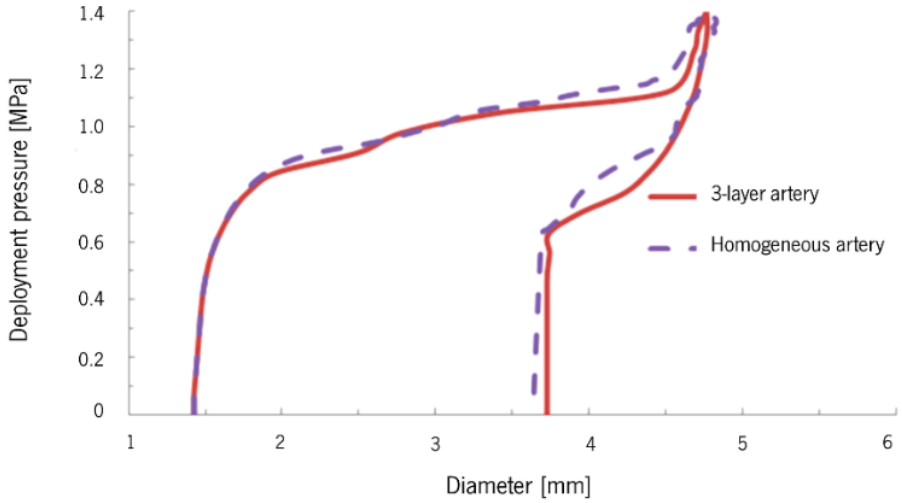

Figure 2.6 – Results of diameter change of the stent for 3-layer and homogeneous artery models obtained from Schiavone and Zhao [103].

In addition to the structural composition of the blood vessel, artery material displays a highly nonlinear anisotropic behavior across the longitudinal and circumferential directions, which provides an additional modeling issue [102]. Due to the difficulty of modeling the material behavior of the blood artery, various models were used to explain it, with the anisotropy of the material being largely neglected. Using the Mooney-Rivlin constitutive equation or the polynomial model [72], some authors [104–107] defined the blood vessel as hyperelastic, while others [80,108,109] considered them as linear isotropic. Schiavone *et al.* [97,102] proposed a different approach in which vessel anisotropy was considered, and the obtained results were compared to those of isotropic formulations. In this instance, a Holzapfel-Gasser-Ogden formulation was applied, and the obtained results showed that the rate of artery dilation was almost identical for both models. However, it had been noticed a difference in stent expansion at peak pressure (1.40 MPa): a diameter of 4.80 mm for the isotropic model versus a diameter of 4.70 mm for the anisotropic model. Still, the final diameter of the stent after the balloon deflation was comparable since the isotropic model presented higher elastic recoil than the anisotropic one. According to Schiavone and Zhao [102], by presenting a higher elastic recoil, an additional compression on the stent is imposed, leading to an increase in the stress induced in the stent by the artery when an isotropic model is adopted.

Regarding the stress imposed on the artery, while there were no significant differences, with its maximum value being 0.70 MPa and 0.65 MPa for anisotropic and isotropic models, respectively, it is proposed that the latter has a smaller region susceptible to the greatest stresses. Given the impact this parameter appears to have in the development of later adverse effects such as in-stent restenosis, it is very important to model the artery behavior as close as possible to the real one, which is why the adoption of an anisotropic formulation must be considered. Indeed, the same conclusion has been shared by Schmidt *et al.* [110], who found significant differences between the simulations using an isotropic and an anisotropic model for an atherosclerotic artery and pointed to as potential critical the usage of isotropic models for the analysis of arteries during or after supra-physiological loadings, such as it happens during the stenting procedure.

Some authors presented other interesting approaches regarding essential topics that needed to be addressed in artery modeling. An example of such can be found in work developed by Wu *et al.* [107], who studied the stent expansion in a curved vessel and compared the results obtained with those of a straight model. The single-layer vessel was modeled as a hyperelastic material using a four-parameter Mooney-Rivlin constitutive equation, and pressure of 0.0133 MPa was applied to the inner surface of the artery to mimic the blood pressure in the vessel. The results showed that the stent properly conformed to the straight vessel but could not do it in the curved configuration, especially at its ends. In this scenario, the stent straightened the middle vessel with full expansion and bent by the curved tissue after deflation, although the central section remained straightened. Additionally, the maximum tissue prolapse in the curved vessel was nearly double that of the straight model, as the distribution of tissue stresses was more uniform in the latter, which also exhibited lower values of maximum stress on both the artery and the plaque. These results show an increased risk of both restenosis and acute thrombus in the curved vessel model due to the high levels of stress induced in the vessel and the excessive tissue prolapse. Thus, stent design must be considered according to the clinical situation one intends to treat. The nonconformity of the stent, which may be the source of the reported difficulties, is mainly attributable to inadequate deformation of the link parts of the stent geometry, particularly at its ends, and may be addressed by redesigning the stent geometry.

The suitability of commercial stents for curved vessels has been evaluated according to different criteria proposed by several authors, including factors such as trackability, flexibility, conformability, or stress induced on the artery wall. The performance of the stents regarding these metrics indicated that some commercial stents might satisfy some criteria. Still, almost all of them are far from practical application

for highly curved vessels [111], drawing an opportunity to develop design optimization methodologies to meet such requirements.

A resume of the different approaches proposed to model the blood vessel is presented in Table 2.8.

Table 2.8 – Resume table of blood vessel modeling strategies regarding both geometry and material model.

Author	Geometry	Configuration	Material Model
[80]	Cylindrical Vessel	Single-Layer	Linear Isotropic
[77]	Cylindrical Vessel	Single-Layer	Four-parameter Mooney-Rivlin Hyperelastic Model
[87,90,105]	Cylindrical Vessel	Single-Layer	Five-parameter Mooney-Rivlin Hyperelastic Model
[58,85,86,98,102,103,112,113]	Cylindrical Vessel	Three-Layers	Third-order Ogden Hyperelastic Model
[114]	Curved Vessel	Single-Layer	Third-order Ogden Hyperelastic Model
[107]	Curved Vessel	Single-Layer	Four-parameter Mooney-Rivlin Hyperelastic Model
[72,101]	Cylindrical Vessel	Single-Layer	Polynomial Hyperelastic Model
[89,102,103]	Cylindrical Vessel	Three Layers	Hozapfel-Gasser-Ogden Model

The expansion of a stent inside a blood vessel will create significant stresses on both the artery and the plaque, which may damage the tissue and cause in-stent restenosis. Several factors influence the level of injury provoked by the stent on the arterial tissue, namely the stent design, the configuration of the artery, the expanding pressures used to inflate the balloon, and the mechanical properties of both the artery and the plaque [89].

2.3.4. Numerical modeling of stent functional behavior – the role of design optimization

Beyond the structural analysis of the deployment of the stent in the occluded vessel, several other works were developed to study phenomena that are also involved in the process, some of which focused on the fatigue life analysis of the stents, which is considered an important topic since that device is subjected to cyclic loads caused by the pulsatile blood flow and might fail due to it [115–117].

In addition, it is essential to comprehend the development of the stent's mechanical characteristics with material degradation, primarily for modeling and forecasting the device's function. Follow-up studies of

clinical trials reported that artery remodeling occurred after stent implantation, which translated into the reduction of the lumen area due to the stent's support ability loss [118]. According to the data gathered, the device failure was primarily driven by the early recoil, probably due to insufficient scaffolding time and loss of radial strength [119]. The deterioration of the material's mechanical properties must be compatible with the time required for the blood vessel to heal, providing support during the whole process. The evolution of the mechanical properties as a function of the immersion time is an essential input for the numerical modeling of stent performance during its degradation allowing for failure prediction. Indeed, the device's design and material processing may help control the mechanical integrity and scaffolding effect losses through degradation behavior tuning.

Nonetheless, although some work has been published on the scope of mechanical properties' relationship with immersion time [120–122], the literature discussing its application to FEA is limited. Indeed, only a single approach based on stress-strain curves of a degraded Absorb stent was reported by Qiu *et al.* [123]. The degradation process was modeled by incorporating the change of material property as a function of time, and the interaction of the scaffold with the blood vessel was investigated. The results demonstrated that over degradation times, the scaffold stress increased initially and then gradually decreased as the scaffold material's yield stress changed, whereas the plaque and arterial layers showed a continuous decrease in stress.

On the other hand, design optimization has been the subject of several recent publications. As stated previously, there is evidence that the stent geometry influences not only the deployment parameters such as expanding pressure and expanded diameter but also the performance parameters, like dogboning, foreshortening, and elastic recoil, which are correlated with the inflicted damage to the arterial vessel and stress during both balloon and stent expansion [124–126]. Consequently, stent geometry optimization is one of the most critical topics in stenting process studies, and different approaches are reported in the literature.

The optimization process may concentrate on one of the parts of the stent structure (ring or linkage elements) or the whole structure. Some authors, like Imani *et al.* [77], studied the influence of the stent design by simulating different geometric models, comparing the obtained results in terms of stress distribution, the relation between required expansion pressure and expanded diameter, and dogboning. In a further attempt, Roy and Chanda [123] developed a study in which six commercially available stents were tested under deployment conditions but neglected all the other elements. In addition to the geometric differences between the considered models - Palmaz-Schatz, CYPHER (Cordis, J&J), S670,

Driver (Medtronic, USA), Taxus Express, and Element (Boston Scientific, USA) – the applied materials were also different, including 316L stainless steel, platinum-chromium, cobalt-chromium, nickel-titanium, tantalum, and magnesium WE43. The obtained results concluded that, from a material perspective, tantalum, nitinol, and magnesium WE43 were more prone to high-stress development; however, once nitinol's ultimate tensile strength and yield strength are higher, this was a better option when compared with the other two.

On a different approach, the role of the linkage element of the stent structure on stent performance was studied by Azouzi *et al.* [127], that tested four different bridges shape and compared obtained results for von Mises stress under bending and torsion solicitations.

Although these approaches may provide some insight into the impact of certain geometric characteristics on the stent behavior and performance, a parametric optimization study embraces a larger group of options, allowing a better perspective of the real impact of each design variable in the stent behavior. Some authors adopted such a strategy and developed several works in this scope. As verified for the study of the stenting process, the optimization models may also present different complexity levels. Overall, the optimization process must accomplish the defined objectives by simultaneously manipulating the control variables and respecting a set of constraints.

Li *et al.* [93] carried out a shape optimization based on a parametric model and defined an objective function whose minimization allowed to maximize the radial gain and minimize the intrinsic elastic recoil, radial loss, and dogboning. Furthermore, some conditions needed to be satisfied, namely (i) the von Mises stress must be inferior to ultimate tensile strength, and (ii) the foreshortening must be lower than 2.0 %. The result of the work was an optimized stent geometry considering the referred objectives and constraints. In the work of Amirjani *et al.* [104], a multi-parameter CAD model where the evaluated parameters were the stent struts width was developed, and its influence on von Mises stress over the stent and artery, the stent recoil, and the wall shear stress on inner arterial wall tissue was assessed. The authors used a model composed of the artery and the stent and developed a complete study that included mechanobiological, hemodynamic, and drug delivery simulations. The suitable boundary conditions were defined for each study, using a friction coefficient equal to 0.045 for stent/endothelial cells of the artery pair and a blood pressure of 0.013 MPa. The drug delivery of heparin and paclitaxel was tested, and the process was described by Fick's law, using Dirichlet and Newmann boundary conditions. The optimization process had multiple objectives: (i) to improve the mechanical stability by minimizing von Mises stress over the stent; (ii) to reduce the risk of biological damage of artery – ISR – by minimizing von Mises stress

over the arterial wall tissue; (iii) to minimize stent distortion after loading, namely the recoil phenomenon; (iv) to minimize the wall shear stress on inner arterial wall tissue. This process resulted in a set of values for the defined parameters (stent widths) that granted the best commitment between the drawn objectives.

A different methodology was presented by Li *et al.* [108], who developed a multi-objective optimization method based on the Kriging surrogate model, aiming to decrease both dogboning and radial elastic recoil of a Palmaz-Schatz stent. The optimized stent geometry decreased the highest value of dogboning by 94% and the radial elastic recoil by 15%. In a more recent study [109], the authors combined the stent and the balloon optimization to improve fatigue resistance and decrease the dogboning effect of the same stent geometry. The final optimized geometry almost wholly eliminated the dogboning effect and improved fatigue life, while radial elastic recoil was reduced by more than 30% and foreshortening decreased by 1.75%. A different vision was proposed by Han and Lu [111], who developed a novel approach for the design of stents intended to be used for curved arteries, which lays on the optimization of the device's deformation behavior, resorting to nonuniform Poisson's ration distribution. Following the conclusions of Raamachandran and Jayavenkateshwaran [128], who stated that the Poisson's ratio of the typical ring and link structures could easily be modified from negative to positive values by changing the length of the link element, the authors sought to locate the cells with negative Poisson's ratio at the regions that need to be lengthened (outer wall of the curved vessels) and cells with positive values at places that need to be shortened (inner wall of the curved stent). For that, the stent structure was divided into small segments whose Poisson's ratio was optimized separately by changing the connection point between the parts. The proposed method was applied to the design of stents for both a single curvature artery and a patient-specific multi-curvature vessel. The simulation results showed that the optimized nonuniform stents could perform the curvature along with the expansion of the balloon, exhibiting the minimum strain energy and straightening effects on the artery wall compared to the traditional stent models. Such improvement is suggested to contribute to the significant decrease of the in-stent restenosis risk.

In an attempt that considers the constraints imposed by the manufacturing process, namely the dimensional ones, Gomes *et al.* [129] proposed an optimization methodology for two different stent geometries (Palmaz-Schatz-based model and NG model) of biodegradable magnesium stents obtained by ultrasonic-microcasting regarding some standard performance parameters. Such an approach allowed to achieve a significant reduction of required expansion pressure (30% for the Palmaz-Schatz model and

55% for the NG model) and dogboning and foreshortening found a decrease of 97.3% and 86.6%, respectively, for Palmaz–Schatz model, while for NG model such values were 13.6% and 50.0%.

The enhancement of devices' radial strength has also been considered the main objective of some recent studies, mainly concerning polymeric and magnesium stents. This tendency is justified by the inferior mechanical properties of these materials compared to stainless steel, which demands higher strut thickness to withstand the mechanical strength requirements for vessel support during the healing process. However, thicker dimensions make the devices prone to in-stent restenosis, so efforts must be made to find alternative designs to achieve optimal overall outcomes. In this regard, Li *et al.* [130] used response surface models to optimize a BioMatrix stent by modifying its support ring structure. The optimized geometry exhibited lower thickness (100 μm vs. 150 μm) while providing comparable radial strength and significantly inferior maximum principal strain.

In addition to the design modification, other possibilities exist to improve stent performance, such as that proposed by Khosravi *et al.* [131]. In this work, the authors suggested applying functionally graded materials to achieve better results regarding the dogboning metric, a supposition confirmed by the results obtained.

The analysis of the work published in the scope of the application of FEM to the study of stenting procedure allows for identifying a window of opportunity concerning the development of specific models that consider the manufacturing process's singularities.

In this sense, the present work aims at developing a numerical optimization routine capable of taking advantage of the options provided by a new manufacturing process – ultrasonic-microcasting – to design a novel biodegradable magnesium stent that may be seen as an option for the treatment of blood vessel occlusions. Such a manufacturing technique allows not only a broad new set of possible stent geometries, namely with cross-section variation but also enables the processing of the material to achieve better mechanical properties such as ductility, which are crucial for the performance of this device in both deployment and service period.

CHAPTER REFERENCES

[1] D.W.Y. Toong, J.C.K. Ng, Y. Huang, P.E.H. Wong, H.L. Leo, S.S. Venkatraman, H.Y. Ang, Bioresorbable metals in cardiovascular stents: Material insights and progress, Materialia 12 (2020) 100727. https://doi.org/10.1016/j.mtla.2020.100727.

[2] M.A. Azmah Hanim, B.T.H. Tuah Baharudin, Dermot Brabazon, Saleem Hashmi, Biodegradable Metal Heart Stent: Characteristics, Material Options and Preliminary Testing Method, in: Reference Module in Materials Science and Materials Engineering, Elsevier, 2018.

[3] H.Y. Ang, H. Bulluck, P. Wong, S.S. Venkatraman, Y. Huang, N. Foin, Bioresorbable stents: Current and upcoming bioresorbable technologies, International journal of cardiology 228 (2017) 931–939. https://doi.org/10.1016/j.ijcard.2016.11.258.

[4] T. Sharkawi, F. Cornhill, A. Lafont, P. Sabaria, M. Vert, Intravascular bioresorbable polymeric stents: a potential alternative to current drug eluting metal stents, Journal of pharmaceutical sciences 96 (2007) 2829–2837. https://doi.org/10.1002/jps.20957.

[5] P.W.J.C. Serruys, Bioresorbable Scaffolds: From Basic Concept to Clinical Applications, Taylor & Francis Group, Milton, 2017.

[6] D. Regazzoli, P.P. Leone, A. Colombo, A. Latib, New generation bioresorbable scaffold technologies: an update on novel devices and clinical results, Journal of thoracic disease 9 (2017) S979-S985. https://doi.org/10.21037/jtd.2017.07.104.

[7] C. Briguori, C. Sarais, P. Pagnotta, F. Liistro, M. Montorfano, A. Chieffo, F. Sgura, N. Corvaja, R. Albiero, G. Stankovic, C. Toutoutzas, E. Bonizzoni, C. Di Mario, A. Colombo, In-stent restenosis in small coronary arteries, Journal of the American College of Cardiology 40 (2002) 403–409. https://doi.org/10.1016/S0735-1097(02)01989-7.

[8] M. Iantorno, M.J. Lipinski, H.M. Garcia-Garcia, B.J. Forrestal, T. Rogers, D. Gajanana, K.D. Buchanan, R. Torguson, W.S. Weintraub, R. Waksman, Meta-Analysis of the Impact of Strut Thickness on Outcomes in Patients With Drug-Eluting Stents in a Coronary Artery, The American journal of cardiology 122 (2018) 1652–1660. https://doi.org/10.1016/j.amjcard.2018.07.040.

[9] J.ü. Pache, A. Kastrati, J. Mehilli, H. Schühlen, F. Dotzer, J.ö. Hausleiter, M. Fleckenstein, F.-J. Neumann, U. Sattelberger, C. Schmitt, M. Müller, J. Dirschinger, A. Schömig, Intracoronary stenting and angiographic results: strut thickness effect on restenosis outcome (ISAR-STEREO-2) trial, Journal of the American College of Cardiology 41 (2003) 1283–1288. https://doi.org/10.1016/S0735-1097(03)00119-0.

[10] R. Erbel, C. Di Mario, J. Bartunek, J. Bonnier, B. de Bruyne, F.R. Eberli, P. Erne, M. Haude, B. Heublein, M. Horrigan, C. Ilsley, D. Böse, J. Koolen, T.F. Lüscher, N. Weissman, R. Waksman, Temporary scaffolding of coronary arteries with bioabsorbable magnesium stents: a prospective, non-randomised multicentre trial, Lancet (London, England) 369 (2007) 1869–1875. https://doi.org/10.1016/S0140-6736(07)60853-8.

[11] J. Bennett, Q. de Hemptinne, K. McCutcheon, Magmaris resorbable magnesium scaffold for the treatment of coronary heart disease: overview of its safety and efficacy, Expert review of medical devices 16 (2019) 757–769. https://doi.org/10.1080/17434440.2019.1649133.

[12] N. Li, Y. Zheng, Novel Magnesium Alloys Developed for Biomedical Application: A Review, Journal of Materials Science & Technology 29 (2013) 489–502. https://doi.org/10.1016/j.jmst.2013.02.005.

[13] L. Mao, L. Shen, J. Chen, X. Zhang, M. Kwak, Y. Wu, R. Fan, L. Zhang, J. Pei, G. Yuan, C. Song, J. Ge, W. Ding, A promising biodegradable magnesium alloy suitable for clinical vascular stent application, Scientific reports 7 (2017) 46343. https://doi.org/10.1038/srep46343.

[14] Hyong-Min Kim and Deep Jariwala, The Not-So-Rare Earth Elements: A Question of Supply and Demand.

[15] M.K. Kulekci, Magnesium and its alloys applications in automotive industry, Int J Adv Manuf Technol 39 (2008) 851–865. https://doi.org/10.1007/s00170-007-1279-2.

[16] A. Dziubińska, A. Gontarz, M. Dziubiński, M. Barszcz, THE FORMING OF MAGNESIUM ALLOY FORGINGS FOR AIRCRAFT AND AUTOMOTIVE APPLICATIONS, Adv. Sci. Technol. Res. J. 10 (2016) 158–168. https://doi.org/10.12913/22998624/64003.

[17] P. Emadi, C. Ravindran, The Influence of High Temperature Ultrasonic Processing Time on the Microstructure and Mechanical Properties AZ91E Magnesium Alloy, JOURNAL OF MATERIALS ENGINEERING AND PERFORMANCE 30 (2021) 1188–1199. https://doi.org/10.1007/s11665-020-05419-z.

[18] Y. Kojima, Project of Platform Science and Technology for Advanced Magnesium Alloys, Materials Transactions 42 (2001) 1154–1159.

[19] H.E. Friedrich, B.L. Mordike, Magnesium Technology (Metallurgy, Design Data, Applications), Springer International Publishing, Berlin, 2006.

[20] X. Zhang, H.R. Kotadia, J. Depner, M. Qian, A. Das, Effect of Ultrasonication on the Solidification Microstructure in Al and Mg-Alloys, in: C. Chesonis (Ed.), Light Metals 2019, Springer International Publishing, Cham, 2019, pp. 1589–1595.

[21] Y. Yang, X. Xiong, J. Chen, X. Peng, D. Chen, F. Pan, Research advances in magnesium and magnesium alloys worldwide in 2020, Journal of Magnesium and Alloys 9 (2021) 705–747. https://doi.org/10.1016/j.jma.2021.04.001.

[22] M. Khosro Aghayani, B. Niroumand, Effects of ultrasonic treatment on microstructure and tensile strength of AZ91 magnesium alloy, Journal of Alloys and Compounds 509 (2011) 114–122. https://doi.org/10.1016/j.jallcom.2010.08.139.

[23] B. Patel, G.P. Chaudhari, P.P. Bhingole, Microstructural evolution in ultrasonicated AS41 magnesium alloy, Materials Letters 66 (2012) 335–338. https://doi.org/10.1016/j.matlet.2011.08.113.

[24] X. Liu, Y. Osawa, S. Takamori, T. Mukai, Grain refinement of AZ91 alloy by introducing ultrasonic vibration during solidification, Materials Letters 62 (2008) 2872–2875. https://doi.org/10.1016/j.matlet.2008.01.063.

[25] T.Y. Kwak, W.J. Kim, Hot compression behavior of the 1 wt% calcium containing Mg–8Al–0.5Zn (AZ80) alloy fabricated using electromagnetic casting technology, Materials Science and Engineering: A 615 (2014) 222–230. https://doi.org/10.1016/j.msea.2014.07.025.

[26] M. Easton, C.H.J. Davies, M.R. Barnett, F. Pravdic, Effect of Solidification Grain Refinement on the Development of Wrought Mg Alloys, MSF 539-543 (2007) 1729–1734. https://doi.org/10.4028/www.scientific.net/MSF.539-543.1729.

[27] M. Qian, A. Ramirez, A. Das, D.H. StJohn, The effect of solute on ultrasonic grain refinement of magnesium alloys, Journal of Crystal Growth 312 (2010) 2267–2272. https://doi.org/10.1016/j.jcrysgro.2010.04.035.

[28] L. Jiang, W. Liu, G. Wu, W. Ding, Effect of chemical composition on the microstructure, tensile properties and fatigue behavior of sand-cast Mg–Gd–Y–Zr alloy, Materials Science and Engineering: A 612 (2014) 293–301. https://doi.org/10.1016/j.msea.2014.06.049.

[29] Z. Li, M. Chen, W. Li, H. Zheng, C. You, D. Liu, F. Jin, The synergistic effect of trace Sr and Zr on the microstructure and properties of a biodegradable Mg-Zn-Zr-Sr alloy, Journal of Alloys and Compounds 702 (2017) 290–302. https://doi.org/10.1016/j.jallcom.2017.01.178.

[30] B. Nagasivamuni, G. Wang, D.H. StJohn, M.S. Dargusch, Effect of ultrasonic treatment on the alloying and grain refinement efficiency of a Mg – Zr master alloy added to magnesium at hypo- and hyper-peritectic compositions, Journal of Crystal Growth 512 (2019) 20–32. https://doi.org/10.1016/j.jcrysgro.2019.02.004.

[31] D. StJohn, M. Qian, M.A. Easton, C. Peng, Z. Hildebrand, Grain Refinement of Magnesium Alloys, Metall and Mat Trans A 36 (2005) 1669–1679.

[32] M. Li, T. Tamura, N. Omura, Y. Murakami, S. Tada, Grain refinement of AZCa912 alloys solidified by an optimized electromagnetic stirring technique, Journal of Materials Processing Technology 235 (2016) 114–120. https://doi.org/10.1016/j.jmatprotec.2016.04.024.

[33] N. Balasubramani, G. Wang, D.H. StJohn, M.S. Dargusch, The Poisoning Effect of Al and Be on Mg—1 wt.% Zr Alloy and the Role of Ultrasonic Treatment on Grain Refinement, Frontiers in Materials 6 (2019) 322. https://doi.org/10.3389/fmats.2019.00322.

[34] E.F. Emley, Principles of Magnesium Technology, Pergamon Press, Oxford, 1966.

[35] I.J. Polmear, Recent Developments in Light Alloys, Materials Transactions 37 (1996) 12–31.

[36] M.O. Pekguleryuz, E. Baril, Development of Creep Resistant Mg-Al-Sr Alloys, Magnesium Technology (2001) 119–126.

[37] H.-M. Guo, A.-s. Zhang, B. Hu, Y. Ding, X.-B. Liu, Refining microstructure of AZ91 magnesium alloy by introducing limited angular oscillation during initial stage of solidification, Materials Science and Engineering: A 532 (2012) 221–229. https://doi.org/10.1016/j.msea.2011.10.083.

[38] M. Li, T. Tamura, K. Miwa, Controlling microstructures of AZ31 magnesium alloys by an electromagnetic vibration technique during solidification: From experimental observation to theoretical understanding, Acta Materialia 55 (2007) 4635–4643. https://doi.org/10.1016/j.actamat.2007.04.035.

[39] Y.-L. Gao, Q.-S. Li, Y.-Y. Gong, Q.-J. Zhai, Comparative study on structural transformation of low-melting pure Al and high-melting stainless steel under external pulsed magnetic field, Materials Letters 61 (2007) 4011–4014. https://doi.org/10.1016/j.matlet.2007.01.007.

[40] J. Zhao, Y. Cheng, K. Han, X. Zhang, Z. Xu, Q. Zhai, Numerical and experimental studies of surface-pulsed magneto-oscillation on solidification, Journal of Materials Processing Technology 229 (2016) 286–293. https://doi.org/10.1016/j.jmatprotec.2015.09.027.

[41] Y. Yang, J. Wang, T. Wang, C. Liu, Z. Zhang, Effects of ultrasonic treatment on microstructures of AZ91 alloy, Transactions of Nonferrous Metals Society of China 24 (2014) 76–81. https://doi.org/10.1016/S1003-6326(14)63030-2.

[42] X. Zhang, H.R. Kotadia, J. Depner, M. Qian, A. Das, Effect of Ultrasonication on the Solidification Microstructure in Al and Mg-Alloys, in: C. Chesonis (Ed.), Light Metals 2019, Springer International Publishing, Cham, 2019, pp. 1589–1595.

[43] M. Qian, A. Ramirez, A. Das, Ultrasonic refinement of magnesium by cavitation: Clarifying the role of wall crystals, Journal of Crystal Growth 311 (2009) 3708–3715. https://doi.org/10.1016/j.jcrysgro.2009.04.036.

[44] V.M. Garamus, W. Limberg, M. Serdechnova, Di Mei, S.V. Lamaka, T. Ebel, R. Willumeit-Römer, Degradation of Titanium Sintered with Magnesium: Effect of Hydrogen Uptake, Metals 11 (2021) 527. https://doi.org/10.3390/met11040527.

[45] K.B. Nie, X.J. Wang, K. Wu, M.Y. Zheng, X.S. Hu, Effect of ultrasonic vibration and solution heat treatment on microstructures and tensile properties of AZ91 alloy, Materials Science and Engineering: A 528 (2011) 7484–7487. https://doi.org/10.1016/j.msea.2011.06.072.

[46] X. Liu, Y. Osawa, S. Takamori, T. Mukai, Microstructure and mechanical properties of AZ91 alloy produced with ultrasonic vibration, Materials Science and Engineering: A 487 (2008) 120–123. https://doi.org/10.1016/j.msea.2007.09.071.

[47] A. Ramirez, M. Qian, B. Davis, T. Wilks, D.H. StJohn, Potency of high-intensity ultrasonic treatment for grain refinement of magnesium alloys, Scripta Materialia 59 (2008) 19–22. https://doi.org/10.1016/j.scriptamat.2008.02.017.

[48] D. Gao, Z. Li, Q. Han, Q. Zhai, Effect of ultrasonic power on microstructure and mechanical properties of AZ91 alloy, Materials Science and Engineering: A 502 (2009) 2–5. https://doi.org/10.1016/j.msea.2008.12.005.

[49] L. YAO, H. HAO, S.-h. JI, C.-f. FANG, X.-g. ZHANG, Effects of ultrasonic vibration on solidification structure and properties of Mg-8Li-3Al alloy, Transactions of Nonferrous Metals Society of China 21 (2011) 1241–1246. https://doi.org/10.1016/S1003-6326(11)60848-0.

[50] H. Puga, V. Carneiro, J. Barbosa, V. Vieira, Effect of Ultrasonic Treatment in the Static and Dynamic Mechanical Behavior of AZ91D Mg Alloy, Metals 5 (2015) 2210–2221. https://doi.org/10.3390/met5042210.

[51] X. Hansong, L. Di, Y. Gang, Z. Dingfei, Ultrasonic Effects on Microstructure Evolution and Mechanical Properties of AZ80 Magnesium Alloy, Rare Metal Materials and Engineering 45 (2016) 1401–1405. https://doi.org/10.1016/S1875-5372(16)30121-7.

[52] Y.J. Chen, W.N. Hsu, J.R. Shih, The Effect of Ultrasonic Treatment on Microstructural and Mechanical Properties of Cast Magnesium Alloys, Materials Transaction 50 (2009) 401–408.

[53] Z. Shao, Q. Le, Z. Zhang, J. Cui, Effect of ultrasonic power on grain refinement and purification processing of AZ80 alloy by ultrasonic treatment, Met. Mater. Int. 18 (2012) 209–215. https://doi.org/10.1007/s12540-012-2002-x.

[54] S. Ning, X. Chen, Q. Le, H. Wang, C. Hu, Effect of ultrasonic frequency on cavitation behavior, microstructure and mechanical properties of AZ80 magnesium alloy, Mater. Res. Express 6 (2019) 0865d9. https://doi.org/10.1088/2053-1591/ab24f0.

[55] A.A. Luo, Magnesium casting technology for structural applications, Journal of Magnesium and Alloys 1 (2013) 2–22. https://doi.org/10.1016/j.jma.2013.02.002.

[56] J.F. King (Ed.), Environmental Challenges Facing the Magnesium Industry – SF6 Replacement, The International Magnesium Association, 2003.

[57] F. Czerwinski, Corrosion of Materials in Liquid Magnesium Alloys and Its Prevention, in: F. Czerwinski (Ed.), Magnesium Alloys - Properties in Solid and Liquid States, InTech, 2014.

[58] X. Zeng, Q. Wang, Y. Lü, W. Ding, Y. Zhu, C. Zhai, C. Lu, X. Xu, Behavior of surface oxidation on molten Mg–9Al–0.5Zn–0.3Be alloy, Materials Science and Engineering: A 301 (2001) 154–161. https://doi.org/10.1016/S0921-5093(00)01798-6.

[59] X. Chen, Q. Le, Application of Ultrasonics on Preparation of Magnesium Alloys, in: S. Karakuş (Ed.), Sonochemical Reactions, IntechOpen, 2020.

[60] Y. Yang, J. Wang, T. Wang, C. Liu, Z. Zhang, Effects of ultrasonic treatment on microstructures of AZ91 alloy, Transactions of Nonferrous Metals Society of China 24 (2014) 76–81. https://doi.org/10.1016/S1003-6326(14)63030-2.

[61] L. Xu, X. Liu, K. Sun, R. Fu, G. Wang, Corrosion Behavior in Magnesium-Based Alloys for Biomedical Applications, Materials (Basel, Switzerland) 15 (2022). https://doi.org/10.3390/ma15072613.

[62] F. Meng, S. Lv, Q. Yang, P. Qin, J. Zhang, K. Guan, Y. Huang, N. Hort, B. Li, X. Liu, J. Meng, Developing a die casting magnesium alloy with excellent mechanical performance by controlling intermetallic phase, Journal of Alloys and Compounds 795 (2019) 436–445. https://doi.org/10.1016/j.jallcom.2019.04.346.

[63] N. Ono, R. Nowak, S. Miura, Effect of deformation temperature on Hall–Petch relationship registered for polycrystalline magnesium, Materials Letters 58 (2004) 39–43. https://doi.org/10.1016/S0167-577X(03)00410-5.

[64] J.A. Spittle, Columnar to equiaxed grain transition in as solidified alloys, International Materials Reviews 51 (2006) 247–269. https://doi.org/10.1179/174328006X102493.

[65] L. Ma, F. Chen, G. Shu, Preparation of fine particulate reinforced metal matrix composites by high intensity ultrasonic treatment, Journal of Materials Science Letters 14 (1995) 649–650. https://doi.org/10.1007/BF00586167.

[66] M. Khosro Aghayani, B. Niroumand, Effects of ultrasonic treatment on microstructure and tensile strength of AZ91 magnesium alloy, Journal of Alloys and Compounds 509 (2011) 114–122. https://doi.org/10.1016/j.jallcom.2010.08.139.

[67] B. Patel, G.P. Chaudhari, P.P. Bhingole, Microstructural evolution in ultrasonicated AS41 magnesium alloy, Materials Letters 66 (2012) 335–338. https://doi.org/10.1016/j.matlet.2011.08.113.

[68] X. Liu, Y. Osawa, S. Takamori, T. Mukai, Grain refinement of AZ91 alloy by introducing ultrasonic vibration during solidification, Materials Letters 62 (2008) 2872–2875. https://doi.org/10.1016/j.matlet.2008.01.063.

[69] A.A. Nayeb-Hashemi, J.B. Clark, ASM International, Phase Diagrams of Binary Magnesium Alloys, Metals Park, Ohio, 1988.

[70] M. Driscoll, The Impact of the Finite Element Method on Medical Device Design, J. Med. Biol. Eng. 39 (2019) 171–172. https://doi.org/10.1007/s40846-018-0428-4.

[71] F.D. Whitcher, Simulation of in vivo loading conditions of nitinol vascular stent structures, Computers & Structures 64 (1997) 1005–1011. https://doi.org/10.1016/S0045-7949(97)00014-X.

[72] F. Auricchio, M. Di LORETO, E. SACCO, Finite-element Analysis of a Stenotic Artery Revascularization Through a Stent Insertion, Computer Methods in Biomechanics and Biomedical Engineering 4 (2001) 249–263. https://doi.org/10.1080/10255840108908007.

[73] Y. Li, Y. Wang, Z. Shen, F. Miao, J. Wang, Y. Sun, S. Zhu, Y. Zheng, S. Guan, A biodegradable magnesium alloy vascular stent structure: Design, optimisation and evaluation, Acta biomaterialia 142 (2022) 402–412. https://doi.org/10.1016/j.actbio.2022.01.045.

[74] B.S.P.K. Kandala, G. Zhang, C. LCorriveau, M. Paquin, M. Chagnon, D. Begun, V. Shanov, Preliminary study on modeling, fabrication by photo-chemical etching and in vivo testing of biodegradable magnesium AZ31 stents, Bioactive materials 6 (2021) 1663–1675. https://doi.org/10.1016/j.bioactmat.2020.11.012.

[75] H. Bahreinizad, M. Salimi Bani, A. Khosravi, A. Karimi, A numerical study on the application of the functionally graded bioabsorbable materials in the stent design, ARTRES 24 (2018) 1. https://doi.org/10.1016/j.artres.2018.09.001.

[76] W. Fu, G. Cheng, R. Yan, A. Qiao, Numerical investigations of the flexibility of intravascular braided stent, J. Mech. Med. Biol. 17 (2017) 1750075. https://doi.org/10.1142/S0219519417500750.

[77] M. Imani, A.M. Goudarzi, D. Ganji, A.L. Aghili, The comprehensive finite element model for stenting: The influence of stent design on the outcome after coronary stent placement, Journal of Theoretical and Applied Mechanics 51 (2013) 639–648.

[78] F. Migliavacca, L. Petrini, M. Colombo, F. Auricchio, R. Pietrabissa, Mechanical behavior of coronary stents investigated through the finite element method, Journal of Biomechanics 35 (2002) 803–811. https://doi.org/10.1016/S0021-9290(02)00033-7.

[79] S.N. David Chua, B.J. Mac Donald, M.S.J. Hashmi, Finite element simulation of stent and balloon interaction, Journal of Materials Processing Technology 143-144 (2003) 591–597. https://doi.org/10.1016/S0924-0136(03)00435-7.

[80] S.N. David Chua, B.J. MacDonald, M.S.J. Hashmi, Finite element simulation of slotted tube (stent) with the presence of plaque and artery by balloon expansion, Journal of Materials Processing Technology 155-156 (2004) 1772–1779. https://doi.org/10.1016/j.jmatprotec.2004.04.396.

[81] D.K. Liang, D.Z. Yang, M. Qi, W.Q. Wang, Finite element analysis of the implantation of a balloon-expandable stent in a stenosed artery, International journal of cardiology 104 (2005) 314–318. https://doi.org/10.1016/j.ijcard.2004.12.033.

[82] F. Gervaso, C. Capelli, L. Petrini, S. Lattanzio, L. Di Virgilio, F. Migliavacca, On the effects of different strategies in modeling balloon-expandable stenting by means of finite element method, Journal of Biomechanics 41 (2008) 1206–1212. https://doi.org/10.1016/j.jbiomech.2008.01.027.

[83] M. de Beule, P. Mortier, S.G. Carlier, B. Verhegghe, R. van Impe, P. Verdonck, Realistic finite element-based stent design: the impact of balloon folding, Journal of Biomechanics 41 (2008) 383–389. https://doi.org/10.1016/j.jbiomech.2007.08.014.

[84] F. Migliavacca, L. Petrini, V. Montanari, I. Quagliana, F. Auricchio, G. Dubini, A predictive study of the mechanical behavior of coronary stents by computer modeling, Medical engineering & physics 27 (2005) 13–18. https://doi.org/10.1016/j.medengphy.2004.08.012.

[85] D. Martin, F. Boyle, Finite element analysis of balloon-expandable coronary stent deployment: influence of angioplasty balloon configuration, International journal for numerical methods in biomedical engineering 29 (2013) 1161–1175. https://doi.org/10.1002/cnm.2557.

[86] B. Beigzadeh, S.A. Mirmohammadi, M.R. Ayatollahi, A numerical study on the effect of geometrical parameters and loading profile on the expansion of stent, Bio-medical materials and engineering 28 (2017) 463–476. https://doi.org/10.3233/BME-171691.

[87] N. Eshghi, M.H. Hojjati, M. Imani, A.M. Goudarzi, Finite Element Analysis of Mechanical Behaviors of Coronary Stent, Procedia Engineering 10 (2011) 3056–3061. https://doi.org/10.1016/j.proeng.2011.04.506.

[88] I.V. Gomes, H. Puga, J.L. Alves, Effect of the ultrasonic melt treatment on the deployment outcomes of a magnesium stent manufactured by microcasting: a finite element analysis, in: 6th ENBENG: IEEE Portuguese Meeting in Bioengineering proceedings book 22-23 February 2019, Faculty of Medicine, ISEL, Lisbon, IEEE, [Piscataway, New Jersey], 2019?, pp. 1–4.

[89] A. Karimi, M. Navidbakhsh, H. Yamada, R. Razaghi, A nonlinear finite element simulation of balloon expandable stent for assessment of plaque vulnerability inside a stenotic artery, Medical & biological engineering & computing 52 (2014) 589–599. https://doi.org/10.1007/s11517-014-1163-9.

[90] A. Schiavone, L.G. Zhao, A.A. Abdel-Wahab, Dynamic simulation of stent deployment – effects of design, material and coating, J. Phys.: Conf. Ser. 451 (2013) 12032. https://doi.org/10.1088/1742-6596/451/1/012032.

[91] A. Syaifudin, R. Takeda, K. Sasaki, Development of asymmetric stent for treatment of eccentric plaque, Bio-medical materials and engineering 29 (2018) 299–317. https://doi.org/10.3233/BME-181737.

[92] A. Syaifudin, J.B. Ariatedja, Y. Kaelani, R. Takeda, K. Sasaki, Vulnerability analysis on the interaction between Asymmetric stent and arterial layer, Bio-medical materials and engineering 30 (2019) 309–322. https://doi.org/10.3233/BME-191054.

[93] N. Li, H. Zhang, H. Ouyang, Shape optimization of coronary artery stent based on a parametric model, Finite Elements in Analysis and Design 45 (2009) 468–475. https://doi.org/10.1016/j.finel.2009.01.001.

[94] W.-Q. Wang, D.-K. Liang, D.-Z. Yang, M. Qi, Analysis of the transient expansion behavior and design optimization of coronary stents by finite element method, Journal of Biomechanics 39 (2006) 21–32. https://doi.org/10.1016/j.jbiomech.2004.11.003.

[95] J. Bukala, P. Kwiatkowski, J. Malachowski, Numerical analysis of crimping and inflation process of balloon-expandable coronary stent using implicit solution, International journal for numerical methods in biomedical engineering 33 (2017). https://doi.org/10.1002/cnm.2890.

[96] M. de Beule, P. Mortier, R. van Impe, B. Verhegghe, P. Segers, P. Verdonck, Plasticity in the Mechanical Behavior of Cardiovascular Stents during Stent Preparation (Crimping) and Placement

(Expansion), KEM 340-341 (2007) 847–852. https://doi.org/10.4028/www.scientific.net/KEM.340-341.847.

[97] A. Schiavone, T.-Y. Qiu, L.-G. Zhao, Crimping and deployment of metallic and polymeric stents—finite element modeling, VP 1 (2017). https://doi.org/10.20517/2574-1209.2016.03.

[98] H. Zahedmanesh, D. John Kelly, C. Lally, Simulation of a balloon expandable stent in a realistic coronary artery-Determination of the optimum modeling strategy, Journal of Biomechanics 43 (2010) 2126–2132. https://doi.org/10.1016/j.jbiomech.2010.03.050.

[99] R. He, L.G. Zhao, V.V. Silberschmidt, Y. Liu, F. Vogt, Finite element evaluation of artery damage in deployment of polymeric stent with pre- and post-dilation, Biomechanics and modeling in mechanobiology 19 (2020) 47–60. https://doi.org/10.1007/s10237-019-01194-6.

[100] R. He, L. Zhao, V.V. Silberschmidt, Y. Liu, Mechanistic evaluation of long-term in-stent restenosis based on models of tissue damage and growth, Biomechanics and modeling in mechanobiology 19 (2020) 1425–1446. https://doi.org/10.1007/s10237-019-01279-2.

[101] S. Pant, N.W. Bressloff, G. Limbert, Geometry parameterization and multidisciplinary constrained optimization of coronary stents, Biomechanics and modeling in mechanobiology 11 (2012) 61–82. https://doi.org/10.1007/s10237-011-0293-3.

[102] A. Schiavone, L.G. Zhao, A computational study of stent performance by considering vessel anisotropy and residual stresses, Materials science & engineering. C, Materials for biological applications 62 (2016) 307–316. https://doi.org/10.1016/j.msec.2016.01.064.

[103] A. Schiavone, L.G. Zhao, A study of balloon type, system constraint and artery constitutive model used in finite element simulation of stent deployment, Mech Adv Mater Mod Process 1 (2015). https://doi.org/10.1186/s40759-014-0002-x.

[104] A. Amirjani, M. Yousefi, M. Cheshmaroo, Parametrical optimization of stent design; a numerical-based approach, Computational Materials Science 90 (2014) 210–220. https://doi.org/10.1016/j.commatsci.2014.04.002.

[105] C. Lally, F. Dolan, P.J. Prendergast, Cardiovascular stent design and vessel stresses: a finite element analysis, Journal of Biomechanics 38 (2005) 1574–1581. https://doi.org/10.1016/j.jbiomech.2004.07.022.

[106] I. Pericevic, C. Lally, D. Toner, D.J. Kelly, The influence of plaque composition on underlying arterial wall stress during stent expansion: the case for lesion-specific stents, Medical engineering & physics 31 (2009) 428–433. https://doi.org/10.1016/j.medengphy.2008.11.005.

[107] W. Wu, W.-Q. Wang, D.-Z. Yang, M. Qi, Stent expansion in curved vessel and their interactions: a finite element analysis, Journal of Biomechanics 40 (2007) 2580–2585. https://doi.org/10.1016/j.jbiomech.2006.11.009.

[108] H. Li, J. Gu, M. Wang, D. Zhao, Z. Li, A. Qiao, B. Zhu, Multi-objective optimization of coronary stent using Kriging surrogate model, Biomedical engineering online 15 (2016) 148. https://doi.org/10.1186/s12938-016-0268-9.

[109] H. Li, T. Liu, M. Wang, D. Zhao, A. Qiao, X. Wang, J. Gu, Z. Li, B. Zhu, Design optimization of stent and its dilatation balloon using kriging surrogate model, Biomedical engineering online 16 (2017) 13. https://doi.org/10.1186/s12938-016-0307-6.

[110] T. Schmidt, D. Pandya, D. Balzani, Influence of isotropic and anisotropic material models on the mechanical response in arterial walls as a result of supra-physiological loadings, Mechanics Research Communications 64 (2015) 29–37. https://doi.org/10.1016/j.mechrescom.2014.12.008.

[111] Y. Han, W. Lu, Optimizing the deformation behavior of stent with nonuniform Poisson's ratio distribution for curved artery, Journal of the mechanical behavior of biomedical materials 88 (2018) 442–452. https://doi.org/10.1016/j.jmbbm.2018.09.005.

[112] A. Schiavone, C. Abunassar, S. Hossainy, L.G. Zhao, Computational analysis of mechanical stress-strain interaction of a bioresorbable scaffold with blood vessel, Journal of Biomechanics 49 (2016) 2677–2683. https://doi.org/10.1016/j.jbiomech.2016.05.035.

[113] H. Zahedmanesh, C. Lally, Determination of the influence of stent strut thickness using the finite element method: implications for vascular injury and in-stent restenosis, Medical & biological engineering & computing 47 (2009) 385–393. https://doi.org/10.1007/s11517-009-0432-5.

[114] T. Jung, J.Y. Kim, Finite element structural analysis of self-expandable stent deployment in a curved stenotic artery, J Mech Sci Technol 30 (2016) 3143–3149. https://doi.org/10.1007/s12206-016-0624-5.

[115] R. Guerchais, G. Scalet, A. Constantinescu, F. Auricchio, Micromechanical modeling for the probabilistic failure prediction of stents in high-cycle fatigue, International Journal of Fatigue 87 (2016) 405–417. https://doi.org/10.1016/j.ijfatigue.2016.02.026.

[116] F. Auricchio, A. Constantinescu, M. Conti, G. Scalet, A computational approach for the lifetime prediction of cardiovascular balloon-expandable stents, International Journal of Fatigue 75 (2015) 69–79. https://doi.org/10.1016/j.ijfatigue.2015.02.002.

[117] L. Lei, X. Qi, S. Li, Y. Yang, Y. Hu, B. Li, S. Zhao, Y. Zhang, Finite element analysis for fatigue behavior of a self-expanding Nitinol peripheral stent under physiological biomechanical conditions, Computers in biology and medicine 104 (2019) 205–214. https://doi.org/10.1016/j.compbiomed.2018.11.019.

[118] M. Sabaté, F. Alfonso, A. Cequier, S. Romaní, P. Bordes, A. Serra, A. Iñiguez, P. Salinas, B. García Del Blanco, J. Goicolea, R. Hernández-Antolín, J. Cuesta, J.A. Gómez-Hospital, L. Ortega-Paz, J. Gomez-Lara, S. Brugaletta, Magnesium-Based Resorbable Scaffold Versus Permanent Metallic Sirolimus-Eluting Stent in Patients With ST-Segment Elevation Myocardial Infarction: The MAGSTEMI Randomized Clinical Trial, Circulation 140 (2019) 1904–1916. https://doi.org/10.1161/CIRCULATIONAHA.119.043467.

[119] Q. de Hemptinne, P. Xaplanteris, A. Guédès, F. Demeure, B. Vandeloo, C. Dugauquier, F. Picard, D.W. Warne, T. Pilgrim, J.F. Iglesias, J. Bennett, Magmaris Resorbable Magnesium Scaffold Versus Conventional Drug-Eluting Stent in ST-Segment Elevation Myocardial Infarction: 1-Year Results of a Propensity-Score-Matching Comparison, Cardiovascular revascularization medicine including molecular interventions 43 (2022) 28–35. https://doi.org/10.1016/j.carrev.2022.05.028.

[120] I. Adekanmbi, C.Z. Mosher, H.H. Lu, M. Riehle, H. Kubba, K.E. Tanner, Mechanical behavior of biodegradable AZ31 magnesium alloy after long term in vitro degradation, Materials science & engineering. C, Materials for biological applications 77 (2017) 1135–1144. https://doi.org/10.1016/j.msec.2017.03.216.

[121] K. van Gaalen, C. Quinn, F. Benn, P.E. McHugh, A. Kopp, T.J. Vaughan, Linking the effect of localised pitting corrosion with mechanical integrity of a rare earth magnesium alloy for implant use, Bioactive materials 21 (2023) 32–43. https://doi.org/10.1016/j.bioactmat.2022.08.004.

[122] A. Krause, N. von der Höh, D. Bormann, C. Krause, F.-W. Bach, H. Windhagen, A. Meyer-Lindenberg, Degradation behavior and mechanical properties of magnesium implants in rabbit tibiae, J Mater Sci 45 (2010) 624–632. https://doi.org/10.1007/s10853-009-3936-3.

[123] T. Qiu, R. He, C. Abunassar, S. Hossainy, L.G. Zhao, Effect of two-year degradation on mechanical interaction between a bioresorbable scaffold and blood vessel, Journal of the mechanical behavior of biomedical materials 78 (2018) 254–265. https://doi.org/10.1016/j.jmbbm.2017.11.031.

[124] C. Rogers, D.Y. Tseng, J.C. Squire, E.R. Edelman, Balloon-artery interactions during stent placement: a finite element analysis approach to pressure, compliance, and stent design as contributors to vascular injury, Circulation research 84 (1999) 378–383. https://doi.org/10.1161/01.res.84.4.378.

[125] A. Kastrati, J. Mehilli, J. Dirschinger, J. Pache, K. Ulm, H. Schühlen, M. Seyfarth, C. Schmitt, R. Blasini, F.J. Neumann, A. Schömig, Restenosis after coronary placement of various stent types, The American journal of cardiology 87 (2001) 34–39. https://doi.org/10.1016/s0002-9149(00)01268-6.

[126] M.A. Geith, L. Nothdurfter, M. Heiml, E. Agrafiotis, M. Gruber, G. Sommer, T.G. Schratzenstaller, G.A. Holzapfel, Quantifying stent-induced damage in coronary arteries by investigating mechanical and structural alterations, Acta biomaterialia 116 (2020) 285–301. https://doi.org/10.1016/j.actbio.2020.08.016.

[127] M. Azaouzi, A. Makradi, S. Belouettar, Numerical investigations of the structural behavior of a balloon expandable stent design using finite element method, Computational Materials Science 72 (2013) 54–61. https://doi.org/10.1016/j.commatsci.2013.01.031.

[128] J. Raamachandran, K. Jayavenkateshwaran, Modeling of stents exhibiting negative Poisson's ratio effect, Computer Methods in Biomechanics and Biomedical Engineering 10 (2007) 245–255. https://doi.org/10.1080/10255840701198004.

[129] I.V. Gomes, H. Puga, J.L. Alves, Shape and functional optimization of biodegradable magnesium stents for manufacturing by ultrasonic-microcasting technique, Int J Interact Des Manuf 12 (2018) 1059–1069. https://doi.org/10.1007/s12008-017-0442-8.

[130] Y. Li, J. Wang, K. Sheng, F. Miao, Y. Wang, Y. Zhang, R. Hou, Di Mei, Y. Sun, Y. Zheng, S. Guan, Optimizing structural design on biodegradable magnesium alloy vascular stent for reducing strut thickness and raising radial strength, Materials & Design 220 (2022) 110843. https://doi.org/10.1016/j.matdes.2022.110843.

[131] A. Khosravi, H. Bahreinizad, M.S. Bani, A. Karimi, A numerical study on the application of the functionally graded materials in the stent design, Materials science & engineering. C, Materials for biological applications 73 (2017) 182–188. https://doi.org/10.1016/j.msec.2016.12.034.

CHAPTER 3 – EFFECT OF ULTRASOUND TREATMENT ON THE AZ91D-1.5% Ca DOWNSTREAM PROCESSING: SHIFTING THE HEAT TREATMENT PARADIGM

Due to their exceptional physicochemical and biocompatibility qualities, biodegradable magnesium alloys are among the most promising materials for biomedical devices [1]. Nonetheless, magnesium-based devices face several unresolved obstacles that impede their broad implementation [2]. An example is their inferior mechanical properties compared to the popular medical stainless steel, which makes magnesium-based devices prone to fracture due to their low plastic deformation and high brittleness [3]. Furthermore, under physiological conditions, the corrosion rates of magnesium and its alloys are excessively high, resulting in a loss of mechanical integrity and the inability to radially support the blood vessel before the healing process is complete [4–6].

The material's microstructure, especially the intermetallic phases' composition and shape, is crucial to magnesium alloy's mechanical and corrosion-related properties. This problem becomes even more relevant, given that strategies based on alloying with calcium have been adopted to decrease magnesium reactivity. In fact, casting and handling magnesium alloys is difficult due to their high flammability, demanding a protective atmosphere of SF_6; however, increasing environmental awareness has challenged researchers and industries to develop innovative alternatives to SF_6 [7,8]. The addition of calcium

increases the ignition temperature of magnesium alloys by 200 to 300 °C [9], decreasing their flammability and making their castability less damaging to the environment [9].

On the other hand, calcium-containing magnesium alloys are characterized by a high fraction of coarse intermetallic phases, mainly Al_2Ca and β-$Mg_{17}Al_{12}$, which are seriously detrimental to the material's mechanical and corrosion properties. Intermetallic particles are preferential sites for damage initiation due to their proneness to cracking or void formation promoted by the matrix-particle decohesion, leading to early fracture [10], while they may act as micro-galvanic corrosion sites [11].

Several approaches have been proposed in the literature to modify intermetallics' shape and distribution, aiming to optimize the overall performance of magnesium alloys; from those, heat treatment stands out. Without changing the alloy's base composition, heat treatment can change the morphology and area fraction of the secondary phases, modify the grain size and promote solute redistribution, influencing the material's corrosion and mechanical properties [12].

This chapter presents the study of the effect of the ultrasound treatment on the as-cast microstructure of an AZ91D-1.5% Ca and its implications in downstream processing. The optimization of solution heat treatment for the dissolution of intermetallics was then followed by aging heat treatment to explore its potential for mechanical properties improvement.

3.1. ULTRASOUND TREATMENT OF AZ91D-1.5%CA – CONTINUOUS APPROACH

3.1.1. MATERIALS, PROCEDURES AND CHARACTERIZATION

300 grams of AZ91D-1.5%Ca alloy were melted in a SiALON crucible under an argon protective atmosphere using an electrical resistance furnace. The chemical composition of the alloy is shown in Table 3.1.

Table 3.1 – Chemical composition of AZ91D-1.5% Ca alloy (wt. %).

Alloy	Mg	Al	Zn	Mn	Ca
AZ91D-1.5%Ca	Bal.	9.7	0.5	0.2	1.5

The crucible and the furnace were pre-heated to 450 °C to eliminate humidity and moisture. The melt was held at 620 °C ± 5 °C for 20 minutes to allow the formation of the CaO protective layer, after what it was heated to 660 °C ± 5 °C, and held for homogenization for 10 min. The molten metal was then ultrasonically degassed, resorting to the apparatus presented in Figure 3.1 After the degassing procedure (4 minutes), the molten metal was poured into a pre-heated metallic mold (350 °C ± 5 °C) coupled to an ultrasonic device, as represented in Figure 3.2. Ultrasonic vibration was continuously applied to the

solidifying melt until 525 °C ± 5 °C. For comparison purposes, experiments without ultrasonic vibration were also conducted. Ten samples were cast for each experimental condition, with seven used for mechanical testing and three for microstructure characterization.

All tests using the ultrasonic vibration were conducted using a multifrequency multimode modulation (MMM) technology consisting of a high-power ultrasonic transducer, a booster with amplification of 1:2.5, a holed waveguide (diameter of 35 mm), and the medium (liquid or mold + liquid). The ultrasonic device presented a sweeping-frequency capability of adaptively modulating waveform generated by an MMM ultrasonic generator. The equipment was fully controlled through dedicated software developed by MPI (Le Locle, Switzerland). With the implemented feedback loop, the most efficient ultrasonic parameters for the selected resonant frequency and electric power were adjusted to produce the medium's highest amplitude and the largest frequency spectrum. Tests were performed using 400 W electric power and 19.8 kHz frequency using ± 0.25 kHz sweeping.

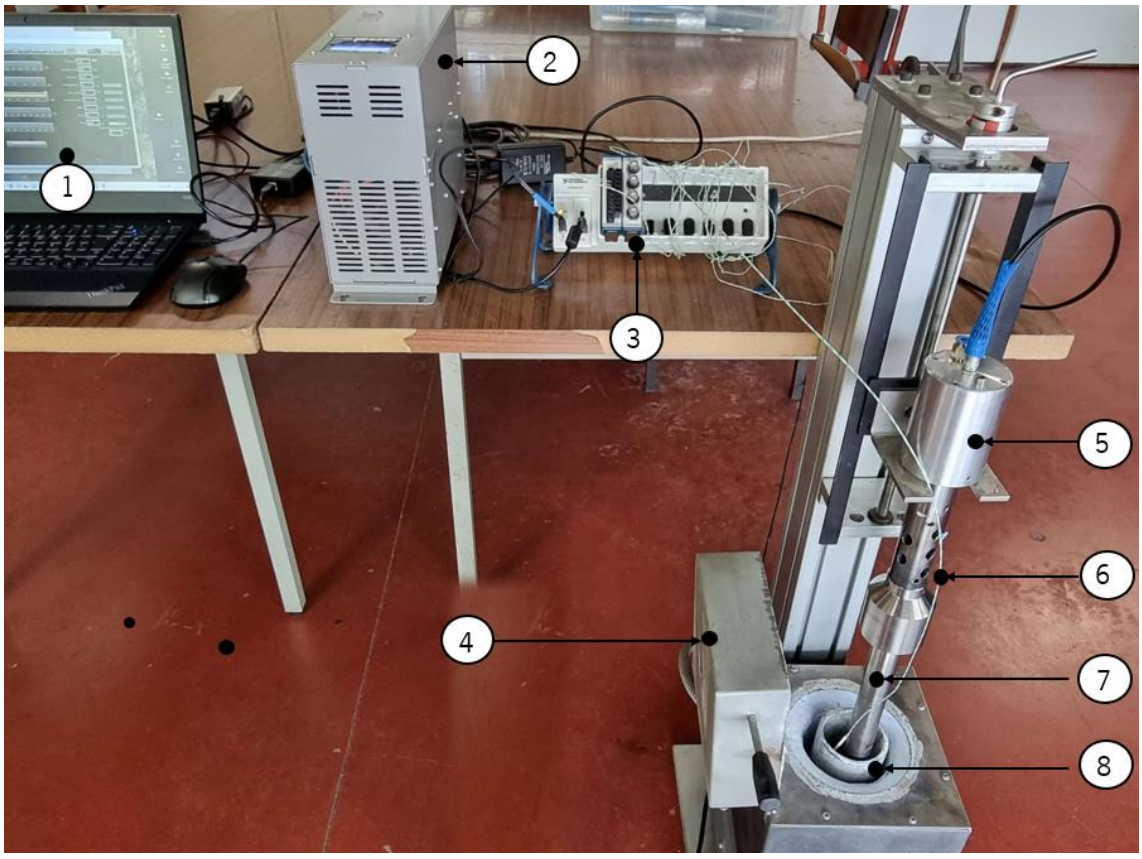

Figure 3.1 – Ultrasonic degassing apparatus. (1) Dedicated Sofware; (2) MMM generator; (3) CompactDAQ (cDAQ); (4) Resistance Furnace; (5) Transducer 20 kHz; (6) Termocouple type-K; (7) Acoustic radiator; (8) SiALON Crucible.

Figure 3.2 - Experimental apparatus: (a) Resistance melt furnance equipped with a SiALON Crucible; (b) Mold-Ultrasonic system assembly.

A LabVIEW-based dedicated program was used with a CompactDAQ (cDAQ) National Instruments system to monitor and acquire metal and steel die temperatures online.

Samples for hardness testing and microstructural characterization were ground with SiC papers, polished with 1 μm polycrystalline diamond suspension, followed by oxide polishing using 0.02 μm colloidal silica to avoid the work-hardening caused by conventional grinding. Before optical microscopy analysis, samples were etched with a 4% solution of HNO_3 in ethanol to reveal the microstructure (LEICA DM2500 M). A deep etching technique based on the selective dissolution of the matrix was applied to study the intermetallics' shape. More detailed analysis concerning the phase's morphology and chemical composition was performed by resorting to a JSM-6010LV (JEOL, Japan) Scanning Electron Microscope (SEM) equipped with an energy dispersive spectroscope (EDS) (INCAx-act, PentaFET Precision, Oxford Instruments).

3.1.2. Results and discussion

Figure 3.3 (a) and (b) show, respectively, the microstructure of non-treated and ultrasound-treated (hereafter referred to as US-treated) samples in the as-cast condition. Both microstructures were characterized by the presence of the same phases, identified by EDS analysis as primary α-Mg and secondary β-$Mg_{17}Al_{12}$ and Al_2Ca phases (Figure 3.3 (c) and (d)). The application of ultrasonic vibration during the solidification is suggested to have remarkably modified the morphology of the intermetallic phases, namely of the eutectic β-$Mg_{17}Al_{12}$, along with the refinement of the α-Mg phase, which showed a

decrease of the grain size from 80 ± 8 μm to 32 ± 4 μm. An increased tendency of small and homogeneously distributed divorced β-$Mg_{17}Al_{12}$ was noticed, which may be justified by the higher cooling rate promoted by the acoustic streaming [13]. Additionally, the refinement of the α-Mg phase may have led to the refinement of the β-$Mg_{17}Al_{12}$ phase once the intermetallic is formed in the spaces between the grains [14].

In contrast, in the absence of the ultrasonic vibration, the β-$Mg_{17}Al_{12}$ phase was considerably coarser and presented mostly a partially divorced morphology typical of lower cooling rates. A combination of reticular intermetallic distributed along the grain boundaries and coarse skeleton-like particles could be observed. The intermetallic network became discontinuous and fragmented after ultrasonic vibration application, exhibiting a more uniform dispersion.

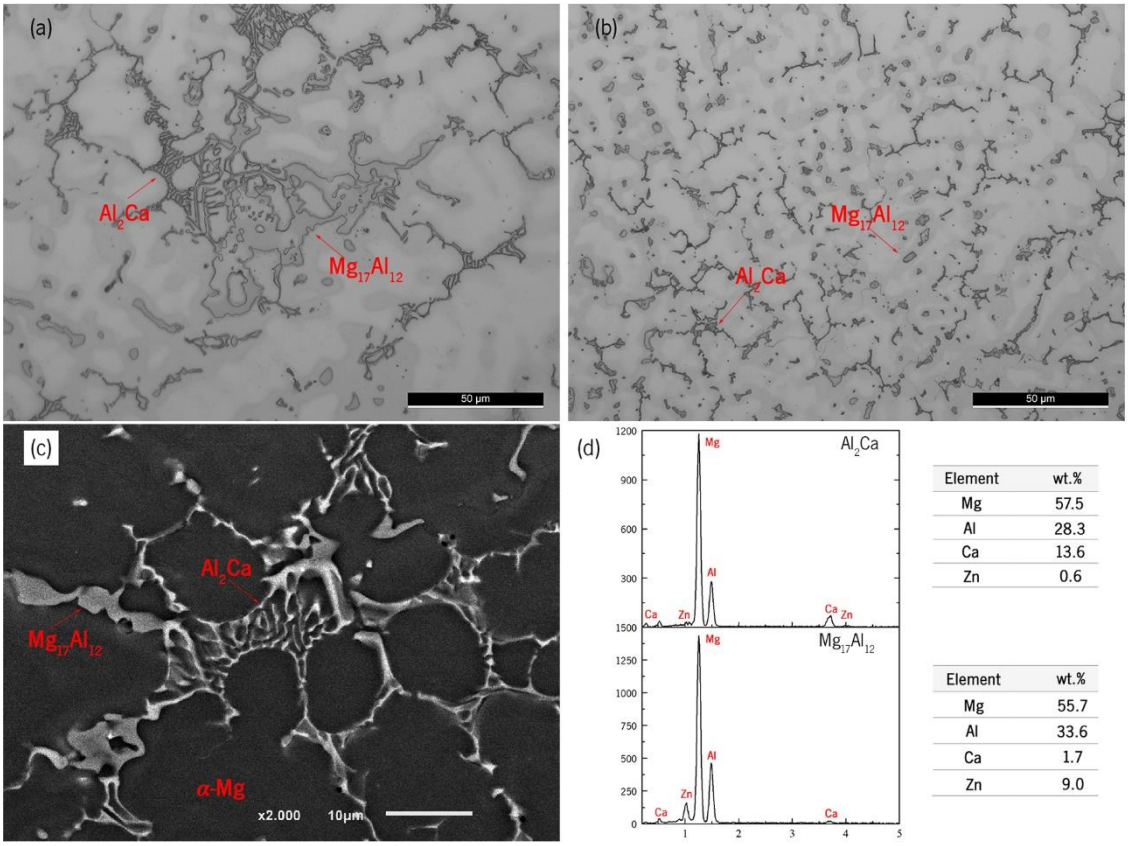

Figure 3.3 – Microstructure of (a) non- and (b) US-treated samples in the as-cast condition, (c) SEM image of the phases identified through EDS analyses (d).

In addition to the modification of the β-$Mg_{17}Al_{12}$ phase morphology, remarkable changes in the morphology and distribution of the Al_2Ca phase were found, as shown in Figure 3.4.

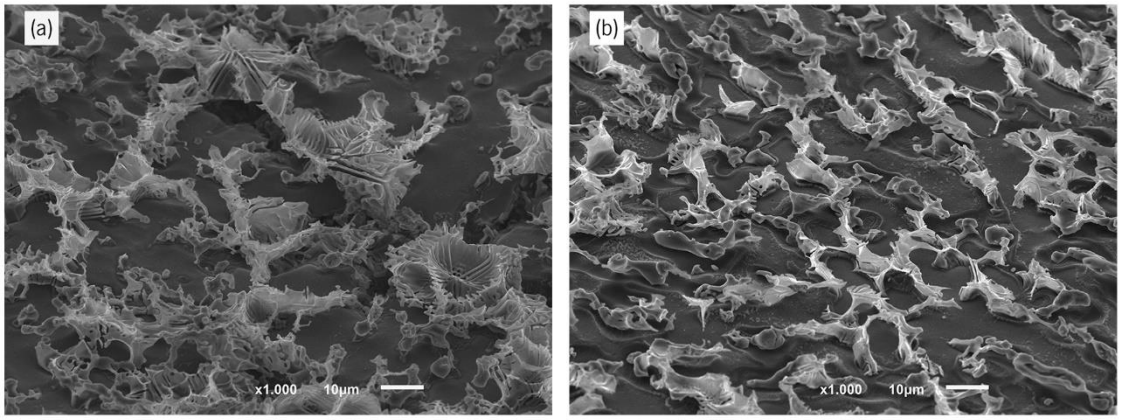

Figure 3.4 – Deep-etched microstructures of (a) non- and (b) US-treated samples.

Deeply etched microstructures allowed for a more detailed investigation of the intermetallics morphology, demonstrating that both non- and US-treated samples had a lamellar Al_2Ca phase with distinct morphological features. In contrast to the non-treated sample, which exhibited a rosette-like structure for the Al_2Ca intermetallic, the US-treated sample developed an epitaxial platelet shape from the α-Mg phase. Ultrasonic vibration at a temperature range near Al_2Ca formation may have inhibited intermetallic development, resulting in its modification and homogenous distribution [15]. It has been observed that this modification of the intermetallic morphology increases the alloy's strength and ductility, highlighting the possibility of ultrasound treatment to improve its performance in the as-cast condition.

3.2. Optimization of solution heat treatment of AZ91D-1.5%Ca

Solution heat treatment has been proven effective in dissolving the intermetallics commonly found in magnesium alloys such as AZ91D. During the heat treatment, precipitates are dissolved into the matrix, resulting in a more homogenous distribution of the alloying elements [16]. This microstructure modification may be related to changes in the material's mechanical and corrosion properties, which may be helpful for biomedical applications.

Nevertheless, despite promising results reported regarding the beneficial effects of the intermetallics' dissolution, the temperature and duration required due to the coarse morphology render this option economically unattractive, while it brings additional issues such as surface oxidation and grain growth [17]. The solution treatment optimization depends on the as-cast microstructure tailoring, which a chemical or physical process can accomplish. Rare Earth elements have been found to refine the α-Mg phase in aluminum-containing magnesium alloys. However, Mg-RE alloys have significant drawbacks, including (i) possible adverse effects such as hepatoxicity promoted by yttrium, cerium, gadolinium, and samarium, among other elements [18], (ii) the high cost associated with their obtention, which, due to

the large quantity required, makes it impractical for industrial applications; (iii) casting issues such as hot-tearing, and (iv) modification of the base alloy composition [19,20]. Otherwise, applying ultrasound treatment to the molten magnesium alloy and/or during its solidification is a simple and cost-effective alternative that has yielded promising results regarding the refinement of primary and intermetallic phases while promoting their uniform distribution in the matrix [14]. Although some work has been published in this regard, there is a lack of research on the impact of ultrasound processing of calcium-containing magnesium alloys, especially concerning its effect on the outcomes of the subsequent processing routes for biomedical applications.

In this sense, the effect of applying ultrasound treatment during the cooling of an AZ91D-1.5%Ca alloy on the as-cast microstructure was explored. Also, to further investigate the effect of the as-cast microstructure in the subsequent heat treatment, specifically in the kinetics dissolution of the intermetallic phases, solution treatment was performed at different temperatures (385 °C and 415 °C) and periods (from 120 to 1440 minutes). This research reveals the possibility of modifying the as-cast microstructure to enhance the solution treatment of magnesium-calcium alloys, so making this processing approach economically viable.

3.2.1. Experimental procedure for β-$Mg_{17}Al_{12}$ dissolution

Samples from non- and US-treated cast billets were solution-treated at different temperatures (385 °C and 415 °C) for different periods (120, 300, 720, and 1440 minutes) to promote the β-$Mg_{17}Al_{12}$ dissolution, followed by water quenching at room temperature to prevent further phase transformation by residual heat. The metallographic preparation of samples was performed according to the procedure presented in the previous section (3.1.1). SEM analyses were carried out to study the intermetallics shape and fraction evolution as a function of both temperature and duration of heat treatment. Also, phase identification was performed by X-ray diffraction (XRD) on a Bruker AXS D8 Discover with Cu-Kα radiation (λ = 1,54060 Å), scanning from 0° to 90° at a scanning speed of 0.02°/s. Hardness tests were conducted using an Officine Galileo Mod. D200 tester under a load of 50 gf with a dwelling time of 15 s. A minimum of five indentations were averaged for each reported hardness measurement.

3.2.2. Results and Discussion

A. Microstructural evolution of non- and US-treated samples

The microstructure evolution of the non- and US-treated samples solutionized at 385 °C is presented in Figure 3.5 for solution treatment duration from 120 to 1440 minutes.

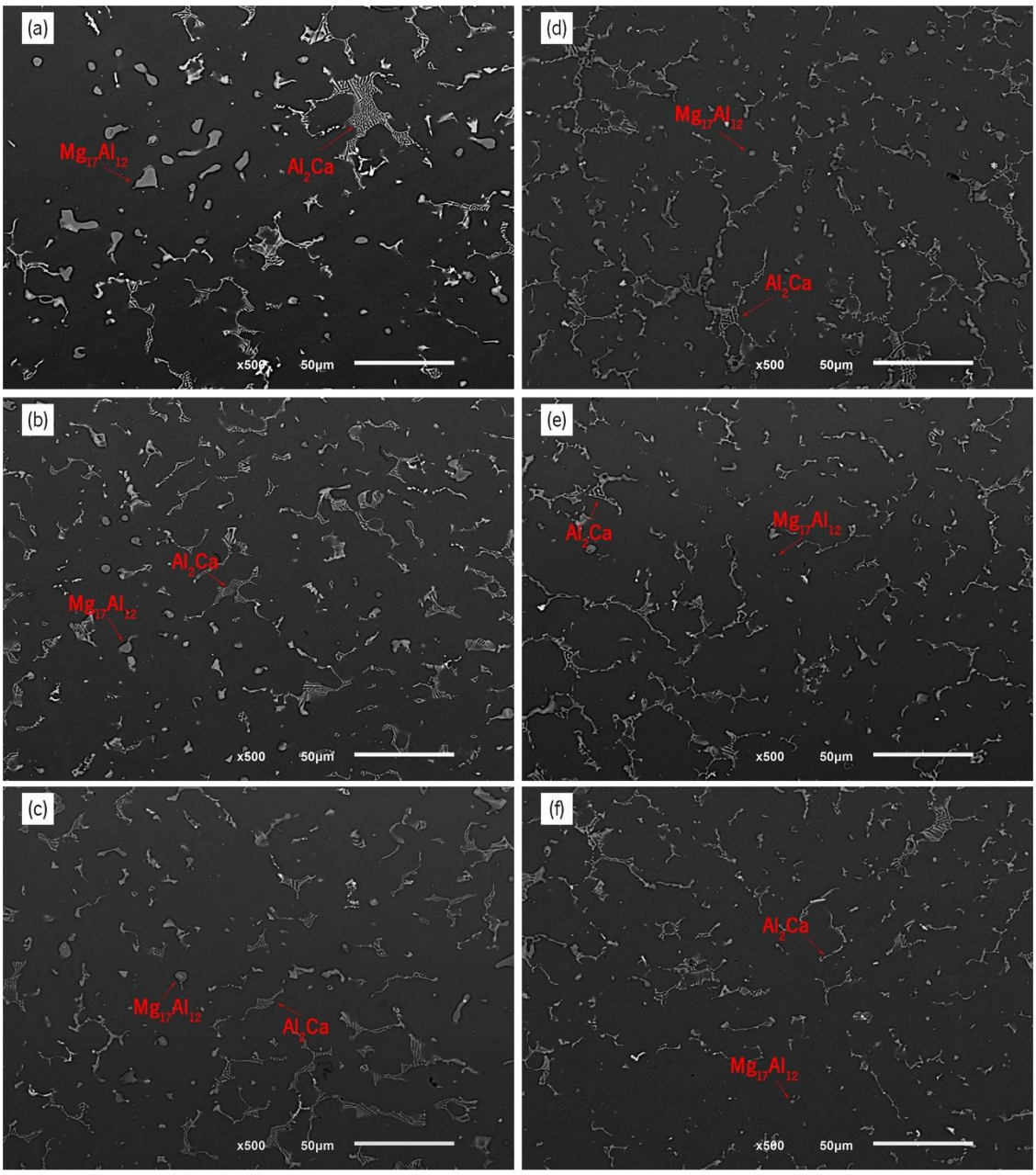

Figure 3.5 – Evolution of the microstructure of non-treated (a, b, c) and US-treated (d, e, f) samples during solution treatment at 385 °C for 120, 300, and 1440 min, respectively.

As seen in Figure 3.5 (a)-(c), there was no detectable difference in the morphology of β-$Mg_{17}Al_{12}$ in the non-treated sample, regardless of the holding time. Indeed, coarse particles could be found even after 1440 minutes of treatment (Figure 3.5 (c)), suggesting that no considerable dissolution occurred under these conditions. During the first treatment hours, the US-treated samples exhibited a reduction in the β-$Mg_{17}Al_{12}$ phase (Figure 3.5 (d)-(e)), and after 120 minutes, just a few particles remained (Figure 3.5 (f)). The difference observed in response to solution treatment at 385 °C of the non- and US-treated samples is suggested to lay essentially in two factors: (i) coarser particles require more time and/or higher

temperature to dissolve [21] and (ii) according to EDS results, the concentration of aluminum in the matrix surrounding the β-$Mg_{17}Al_{12}$ phase in the non-treated sample is higher than the observed in the US-treated one, making the diffusion process more difficult due to the lower aluminum gradient. Therefore, a longer time may be required for the homogeneity of the aluminum distribution throughout the matrix so that intermetallic dissolution may occur.

As demonstrated in Figure 3.6, microstructural changes could be observed in both non- and US-treated samples by increasing the solution treatment temperature to 415 °C.

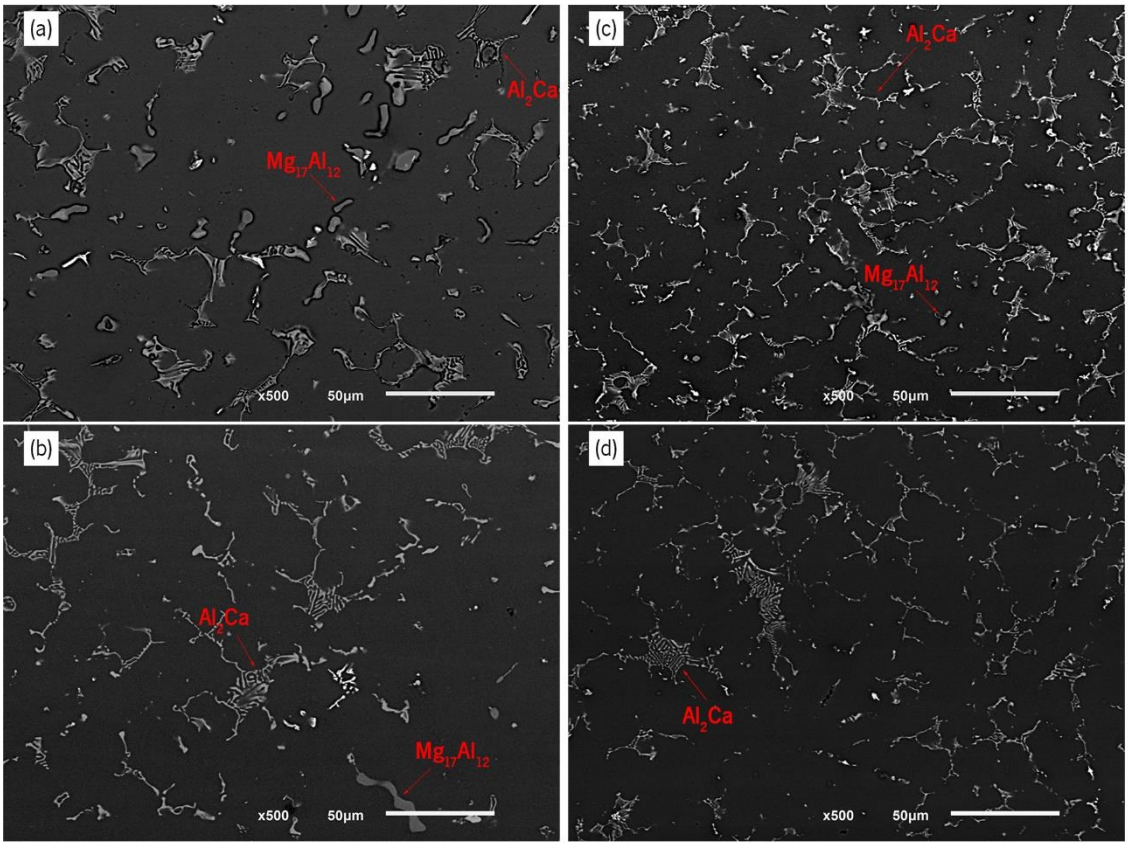

Figure 3.6 – Microstructure of non- (a, b) and US-treated (c, d) samples solutionized at 415 °C for 120 and 1440 min, respectively.

In the non-treated sample, although a reduction of the presence of β-$Mg_{17}Al_{12}$ was evident even after only 120 minutes (Figure 3.6 (a)), some coarse particles remained regardless of the duration of the heat treatment (Figure 3.6 (b)), indicating that more prolonged solution treatment could be necessary to dissolve them further. In contrast, after 120 minutes of solution treatment (Figure 3.6 (c)), only tiny β-$Mg_{17}Al_{12}$ particles were detected in the US-treated sample, suggesting that this intermetallics phase had been almost completely dissolved after 1440 minutes (Figure 3.6 (d)). These findings were confirmed by the XRD results (see Figure 3.7), which showed that after heat treatment at 415 °C for 1440 min, no β-

$Mg_{17}Al_{12}$ peaks were detected in the US-treated sample, conversely to the non-treated one. Also, the results obtained showed that the Al_2Ca phase was present regardless of the processing conditions, stressing its high thermal stability.

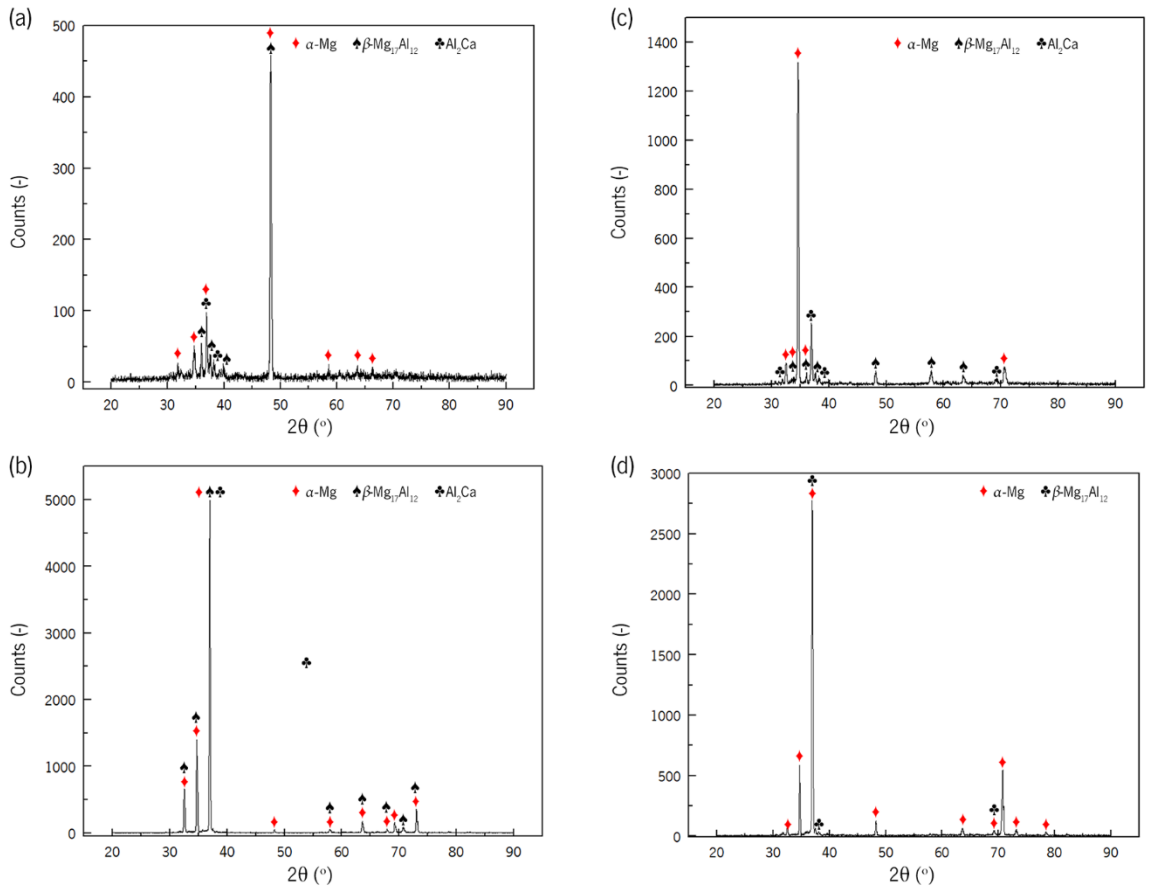

Figure 3.7 – XRD analyses of non- (a,b) and US-treated (c,d) samples in the as-cast and solution-treated at 415 °C for 1440 minutes conditions.

Figure 3.8 shows the evolution of the intermetallic phases' area fraction as a function of the solution treatment time, assessed through microstructures' image analysis. Due to their inability to be distinguished, all intermetallics' surface areas were included in the measurements. However, given that both Al_2Ca and Al-Mn phases are thermally stable and do not dissolve at the temperature used for the heat treatment [10,22], it was assumed that reduction in the area fraction corresponded only to the dissolution of the β-$Mg_{17}Al_{12}$ phase.

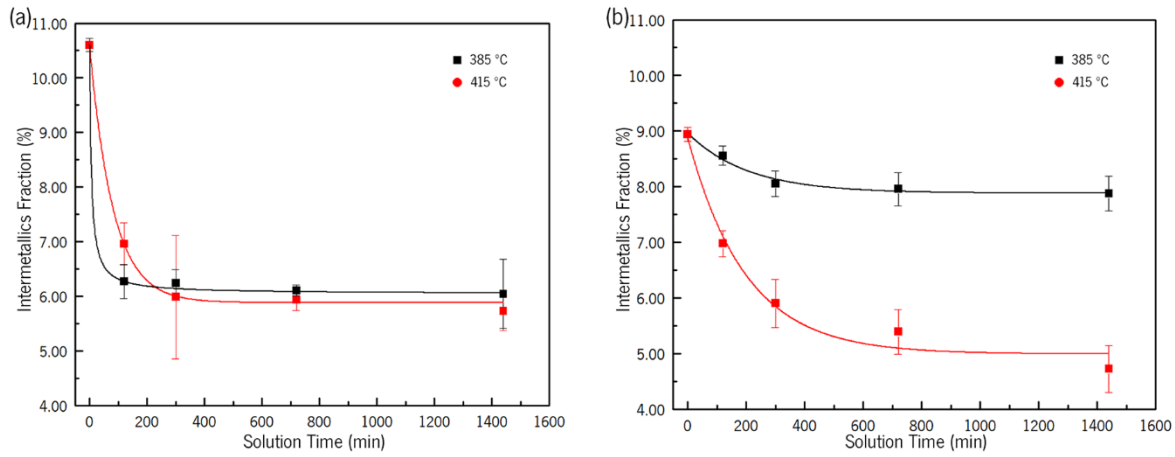

Figure 3.8 – Evolution of intermetallics' area fraction during solution treatment at 385 °C and 415 °C of (a) non- and (b) US-treated samples.

The non-treated sample demonstrated a higher intermetallics area fraction than the US-treated one, which may be explained by the increased cooling rate and reduced segregation promoted by the ultrasound treatment. These results are in line with those of Khan *et al.* [24] and Jixue *et al.* [25], who studied the effect of cooling rate on microsegregation in magnesium-based alloys, as well as with the observations of He *et al.* [26], who discovered that faster cooling suppressed the formation of intermetallics in aluminum-based alloys. The lowest intermetallic area fraction was attained following solution treatment of the US-treated sample for 1440 minutes (4.7%), whereas the minimum value for the non-treated sample under the same conditions was around 5.8%. Regardless of the processing conditions, a higher solution treatment temperature resulted in a quicker reduction of intermetallics, although the difference was not meaningful for the non-treated sample.

The evolution of the area fraction differed significantly between non-treated and US-treated samples. During the first stage of solution treatment, the non-treated samples exhibited a sharp decrease in the intermetallics fraction area, which may be attributed to the fast dissolution of the smaller particles. However, the value stabilized when the solution treatment was extended from 300 min, indicating that further dissolution hardly occurred. As previously reported by Papaefthymiou *et al.* [23] for copper alloys, these results reveal that coarse intermetallic particles were not dissolved into the matrix even after 1440 minutes, which may indicate that a higher temperature is necessary to accomplish complete dissolution. On the other hand, US-treated samples demonstrated a steady decline in the intermetallics area fraction, although less pronounced in the final stages of the solution treatment, mainly at 415 °C. Despite the superior dissolution rate observed for solution treatment at a higher temperature, the intermetallics area fraction was nearly the same at 385 °C and 415 °C after heat treatment for 1440 min. Nonetheless,

solution treatment at a higher temperature allowed for a lower intermetallic fraction in a shorter period. However, such a difference tended to decrease as the heat treatment duration increased, meaning a progressively lower dissolution rate, especially from 720 min.

The dissolution kinetics of the β-$Mg_{17}Al_{12}$ phase can be described by the Johnson–Mehl–Avrami–Kolmogorov (JMAK) equation as follows:

$$f = 1 - \exp(-kt^n) \quad (1)$$

where f is the fraction dissolved at time t at a constant temperature, and k and n are the temperature-dependent isothermal rate constant and the Avrami exponent, respectively, which characterize the transformation process. By evaluating the experimental data and plotting $\ln(\ln(1/(1-f)))$ versus $\ln(t)$, t and n values can be determined for non- and US-treated samples for both solution treatment conditions, as depicted in Figure 3.9. The values of k and n are presented in Table 3.2.

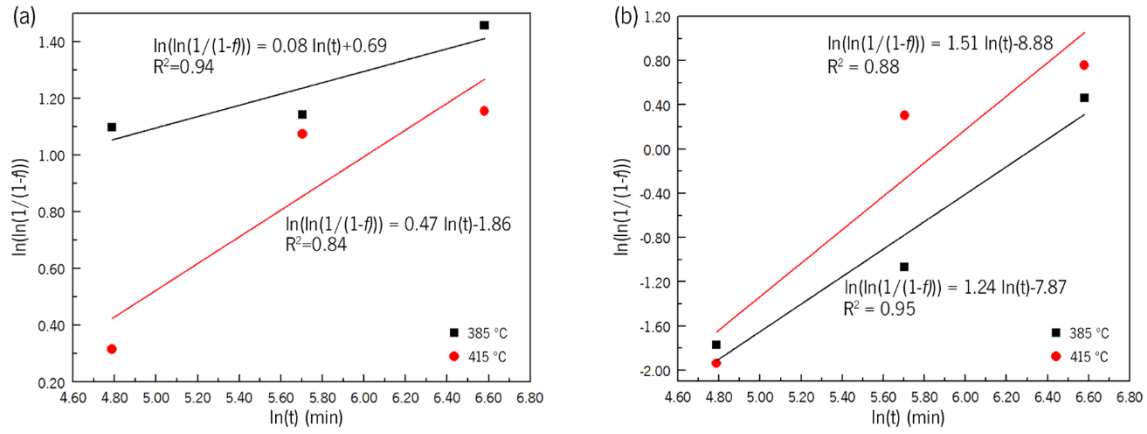

Figure 3.9 – Plot of $\ln(\ln(1/(1-f)))$ versus $\ln(t)$ for (a) non- and (b) US-treated samples.

Table 3.2 – Constants of JMAK equation for non- and US-treated samples solution-treated at 385 °C and 415 °C, obtained from Figure 3.9.

Condition	**Solution Temperature** [°C]	n [-]	k [-]
Non-treated	385 °C	0.08	0.69
	415 °C	0.47	-1.86
US-treated	385 °C	1.24	-7.87
	415 °C	1.51	-8.88

The dissolution of the intermetallic phase is controlled by diffusion, which slowed down as the solution treatment duration increased. This behavior is due to the increase in aluminum content in the matrix surrounding the intermetallic particles, reducing the concentration gradient and, thereby, the dissolution phenomenon' driving force. Also, the low diffusivity of aluminum in magnesium demands a longer time to diffuse the solute to the matrix further, leading to a lower dissolution rate [11].

The evolution of the intermetallics dissolved fraction obtained experimentally and by JMAK equation solving is presented in Figure 3.10. The results showed that the dissolution of the intermetallic phases was well described by the JMAK equation during the solution treatment, as evidenced by the good agreement between the experimental and calculated results. The non-treated samples achieved higher intermetallics dissolved fractions at the early stages of the solution treatment, which is explained by the heat treatment being capable of dissolving only a small amount of intermetallics. In this way, the solution treatment allowed mostly for dissolving small particles, meaning that the process developed fast. However, the intermetallics area fraction reduction was not as significant as that observed for US-treated samples, as depicted in Figure 3.8. The higher dissolution rate observed for US-treated samples is suggested to be the result of the combination of fine intermetallics and homogeneous distribution of solutes through the matrix, establishing a gradient of composition that allowed aluminum to migrate from the intermetallic.

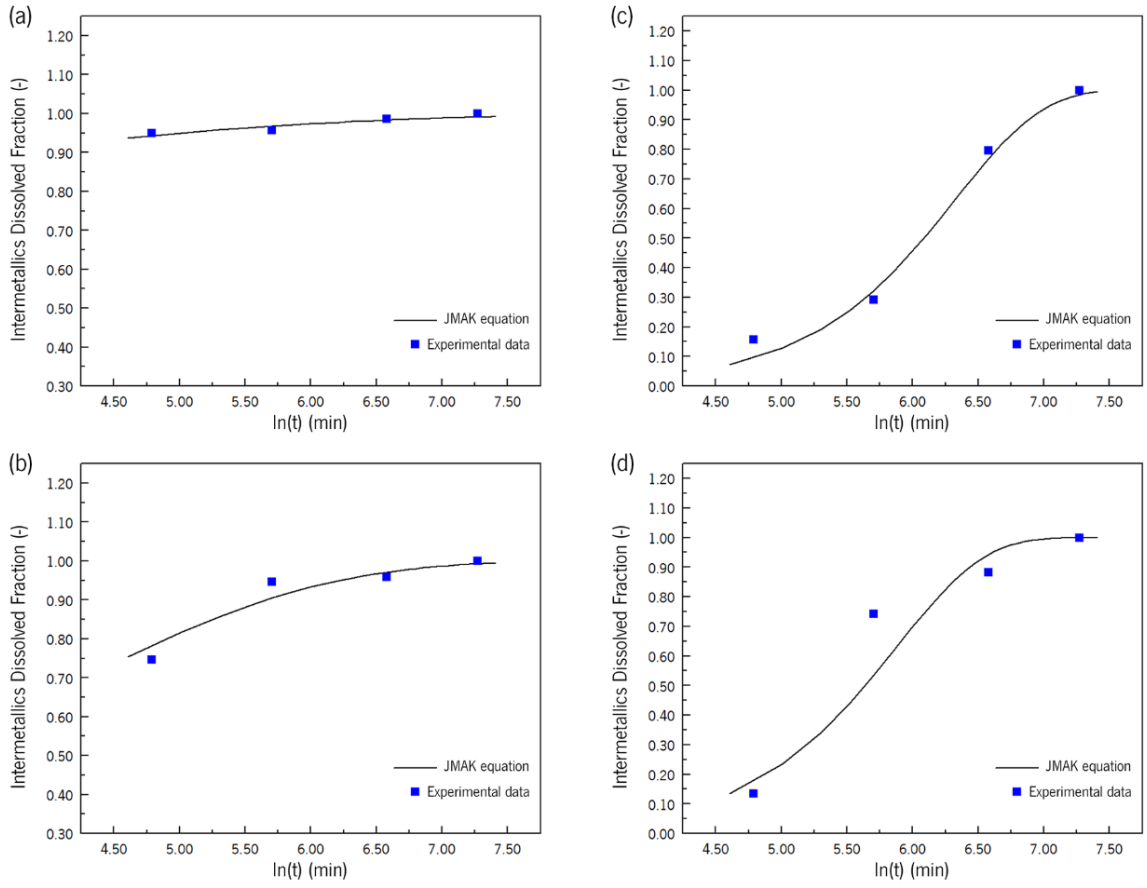

Figure 3.10 – Intermetallic dissolved fraction obtained experimentally and by JMAK equation solving for (a,b) non- and (c,d) US-treated samples solution-treated at 385 °C (a,c) and 415 °C (b,d).

B. HARDNESS EVOLUTION OF NON- AND US-TREATED SAMPLES

The hardness curves for the non-treated and US-treated samples are presented in Figure 3.11. The evolution of both samples' hardness agrees with the microstructural changes described above.

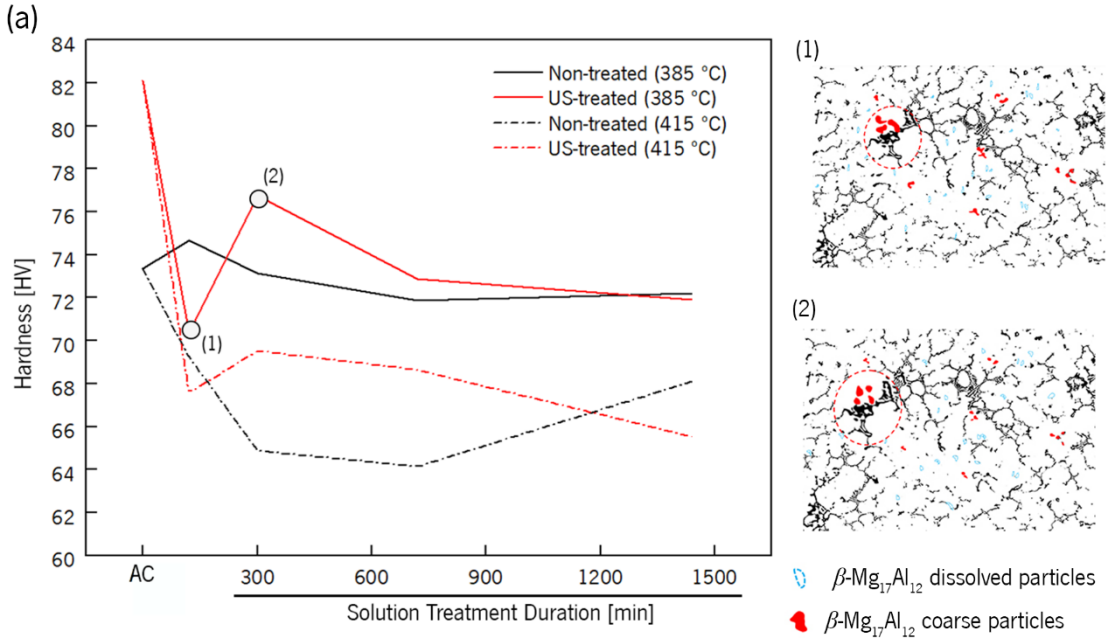

Figure 3.11 – (a) Hardness curves for the non-treated and US-treated samples solutionized at 385 °C and 415 °C for different periods; (1) and (2) representation of the dissolution process of β-Mg17Al12 particles in the US-treated samples after 2 h and 5 h.

In the as-cast state, the hardness of non- and US-treated samples was higher. In this condition, the US-treated sample exhibited a significantly higher hardness, resulting from the refined microstructure. The difference in the hardness of the non- and US-treated samples showed a tendency to decrease as the solution treatment proceeded. While for the non-treated sample solution-treated at 385 °C, the hardness value remained nearly constant throughout the treatment due to the lack of microstructural evolution, a sharp decrease in the hardness of the US-treated one was observed during the first 2 h of solution treatment, followed by its increasing. The inversion in the hardness-decreasing tendency of the US-treated sample is suggested to be resultant of the balance between two mechanisms that act contrarily: (i) within the first hours of the solution treatment, the smallest β-$Mg_{17}Al_{12}$ particles dissolved into the matrix (see Figure 3.11 (1)), leading to the softening of the material once this is the hardest phase of the material [24]; (ii) as solution treatment proceeded to 5 h, the coarser β-$Mg_{17}Al_{12}$ particles continued dissolving, decreasing their size (see Figure 3.11 (2)) and becoming more evenly distributed, which led to an increase

in the hardness [25]. For more prolonged treatment, most of the β-$Mg_{17}Al_{12}$ dissolved, and the particles' barrier effect faded out, causing the hardness value to decrease and stabilize.

When the solution treatment was performed at 415 °C, the hardness of both non- and US-treated samples decreased due to the dissolution of the β-$Mg_{17}Al_{12}$ phase. The dissolution of the intermetallic phase is mediated by the diffusion process, which is favored by the temperature increase, occurring faster. This way, despite the remarkable differences observed between the as-cast microstructures of non- and US-treated samples, β-$Mg_{17}Al_{12}$ dissolution occurred in both. The increase in the solution treatment temperature also contributed to the enhancement of aluminum diffusivity in magnesium, shortening the time required for achieving a homogenous aluminum concentration in the matrix and, thereby, a suitable concentration gradient to promote intermetallic dissolution. However, given the coarse and partially divorced morphology of the β-$Mg_{17}Al_{12}$ in the non-treated sample, this process is suggested to take longer than in the US-treated sample, and a continuous decrease in the material's hardness could be observed until after 12 h. The hardness of the sample increased after 24 h, which may have been promoted by the presence of smaller and rounder intermetallic particles resulting from the dissolution of coarser ones. As previously suggested, these smaller and rounder particles of the intermetallic phase can offer an enhanced combination of strength and elongation [26]. Nevertheless, a continuous decrease in the US-treated sample hardness was observed. Grain growth promoted by prolonged exposure to high temperature may explain this tendency as the average grain size increases, and the reduced β-$Mg_{17}Al_{12}$ fraction has been reported to lead to the alloy softening [27].

Considering the results obtained, it is possible to conclude that the significant difference in the dissolution rate of the β-$Mg_{17}Al_{12}$ during solution treatment between the non- and US-treated specimens may be justified mainly through the particles' morphology, composition and distribution in the as-cast state along with the aluminum concentration in the matrix. In the non-treated sample, β-$Mg_{17}Al_{12}$ appeared mainly as non-uniformly distributed partially divorced coarse lumps characterized by a small interfacial area for aluminum atoms diffusion, hindering their dissolution [26]. The concentration gradient in the partially divorced eutectic found in the non-treated sample was not uniform, which, together with the high aluminum concentration in their surroundings, led to the dissolution of the intermetallic to be slowed down [28]. Moreover, part of the added calcium was dissolved in the β-$Mg_{17}Al_{12}$, which is known to increase the thermal stability of this phase. According to the EDS results shown in Figure 3.12, the amount of calcium dissolved in the β-$Mg_{17}Al_{12}$ was higher in the non-treated sample than in the US-treated one. This difference, allied to the larger intermetallic particles and higher aluminum concentration in their

surroundings, can explain the lower dissolution rates of the non-treated sample. Also, the US-treated sample exhibited smaller and evenly distributed β-$Mg_{17}Al_{12}$ throughout the alloy, reducing the diffusion distance and, therefore, shortening the time required for the dissolution process.

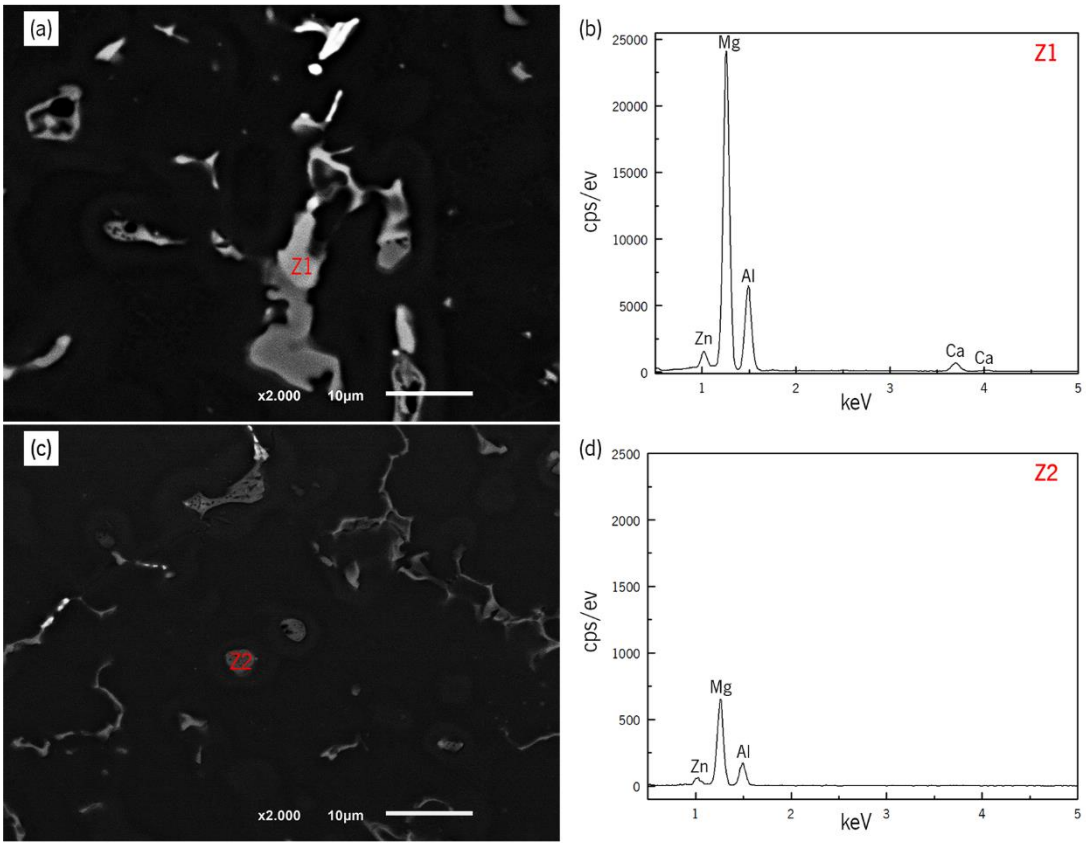

Figure 3.12 – SEM image of β-Mg17Al12 particle in the (a) non-treated and (b) US-treated samples; (c) and (d) composition of Z1 and Z2, respectively.

3.3. ARTIFICIAL AGING OF AZ91D-1.5%CA

The trade-off between magnesium alloys' strength and ductility is still a challenge that has been addressed by several authors in the last few years [29–31]. Significant attention has been paid to wrought magnesium alloys, resulting in significant advances [32–34], while casting magnesium alloys has been neglected in terms of processing and optimization [35]. A substantial fraction of intermetallic phases formed during the solidification process of the alloys, which can play a role in the material's behavior. In fact, the intermetallics' morphology and distribution can strongly influence the material's mechanical and corrosion properties, suggesting the possibility of optimizing its performance by controlling its microstructure.

As the predominant intermetallic phase in AZ91D magnesium alloy, β-$Mg_{17}Al_{12}$ precipitates may enhance the material's strength, but at the expense of its ductility. The precipitation of this phase from the

supersaturated matrix may assume two different and competitive modes: discontinuous and continuous precipitation. Discontinuous precipitates exhibit an elliptical or lamellar shape composed of β-$Mg_{17}Al_{12}$ and aluminum-enriched α-Mg and form mainly at the grain boundaries, growing inward [36]. Continuous precipitates, on the other hand, are characterized by a lozenge-shaped plate phase known as the Widmanstätten phase, which nucleates and grows inside the α-Mg grains with a primary habit plane parallel to the [0001] basal plane of the matrix [36,37]. The contribution of each precipitate type to the material's mechanical properties is not yet fully understood, and the literature offers conflicting views. Some authors [38,39] claimed that continuous precipitates could endow the material with a superior age-hardening response, given that discontinuous precipitate morphology could lead to early fracture [39,40]. From a different perspective, discontinuous precipitates were suggested to play the leading role in aging hardening due to the thin plates being parallel to the basal plane, easing the dislocation gliding [36,41].

Solution treatment followed by artificial aging has proven to be able to tailor the morphology of the β-$Mg_{17}Al_{12}$ precipitates by controlling both the temperature and duration of the heat treatment [42–44]. However, it has been noted that magnesium alloys aged at temperatures below 200 °C require long aging periods to attain their peak-aged condition [45,46], turning the process energy-intensive and expensive. On the other hand, ultrasound treatment has been intensively explored for microstructural modification, and it has been demonstrated that it can promote peak-aging conditions in a shorter time span in aluminum alloys [47]. Moreover, ultrasonic excitation may grant a refined microstructure with a smaller grain size [14] as well as the formation of vacancies [48], both features deeply related to the formation of discontinuous and continuous precipitates, respectively [40].

This work details the influence of ultrasound treatment on an AZ91D-1.5%Ca (wt.%) solidifying melt in its microstructure and, thereby, in its age-hardening response. The heat-treated samples' hardness evolution was investigated for non- and ultrasound-treated conditions, and the precipitates formed were comprehensively characterized. Moreover, tensile mechanical properties of the material in the as-cast, solution-treated and peak-aging states are determined at room temperature.

3.3.1. Experimental procedure for β-Mg17Al12 precipitation

Samples from non- and US-treated cast billets were subjected to an 8-hour solution heat treatment at 415 °C, followed by quenching in water at room temperature to avoid additional phase transition. Solution-treated samples from non- and ultrasound-treated alloys were kept to determine their properties. Artificial aging was then carried out by maintaining the samples at 175 °C for 240 to 4920 minutes. Samples' metallographic preparation for OM and SEM analyses and hardness testing was carried out according to

the procedure presented in the previous section. Casted samples were machined to sheet tensile specimens (type B, according to ISO 6892-1) with a 3.0 mm thickness and a 100 ± 0.50 mm proof length. Universal testing equipment (INSTRON 8874) was used to perform tensile testing with a 1 mm/s displacement rate until the specimens' fracture occurred and a load drop was observed. Seven samples were tested for non- and US-treated alloy in the as-cast, solutionized, and peak aging conditions.

3.3.2. Results and Discussion

A. Microstructure of solution-treated and artificially aged samples

Figure 3.13 presents the microstructure of non- and ultrasound-treated samples after solution treatment at 415 °C for 8 hours. As it can be observed, β-$Mg_{17}Al_{12}$ was nearly fully dissolved in the ultrasound-treated samples, whereas small particles could still be observed in the non-treated ones (Figure 3.13 (b)). Thus, it is hypothesized that the dissolving process evolved differently depending on the processing conditions, and the initial microstructure may have influenced the observed discrepancies. As noted in the preceding sections, the non-treated sample exhibited β-$Mg_{17}Al_{12}$ coarse bulk particles, which may have contributed to its insufficient solutionization due to a slower dissolving rate (Figure 3.13 (a)). In addition, it was found that the remaining β-$Mg_{17}Al_{12}$ particles on the ultrasound-treated sample contained calcium in their composition, which has been proven to boost the thermal stability of this phase and inhibit its dissolution [49].

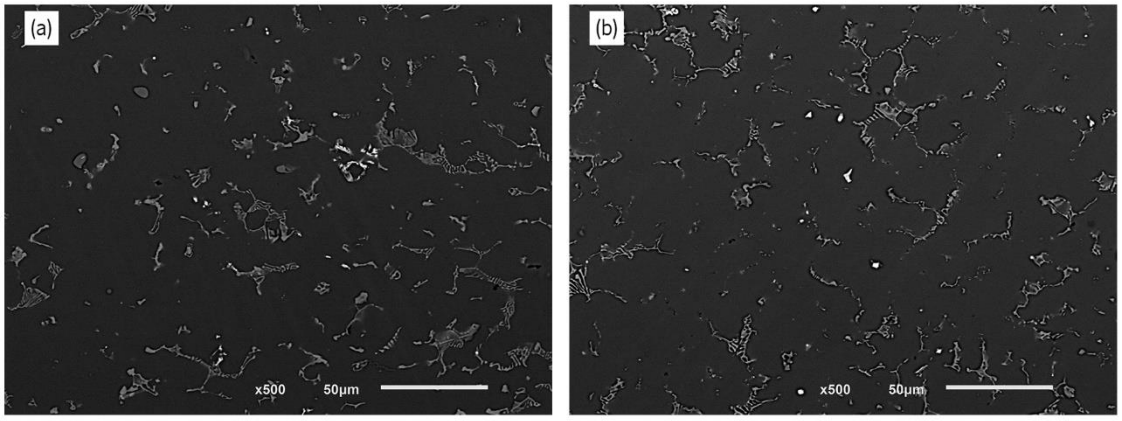

Figure 3.13 – Microstructure of (a) non- and (b) ultrasound-treated samples after solution treatment at 415 °C for 8 hours.

SEM micrographs of the non- and ultrasound-treated samples at the peak-age condition at 175 °C are shown in Figure 3.14, along with the EDS analysis results of the identified precipitates.

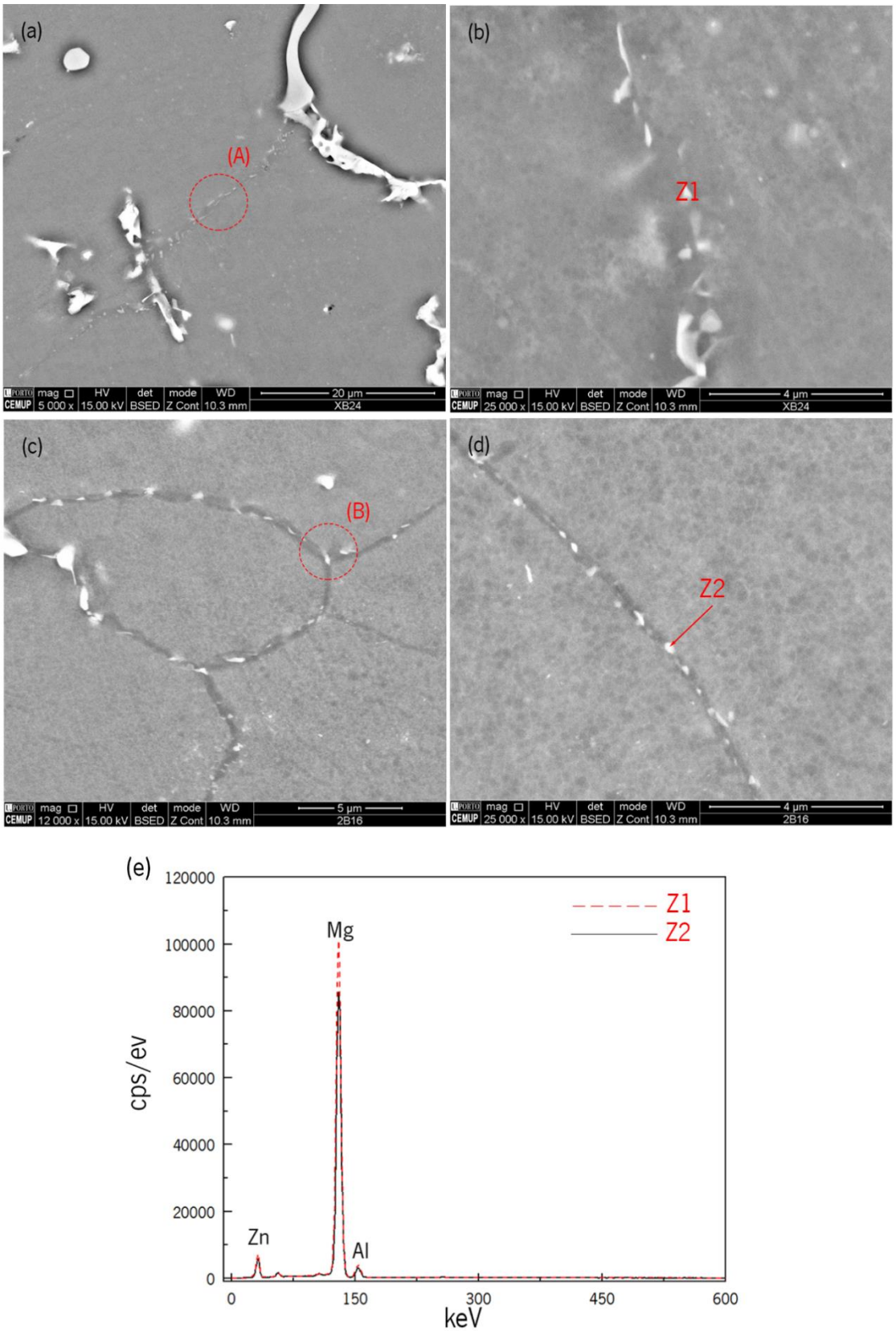

Figure 3.14 – SEM micrographs of the discontinuous β-$Mg_{17}Al_{12}$ precipitates found in (a,b) non- and (c,d) US-treated samples, after aging at 175 °C for 24 h and 16 h respectively; (e) EDS analysis of the particles identified as Z1 and Z2 in (b) and (d).

During the aging treatment, two types of precipitates – continuous and discontinuous - may form and develop competitively as they nucleate and grow at different rates [55,56]. Although their chemical composition is the same, their morphology differs; thereby, their strengthening action is distinct. In this case, both non- and ultrasound-treated samples exhibited only discontinuous precipitates, which may be explained by the low aging temperature adopted [57]. Most precipitates were found along the grain boundaries – intergranular precipitates – and presented an elliptical shape. The different processing conditions are suggested to result in the modification of the precipitates, not primarily of their shape, but of their size and number density. Indeed, the non-treated sample was characterized by a lower number of precipitates whose size was larger than that of the ultrasound-treated samples. Furthermore, it can be suggested that the precipitates grew and coalesced, forming massive bulk structures like the ones presented in Figure 3.15

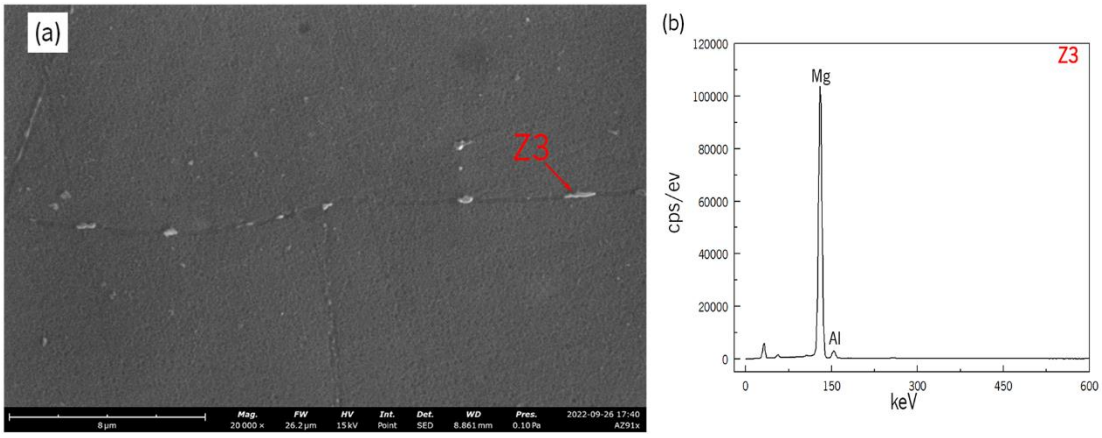

Figure 3.15 – SEM micrograph of β-$Mg_{17}Al_{12}$ bulk precipitates found at grain boundaries of non-treated material after aging at 175 °C for 24 h; (b) EDS analysis of the Z3 particle identified in (a).

Conversely, the ultrasound-treated sample showed a higher number of smaller β-$Mg_{17}Al_{12}$ precipitates distributed along the grain boundaries, which may be a result of the finer microstructure, *i.e.*, the smaller grain size of the material. The grain refinement of the alloy results in increased grain boundaries, providing more nucleation sites for β-$Mg_{17}Al_{12}$ discontinuous precipitates and, thereby, promoting faster aging kinetics [26,38].

B. HARDNESS CURVE OF NON- AND US-TREATED SAMPLES

Figure 3.16 shows the hardness progression under as-cast, solution-treated, and artificially aged conditions for both non- and ultrasound-treated samples.

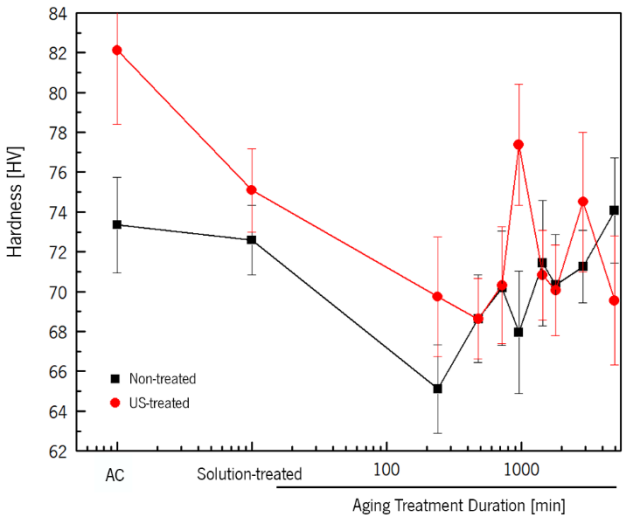

Figure 3.16 – Average Vickers hardness of the non- and US-treated samples during artificial aging.

The ultrasound-treated alloy exhibited higher hardness than the non-treated one, which may be attributed to its finer microstructure. It has been claimed that the refinement of the α-Mg and intermetallic phases substantially affects the material's mechanical properties, namely its hardness. Moreover, increasing grain boundaries led to an increase in the density of small precipitates, thus improving the mechanical properties.

Conversely, in the non-treated samples, the coarser morphology of the precipitates led to an increased interspacing between them, resulting in a reduced capacity to inhibit dislocation movement and, thus, lower hardness values. [50]. Similar findings were reported by Lai *et al.* [45], who studied the effect of aging conditions on the morphology of the β-$Mg_{17}Al_{12}$ precipitates and concluded that smaller and more numerous precipitates led to a higher peak hardness.

Due to the dissolution of the precipitates after solution treatment, which promotes material softening [51], the material's hardness dropped dramatically, regardless of the processing conditions. The hardness of the ultrasound-treated alloy remained higher than that of the non-treated one in the solutionized condition due to the grain boundary strengthening effect granted by the grain refinement. At this stage, no contribution of precipitation strengthening is considered in the ultrasound-treated sample since most of the precipitates were dissolved after solution treatment. On the other hand, a more gradual decline in the hardness in the non-treated material may be attributable to the presence of undissolved β-$Mg_{17}Al_{12}$ intermetallic, whose size may have been decreased throughout the procedure, favoring its ability to prevent dislocation movement.

The behavior of the hardness curves of the non- and ultrasound-treated alloys indicates that the processing conditions of the material may profoundly influence their aging response. Indeed, although the typical hardness increase was seen in both non- and ultrasound-treated samples, the former presented a longer incubation period, with the hardness value remaining almost constant until aging for 240 minutes. In contrast, the short incubation period of the ultrasound-treated alloy suggests accelerated aging kinetics of β-$Mg_{17}Al_{12}$ precipitates compared to the non-treated sample. Comparable results were reported by Wang *et al.* [26]. The authors investigated the influence of the manufacturing process - high-pressure die casting or rheo-diecasting - on the material's aging response and found that the latter showed faster dissolution during the solution heat treatment and accelerated aging kinetics.

After the incubation stage, the hardness of both non- and ultrasound-treated samples increased, although at a higher rate for the latter. The ultrasound-treated alloy reached its peak-aged condition at 960 minutes, following which its hardness value decreased sharply, whereas the non-treated alloy showed increasing hardness throughout the entire time range considered. The larger grain size is suggested to significantly reduce the nucleation rate, delaying the aging response of the material and resulting in the non-treated sample not achieving the peak-aging condition within the time interval considered [52]. Even so, and for comparison's sake, aging treatment for 1440 minutes was hereafter referred to as the peak-aging condition of the non-treated sample, corresponding to the highest hardness value observed within the heat treatment period considered. Indeed, after 4920 minutes of aging, the non-treated samples exhibited a value comparable to that of the as-cast condition (74 HV vs. 73 HV) and still showed a tendency toward increasing hardness, which may indicate that peak aging has not yet been reached and could be higher. However, the ultrasound-treated sample showed the highest hardness in the as-cast condition (82 HV), with peak-aged hardness 5.7 % lower (77 HV). According to Zhang *et al.* [53] and Dumpala *et al.* [27], the coarsening of grains during the solution treatment may be responsible for this behavior.

Nonetheless, the treatment of magnesium alloy by ultrasound has demonstrated the potential to refine the microstructure, which has proven to be effective in shortening the time needed for achieving the peak age condition. Also, the difference between the aged non- and ultrasound-treated samples after 240 minutes of aging is superior to that observed in the solution-treated condition, which further supports the hypothesis that ultrasonic processing plays a role in the precipitation behavior of the material and precipitation hardening took place by then. In this sense, the increased hardness value obtained for the ultrasound-treated sample may have resulted from the combined impact of accelerated precipitation and grain boundary strengthening, which is consistent with the findings of Kim *et al.* [54]. Even so, no

significant increase in hardness was seen after the aging treatment compared to the as-cast condition for either processing method. However, a 3–4 HV increase was observed compared to the solutionized condition. These results are in the same magnitude order as those reported by Suzuki *et al.* [55] and Barbenger *et al.* [56] for Mg-Al-Ca and Mg-Ca-Zn alloys, respectively, demonstrating the poor age-hardening response of these alloys.

Moreover, due to the formation of the Al_2Ca phase during the alloy solidification, there is a low fraction of β-$Mg_{17}Al_{12}$ phase in the as-cast state as well as reduced aluminum content on the α-Mg phase, limiting the solute availability after solution heat treatment. In this sense, given the direct relationship between the transformation rate during the aging treatment and the solute atoms amount available in the supersaturated matrix, lower peak hardness values are obtained by calcium-containing magnesium alloys compared with those without this element [57].

C. TENSILE PROPERTIES

The application of ultrasound treatment has been proven effective in enhancing the mechanical properties of magnesium alloys, namely AZ91D [14]. However, it is still unknown whether as-cast microstructure affects the tensile behavior of heat-treated materials.

The results of the tensile tests performed on the non- and ultrasound-treated AZ91D-1.5%Ca in the as-cast, solutionized, and peak-aged conditions are presented in Table 3.3.

Table 3.3 – Tensile properties of non- and US-treated material in the as-cast, solutionized and aged conditions.

Test	Condition	Yield Strength [MPa]	Tensile Strength [MPa]	Elongation at break [%]
Non-treated	As-cast	89 ± 5	110 ± 7	1.75 ± 0.34
	T4	137 ± 7	146 ± 8	2.04 ± 0.93
	T6 – Peak-age condition (1440 minutes)	100 ± 4	115 ± 4	1.73 ± 0.71
US-treated	As-cast	125 ± 8	164 ± 6	3.02 ± 0.25
	T4	158 ± 6	204 ± 8	4.31 ± 1.34
	T6 – Peak-age condition (960 minutes)	142 ± 6	169 ± 8	2.69 ± 0.89

The results demonstrated that the ultrasound-treated material significantly increased mechanical performance under all the tested conditions. In the as-cast state, the tensile strength of the ultrasound-treated material was about 50% higher than that presented by the non-treated one, stressing the grain refinement's role in the material's mechanical resistance. Nonetheless, the increased elongation at

fracture constitutes the most impressive result, with an enhancement of about 72.5% when ultrasound treatment is applied. In this sense, the microstructure characteristics may be considered a critical factor for the static mechanical properties of the alloy. The conjunction of smaller grain size and refined and more uniform distributed intermetallic phases grant remarkably improved mechanical properties, while the continuous network of brittle β-$Mg_{17}Al_{12}$ phase found in the non-treated sample is associated with poor mechanical properties [58]. According to Du *et al.* [59], such modifications decrease the stress concentration points, improving ductility by preventing early fracture.

Compared with the as-cast condition, the solutionized samples exhibited higher elongation and tensile strength regardless of ultrasound treatment application. However, the non-treated sample showed a more significant improvement in the tensile strength than that observed for the elongation, which was the opposite scenario of the ultrasound-treated samples. The increase in the tensile strength observed in the non-treated sample may be promoted by the dissolution of part of the coarse precipitates, which constitute preferential sites for fracture initiation and act as a continuous easy crack path. On the other hand, the dissolution of these precipitates occurred to a greater extent in the ultrasound-treated sample, leading to the matrix being dopped with aluminum atoms and easing the basal-lane deformation twinning in the magnesium alloys and, thereby enhancing the elongation [60,61].

Concerning the results of the aging treatment, non- and ultrasound-treated materials showed a decrease in both tensile strength and elongation. Such a loss of the materials' mechanical properties may be promoted by forming precipitates which, conversely to what is observed for aluminum alloys, may harm the mechanical resistance. In fact, under the considered aging conditions, discontinuous precipitates formed at the grain boundaries, showing small interface bonding strength and weakening the bonding force between grains [62]. In this sense, the microcracks are suggested to form preferentially in the β-$Mg_{17}Al_{12}$/α-Mg, interfaces, promoting early intergranular fracture due to their growth and propagation along the grain boundaries [63]. In agreement with these findings, the higher tensile strength and elongation values observed in the ultrasound-treated material after solution treatment compared to the peak age properties appears to confirm that the precipitation of the β-$Mg_{17}Al_{12}$ has an overall deleterious effect on the mechanical behavior of the material. Moreover, the elongation decline showed by the non-treated material after aging may be explained by the presence of coarse intermetallic particles that did not fully dissolve and are likely to crack at low strains. This detrimental effect did not significantly compromise the ductility in the solution-treated condition due to the softer matrix, which worked to delay the cracking [64], but played a critical role in decreasing the material's mechanical strength after aging treatment.

According to the results obtained, it can be concluded that AZ91D-1.5%Ca has a limited aging potential under the considered conditions. In fact, no significant improvement in the material's mechanical properties could be achieved through the adopted heat treatment scheme. Such a poor aging response may be explained mainly by two factors: (i) the addition of calcium promotes the formation of the Al_2Ca intermetallic phase during the material solidification and suppresses the formation of the β-$Mg_{17}Al_{12}$ phase. Given its high thermal stability, the Al_2Ca phase did not dissolve during the solution treatment, causing the aluminum content available to precipitate during subsequent aging treatment to be extremely low; on the other hand, (ii) the discontinuous precipitates formed along the grain boundaries consumed the available solute content, promoting the depletion of continuous precipitation, which could further improve the mechanical performance of the material [46].

Optimizing the solution treatment to dissolve the Al_2Ca phase and applying ultrasound treatment during the casting process may constitute a route to enhance the aging response of the AZ91D-1.5% alloy. In fact, applying ultrasonic vibration during the material solidification can promote an excess of vacancies, which act as nucleation sites for continuous precipitates. Such conditions, together with a higher available aluminum content granted by the dissolution of the Al_2Ca intermetallic, can enhance the material's response to the aging treatment by tailoring the morphology of resultant precipitates.

3.4. SUMMARY AND CONCLUSIONS

Applying ultrasound treatment during AZ91D-1.5%Ca alloy cooling has significantly changed its microstructure, promoting the refinement of β-$Mg_{17}Al_{12}$ and Al_2Ca intermetallic phases. In the as-cast state, the ultrasound-treated sample exhibited higher hardness which is suggested to be yielded by the refined microstructure. A faster dissolution rate was also observed, which is explained by a divorced and uniformly distributed small β-$Mg_{17}Al_{12}$ eutectic phase with a lower calcium content. It has been demonstrated that tailoring the as-cast microstructure through ultrasound treatment is a promising route for optimizing the solution treatment, enabling a reduction in the temperature and time needed. The results obtained showed a stabilization of the intermetallics' fraction for solution treatment performed at 415 °C for periods longer than 720 minutes, which may indicate that the dissolution of β-$Mg_{17}Al_{12}$ was nearly complete by then. When the heat treatment was performed at 385 °C, a decrease in the dissolution kinetics could be observed, and a complete dissolution could be observed only after 1440 minutes.

Conversely, the complete dissolution of the β-$Mg_{17}Al_{12}$ phase of the non-treated sample was not possible under any of the considered conditions. The intermetallic phase's coarse morphology may be a reason for these findings, as it can be associated with lower dissolution kinetics.

Concerning the aging treatment outcomes, accelerated precipitation kinetics is suggested to be promoted by the ultrasound treatment, as precipitation hardening could be observed for shorter heat treatment durations compared to non-treated samples. Indeed, the hardness curve of the non-treated material may suggest that peak aging was not achieved under the tested conditions, which indicates that aging for periods longer than 4920 minutes may be required. Ultrasound-treated, on the other hand, appeared to reach the peak-aging condition after 960 minutes, although displaying a hardness value lower than that of the as-cast condition.

The tensile testing results further confirmed the superior mechanical properties of the ultrasound-treated samples in the as-cast, solution- and age-treated states. Compared with the non-treated material, the ultimate tensile could be enhanced by at least 40.0% in all the considered conditions, while elongation showed an even more expressive increase, especially in the as-cast and solution-treated states. The tensile properties showed a decrease in the peak-age regardless of the previous processing condition, which could be attributed to the formation of precipitates at the grain boundaries that promote the formation of microcracks and intergranular early fracture.

CHAPTER REFERENCES

[1] R. Krishnan, S. Pandiaraj, S. Muthusamy, H. Panchal, M.S. Alsoufi, A.M.M. Ibrahim, A. Elsheikh, Biodegradable magnesium metal matrix composites for biomedical implants: synthesis, mechanical performance, and corrosion behavior – a review, Journal of Materials Research and Technology 20 (2022) 650–670. https://doi.org/10.1016/j.jmrt.2022.06.178.

[2] F. Abdiyan, R. Mahmudi, H.M. Ghasemi, Effect of Mn addition on the microstructure, mechanical properties and corrosion resistance of a biodegradable Mg–Gd–Zn alloy, Materials Chemistry and Physics 271 (2021) 124878. https://doi.org/10.1016/j.matchemphys.2021.124878.

[3] P. Erne, M. Schier, T.J. Resink, The road to bioabsorbable stents: reaching clinical reality?, Cardiovascular and interventional radiology 29 (2006) 11–16. https://doi.org/10.1007/s00270-004-0341-9.

[4] D. Liu, Y. Liu, Y. Zhao, Y. Huang, M. Chen, The hot deformation behavior and microstructure evolution of HA/Mg-3Zn-0.8Zr composites for biomedical application, Materials science & engineering. C, Materials for biological applications 77 (2017) 690–697. https://doi.org/10.1016/j.msec.2017.03.239.

[5] A. Kumar, P.M. Pandey, Statistical modeling of mechanical properties and bio-corrosion behavior of Mg3Zn1Ca15Nb fabricated using microwave sintering, Journal of Alloys and Compounds 854 (2021) 156211. https://doi.org/10.1016/j.jallcom.2020.156211.

[6] A. Vahid, P. Hodgson, Y. Li, Reinforced magnesium composites by metallic particles for biomedical applications, Materials Science and Engineering: A 685 (2017) 349–357. https://doi.org/10.1016/j.msea.2017.01.017.

[7] S.-i. Inoue, M. Yamasaki, Y. Kawamura, Formation of an incombustible oxide film on a molten Mg-Al-Ca alloy, Corrosion Science 122 (2017) 118–122. https://doi.org/10.1016/j.corsci.2017.01.026.

[8] D. Dvorsky, J. Kubasek, D. Vojtech, P. Minarik, Novel aircraft Mg-Y-Gd-Ca alloys with high ignition temperature and suppressed flammability, Materials Letters 264 (2020) 127313. https://doi.org/10.1016/j.matlet.2020.127313.

[9] X. Zeng, Q. Wang, Y. Lü, W. Ding, Y. Zhu, C. Zhai, C. Lu, X. Xu, Behavior of surface oxidation on molten Mg–9Al–0.5Zn–0.3Be alloy, Materials Science and Engineering: A 301 (2001) 154–161. https://doi.org/10.1016/S0921-5093(00)01798-6.

[10] X. Huang, Y. Chino, H. Ueda, M. Inoue, F. Kido, T. Matsumoto, Improvement of mechanical properties of extruded AZX912 magnesium alloy using high-temperature solution treatment, J. Mater. Res. 34 (2019) 3725–3734. https://doi.org/10.1557/jmr.2019.281.

[11] K. Kadali, D. Dubey, R. Sarvesha, H. Kancharla, J. Jain, K. Mondal, S.S. Singh, Dissolution Kinetics of Mg17Al12 Eutectic Phase and Its Effect on Corrosion Behavior of As-Cast AZ80 Magnesium Alloy, JOM 71 (2019) 2209–2218. https://doi.org/10.1007/s11837-019-03470-3.

[12] M. Mohammadi Zerankeshi, R. Alizadeh, E. Gerashi, M. Asadollahi, T.G. Langdon, Effects of heat treatment on the corrosion behavior and mechanical properties of biodegradable Mg alloys, Journal of Magnesium and Alloys 10 (2022) 1737–1785. https://doi.org/10.1016/j.jma.2022.04.010.

[13] A.K. Dahle, Y.C. Lee, M.D. Nave, P.L. Schaffer, D.H. StJohn, Development of the as-cast microstructure in magnesium–aluminium alloys, Journal of Light Metals 1 (2001) 61–72. https://doi.org/10.1016/S1471-5317(00)00007-9.

[14] H. Puga, V. Carneiro, J. Barbosa, V. Vieira, Effect of Ultrasonic Treatment in the Static and Dynamic Mechanical Behavior of AZ91D Mg Alloy, Metals 5 (2015) 2210–2221. https://doi.org/10.3390/met5042210.

[15] B. Tang, S.-S. Li, X.-S. Wang, D.-B. Zeng, R. Wu, An investigation on hot-crack mechanism of Ca addition into AZ91D alloy, J Mater Sci 40 (2005) 2931–2936. https://doi.org/10.1007/s10853-005-2440-7.

[16] Y. Kang, B. Du, Y. Li, B. Wang, L. Sheng, L. Shao, Y. Zheng, T. Xi, Optimizing mechanical property and cytocompatibility of the biodegradable Mg-Zn-Y-Nd alloy by hot extrusion and heat treatment, Journal of Materials Science & Technology 35 (2019) 6–18. https://doi.org/10.1016/j.jmst.2018.09.020.

[17] A.H. Feng, Z.Y. Ma, Enhanced mechanical properties of Mg–Al–Zn cast alloy via friction stir processing, Scripta Materialia 56 (2007) 397–400. https://doi.org/10.1016/j.scriptamat.2006.10.035.

[18] W. Weng, A. Biesiekierski, Y. Li, M. Dargusch, C. Wen, A review of the physiological impact of rare earth elements and their uses in biomedical Mg alloys, Acta biomaterialia 130 (2021) 80–97. https://doi.org/10.1016/j.actbio.2021.06.004.

[19] H. Pan, Y. Ren, H. Fu, H. Zhao, L. Wang, X. Meng, G. Qin, Recent developments in rare-earth free wrought magnesium alloys having high strength: A review, Journal of Alloys and Compounds 663 (2016) 321–331. https://doi.org/10.1016/j.jallcom.2015.12.057.

[20] J. Song, F. Pan, B. Jiang, A. Atrens, M.-X. Zhang, Y. Lu, A review on hot tearing of magnesium alloys, Journal of Magnesium and Alloys 4 (2016) 151–172. https://doi.org/10.1016/j.jma.2016.08.003.

[21] T. Zhu, Z.W. Chen, W. Gao, Dissolution of Eutectic β-Mg17Al12 Phase in Magnesium AZ91 Cast Alloy at Temperatures Close to Eutectic Temperature, J. of Materi Eng and Perform 19 (2010) 860–867. https://doi.org/10.1007/s11665-009-9539-y.

[22] Y. Wang, M. Xia, Z. Fan, X. Zhou, G.E. Thompson, The effect of Al8Mn5 intermetallic particles on grain size of as-cast Mg–Al–Zn AZ91D alloy, Intermetallics 18 (2010) 1683–1689. https://doi.org/10.1016/j.intermet.2010.05.004.

[23] S. Papaefthymiou, M. Bouzouni, E. Gavalas, Theoretical Study of Particle Dissolution during Homogenization in Cu–Fe–P Alloy, Metals 8 (2018) 455. https://doi.org/10.3390/met8060455.

[24] M. Liu, Q. Wang, Z. Liu, G. Yuan, G. Wu, Y. Zhu, W. Ding, Behavior of Mg–Al–Ca alloy during solution heat treatment at 415 ◦C, Journal of Materials Science Letters 21 (2002) 1281–1283. https://doi.org/10.1023/A:1016567421956.

[25] R.R. Kulkarni, N. Prabhu, P.D. Hodgson, B.P. Kashyap, Kinetics of γ-$Mg_{17}Al_{12}$ Phase Dissolution and its Effect on Room Temperature Tensile Properties in As-Cast AZ80 Magnesium Alloy, SSP 209 (2013) 207–211. https://doi.org/10.4028/www.scientific.net/SSP.209.207.

[26] Y. Wang, G. Liu, Z. Fan, Microstructural evolution of rheo-diecast AZ91D magnesium alloy during heat treatment, Acta Materialia 54 (2006) 689–699. https://doi.org/10.1016/j.actamat.2005.09.033.

[27] S.C. V, R. Dumpala, A.K. S, K. VV, R.S. B, Influence of heat treatment on the machinability and corrosion behavior of AZ91 Mg alloy, Journal of Magnesium and Alloys 6 (2018) 52–58. https://doi.org/10.1016/j.jma.2017.12.001.

[28] R.R. Kulkarni, N. Prabhu, P.D. Hodgson, B.P. Kashyap, Phase dissolution of γ-Mg17Al12 during homogenization of as-cast AZ80 Magnesium alloy and its effect on room temperature mechanical properties, in: S.N. Mathaudhu, W.H. Sillekens, N.R. Neelameggham, N. Hort (Eds.), Magnesium Technology 2012, Springer International Publishing; Imprint; Springer, Cham, 2016, pp. 543–548.

[29] S. Jo, L. Whitmore, S. Woo, A.U. Aramburu, D. Letzig, S. Yi, Excellent age hardenability with the controllable microstructure of AXW100 magnesium sheet alloy, Scientific reports 10 (2020) 22413. https://doi.org/10.1038/s41598-020-79390-z.

[30] H.-Y. Wang, Z.-P. Yu, L. Zhang, C.-G. Liu, M. Zha, C. Wang, Q.-C. Jiang, Achieving high strength and high ductility in magnesium alloy using hard-plate rolling (HPR) process, Scientific reports 5 (2015) 17100. https://doi.org/10.1038/srep17100.

[31] T. Han, G. Huang, H. Li, L. Wang, H. Zhang, F. Pan, Strength-ductility balance of AZ31 magnesium alloy via accumulated extrusion bonding combined with two-stage artificial cooling, Journal of Magnesium and Alloys 26 (2021) 2043. https://doi.org/10.1016/j.jma.2021.06.025.

[32] R. Shi, J. Miao, T. Avey, A.A. Luo, A new magnesium sheet alloy with high tensile properties and room-temperature formability, Scientific reports 10 (2020) 10044. https://doi.org/10.1038/s41598-020-67161-9.

[33] S.K. Panigrahi, R.S. Mishra, R.C. Brennan, K. Cho, Achieving extraordinary structural efficiency in a wrought magnesium rare earth alloy, Materials Research Letters 8 (2020) 151–157. https://doi.org/10.1080/21663831.2020.1719227.

[34] D. Bu, T. Li, X. Han, Z. Du, J. Yuan, K. Zhang, Y. Li, Y. Peng, Z. Pang, C. Zhao, Enhancing strength and ductility in back extruded WE71 magnesium alloy cylindrical parts by introduction of multi-direction forging process, Journal of Rare Earths 5 (2022) 239. https://doi.org/10.1016/j.jre.2022.03.001.

[35] K. Korgiopoulos, B. Langelier, M. Pekguleryuz, Mg17Al12 phase refinement and the improved mechanical performance of Mg–6Al alloy with trace erbium addition, Materials Science and Engineering: A 812 (2021) 141075. https://doi.org/10.1016/j.msea.2021.141075.

[36] K. Zhang, H. Li, X. Liang, Z. Chen, L. Wang, Discontinuous and continuous precipitation characteristics and mechanical properties of a AZ80A magnesium alloy at different aging temperatures, Materials Characterization 161 (2020) 110146. https://doi.org/10.1016/j.matchar.2020.110146.

[37] S. Celotto, TEM study of continuous precipitation in mg±9 wt%al±1 wt%zn alloy, Acta Materialia 48 (2000) 1775–1787. https://doi.org/10.1016/S1359-6454(00)00004-5.

[38] A.F. Abd El-Rehim, H.Y. Zahran, H.M. Al-Masoud, D.M. Habashy, Microhardness and microstructure characteristics of AZ91 magnesium alloy under different cooling rate conditions, Mater. Res. Express 6 (2019) 86572. https://doi.org/10.1088/2053-1591/ab1ad6.

[39] C.M. Cepeda-Jiménez, M.T. Pérez-Prado, Microplasticity-based rationalization of the room temperature yield asymmetry in conventional polycrystalline Mg alloys, Acta Materialia 108 (2016) 304–316. https://doi.org/10.1016/j.actamat.2016.02.023.

[40] A.F. Abd El-Rehim, H.Y. Zahran, H.M. Al-Masoud, D.M. Habashy, Microhardness and microstructure characteristics of AZ91 magnesium alloy under different cooling rate conditions, Mater. Res. Express 6 (2019) 86572. https://doi.org/10.1088/2053-1591/ab1ad6.

[41] J.U. Lee, S.-H. Kim, Y.J. Kim, S.H. Park, Effects of homogenization time on aging behavior and mechanical properties of AZ91 alloy, Materials Science and Engineering: A 714 (2018) 49–58. https://doi.org/10.1016/j.msea.2017.12.061.

[42] Y. Guo, G. Quan, M. Celikin, L. Ren, Y. Zhan, L. Fan, H. Pan, Effect of heat treatment on the microstructure and mechanical properties of AZ80M magnesium alloy fabricated by wire arc additive manufacturing, Journal of Magnesium and Alloys 10 (2022) 1930–1940. https://doi.org/10.1016/j.jma.2021.04.006.

[43] M. Fatmi, A. Djemli, A. Ouali, T. Chihi, M.A. Ghebouli, H. Belhouchet, Heat treatment and kinetics of precipitation of β-Mg17Al12 phase in AZ91 alloy, Results in Physics 10 (2018) 693–698. https://doi.org/10.1016/j.rinp.2018.07.009.

[44] J.-Y. Kim, J.-W. Byeon, Quantitative relation of discontinuous and continuous Mg17Al12 precipitates with corrosion rate of AZ91D magnesium alloy, Materials Characterization 174 (2021) 111015. https://doi.org/10.1016/j.matchar.2021.111015.

[45] E. Contreras-Piedras, R. Esquivel-Gonzalez, V.M. López-Hirata, M.L. Saucedo-Muñoz, A.M. Paniagua-Mercado, H.J. Dorantes-Rosales, Growth kinetics of cellular precipitation in a Mg–8.5Al–0.5Zn–0.2Mn (wt.%) alloy, Materials Science and Engineering: A 527 (2010) 7775–7778. https://doi.org/10.1016/j.msea.2010.08.052.

[46] W.-J. Lai, Y.-Y. Li, Y.-F. Hsu, S. Trong, W.-H. Wang, Aging behavior and precipitate morphologies in Mg–7.7Al–0.5Zn–0.3Mn (wt.%) alloy, Journal of Alloys and Compounds 476 (2009) 118–124. https://doi.org/10.1016/j.jallcom.2008.08.043.

[47] H. Puga, V.H. Carneiro, Light-Alloy Melt Ultrasonication: Shorter T6 with Higher Precipitation Strengthening, Met. Mater. Int. 27 (2021) 3195–3204. https://doi.org/10.1007/s12540-020-00798-3.

[48] Y. Hu, H. Liu, H. Fujii, H. Araki, K. Sugita, K. Liu, Ultrasonic-induced excess vacancies in friction stir processing and exploration of acoustoplastic effect, Scr. Mater. 185 (2020) 117–121. https://doi.org/10.1016/j.scriptamat.2020.05.017.

[49] J.-H. Jun, Damping behaviors of as-cast and solution-treated AZ91–Ca magnesium alloys, J. Alloys Compd. 610 (2014) 169–172. https://doi.org/10.1016/j.jallcom.2014.04.214.

[50] W. Xu, J. Yu, L. Jia, C. Gao, Z. Miao, G. Wu, G. Li, Z. Zhang, Grain refinement impact on the mechanical properties and wear behavior of Mg-9Gd-3Y-2Zn-0.5Zr alloy after decreasing temperature reciprocating upsetting-extrusion, Journal of Magnesium and Alloys 7 (2021) 672. https://doi.org/10.1016/j.jma.2021.03.021.

[51] G.M. Lee, J.U. Lee, S.H. Park, Effects of post-heat treatment on microstructure, tensile properties, and bending properties of extruded AZ80 alloy, Journal of Materials Research and Technology 12 (2021) 1039–1050. https://doi.org/10.1016/j.jmrt.2021.03.046.

[52] L.-j. Yang, Y.-h. Wei, L.-f. Hou, Microstructure evolution of thixomolding AZ91D magnesium alloy during heat treatment, J Mater Sci 45 (2010) 3626–3634. https://doi.org/10.1007/s10853-010-4408-5.

[53] Z. Zhang, L. Wang, R. Zhang, D. Yin, Z. Zhao, P. Bai, B. Liu, F. Wang, Effect of solution annealing on microstructures and corrosion behavior of wire and arc additive manufactured AZ91 magnesium alloy in sodium chloride solution, Journal of Materials Research and Technology 18 (2022) 416–427. https://doi.org/10.1016/j.jmrt.2022.02.092.

[54] S.-H. Kim, J.U. Lee, Y.J. Kim, J.H. Bae, B.S. You, S.H. Park, Accelerated precipitation behavior of cast Mg-Al-Zn alloy by grain refinement, Journal of Materials Science & Technology 34 (2018) 265–276. https://doi.org/10.1016/j.jmst.2017.11.019.

[55] A. Suzuki, N.D. Saddock, J.R. TerBush, B.R. Powell, J.W. Jones, T.M. Pollock, Precipitation Strengthening of a Mg-Al-Ca–Based AXJ530 Die-cast Alloy, Metall and Mat Trans A 39 (2008) 696–702. https://doi.org/10.1007/s11661-007-9455-4.

[56] M. Bamberger, G. Levi, J.B. Vander Sande, Precipitation hardening in Mg-Ca-Zn alloys, Metallurgical and Materials Transactions A 37A (2006) 481–487. https://doi.org/10.1007/s11661-006-0019-9.

[57] B. Amir Esgandari, H. Mehrjoo, B. Nami, S.M. Miresmaeili, The effect of Ca and RE elements on the precipitation kinetics of Mg17Al12 phase during artificial aging of magnesium alloy AZ91, Mater. Sci. Eng. A 528 (2011) 5018–5024. https://doi.org/10.1016/j.msea.2011.03.022.

[58] M. Khosro Aghayani, B. Niroumand, Effects of ultrasonic treatment on microstructure and tensile strength of AZ91 magnesium alloy, Journal of Alloys and Compounds 509 (2011) 114–122. https://doi.org/10.1016/j.jallcom.2010.08.139.

[59] X. Du, E. Zhang, Microstructure and mechanical behavior of semi-solid die-casting AZ91D magnesium alloy, Materials Letters 61 (2007) 2333–2337. https://doi.org/10.1016/j.matlet.2006.09.007.

[60] M. Muzyk, Z. Pakiela, K.J. Kurzydlowski, Generalized stacking fault energy in magnesium alloys: Density functional theory calculations, Scripta Materialia 66 (2012) 219–222. https://doi.org/10.1016/j.scriptamat.2011.10.038.

[61] H. Jia, X. Feng, Y. Yang, Influence of solution treatment on microstructure, mechanical and corrosion properties of Mg-4Zn alloy, Journal of Magnesium and Alloys 3 (2015) 247–252. https://doi.org/10.1016/j.jma.2015.08.006.

[62] Di Tie, Y. Jiang, R. Guan, M. Chen, J. Jiang, F. Gao, X. Lu, Z. Zhao, The Evolution of Microstructure, Mechanical Properties and Fracture Behavior with Increasing Lanthanum Content in AZ91 Alloy, Metals 10 (2020) 1256. https://doi.org/10.3390/met10091256.

[63] M. Teschke, A. Koch, F. Walther, Comparison of High-Temperature Compression and Compression-Comp ressionFatigue Behavior of Magnesium Alloys DieMag422 and AE42, Materials (Basel, Switzerland) 13 (2020). https://doi.org/10.3390/ma13030497.

[64] C.H. Cáceres, C.J. Davidson, J.R. Griffiths, C.L. Newton, Effects of solidification rate and aging on the microstructure and mechanical properties of AZ91 alloy, Materials Science and Engineering: A 325 (2002) 344–355. https://doi.org/10.1016/S0921-5093(01)01467-8.

CHAPTER 4 – ULTRASOUND MELT TREATMENT AS THE ROUTE FOR ENHANCING MECHANICAL AND CORROSION PROPERTIES OF EXTRUDED AZ91D-1%Ca Wires

In recent years, a significant amount of research has been conducted in the field of metal-based biomedical implants. This has been primarily driven by the development of novel biodegradable metals that offer advantages over traditional techniques based on permanent materials such as stainless steel and cobalt- and titanium-based alloys [1]. The new generation of biodegradable metal-based implants offers the opportunities to combine improved mechanical properties with biodegradable materials, whose controlled degradation allows their disintegration, alongside tissue healing, without hazardous responses [2].

Magnesium-based biomaterials are promising candidates for the production of biodegradable stents due to their remarkable advantages, which include stimulating the proliferation of specific cell types [3] and excellent biocompatibility [2,4,5]. Since magnesium is an essential element for the human body, any excess of this element can be safely excreted through the urine [6].

Magnesium and its alloys have been explored for many applications, such as bone replacements, fracture fixation devices, stents, and suture materials, and as a support for phosphate cement or biodegradable polymeric materials [7]. However, under physiological conditions, the rate of degradation of materials

based on magnesium is exceptionally high, resulting in the loss of the implant's mechanical qualities and integrity before the completion of the healing process [2,8,9].

Micro-alloying, microstructural tailoring, and surface modification by coating are a few methods developed to increase magnesium alloys' corrosion resistance [10]. The deposition of a coating layer on the surface of the material protects the substrate from corrosive fluids. Promising findings have been published on using bioactive coatings to lower the corrosion rate of magnesium alloys while simultaneously encouraging healing [11–13]. Nonetheless, most coating techniques have important drawbacks, including poor adhesion to the substrate and limited mechanical properties of the polymeric coatings [14], difficulty in maintaining a uniform coating thickness [15], formation of cracks and pores [16], as well as a high cost and the requirement of specialized knowledge [17]. On the other hand, the techniques of micro-alloying and microstructural tuning aim to increase the matrix's anodic stability, hence reducing galvanic corrosion and, consequently, the dissolution of the magnesium substrate [18]. Despite this, the solubility of most alloying elements in magnesium is low, which leads to the formation of intermetallic phases. Depending on their number, shape, and dispersion [10], these phases can either speed up the corrosion of magnesium alloys or improve their resistance. Therefore, microstructural control is an interesting way to adjust magnesium alloy's corrosion behavior without affecting its chemical composition. This may be accomplished by modifying the microstructure of the magnesium alloy. Thus, it is feasible to simultaneously increase the mechanical qualities and corrosion resistance [19–21].

Including the ultrasound treatment to produce the cast ingots to be used in the extrusion process may constitute a novel, time- and cost-efficient approach for tailoring the material's microstructure and, thereby, its corrosion behavior. Indeed, compared to the currently applied methods, ultrasound processing represents a competitive pathway. This is because its energy and time requirements are significantly lower than those demanded by techniques based on heat treatment, and it does not require the chemical modification of the base alloy.

In this study, an AZ91D-1%Ca melt was processed through ultrasound treatment, and the cast ingot was extruded. The corrosion behavior of the non- and ultrasound-treated alloys was evaluated under simulated physiological conditions, and the results were analyzed in the light of the as-cast microstructure of the extruded microstructure and the intermetallic morphology. Furthermore, the analysis of the deterioration of the mechanical properties of the extruded wires due to corrosion was conducted since the wires are intended for use in the production of stents and must thus withstand specific conditions.

4.1. EXPERIMENTAL PROCEDURE

4.1.1. FABRICATION OF THE AZ91D-1% WIRES

400 g of AZ91D-1%Ca were melted in a SiAlON crucible under an argon environment. To reduce humidity and moisture and avoid melt contamination, both material and tools were pre-heated at 450 °C. The melt was kept at 620 °C ± 5 °C for 20 min to allow the formation of the protective oxide layer, following which its temperature was raised to 680 °C ± 5 °C and held for homogenization. The pre-heated acoustic radiator was immersed 15 mm into the melt, and ultrasonic vibration (300 W, 20.1 ± 0.25 kHz) was applied isothermally for 120 seconds. After the ultrasound treatment, the melt was poured into a metallic mold pre-heated to 250 °C ± 5 °C to produce a 150 mm long and 50 mm diameter billet to suit the extruder container. The same material was also processed as described but without the ultrasound treatment to serve as a control. The apparatus used to perform the study described is presented in Chapter 3.

Before extrusion, both cast billets were heated at the extrusion temperature (350 °C) for 30 minutes. For the extrusion, a 2.5 MN automated press (Müller Engineering GmbH & Co. KG, Todtenweis/Sand, Germany) was employed at a speed of 0.1 mm/s. A die with four nozzles with a 1 mm diameter was placed equidistantly from the center position and enabled the simultaneous extrusion of four wires. The wires were coiled using a spool coiler with 80 mm coupled to the extrusion press. An offset per rotation of the spools of 1.1 mm was applied to adjust the winding pattern. The low initial tension at a maximum of 350 N was set during coiling to avoid early fracture of the wires.

As-cast and as-extruded samples were ground through progressively finer grades of silicon carbide abrasive papers, from P600 to P4000, and polished with a suspension of 1 μm diamond suspension for microstructural analysis. An oxide polishing solution was used as the last stage to minimize work-hardening caused by ordinary grinding. The grain of the as-cast and as-extruded samples was revealed by etching with 4% HNO_3 solution in ethanol and acetic-picral solution, respectively, and observed through OM (LEICA DM2500 M).

4.1.2. CORROSION EXPERIMENTS IN SIMULATED PHYSIOLOGICAL CONDITIONS

Choosing the suitable physiological fluid is of utmost importance when studying the degradation behavior of magnesium-based materials, as it may significantly change depending on the simulated body fluids [22]. Among the different solutions used to simulate the physiological environment, Earle's Balanced Salt Solution (EBSS) has been widely used for *in vitro* testing of biodegradable magnesium materials as it is suggested that the degradation rate is comparable to *in vivo* conditions [23–25]. This way, dynamic

immersion experiments were conducted using EBSS as the corrosive medium, whose composition is shown in Table 4.1.

Table 4.1 – EBSS chemical composition.

Chemicals	Concentration (g/L)
$CaCl_2$	0.20
$MgSO_4$	0.097
KCl	0.40
$NaHCO_3$	2.20
NaCl	6.80
NaH_2PO_4	0.14
Glucose	1.00

Figure 4.1 depicts the schematic design of the dynamic immersion testing wires device.

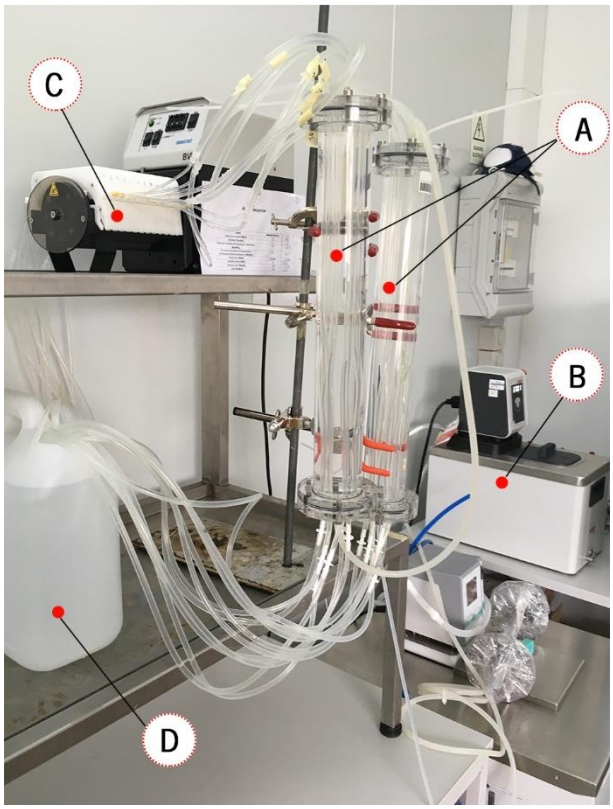

Figure 4.1 – Dynamic immersion test apparatus: (A) acrylic columns containing water at 37 °C, (B) water bath, (C) peristaltic pump, and (D) EBSS reservoir.

The wires were encased into antifatigue silicone tubes used as conduits and inserted into an acrylic column (A) filled with water at 37 °C provided by a circulating water bath (B). A peristaltic pump maintained a steady medium flow of 25 ml/min through the silicone tubes (C). Two reservoirs (D) were used to segregate the solution circulating within the channels containing non- and Ultrasound-treated

samples to study the manufacturing process's influence on the material's corrosion behavior. Three replicates of each manufacturing condition were tested for 4 and 6 hours and 2, 3, and 7 days, while the volume of EBSS was kept constant at 5 L.

4.1.3. CHARACTERIZATION OF THE NON- AND US-TREATED SAMPLES

Before and after corrosion products removal, SEM with EDS (SEM-EDS JSM-6010LV with INCAx-act, PentaFET Precision, Oxford Instruments) was used to examine the surface morphology and composition of the corroded wires. In addition, surface chemical analysis was done using XPS (Shimadzu Kratos Supra Axis) with a monochromatic Al Kα X-ray (1486.6 eV) operating with an X-ray source of 225 W. Samples were analyzed under vacuum with a pass energy of 160.0 eV in the survey scans and 20.0 eV for high-resolution scans. All spectrum peaks were measured relative to the peak binding energy of the C 1s peaks of carbon atoms of the hydrocarbon segments, which was 285.0 eV.

The corrosion products were removed by soaking the wires for 15 minutes in chromic acid (200 g/L) at room temperature. This work confirmed that chromate acid could eliminate corrosion products without destroying the metallic substrate, confirming previously published findings [28,29]. The samples were then sequentially cleaned with deionized water and ethanol. The weight loss Δm (mg) was determined using the difference between the original and final mass of the wires after cleaning using the following equation to obtain the corrosion rate CR (mm/year):

$$CR = 2.1 \times \frac{\Delta m}{A \times t} \tag{4.1}$$

where A is the surface area of the samples (cm^2) and t is the immersion time (days).

The non-deteriorated and degraded wires were subjected to tensile tests using universal testing equipment (H100KS "Hounsfield Universal Testing Instrument) fitted with a 500 N load cell at a constant cross-head speed of 1 mm/s. The ultimate tensile strength and elongation were calculated by averaging the results of ten separate tests.

4.2. RESULTS AND DISCUSSION

4.2.1. CHARACTERIZATION OF THE MATERIAL'S MICROSTRUCTURE PRIOR TO THE IMMERSION TEST

The microstructures obtained through OM and SEM of the non- and ultrasound-treated alloys in the as-cast and as-extruded conditions are shown in Figure 4.2.

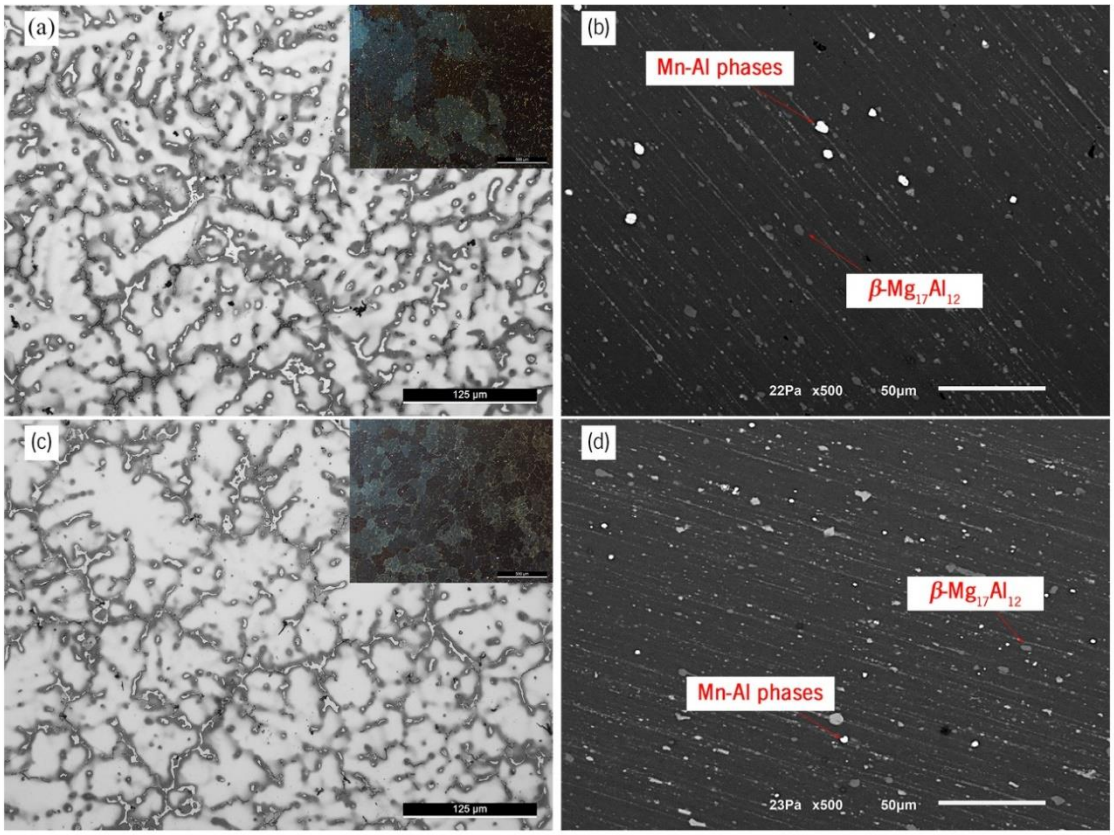

Figure 4.2 – Microstructure of the (a,b) non- and (c,d) ultrasound-treated samples in the as-cast and as-extruded condition obtained through OM and SEM techniques.

The microstructures of both non- and ultrasound-treated samples are composed of α-Mg, eutectic β-$Mg_{17}Al_{12}$, and a minor fraction of Al-Mn-rich phases. As Nam *et al.* [26] reported, calcium added to the alloy was dissolved in the β-$Mg_{17}Al_{12}$ owing to its low solubility in the matrix and insufficient content to establish a new phase [26]. The application of ultrasound treatment enhanced the microstructure, forming α-Mg grains that were smaller and more spherical, with finer intermetallic dispersed more uniformly along their boundaries. The eutectic β-$Mg_{17}Al_{12}$ massive lumps were replaced by short and thin networks, a phenomenon previously observed by Emadi *et al.* [27]. According to several studies, ultrasound treatment could refine the grain and secondary phases through a combination of mechanisms, namely (i) cavitation-enhanced nucleation [28,29], (ii) improvement of the wettability of particles [27,30,31], and thus increase the active nucleus, and (iii) ultrasonic streaming that homogenizes the solute distribution [32], promoting the uniform precipitation of the fine intermetallics that would otherwise segregate and form coarse particles [33].

As a result of the material suffering significant plastic deformation at high temperatures during extrusion, the microstructures of non- and ultrasound-treated samples became more similar in the as-extruded state. A typical banded structure was observed with greatly refined α-Mg grains and broken into smaller particles

of β-$Mg_{17}Al_{12}$ phase stretched into strips and forced to scatter along the extrusion direction forming the characteristic clustering of precipitates [34]. Despite the microstructural differences being more pronounced in the as-cast state, the ultrasound-treated sample exhibited significantly smaller intermetallics than the non-treated material following extrusion. In fact, both β-$Mg_{17}Al_{12}$ and Al-Mn rich phases appeared to be finer, rounder, and more uniformly distributed in the ultrasound-treated material than in the non-treated one.

4.2.2. CORROSION TESTS

Under neutral and alkaline circumstances, the following equation describes the corrosion processes contributing to magnesium and its alloys' degradation.

$$Mg + 2H_2O \rightarrow Mg(OH)_2 + H_2 \tag{4.2}$$

This reaction, however, is a generalization of the corrosion process and does not account for the unique characteristics of each material or stage of corrosion. An example is the deterioration of corrosion resistance of the naturally formed oxide or passive film after a specific exposure time. Once the critical exposure time has been exceeded and galvanic corrosion begins, an alloy's corrosion resistance may change. Thus, the corrosion characteristics of magnesium alloys depend on the kind and integrity of the oxide layer generated on their surfaces and the matrix composition of cathodic components [35]. Also, hydrogen is not always produced as a result of magnesium corrosion; hence weight loss tests are preferred to the hydrogen evolution experiments for accurately determining the corrosion rate of the material [36]. Figure 4.3 illustrates the corrosion rate of non- and ultrasound-treated wires in EBSS based on the weight loss of the wires.

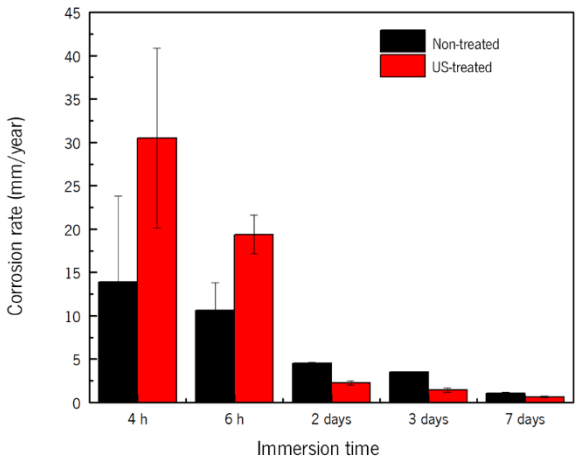

Figure 4.3 – Corrosion rate of the non- and US-treated samples.

For short immersion intervals (up to 6 hours), the corrosion rate of the ultrasound-treated samples was significantly greater than that of the non-treated ones. However, this trend reversed over longer immersion durations (up to 7 days), and the corrosion rate of the ultrasound-treated samples steadily reduced, showing enhanced corrosion resistance. In fact, after immersion for 7 days, the corrosion rate of the non-treated material was nearly double of the ultrasound-treated one (1.15 vs. 0.6 mm/year). Nonetheless, the ultrasound treatment's corrosion resistance was inefficient in meeting the requirement for coronary stent manufacturing since a maximum corrosion rate of 0.5 mm/year is mandatory [37]. As the homogeneity and morphology of secondary phases have been identified as determining factors in the nature and evolution of the corrosion phenomenon, the microstructure characteristics of the non- and ultrasound-treated samples may explain the differences observed in the material's corrosion behavior [38,39]. Particularly, the size and distribution of the intermetallic phases, such as the β-$Mg_{17}Al_{12}$ phase, may determine whether its presence improves or deteriorates the corrosion resistance of the alloy, shedding light on the ultrasound treatment potential to modify its corrosion behavior due to its ability to alter the microstructure of the materials [4]. Applying the ultrasound treatment to the AZ91D-1%Ca melt before extrusion promoted the refinement of the as-extruded samples, resulting in a more homogeneous composition and a refined microstructure characterized by smaller and spherical intermetallics particles evenly distributed throughout the matrix. In this sense, substantial variations in the reaction of the materials following exposure to a corrosive media were detected, demonstrating a connection between the microstructural characteristics and the corrosion behavior.

Figure 4.4 depicts the wires' surface morphology (SEM) after 6 hours of immersion in EBSS.

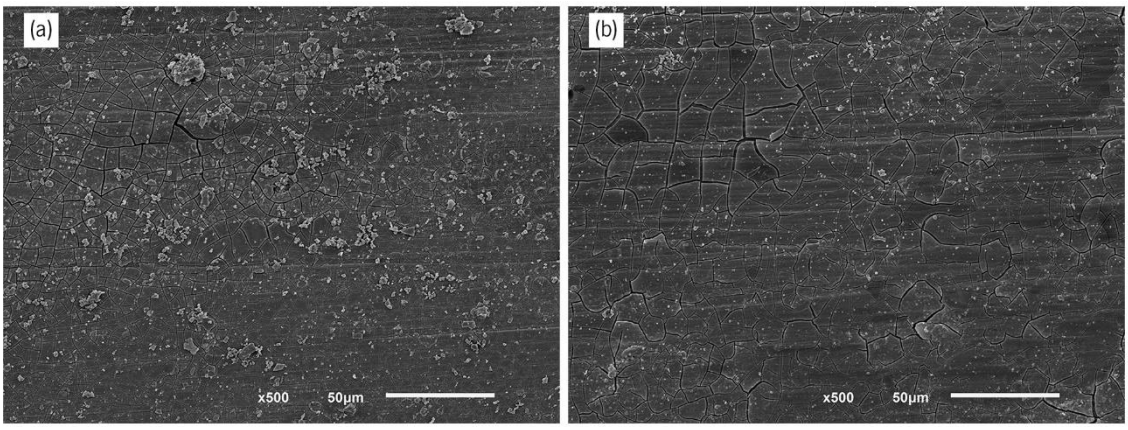

Figure 4.4 – Surface morphology of the (a) non- and (b) ultrasound-treated wires after immersion for 6 hours in EBSS.

Localized clusters of white particles could be visible in the non-treated sample. In contrast, identical white particles were more evenly distributed on the surface of the ultrasound-treated material, where deeper

fissures than those detected in the non-treated sample suggested the existence of a thicker corrosion layer. These findings are consistent with the increased corrosion rate reported at this immersion stage since a quicker deterioration rate should result in more corrosion products deposited on the exposed surface.

By extending the immersion period beyond 6 hours, a change in the corrosion behavior was observed, with the ultrasound-treated sample exhibiting the lowest corrosion rates, which translated into a difference in the corrosion products and marks. Figure 4.5 and Figure 4.6 show the corrosion morphology of the non- and ultrasound-treated wires after immersion for 72 hours and 7 days prior to and after corrosion products removal. In Figure 4.5 (a), white particles agglomerates are stacked on cracked blocks of corrosion products, which can be observed on the surface of the non-treated wire. Additionally, mud cracking of the corrosion layer was observed, indicating the produced film's low integrity, which might limit its ability to prevent additional corrosion.

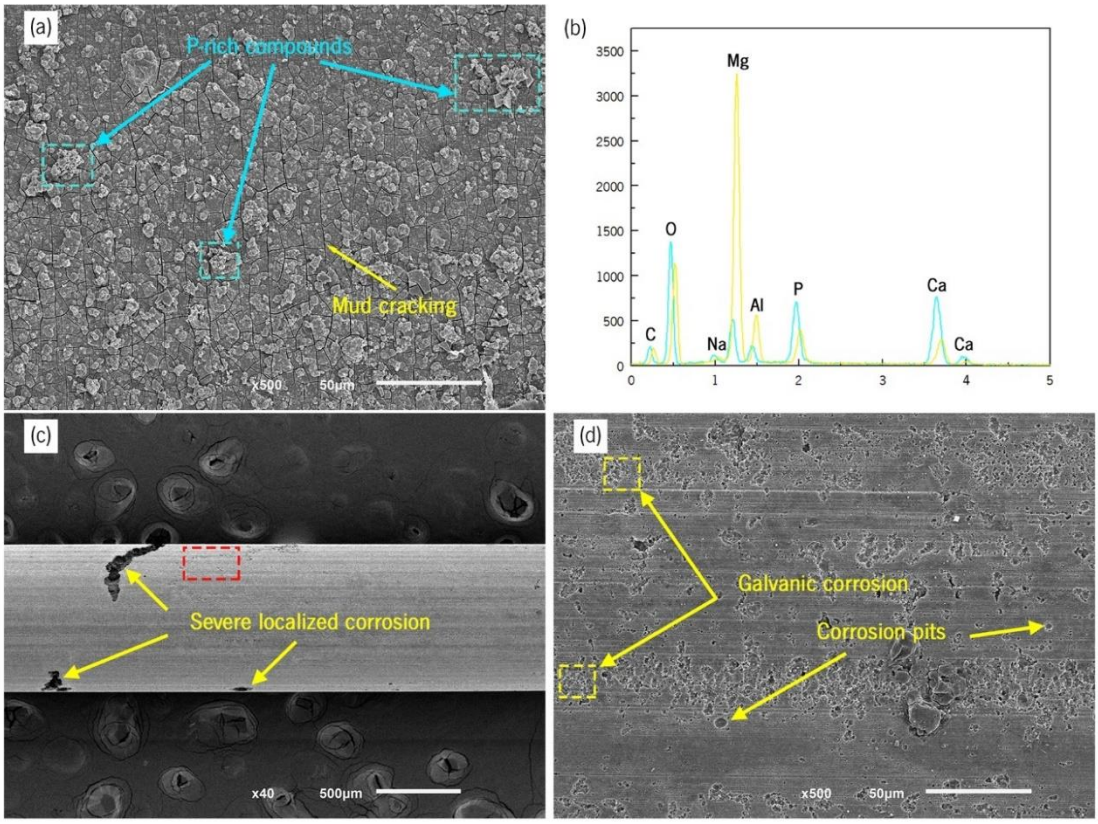

Figure 4.5 – Surface morphology of the non-treated samples (a,b) before and (c,d) after removing corrosion products – 72 hours immersion.

The formation of fissures on the film's surface compromises its integrity and adhesion and exposes the magnesium substrate, permitting contact with the corrosive solution and accelerating its attack. After removing the corrosion products, significant localized corrosion was found (Figure 4.5 (c)) along the

extrusion direction, and micro-galvanic corrosion characteristic morphology with a few corrosion pits was revealed (Figure 4.5 (d)) [40]. Corrosion marks were dispersed in bands along the extrusion streamlines, corresponding to the intermetallics distribution seen in Figure 4.2 (b). In the US-treated sample (Figure 4.6), small agglomerates of white compounds with a cobweb-like structure similar to those described by Song *et al.* [41] were observed, with a reduced number of powder-like corrosion products (Figure 4.6 (a)) also being observed on the surface. Only a small area exhibited mud cracking, and the corrosion layer seemed more compact and consistent. The wire's surface showed a mix of galvanic and smooth pitting corrosion morphologies in the absence of corrosion products (Figure 4.6 (c) and (d)). In contrast to the non-treated samples, the corrosion marks were equally distributed over the surface, and there was no evidence of significant localized corrosion.

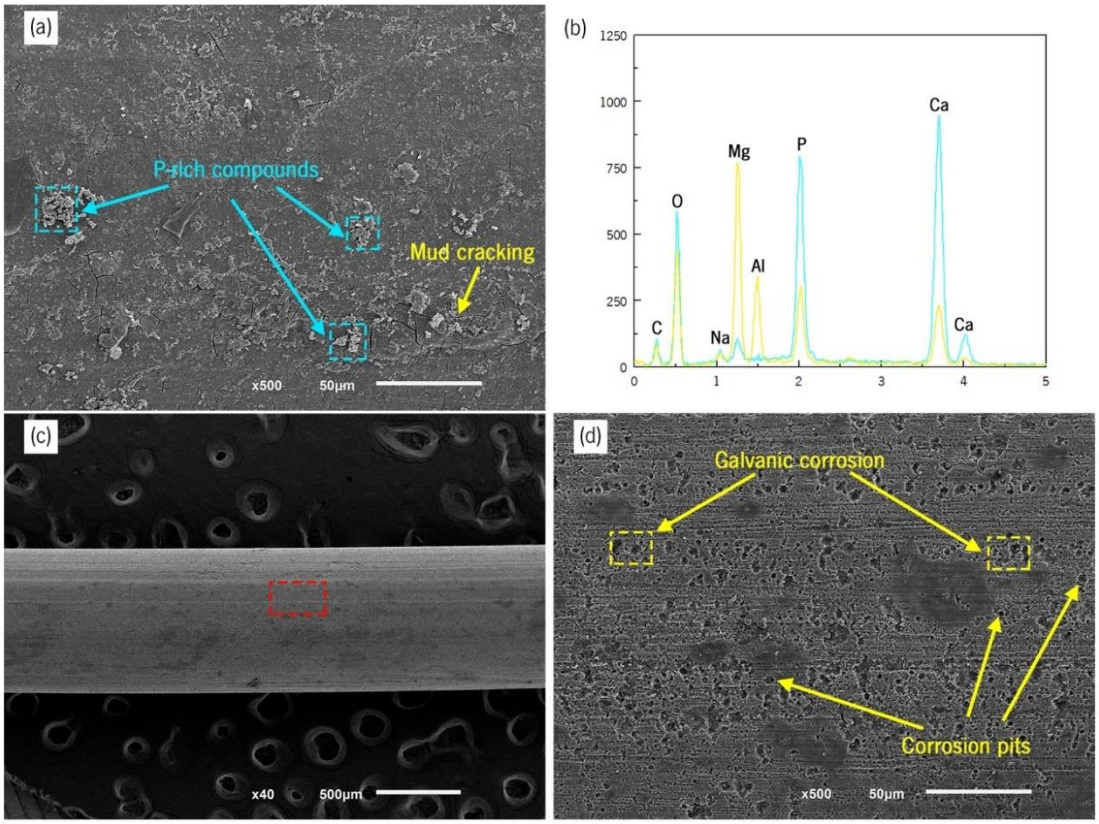

Figure 4.6 – Surface morphology of the ultrasound-treated samples (a,b) before and (c,d) after removing corrosion products – 72 hours immersion.

The results of the EDS analysis (Figure 4.5 (b) and Figure 4.6 (b)) of the corrosion products formed on the wire's surface identified the presence of magnesium, oxygen, calcium, and phosphorus, which have been assigned to the precipitation of $Mg_xCa_y(PO_4)_z$ – white compounds – and $Mg(OH)_2$ – mud layer. Additionally, the presence of carbon and sodium also suggested the precipitation of other magnesium phosphates in the form of $Na_4Mg(PO_4)_2$ and $Mg(PO_4)OH$), and magnesium carbonate ($MgCO_3$) [37,42].

As illustrated in Figure 4.7 and Figure 4.8 display the surface morphology of the non- and ultrasound-treated samples after immersion for 7 days. As it can be observed, the variations in the corrosion morphology of the non- and ultrasound-treated wires became more pronounced. The corrosion products of the non-treated sample had a more regular shape (Figure 4.7 (a)), with a few clusters stacked on the substrate and a P- and Ca-rich white material formed over them (Figure 4.7 (b)). No apparent fractures in the corrosion layer indicated an increase in its integrity and a correspondingly decreased corrosion rate (Figure 4.3). However, the rupture of the corrosion layer in the central region of the cobweb-shaped agglomerates could be found, being flaked away and exposing the material substrate. As shown in Figure 4.7 (c), the wire's surface severely deteriorated after the corrosion products were removed, and extensive, severe localized corrosion was noticeable. Also, as previously seen after 72 hours of immersion, micro-galvanic corrosion was evident (Figure 4.7 (d)), as were irregular holes caused by severe localized corrosion. The ultrasound-treated wire (Figure 4.8) exhibited large regions covered with snowflake-shaped corrosion products with higher thickness than those observed in the non-treated one protruding from the wire's surface (Figure 4.8 (a) and (b)).

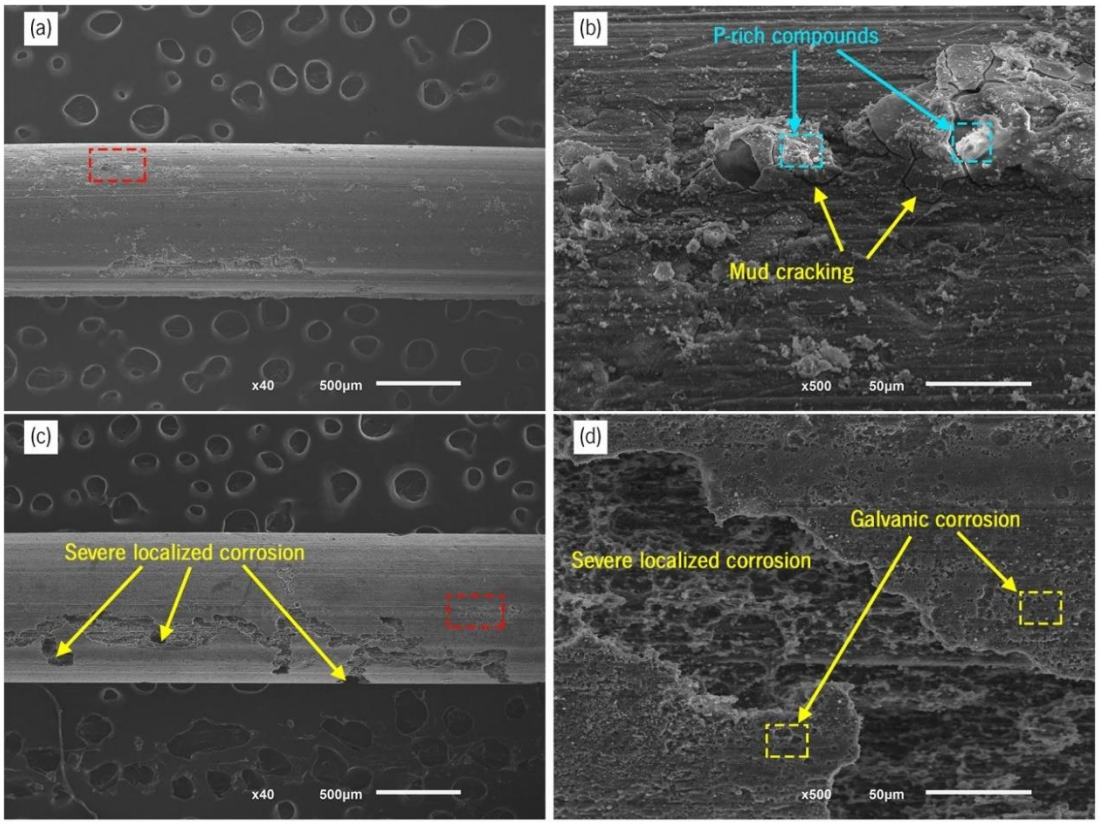

Figure 4.7 – Surface morphology of the non-treated samples (a,b) before and (c,d) after removal of corrosion products – 7 days immersion.

Similarly, a P- and Ca-rich substance seemed to cover a significant proportion of the agglomerates of corrosion products. However, the surface morphology of the ultrasound-treated wires exposed for 72 hours and 7 days was characterized by a uniform layer deposited over the surface with few visible cracks.

In contrast, the surface morphology of non-treated samples was characterized by a cracked film containing several localized aggregates of corrosion products. The ultrasound-treated wire surface displayed significant localized corrosion after the removal of the corrosion products, comparable to that found in the non-treated sample (Figure 4.8 (c) and (d)), although in a smaller region. Circular and deeper corrosion pits were observed with a spherical and rounded form.

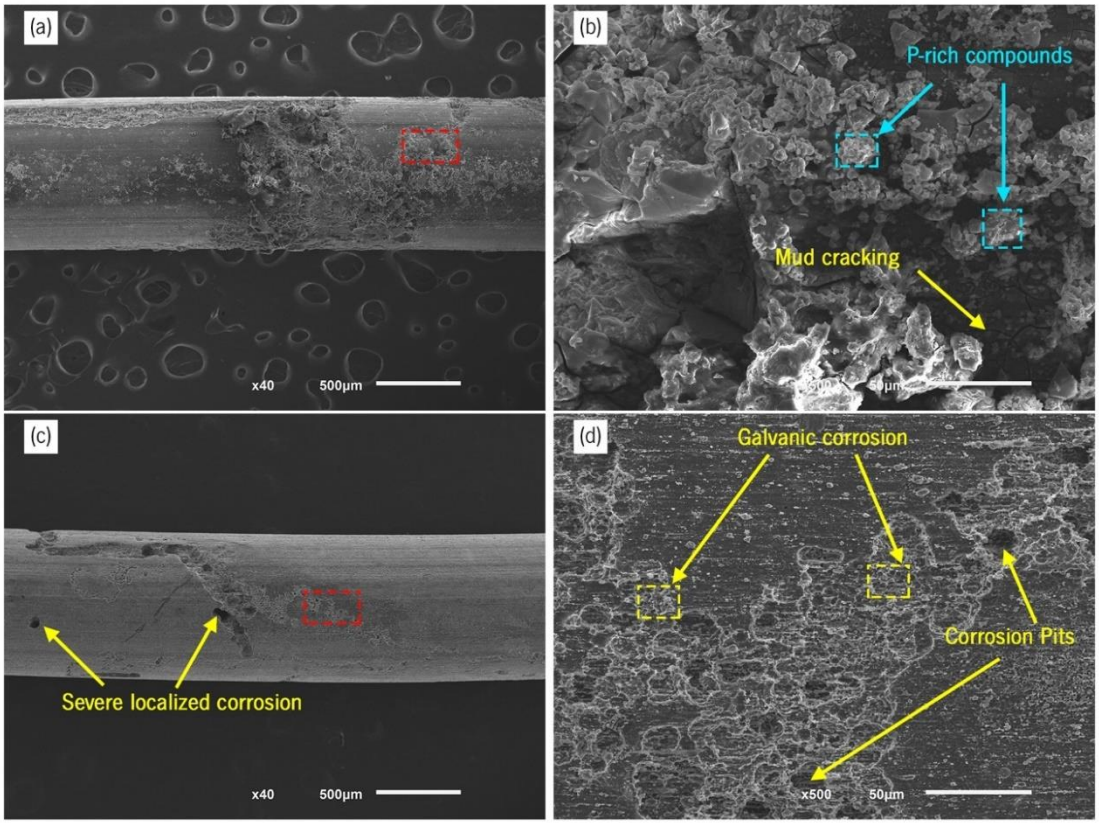

Figure 4.8 – Surface morphology of the Ultrasound-treated samples (a,b) before and (c,d) after removal of corrosion products – 7 days immersion.

The observed variations in the corrosion mark patterns between the non- and ultrasound-treated samples may be attributable to the shape and dispersion of intermetallic phases in the extruded condition. Indeed, Al-Mn and β-$Mg_{17}Al_{12}$ phases have noble potentials relative to the α-Mg matrix and may thus act as cathodes and induce micro-galvanic corrosion, diminishing the alloy's overall performance. Although some authors have hypothesized that a continuous network of secondary phases may act as a barrier to the advancement of corrosion, the intermetallics were disrupted and transformed during the extrusion process, making it impossible to form a web around the α-Mg grains. In both non- and ultrasound-treated

samples, the intermetallic particles behaved as the cathodic phase, encouraging the breakdown of the magnesium matrix. Thus, the deep and large concavities similar to crevice corrosion noticed in the non-treated samples were consistent with the coarser and non-uniform distribution of the intermetallic phases throughout the matrix.

In contrast, the microstructure of the ultrasound-treated samples, which was characterized by a finer and more uniformly disseminated secondary phase, resulted in smaller and more evenly distributed corrosion signs.

To detect and identify the corrosion products deposited on the surface of the wires, XPS analysis was conducted on non- and ultrasound-treated samples. XPS-wide survey scans confirmed the presence of magnesium, aluminum, carbon, oxygen, calcium, and phosphorus in both samples; therefore, high-resolution narrow survey scans were performed for these elements. Magnesium and aluminum peaks came from the substrate of the wires, whereas calcium and phosphorus formed from the corrosion products deposited on their surface. The deconvolution of the XPS spectra for the Mg 2s, C 1s, O 1s, Ca 2p, and P 2p peaks are shown in Figure 4.9. The Mg 2s spectra (Figure 4.9 (a) and (b)) may be fitted to three components: one peak at 87.0 eV, which corresponds to the presence of MgO, and two peaks at 89.0 eV and 89.5 eV, which correspond to the $Mg(OH)_2$ and $MgCO_3$ compounds, respectively [43]. The peaks at 285.0 eV and 289 eV in C 1s spectra (Figure 4.9 (c) and (d)) and (d indicate the existence of C-C/C-H groups, Mg-CO_3, and Ca-CO_3 compounds, while the peaks in the O 1s spectra (Figure 4.9 (e) and (f)) correspond to the binding energy from the PO_4^{3-}, OH^- and CO_3^{2-} groups as well as to oxygen present in the MgO compound [44,45]. Each recognized peak in the Ca 2p spectra (Figure 4.9 (g) and (h exhibits the doublet band typical of calcium-oxygen compounds [44]. Due to spin-orbit splitting, the spectrum breaks into two peaks of Ca 2p3/2 and Ca 2p1/2, further demonstrating the presence of $Ca_{10}(PO_4)_6(OH)_2$ [46]. The peak at 347.8 eV is related to the Ca-O binding energy and hence indicates the existence of the CaO compound, while the peak at around 347.0 eV may suggest that Ca-CO_3 is a component of the corrosion products [44]. In addition, in the P 2p spectra (Figure 4.9 (i) and (j)), two peaks positioned between 133.0 eV to 135.0 eV can be seen, suggesting the presence of phosphates such as Mg-PO_4 and Ca-PO_4 compounds, which is consistent with the high-resolution spectra of Mg 2p and Ca 2p [47,48].

According to the findings of the XPS investigation, the corrosion products formed as a consequence of the magnesium substrate's corrosion were the same for both non- and ultrasound-treated samples. However, ultrasound-treated samples exhibited significantly higher quantities of all the identified compounds.

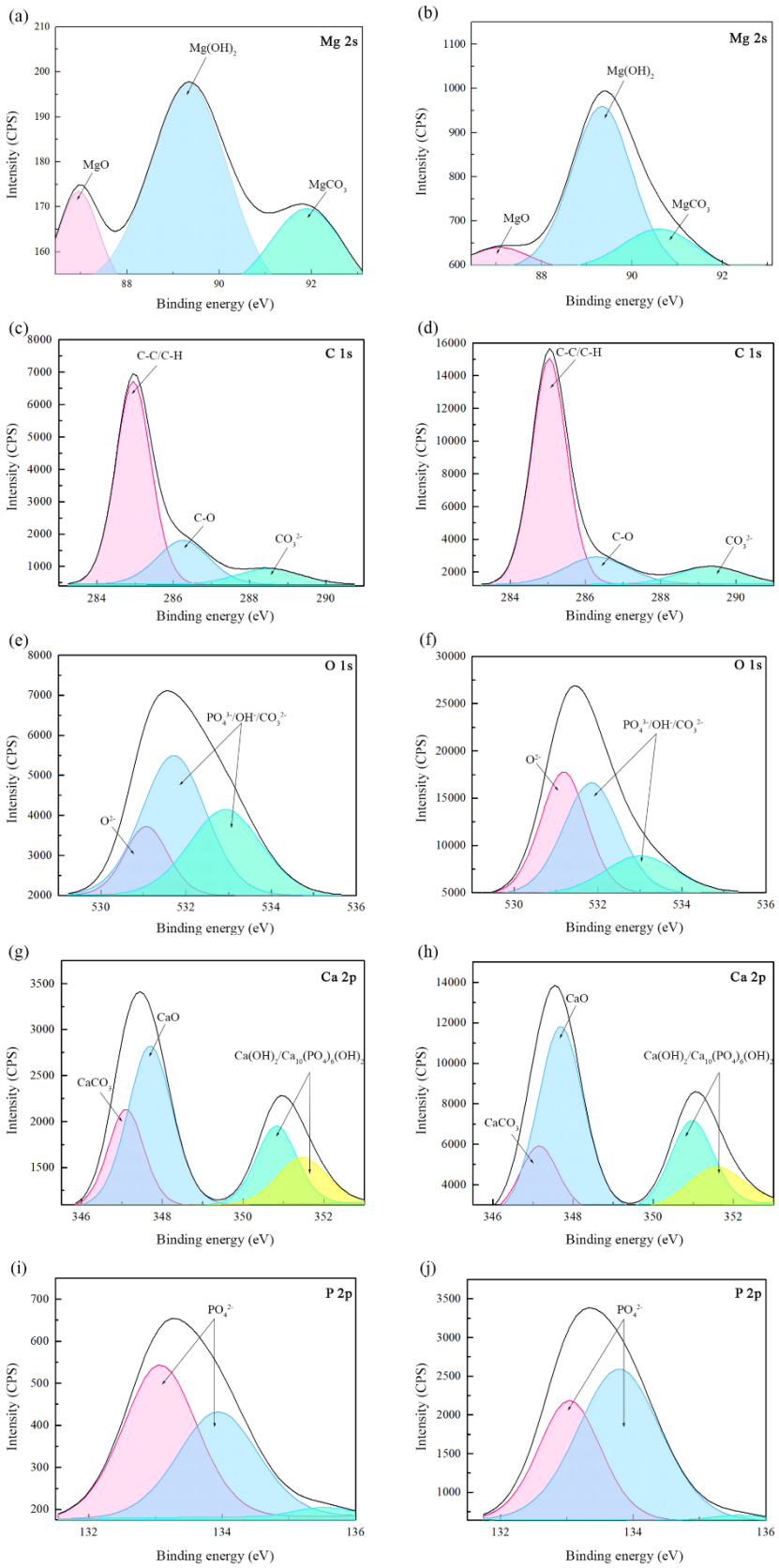

Figure 4.9 – High-resolution XPS spectra for non- (a,c,e,g,i) and ultrasound-treated (b,d,f,h,j) AZ91-1% Ca after immersion in EBSS.

In this sense, the results obtained suggest that the degradation behavior of the ultrasound-treated material has two distinct stages: (i) during the first immersion hours, the ultrasound-treated wire was corroded to a greater extent due to the distribution of the small intermetallics that acted as cathodes, promoting a higher corrosion rate and, hence, the formation of larger quantities of corrosion products, and (ii) a corrosion layer was uniformly deposited on the wires' surface, protecting the substrate and resulting in the degradation being slowed and the corrosion rates decreasing significantly. Furthermore, this morphology facilitated the formation of corrosion pits whose growth led to the detachment of intermetallic particles, impeding the advancement of corrosion to the alloy's core and generating a smoother and more uniform layer. Although the corrosion process was comparable in the non-treated samples, the intermetallics were coarser and formed agglomerates, resulting in severe micro-galvanic corrosion in isolated locations. In addition, as previously reported by Yin *et al.* [38], the localized corrosion quickly spread throughout the material along the coarse intermetallic phase. Choi *et al.* [49] have previously documented the overlap between the morphology of the intermetallics and the corrosion marks in AZ91 following exposure to a corrosive solution, thus supporting the hypothesis herein presented.

In addition, the composition of the corrosion products significantly impacts corrosion resistance and degrading behavior. In fact, if the compounds formed are poorly soluble, the degradation of the substance will be slowed since a portion of the substrate will be coated. The surface conditions influence the corrosion products that can precipitate and, hence, the corrosion protection granted by them. Figure 4.10 shows a model for the corrosion reactions that may occur between the magnesium substrate and the EBSS, as well as for the corrosion products formation.

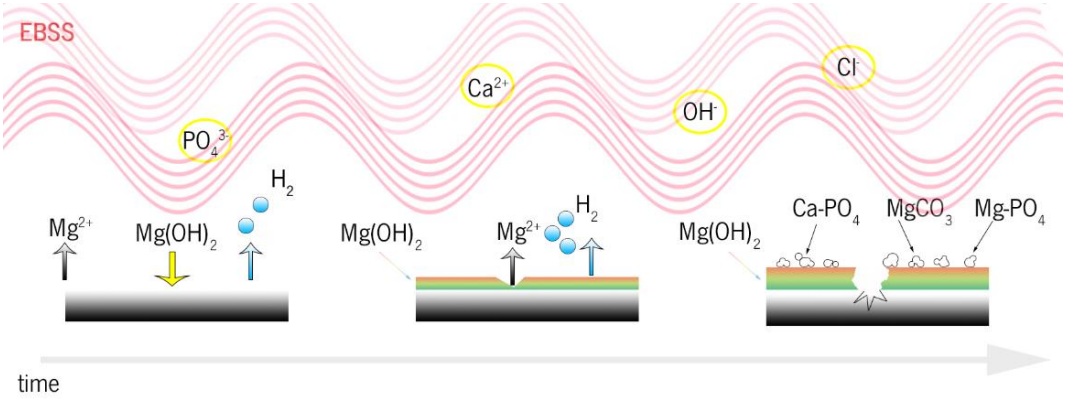

Figure 4.10 – Proposed mechanism for the AZ91 reactions and corrosion products formation in EBSS.

The magnesium substrate is corroded when exposed to aqueous media such as physiological fluids. According to Song *et al.* [46], $Mg(OH)_2$ forms during the first stages of immersion, mainly in the grain boundaries, as the result of the reduction of the water and the oxidation of the magnesium, as follows:

$$Mg \rightarrow Mg^{2+} + 2e^{-} \quad (4.3)$$

$$2H_2O + 2e^{-} \rightarrow H_2 + 2OH^{-} \quad (4.4)$$

$$Mg^{2+} + 2OH^{-} \rightarrow Mg(OH)_2 \quad (4.5)$$

The dissolution and strength of the $Mg(OH)_2$ layer depend deeply on the other chemical species present in the corrosive medium and the immersion time [50]. When exposed to EBSS and as the immersion proceeds, the $Mg(OH)_2$ is partially dissolved through the reaction with Cl^- anions present in the electrolyte:

$$Mg(OH)_2 + 2Cl \rightarrow MgCl_2 + 2OH^{-} \quad (4.6)$$

Such a reaction increases the local pH, favoring the decomposition of the HPO_4^{2-} species into PO_4^{2-} and H_2O as described by equation 4.7:

$$HPO_4^{2-} + OH^{-} \rightarrow PO_4^{3-} + H_2O \quad (4.7)$$

The phosphates released bond preferentially with Ca^{2+} and Mg^{2+} cations, forming white precipitates identified as $Mg_xCa_y(PO_4)_z$ on the surface of the wires, which are found adhered to $Mg(OH)_2$ layer. These corrosion products are not water soluble, providing additional protection to the magnesium substrate.

Additionally, according to Eq. 4.10, the $MgCO_3$ compound can be formed through a reaction between the atmospheric CO_2 or $NaHCO_3$ present in the electrolyte and the Mg^{2+} cations released from the substrate [51,52]:

$$H_2O + CO_2 \rightarrow HCO_3^{-} + H^{+} \quad (4.8)$$

$$NaHCO_3 \rightarrow Na^{+} + HCO_3^{-} \quad (4.9)$$

$$Mg^{2} + HCO_3^{-} \rightarrow MgCO_3 + H^{+} \quad (4.10)$$

The faster corrosion rate exhibited by the ultrasound-treated samples during the first stages of the immersion tests led to forming a thicker $Mg(OH)_2$ film with plenty of phosphorus- and calcium-rich white particles. Hence, higher corrosion resistance was achieved, resulting in a sharp decrease in the corrosion rate after 6 hours.

4.2.3. MECHANICAL CHARACTERIZATION

Figure 4.11 shows the evolution of the ultimate tensile strength (Figure 4.11 (a)) and elongation (Figure 4.11 (b)) of the non- and ultrasound-treated wires with the duration of the degradation tests, i.e., immersion time. Before the immersion test, the non-treated material had the maximum tensile strength (354 MPa vs. 347 MPa); however, the ultrasound-treated significantly exceeded it in terms of elongation

at break (16.7% vs. 20.7%). After the immersion in EBSS, independent of the material processing procedure, both mechanical characteristics deteriorated gradually, which is related to the loss of integrity due to continual mass loss at the interface [53]. After 7 days (168 h) of immersion, the non-treated material decreased tensile strength by around 27.7% and elongation at break by approximately 85.9%. Similarly, ultrasound-treated wires' tensile strength and elongation decreased by 14.3% and 83.2%, respectively. The ultrasound-treated sample exhibited superior mechanical characteristics, with a 15.0% higher final tensile strength than the non-treated sample. Nevertheless, the elongation values were similar after 7 days (168 h) of immersion. In all processing circumstances, the tensile characteristics of the wires declined quickly during the first phases of the degradation tests up to 48 hours but remained almost constant after that. This behavior corresponded with the gradually decreasing corrosion rate, indicating a stabilizing of the materials' deterioration.

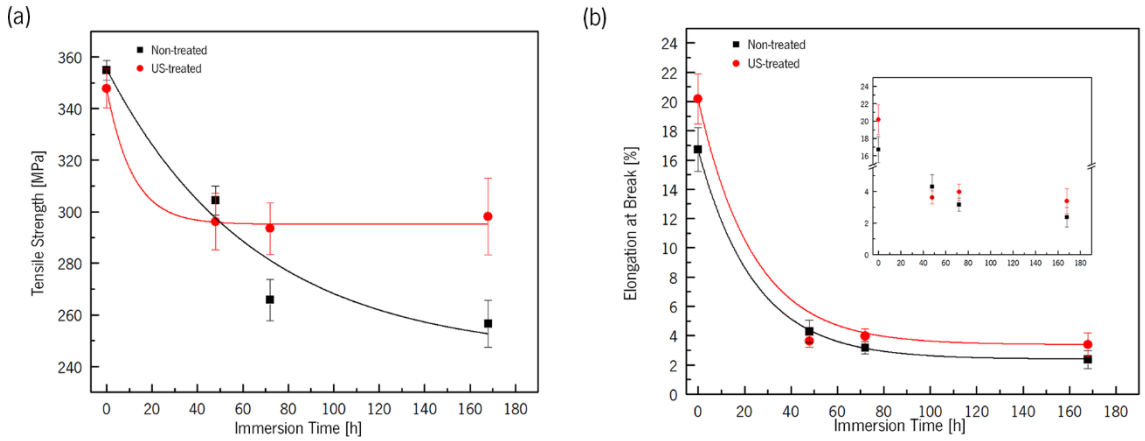

Figure 4.11 – Mechanical properties of the non- and Ultrasound-treated wires: (a) ultimate tensile strength, (b) elongation at break.

The differences observed in the degradation process of the non- and ultrasound-treated materials were reflected in their mechanical response. Due to the finer microstructure, the ultrasound-treated sample had greater elongation in the as-extruded state, although the tensile strength was equivalent to that of the non-treated material. The exposure to EBSS considerably lowered the mechanical properties of both non- and ultrasound-treated samples. Despite so, following exposure to the corrosive media, the disparity in elongation between the non- and ultrasound-treated wires was significantly decreased, becoming approximately equal. In contrast, the tensile strength of the ultrasound-treated samples considerably exceeded that of the non-treated samples after immersion for 72 hours, and this tendency could also be noticed after 7 days (168 h). This change may have been caused by the transmission of the corrosion attack via the coarse intermetallics into the non-treated samples' interior, weakening the material and accelerating its fracture. Furthermore, the loss of material from the surface may encourage its roughening

owing to the creation of depressions and, therefore, produce severe local stress, a phenomenon observed by Linderov *et al.* [54], and that can contribute to the early fracture of wires and, thereby, to reduced tensile strength.

Magnesium alloys are prone to brittle failure, commonly in the form of cleavage or quasi-cleavage fracture, promoted by the limited slip system. However, Li *et al.* [55] have previously described a shift to ductile fracture during hot extrusion due to grain refinement induced by strong plastic deformation.

Using the SEM fractography of the tensile samples, the fracture behavior of the non- and ultrasound-treated specimens before and after 72 h and 7 days (168 h) of immersion in EBSS was investigated (Figure 4.12). Before the immersion tests, both non- and ultrasound-treated fracture surfaces exhibited a combination of a few rough cleavage faces and plastic deformation zones with several dimples (Figure 4.12 (a) and (b)). Secondary phases and oxides could be observed, which might serve as fracture starting sites. Zhou *et al.* [56] previously observed a similar fracture surface pattern comparable with a conventional brittle-ductile failure mechanism. While both samples exhibited comparable fractographic characteristics, the ultrasound-treated wire had more dimples and fewer cleavage planes, which is consistent with its higher elongation at break in the non-degraded state. Following the findings reported by Sozánska *et al.* [34], non- and ultrasound-treated samples immersed in EBSS for 72 hours and 7 days gradually exhibited more cleavage facets and cracks, indicating that intergranular fracture occurred (Figure 4.12 (c)-(f)).

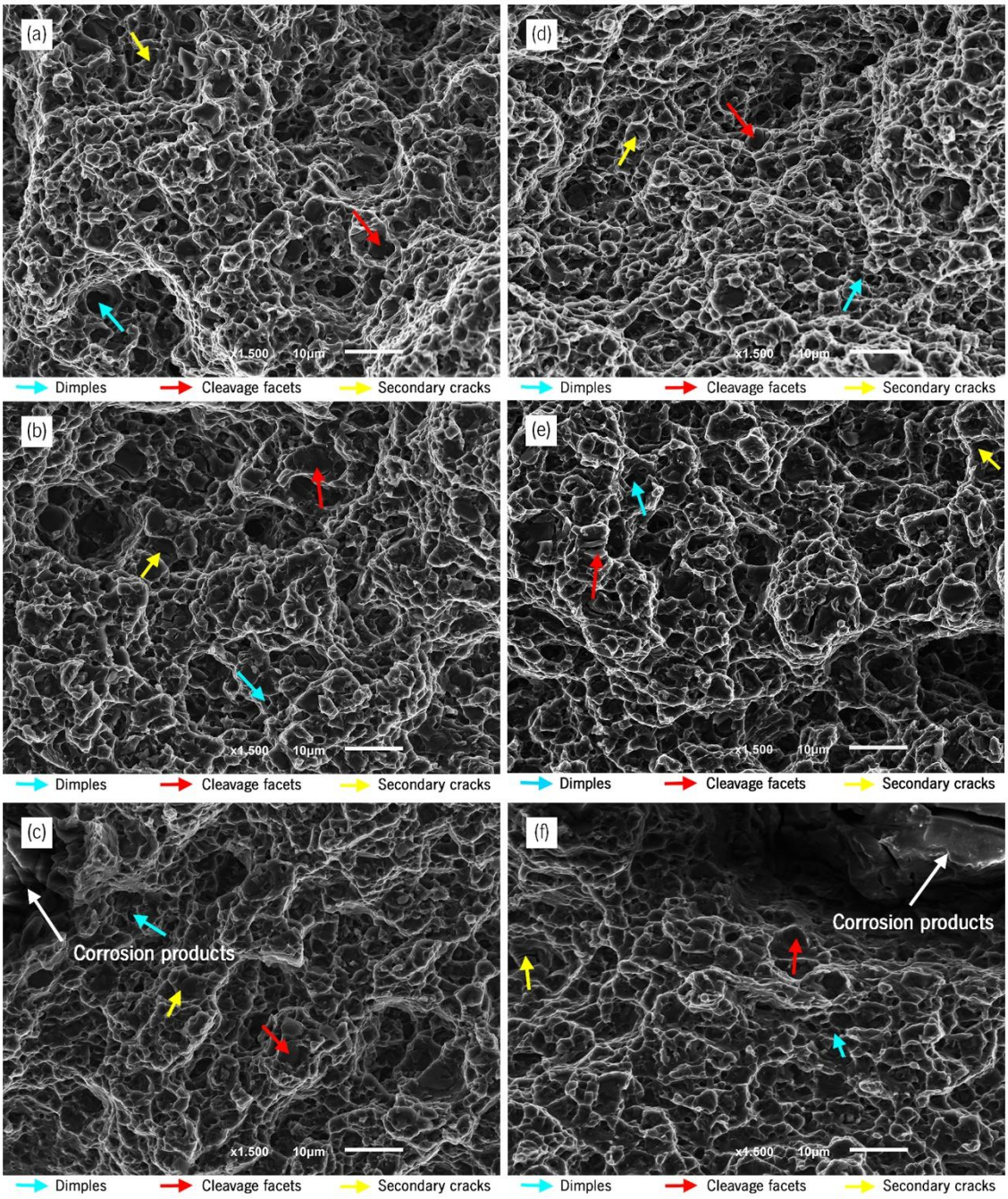

Figure 4.12 – Fractography of the (a,b,c) non-treated and (d,e,f) Ultrasound-treated samples, (a,b) before immersion and after immersion for (c,d) 72 hours and (e,f) 7 days.

4.3. SUMMARY AND CONCLUSIONS

The influence of ultrasound melt treatment on extruded wires' microstructure and corrosion properties was investigated through dynamic immersion tests in EBSS.

The results demonstrated that the material's as-cast microstructure plays an important role in the extruded microstructure, as the ultrasound-treated sample exhibited a refined intermetallic phase compared to the non-treated one after the extrusion process. As a consequence, the corrosion behavior

of both materials displayed significant differences, which was confirmed by the corrosion rate results and the surface morphology of the degraded material, observed through SEM. Up to 6 h of immersion time, the corrosion rate for ultrasound-treated samples was higher than for non-treated ones, with a shift in this tendency for longer immersion periods. Microstructural features, primarily the intermetallics morphology, are suggested to drive the corrosion response of both materials. The existence of small and evenly distributed intermetallic particles in the ultrasound-treated samples is pointed to as the promoter of accelerated degradation of the material in the initial phase of the immersion tests. A corrosion layer covered the wire's surface, delaying further corrosion attacks and translating into a decreased corrosion rate. The uniform microstructure of the samples is also associated with a more uniform degradation, as confirmed by the analysis of the wire's surface after the removal of the corrosion products, which revealed non-signs of severe localized corrosion.

On the contrary, the non-treated samples displayed marks of severe localized corrosion, a result compatible with the intermetallics' coarse morphology, thereby confirming the preferential corrosion attack in such regions.

The composition of the corrosion layer was found to be comparable for both processing conditions. According to the EDS and XPS analyses, the corrosion products included mainly MgO, Mg-CO_3, Ca-CO_3, Mg-PO_4, Ca-PO_4 and $Ca_{10}(PO_4)_6(OH)_2$.

As it was hypothesized, the deterioration of the mechanical properties due to exposure to a corrosive environment occurred regardless of the processing conditions. Higher mechanical properties characterized the ultrasound-treated material compared to the non-treated one, which remained after the immersion tests. Additionally, fractography revealed that intergranular fracture occurred after immersion in EBSS for 72 h and 7 days (168 h), which suggested that intermetallic particles served as fracture starting sites.

CHAPTER REFERENCES

[1] M. Kasaeian-Naeini, M. Sedighi, R. Hashemi, Severe plastic deformation (SPD) of biodegradable magnesium alloys and composites: A review of developments and prospects, Journal of Magnesium and Alloys 10 (2022) 938–955. https://doi.org/10.1016/j.jma.2021.11.006.

[2] V.K. Bommala, M.G. Krishna, C.T. Rao, Magnesium matrix composites for biomedical applications: A review, Journal of Magnesium and Alloys 7 (2019) 72–79. https://doi.org/10.1016/j.jma.2018.11.001.

[3] K. Sternberg, M. Gratz, K. Koeck, J. Mostertz, R. Begunk, M. Loebler, B. Semmling, A. Seidlitz, P. Hildebrandt, G. Homuth, N. Grabow, C. Tuemmler, W. Weitschies, K.-P. Schmitz, H.K. Kroemer, Magnesium used in bioabsorbable stents controls smooth muscle cell proliferation and stimulates endothelial cells in vitro, Journal of biomedical materials research. Part B, Applied biomaterials 100 (2012) 41–50. https://doi.org/10.1002/jbm.b.31918.

[4] J. Dong, T. Lin, H. Shao, H. Wang, X. Wang, K. Song, Q. Li, Advances in degradation behavior of biomedical magnesium alloys: A review, Journal of Alloys and Compounds 908 (2022) 164600. https://doi.org/10.1016/j.jallcom.2022.164600.

[5] Z. Zeng, N. Stanford, C.H.J. Davies, J.-F. Nie, N. Birbilis, Magnesium extrusion alloys: a review of developments and prospects, International Materials Reviews 64 (2019) 27–62. https://doi.org/10.1080/09506608.2017.1421439.

[6] J. Vormann, Magnesium: nutrition and metabolism, Molecular Aspects of Medicine 24 (2003) 27–37. https://doi.org/10.1016/S0098-2997(02)00089-4.

[7] K. TESAŘ, K. BALÍK, Z. SUCHARDA, A. JÄGER, Direct extrusion of thin Mg wires for biomedical applications, Transactions of Nonferrous Metals Society of China 30 (2020) 373–381. https://doi.org/10.1016/S1003-6326(20)65219-0.

[8] J. Zhang, H. Li, W. Wang, H. Huang, J. Pei, H. Qu, G. Yuan, Y. Li, The degradation and transport mechanism of a Mg-Nd-Zn-Zr stent in rabbit common carotid artery: A 20-month study, Acta biomaterialia 69 (2018) 372–384. https://doi.org/10.1016/j.actbio.2018.01.018.

[9] J. Fu, Y. Su, Y.-X. Qin, Y. Zheng, Y. Wang, D. Zhu, Evolution of metallic cardiovascular stent materials: A comparative study among stainless steel, magnesium and zinc, Biomaterials 230 (2020) 119641. https://doi.org/10.1016/j.biomaterials.2019.119641.

[10] P. Du, Di Mei, T. Furushima, S. Zhu, L. Wang, Y. Zhou, S. Guan, In vitro corrosion properties of HTHEed Mg-Zn-Y-Nd alloy microtubes for stent applications: Influence of second phase particles and crystal orientation, Journal of Magnesium and Alloys 10 (2022) 1286–1295. https://doi.org/10.1016/j.jma.2020.12.015.

[11] M.N. Sarian, N. Iqbal, P. Sotoudehbagha, M. Razavi, Q.U. Ahmed, C. Sukotjo, H. Hermawan, Potential bioactive coating system for high-performance absorbable magnesium bone implants, Bioactive materials 12 (2022) 42–63. https://doi.org/10.1016/j.bioactmat.2021.10.034.

[12] C.-J. Pan, L.-Q. Pang, Y. Hou, Y.-B. Lin, T. Gong, T. Liu, W. Ye, H.-Y. Ding, Improving Corrosion Resistance and Biocompatibility of Magnesium Alloy by Sodium Hydroxide and Hydrofluoric Acid Treatments, Applied Sciences 7 (2017) 33. https://doi.org/10.3390/app7010033.

[13] L. Mao, H. Zhu, L. Chen, H. Zhou, G. Yuan, C. Song, Enhancement of corrosion resistance and biocompatibility of Mg-Nd-Zn-Zr alloy achieved with phosphate coating for vascular stent application,

Journal of Materials Research and Technology 9 (2020) 6409–6419. https://doi.org/10.1016/j.jmrt.2020.04.024.

[14] P. Tong, Y. Sheng, R. Hou, M. Iqbal, L. Chen, J. Li, Recent progress on coatings of biomedical magnesium alloy, Smart Materials in Medicine 3 (2022) 104–116. https://doi.org/10.1016/j.smaim.2021.12.007.

[15] M. Rahman, Y. Li, C. Wen, HA coating on Mg alloys for biomedical applications: A review, Journal of Magnesium and Alloys 8 (2020) 929–943. https://doi.org/10.1016/j.jma.2020.05.003.

[16] X. Guo, Y. Hu, K. Yuan, Y. Qiao, Review of the Effect of Surface Coating Modification on Magnesium Alloy Biocompatibility, Materials (Basel, Switzerland) 15 (2022). https://doi.org/10.3390/ma15093291.

[17] N. Singh, U. Batra, K. Kumar, N. Ahuja, A. Mahapatro, Progress in bioactive surface coatings on biodegradable Mg alloys: A critical review towards clinical translation, Bioactive materials 19 (2023) 717–757. https://doi.org/10.1016/j.bioactmat.2022.05.009.

[18] D. Lee, B. Kim, S. Lee, S.-M. Baek, J.C. Kim, H.-T. Son, J.G. Lee, K.-S. Lee, S.S. Park, Enhanced corrosion resistance of Mg–Sn–Zn–Al alloy by Y microalloying, Scripta Materialia 163 (2019) 125–129. https://doi.org/10.1016/j.scriptamat.2019.01.015.

[19] H. Jafari, A.H.M. Tehrani, M. Heydari, Effect of extrusion process on microstructure and mechanical and corrosion properties of biodegradable Mg–5Zn–1.5Y magnesium alloy, Int J Miner Metall Mater 29 (2022) 490–502. https://doi.org/10.1007/s12613-021-2275-5.

[20] P.M. Kalayeh, M. Malekan, A. Bahmani, M. Lotfpour, S.M. Fatemi, S.B. Zonoozi, Combination of severe plastic deformation and heat treatment for enhancing the corrosion resistance of a new Magnesium alloy, Journal of Alloys and Compounds 927 (2022) 166939. https://doi.org/10.1016/j.jallcom.2022.166939.

[21] Y. Zhang, Y. Huang, F. Feyerabend, S. Gavras, Y. Xu, R. Willumeit-Römer, K.U. Kainer, N. Hort, Effects of Intermetallic Microstructure on Degradation of Mg-5Nd Alloy, Metall Mater Trans A 51 (2020) 5498–5515. https://doi.org/10.1007/s11661-020-05926-7.

[22] S. Amukarimi, M. Mozafari, Biodegradable Magnesium Biomaterials-Road to the Clinic, Bioengineering (Basel, Switzerland) 9 (2022). https://doi.org/10.3390/bioengineering9030107.

[23] A. Atrens, S. Johnston, Z. Shi, M.S. Dargusch, Viewpoint - Understanding Mg corrosion in the body for biodegradable medical implants, Scripta Materialia 154 92–100. https://doi.org/10.1016/j.scriptamat.2018.05.021.

[24] Sean Johnston, Zhiming Shi, Jeffrey Venezuela, Cuie Wen, Matthew S. Dargusch, Andrej Atrens, Investigating Mg Biocorrosion In Vitro: Lessons Learned and Recommendations, JOM 71 (2019) 1406–1413. https://doi.org/10.1007/s11837-019-03327-9.

[25] J. Walker, S. Shadanbaz, N.T. Kirkland, E. Stace, T. Woodfield, M.P. Staiger, G.J. Dias, Magnesium alloys: predicting in vivo corrosion with in vitro immersion testing, Journal of biomedical materials research. Part B, Applied biomaterials 100 (2012) 1134–1141. https://doi.org/10.1002/jbm.b.32680.

[26] C. Zhang, C. Li, C. Li, X. Zhao, Effect of Ca and RE (Y, Sm) on microstructure and mechanical properties of as-cast AZ91 magnesium alloy, Mater. Res. Express 8 (2021) 106514. https://doi.org/10.1088/2053-1591/ac2c2e.

[27] P. Emadi, B. Andilab, C. Ravindran, Effects of sonication amplitude on the microstructure and mechanical properties of AZ91E magnesium alloy, Journal of Magnesium and Alloys. https://doi.org/10.1016/j.jma.2022.05.019.

[28] M. Khosro Aghayani, B. Niroumand, Effects of ultrasonic treatment on microstructure and tensile strength of AZ91 magnesium alloy, Journal of Alloys and Compounds 509 (2011) 114–122. https://doi.org/10.1016/j.jallcom.2010.08.139.

[29] B. Patel, G.P. Chaudhari, P.P. Bhingole, Microstructural evolution in ultrasonicated AS41 magnesium alloy, Materials Letters 66 (2012) 335–338. https://doi.org/10.1016/j.matlet.2011.08.113.

[30] H. Puga, V. Carneiro, J. Barbosa, V. Vieira, Effect of Ultrasonic Treatment in the Static and Dynamic Mechanical Behavior of AZ91D Mg Alloy, Metals 5 (2015) 2210–2221. https://doi.org/10.3390/met5042210.

[31] X. Zhang, H.R. Kotadia, J. Depner, M. Qian, A. Das, Effect of Ultrasonication on the Solidification Microstructure in Al and Mg-Alloys, in: C. Chesonis (Ed.), Light metals, Springer Berlin Heidelberg, New York NY, 2019, pp. 1589–1595.

[32] G.I. Eskin, Ultrasonic Treatment of Light Alloy Melts, CRC Press, 1998.

[33] X. Liu, C. Zhang, Z. Zhang, J. Xue, Q. Le, The role of ultrasound in hydrogen removal and microstructure refinement by ultrasonic argon degassing process, Ultrasonics sonochemistry 38 (2017) 455–462. https://doi.org/10.1016/j.ultsonch.2017.03.041.

[34] M. Sozańska, A. Mościcki, Investigation of the Susceptibility of the WE54 Magnesium-Based Alloy to Stress Corrosion Cracking, J. of Materi Eng and Perform 29 (2020) 949–963. https://doi.org/10.1007/s11665-019-04550-w.

[35] J.-Y. Kim, J.-W. Byeon, Quantitative relation of discontinuous and continuous Mg17Al12 precipitates with corrosion rate of AZ91D magnesium alloy, Materials Characterization 174 (2021) 111015. https://doi.org/10.1016/j.matchar.2021.111015.

[36] Di Mei, C. Wang, M. Nienaber, M. Pacheco, A. Barros, S. Neves, R.L. Reis, S. Zhu, J. Bohlen, D. Letzig, S. Guan, M.L. Zheludkevich, S.V. Lamaka, Corrosion behavior of Mg wires for ureteral stent in artificial urine solution, Corrosion Science 189 (2021) 109567. https://doi.org/10.1016/j.corsci.2021.109567.

[37] C. Cai, M.M. Alves, R. Song, Y. Wang, J. Li, M.F. Montemor, Non-destructive corrosion study on a magnesium alloy with mechanical properties tailored for biodegradable cardiovascular stent applications, Journal of Materials Science & Technology 66 (2021) 128–138. https://doi.org/10.1016/j.jmst.2020.07.006.

[38] Z. Yin, Y. Chen, H. Yan, G.-h. Zhou, X.-q. Wu, Z. Hu, Effects of the second phases on corrosion resistance of AZ91-xGd alloys treated with ultrasonic vibration, Journal of Alloys and Compounds 783 (2019) 877–885. https://doi.org/10.1016/j.jallcom.2019.01.002.

[39] M. Mohammadi Zerankeshi, R. Alizadeh, E. Gerashi, M. Asadollahi, T.G. Langdon, Effects of heat treatment on the corrosion behavior and mechanical properties of biodegradable Mg alloys, Journal of Magnesium and Alloys 10 (2022) 1737–1785. https://doi.org/10.1016/j.jma.2022.04.010.

[40] T. Zhang, Y. Shao, G. Meng, Z. Cui, F. Wang, Corrosion of hot extrusion AZ91 magnesium alloy: I-relation between the microstructure and corrosion behavior, Corrosion Science 53 (2011) 1960–1968. https://doi.org/10.1016/j.corsci.2011.02.015.

[41] Y. Song, D. Shan, R. Chen, F. Zhang, E.-H. Han, Biodegradable behaviors of AZ31 magnesium alloy in simulated body fluid, Materials Science and Engineering: C 29 (2009) 1039–1045. https://doi.org/10.1016/j.msec.2008.08.026.

[42] N.M. Elmrabet, Corrosion Control of Magnesium for Stent Applications. PhD Thesis, Nottingham, 2017.

[43] A. Le Febvrier, J. Jensen, P. Eklund, Wet-cleaning of MgO(001): Modification of surface chemistry and effects on thin film growth investigated by x-ray photoelectron spectroscopy and time-of-flight secondary ion mass spectroscopy, Journal of Vacuum Science & Technology A: Vacuum, Surfaces, and Films 35 (2017) 21407. https://doi.org/10.1116/1.4975595.

[44] E.O. López, A. Mello, H. Sendão, L.T. Costa, A.L. Rossi, R.O. Ospina, F.F. Borghi, J.G. Silva Filho, A.M. Rossi, Growth of Crystalline Hydroxyapatite Thin Films at Room Temperature by Tuning the Energy of the RF-Magnetron Sputtering Plasma, ACS Applied Materials & Interfaces 5 (2013) 9435–9445. https://doi.org/10.1021/am4020007.

[45] L. Wang, T. Shinohara, B.-P. Zhang, XPS study of the surface chemistry on AZ31 and AZ91 magnesium alloys in dilute NaCl solution, Applied Surface Science 256 (2010) 5807–5812. https://doi.org/10.1016/j.apsusc.2010.02.058.

[46] Y. Song, D. Shan, R. Chen, F. Zhang, E.-H. Han, Biodegradable behaviors of AZ31 magnesium alloy in simulated body fluid, Materials Science and Engineering: C 29 (2009) 1039–1045. https://doi.org/10.1016/j.msec.2008.08.026.

[47] Y. Xin, K. Huo, T. Hu, G. Tang, P.K. Chu, Corrosion products on biomedical magnesium alloy soaked in simulated body fluids, J. Mater. Res. 24 (2009) 2711–2719. https://doi.org/10.1557/jmr.2009.0323.

[48] S.A. Omar, J. Ballarre, W.H. Schreiner, S.M. Ceré, Micro Raman and XPS surface analysis to understand the electrochemical behavior of AZ31 and AZ91 magnesium alloys as temporary implant materials, Materials Today Communications 31 (2022) 103557. https://doi.org/10.1016/j.mtcomm.2022.103557.

[49] K. Choi, J. Shin, H. Kang, The Effect of Solidification Rate on the Corrosion Resistance of Die-Cast AZ91 Magnesium Alloy, Materials (Basel, Switzerland) 15 (2022). https://doi.org/10.3390/ma15031259.

[50] J. Gonzalez, R.Q. Hou, E.P.S. Nidadavolu, R. Willumeit-Römer, F. Feyerabend, Magnesium degradation under physiological conditions - Best practice, Bioactive materials 3 (2018) 174–185. https://doi.org/10.1016/j.bioactmat.2018.01.003.

[51] M. Inigo, Degradation Testing of Magnesium and its Alloys aiming at Biodegradable Implant Applications. PhD Thesis, Belgium, 2016.

[52] J. Majhi, S. Ganguly, A. Basu, A.K. Mondal, Improved corrosion response of squeeze-cast AZ91 magnesium alloy with calcium and bismuth additions, Journal of Alloys and Compounds 873 (2021) 159600. https://doi.org/10.1016/j.jallcom.2021.159600.

[53] W. Ali, A. Mehboob, M.-G. Han, S.-H. Chang, Experimental study on degradation of mechanical properties of biodegradable magnesium alloy (AZ31) wires/poly(lactic acid) composite for bone fracture healing applications, Composite Structures 210 (2019) 914–921. https://doi.org/10.1016/j.compstruct.2018.12.011.

[54] M. Linderov, A. Brilevsky, D. Merson, A. Danyuk, A. Vinogradov, On the Corrosion Fatigue of Magnesium Alloys Aimed at Biomedical Applications: New Insights from the Influence of Testing Frequency and Surface Modification of the Alloy ZK60, Materials (Basel, Switzerland) 15 (2022). https://doi.org/10.3390/ma15020567.

[55] Z. Li, J. Dong, X.Q. Zeng, C. Lu, W.J. Ding, Influence of Mg17Al12 intermetallic compounds on the hot extruded microstructures and mechanical properties of Mg–9Al–1Zn alloy, Materials Science and Engineering: A 466 (2007) 134–139. https://doi.org/10.1016/j.msea.2007.02.029.

[56] P. Zhou, E. Beeh, H.E. Friedrich, T. Grünheid, Mechanical Behavior and Microstructural Analysis of Extruded AZ31B Magnesium Alloy Processed by Backward Extrusion, J. of Materi Eng and Perform 25 (2016) 2866–2877. https://doi.org/10.1007/s11665-016-2131-3.

CHAPTER 5 – FINITE ELEMENT ANALYSIS OF STENT FUNCTIONAL PERFORMANCE

The expansion of the stent is a crucial step in the deployment procedure. Inflation of a balloon inserted within the stent facilitates its expansion, removing the atherosclerotic plaque, reopening the lumen, and restoring normal blood flow.

FEA is a valuable tool that permits the simulation of the stenting procedure and provides essential data for evaluating its results. Thus, the function of the stent's design and material may be comprehensively explored, allowing the procedure to be optimized without needing costly and time-consuming prototype technologies and specialized bench test equipment.

Despite the unique advantages numerical simulation provides to the stent design process, the results offered by such a method are susceptible to problem modeling, i.e., the employed geometry, the constitutive material modeling, and the stated boundary conditions. In this regard, the correct formulation of the problem is imperative to assure suitable and trustworthy results.

Using two distinct geometries and material constitutive formulations, this chapter investigates the adopted balloon modeling strategy's role in the stent deployment procedure. The preferred approach is then implemented to study the impact of the stent material's properties on the expansion process by using the stress-strain curves of the non- and ultrasound-treated cast materials. A shape optimization aiming at

cross-section variation is also performed to take advantage of the geometric features granted by the microcasting manufacturing technique. Finally, the effect of the mechanical properties loss promoted by the exposure to a physiological-inspired medium on the stent functional performance is assessed, resorting to the tensile tests' results of degraded magnesium alloy wires produced from non- and ultrasound-treated billets. An optimization study is carried out to enhance the stent's mechanical performance while accounting for the material's loss of mechanical strength after 7 days of immersion.

5.1. GEOMETRY, MATERIAL CONSTITUTIVE DEFINITION, AND BOUNDARY CONDITIONS OF THE STENT

The NG stent model (see Figure 5.1) with an inner radius of 2.50 mm, length of 12.00 mm, and initial thickness of 0.20 mm was employed in this study's numerical analysis. The stent's dimensions were defined according to the manufacturing process constraints, determined mainly by the minimum feasible thickness. In fact, the filling of thin-walled parts remains challenging, and a minimum thickness of 0.20 mm is currently the lower limit of the microcasting technique [1]. Due to the use of straight lines combined with arcs, this stent was designed to present lower values of foreshortening as the curved link elements may compensate for the length reduction motivated by the radial expansion of the device as they deform along the process.

Given the geometric periodicity of the stent in the circumferential and longitudinal directions in the cylindrical coordinate system and the assumption of isotropic behavior of the material, only one-tenth of the model was taken into account in the studies conducted, reducing the number of degrees of freedom and, consequently, the required computation time, without loss of results accuracy. For this purpose, symmetry conditions were applied in the lateral and central faces of the stent belonging to planes α, β, and γ, as presented in Figure 5.1 (b). Tetrahedral elements were used to mesh the stent, and each study underwent a sensitivity analysis.

The mechanical behavior of the stent magnesium alloy was assumed to be isotropic and elastoplastic with Young's modulus $E = 43\ GPa$ and Poisson ratio ν=0.30. The plastic behavior is modeled by the von Mises yield criterion and the nonlinear isotropic stress-strain hardening curve is described by a Voce-type law defined by Eq. (5.1).

$$Y=Y_0+(Y_{sat}-Y_0)[1-\exp(-C_y\times\bar{\varepsilon}^p)] \tag{5.1}$$

where Y_0 is the initial flow stress, Y_{sat} is the saturation flow stress, C_y is the unitless hardening rate (16), and $\bar{\varepsilon}^p$ is the equivalent plastic strain, work-conjugate of the von Mises equivalent stress.

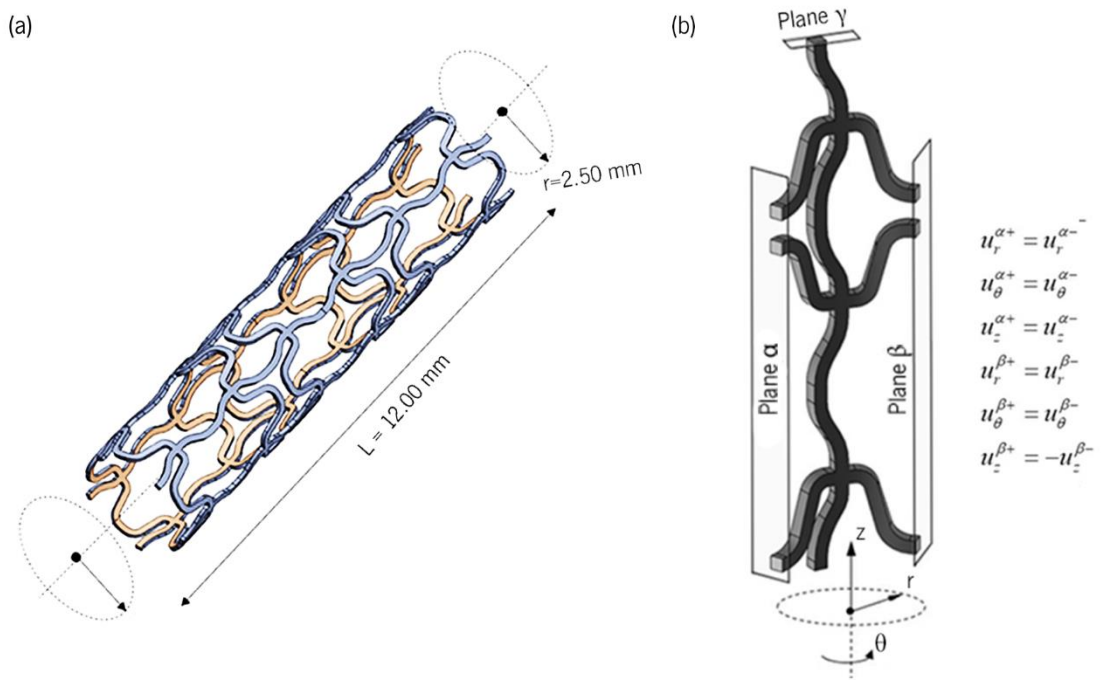

Figure 5.1 – (a) NG stent geometry and (b) symmetry boundary conditions representation.

5.2. NUMERICAL MODELING OF THE INFLATING BALLOON: INFLUENCE OF THE ADOPTED MODELING STRATEGIES

Inflating the balloon placed within the stent expands and compresses the atherosclerotic plaque, which allows the lumen to reopen and restores normal blood flow.

Intravascular procedures such as stenting are pointed to as a trigger of a sequence of cellular and biochemical events that can ultimately lead to death [2–4]. The aggressiveness of the procedure, specifically in terms of balloon features, has been shown to correlate with neointimal thickness [5]. Despite such evidence, most recent efforts to prevent neointimal hyperplasia have focused on the delivery of systemic or local drugs, and little endeavor has been made to understand vessel injury from a mechanical perspective. Since endothelium denudation can trigger neointimal hyperplasia, the relevance of studying all the interactions between the stent, its deployment system, and the blood vessel to prevent restenosis is highlighted. An example is a potentially harmful interaction between the balloon and the artery [6].

The transient expansion of the stent may be influenced by the geometry of the balloon and its expansion profile, highlighting the relevance of studying the impact of balloon modeling on the outcomes of the stent deployment simulation. Indeed, a mismatch between the results provided by the numerical analyses and those observed in the clinical practice can have severe repercussions for the procedure's success, which is why it is vital to assess the impact of each modeling decision.

This section explores a novel approach to determine the influence of ballon modeling strategies in the stenting process with stents intended to be obtained by the ultrasonic-microcasting manufacturing process, considering both the geometry and material models used. In this study, four different approaches were adopted, two concerning the balloon geometry – open- and taper-ended – and two regarding the constitutive material modeling – linear elastic and hyperelastic models. The longitudinal and circumferential configuration profiles of the expanded stent were evaluated, as well as the balloon's behavior during the expansion process, specifically in terms of membrane thickness and transverse and longitudinal section areas.

5.2.1. METHODOLOGY FOR BALLOON INFLATION MODELING

The geometry of the NG stent is used to study the influence of the balloon's geometry and constitutive material modeling on the outcomes of the deployment procedure. The element dimensions and mesh settings for both the open-ended and tapered balloon models are shown in Table 5.1. To mesh the stent and balloon, a total of 12413 and 13863 tetrahedral elements were employed for the open- and taper-ended geometries, respectively. Sensitivity analysis was performed considering the quotient of pressure applied and the stent radius in its mid-section by simulating different mesh sizes.

Table 5.1 – Geometry and mesh parameters of the stent and balloon models.

	Strut width [mm]	Length [mm]	Thickness [mm]	Mesh	Inner radius [mm]	
				N° of elements	Mid-section	End
Stent	0.30	12	0.20	4962	2.50	
Open-ended balloon (OE)	-	14	0.15	7451	2.35	
Taper-ended balloon (TE)	-	14	0.15	8901	2.35	1.00

The balloon geometries were 2.00 mm longer than the stent, 1.00 mm on each side, to minimize the effect of the non-uniform expansion of the balloon at its ends. Indeed, the impact of stent and balloon placement on each other has already been pointed to as a factor that influences the expansion process of the stent due to balloon transient behavior [7]. The assembly of the system stent-balloon is illustrated in Figure 5.2.

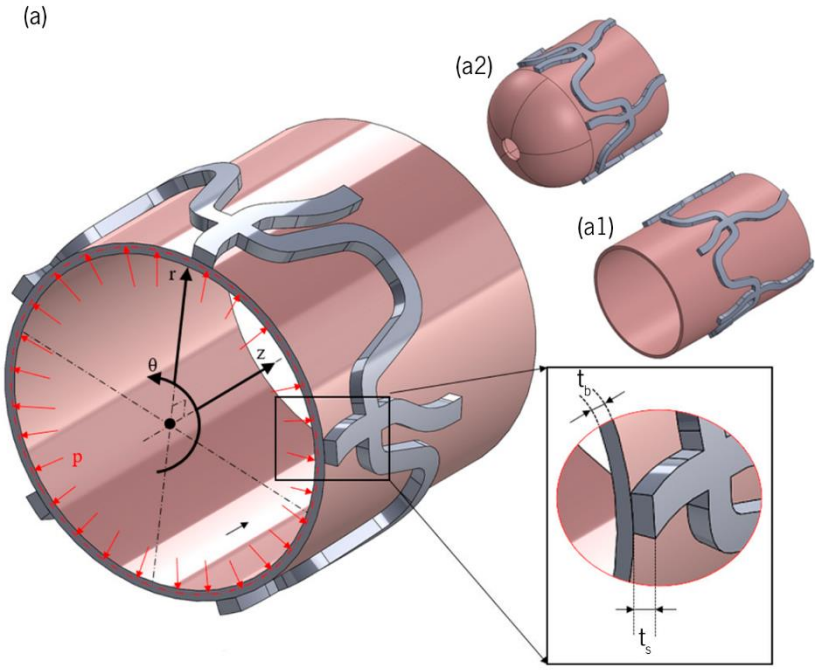

Figure 5.2 – Representation of the balloon-stent system for (a1) open- (OE) balloon and (a2) taper-ended (TE) balloon.

The free expansion of the stent, i.e., without any external constraint, was performed considering the inflation stage during which the pressure p applied to the balloon's inner surface increases until its inner radius is 3.00 mm. The model was solved using the commercial finite-element software *COMSOL Multiphysics*, and since deformation history is time-independent, the pressure was increased linearly with a pseudo-time. An implicit model combined with a direct solver based on the nonlinear Newton-Raphson method was adopted.

As observed for the stent geometry, the balloon model presents geometric periodicity in the cylindrical coordinate system's circumferential and longitudinal directions, allowing to consider only one-tenth of the model. Similarly, symmetry conditions were applied to the lateral and central faces of the balloon. The ends of the open-ended balloon (detail (a1) – Figure 5.2) were set free, and those of the taper-ended balloon (detail (a2) – Figure 5.2) were fully constrained to represent the connection to the catheter.

Frictionless contact between the stent and balloon was assumed [8–10], and an augmented Lagrange formulation was adopted, which generates no penetration and provides better accuracy than the penalty method, although with a higher computational cost.

The constitutive modeling of balloon hyperelastic material (HE), characterized by low elastic modulus and high bulk modulus, is derived from the strain energy density function (W), which represents the energy stored in the material per unit of volume reference and is based on three isochoric strain invariants of the

right Cauchy-Green strain tensor ($\bar{I}_1$, $\bar{I}_2$ and $\bar{I}_3$). Once hyperelastic materials are considered incompressible, $\bar{I}_3$ is equal to 1 and W becomes a function dependent only on $\bar{I}_1$ and $\bar{I}_2$.

Mooney-Rivlin models are one of the possible formulations for the description of the behavior of hyperelastic materials, whose generic expression is given by Eq. (5.2):

$$W = \sum_i \sum_j C_{ij} (\bar{I}_1 - 3)^i (\bar{I}_2 - 3)^j + \frac{1}{2} k (J_{el} - 1)^2 \tag{5.2}$$

where $\bar{I}_1$ and $\bar{I}_2$ .are the first and second invariant of the left isochoric Cauchy-Green strain tensor, J_{el} is the elastic Jacobian, k is the bulk modulus, and C_{ij} are model parameters. In this study, and according to Eq. (5.3), a two-parameter Mooney-Rivlin model was adopted to describe the behavior of polyurethane rubber, using the values of the material constants presented in Table 5.2

$$W = [C_{10}(\bar{I}_1 - 3) + C_{01}(\bar{I}_2 - 3)] + \frac{1}{2} k (J_{el} - 1)^2 \tag{5.3}$$

Table 5.2 – Material constants for hyperplastic and linear elastic material models.

Material model	Material properties						References
	C_{10} [MPa]	C_{01} [MPa]	k [MPa]	E [MPa]	ν [-]	ρ [Kg/m³]	
HE	1.03	3.69	10^4	-	-	-	[11]
LE	-	-	-	10	0.49	1100	[12,13]

The second Piola-Kirchhoff stress tensor (π) is then given by Eq. (5.4) as follows:

$$\pi = \frac{\partial W}{\partial E} \tag{5.4}$$

where E is the Green-Lagrange strain tensor, defined as:

$$E = \frac{1}{2}(C - I) \tag{5.5}$$

being C the right Cauchy-Green tensor expressed by the deformation gradient F :

$$C = F^T F \tag{5.6}$$

The state of stress at a material point in its deformed configuration is defined by the Cauchy stress tensor, which is given by:

$$\sigma = \frac{1}{J_{el}} F \pi F^T \tag{5.7}$$

Regarding the linear elastic (LE) behavior modeling of balloon material (Table 5.2), Hooke's law is used, which is described as follows:

$$\sigma = C^{el} : \varepsilon \tag{5.8}$$

being ε the infinitesimal strain tensor and C^{el} the fourth-order stiffness tensor, defined as:

$$C_{ijkm}^{el} = \lambda \delta_{ij} \delta_{km} + \mu(\delta_{ik} \delta_{jm} + \delta_{im} \delta_{kj}) \tag{5.9}$$

where λ and μ are the Lamé parameters and δ is the Kronecker delta.

5.2.2. Results and Discussion

A. Stent and balloon expansion profiles

Figure 5.3 shows the evolution of the stent radius and dogboning as a function of the pressure applied to the inner surface of the balloon, considering a point belonging to the stent's mid-section plane. To assess the effect of the balloon material model and geometry on the expansion behavior of the stent, a statistical analysis was run resorting to *IBM® SPSS®* software. A *p*-value < 0.05 (95% confidence interval) was considered the criteria for limited statistical significance.

Since the evolution of the stent radius follows a normal distribution, according to the Kolmogorov-Smirnov test, an independent samples *t-test* to compare the LE and HE material models was conducted. According to the *p*-value result, no significant difference was found for the material used ($p = 0.932$). Likewise, no statistical significance was verified when the OE and TE balloons geometry to expand the stent were used ($p = 0.857$).

Concerning the dogboning parameter, its maximum value occurred at the last step of the simulation for both hyperelastic models, with values equal to 6.20% and 6.00% for the OE-HE and TE-HE models, respectively (Figure 5.3 – green arrows). For linear elastic models, the dogboning parameter reached its maximum absolute value a few steps before the expansion was complete, being 2.45% for the OE-LE model and 2.77% for TE-LE (Figure 5.3 – red arrows).). Adopting a linear elastic model resulted in an average dogboning outcome of approximately 43.0% lower than when a hyperelastic model was used.

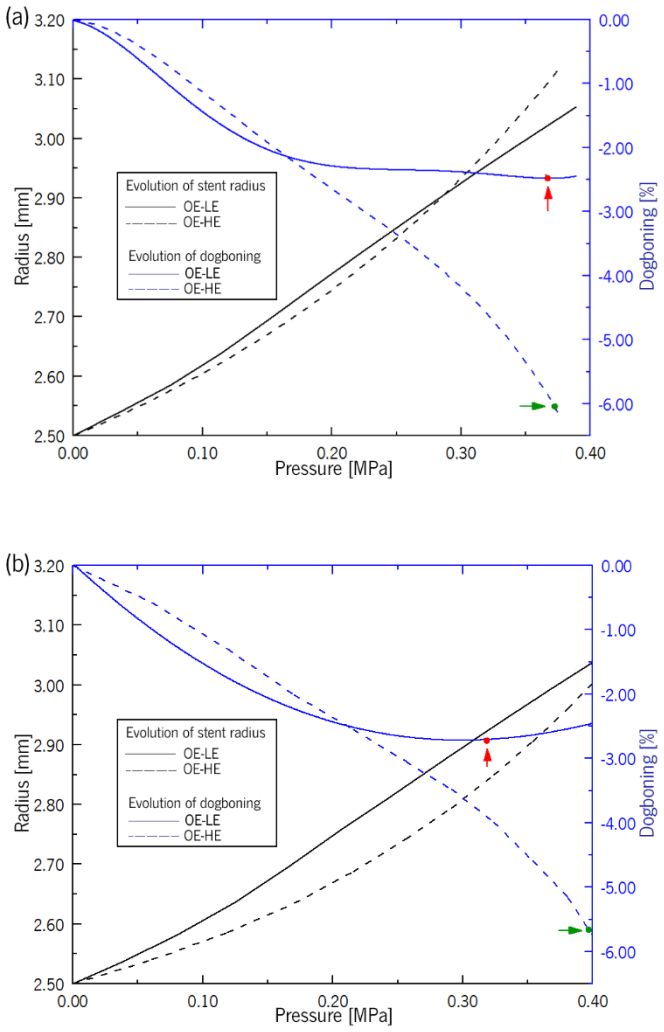

Figure 5.3 – Stent radius and dogboning as a function of the applied pressure for the different balloon geometries and material models for (a) OE – open-ended balloon and (b) TE – taper-ended balloon.

As noted by Khosravi *et al.* [13], despite the importance of dogboning in stent performance evaluation, this metric may not always be the ideal technique to evaluate the uniformity of the expanded configuration of the stent. In this sense, Figure 5.4 shows the evolution of the stent's radius along its length.

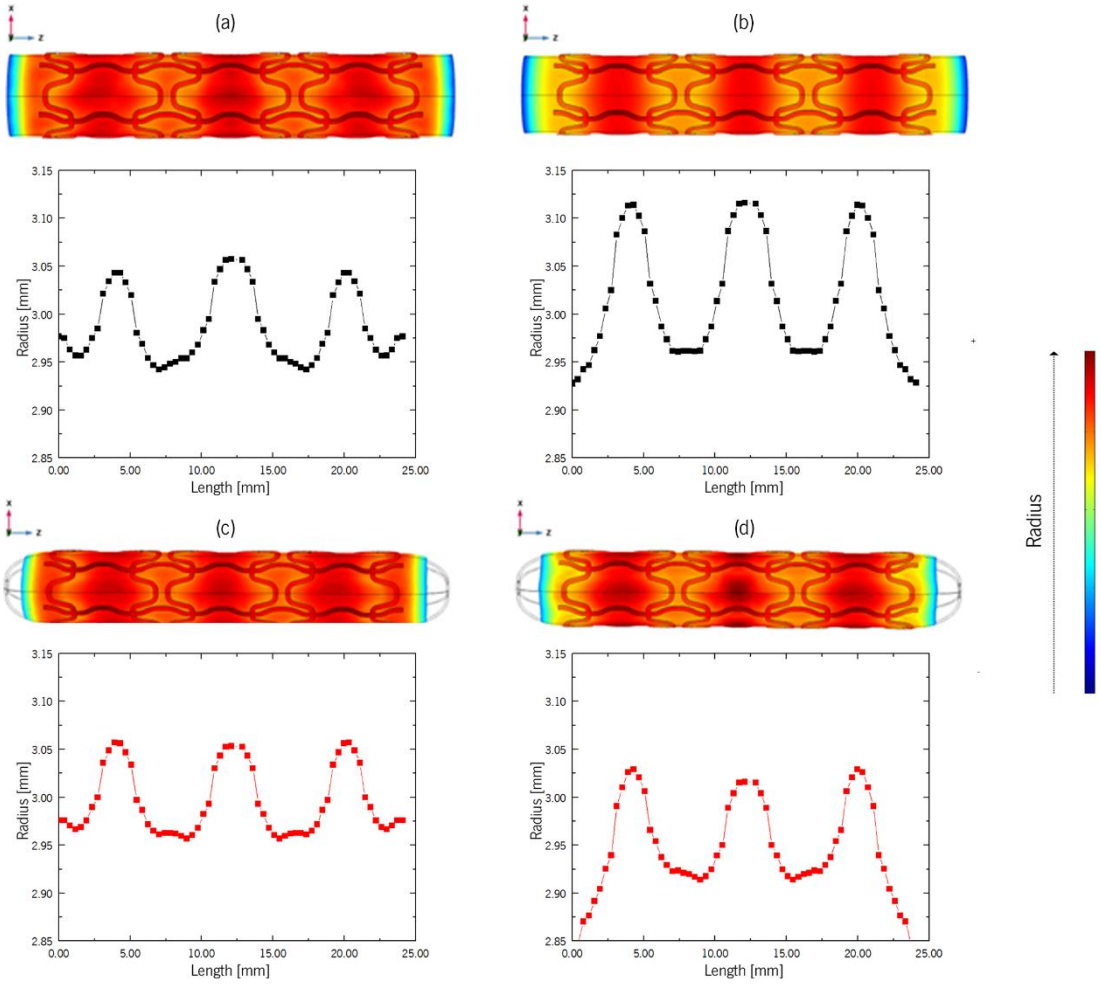

Figure 5.4 – Stent radius assessment along their length as a function of the applied pressure: (a) OE-LE; (b) OE-HE; (c) TE-LE; (d) TE-HE.

As a result of stent geometry, the stent's radius followed a nearly sinusoidal pattern, according to the results. The link element, which connects the stent rings, offers less deformation resistance once it has a lower width and thickness than the stent head. Although the pressure applied to the surface was constant, the balloon was prone to exhibit more significant radial deformations in these regions, and, therefore, the same was observed for the stent. On the other hand, near the stent head, the magnitude of the balloon expansion was inferior due to the presence of wider and thicker structures, the reason why the stent radius was also lower.

In the fully inflated configuration of the linear elastic model, the difference between the highest and lowest stent radius along its longitudinal direction (*zz* axis – Figure 5.4) was less than that seen for the hyperelastic model, independent of the balloon shape used.

The difference was approximately equal to 3.3% and 3.8% for OE-LE and TE-LE models (measured between the distal end and the head of the stent), respectively, and to 6.0% and 6.3% for OE-HE and TE-HE (registered between the central and distal parts of the stent). In the case of hyperelastic models, the existence of well-defined balloon regions between the stent link elements could be noticed. These results suggest the development of balloon bulges through the stent gaps, which may have a negative impact during the deployment procedure. Indeed, non-uniform stent expansion constitutes one of the main causes of adverse events.

The evolution of the inner radius of the balloon in the cylindrical coordinate system is presented in Figure 5.5, for one-fifth of the balloon geometry model in the circumferential direction, considering a transversal plane in its mid-section.

The results suggest that the inner radius of the balloon was not uniform along the circumferential direction, mainly for the composition TE-HE model (Figure 5.5 (d)), with a difference of around 4.0%. The OE-HE model (Figure 5.5 (b)) presented the best radius uniformity (0.2%), being registered a variation of 1.5% to the OE-LE model (Figure 5.5 (a)) and TE-LE (Figure 5.5 (c)).

These differences may be due to the presence/absence of stent structures, which act as a barrier to the expansion of the balloon, influencing the radial deformation of the stent itself. As a compliant balloon is used in this work, it was expected to keep expanding as the pressure increased. Thus, some portions must appear to extrude between stent struts, forming bulges, as experimentally demonstrated by Rogers *et al.* [6]. The obtained results concerning the balloon radius along its length indicate that the linear elastic models (Figure 5.4 (a) and (c)) were not capable of reflecting this effect. Indeed, only hyperelastic models (Figure 5.4 (b) and (d)) demonstrated well-defined balloon regions between the stent link elements with a larger radius than the remaining areas. These results suggest the development of balloon protrusions through the stent gaps, which agrees with the experimental results. Moreover, the balloon radius along the circumferential direction shows that the TE-HE model was the only one to exhibit balloon protrusions at each stent cell (the open region between stent struts). Consequently, it is suggested that this combination of balloon geometry and material model is the one that correlates the best with the clinical and experimental results.

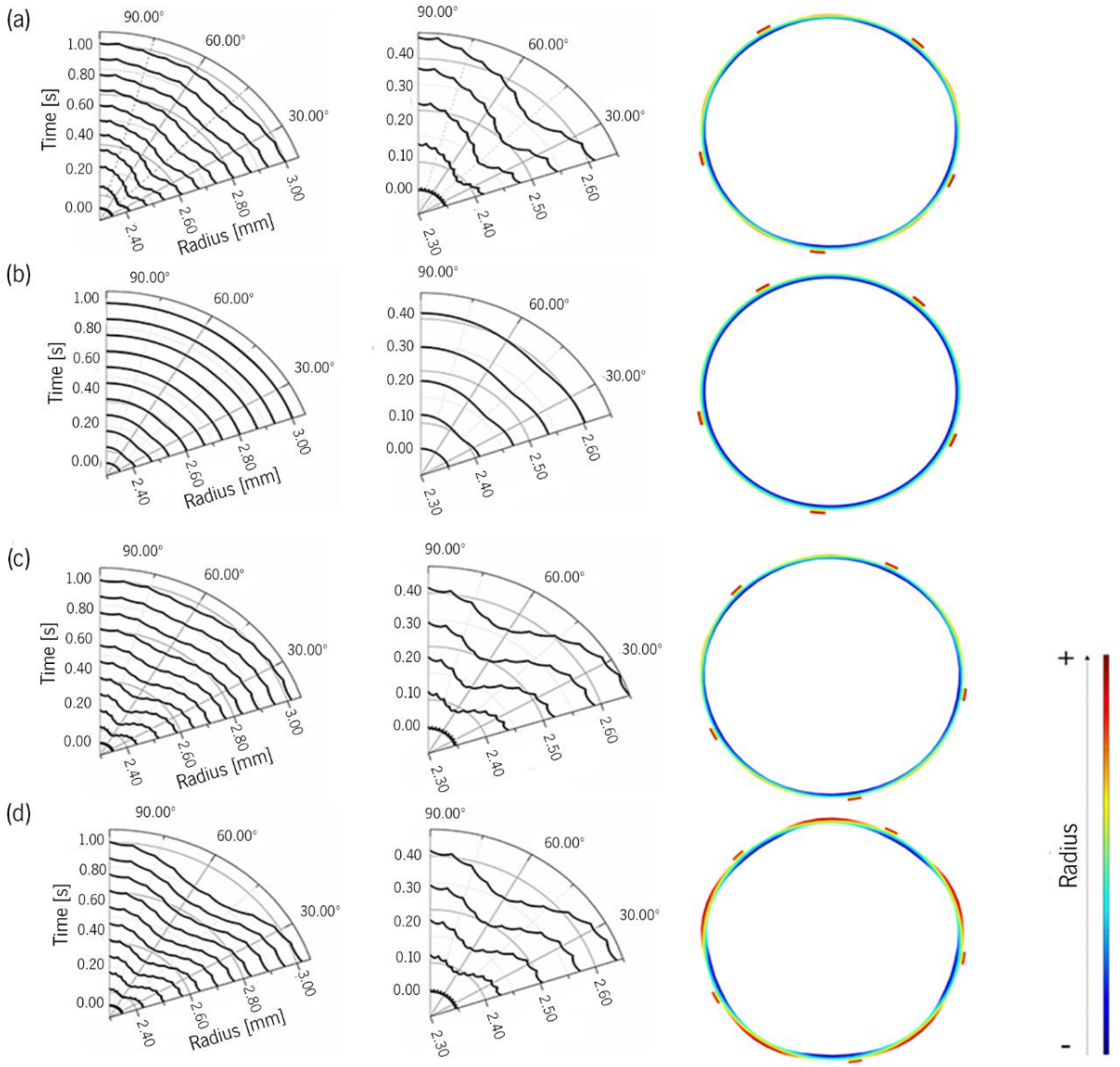

Figure 5.5 – Evolution of the balloon radius in the circumferential direction over inflation time for the considered geometries and material models: (a) OE-LE; (b) OE-HE; (c) TE-LE; (d) TE-HE.

The ability to predict such behavior is paramount since it has been associated with endothelium denudation and, thus, restenosis development [6]. Regardless of the importance of such results, the balloon's geometry is not entirely realistic, given the neglect of the folded configuration. However, it is reasonable to infer that the system's final configuration was comparable to reality, although the transient behavior may show some differences due to the unfolding of the balloon membrane. Therefore, such simplification was judged acceptable.

The discrepancies in the enlarged profile of the stent for the four simulated models may be attributable to the balloon's distinct behavior. The evolution of the balloon's volume (t_b x perimeter x length) during the expansion process was calculated to assess these differences. The calculus showed no significant

variation when the hyperelastic model was applied. Such evidence is a consequence of material incompressibility, contrary to what is verified for the elastic model. In this case, the models experienced a reduction of their volume of 11.4% and 17.8% for the open- and taper-ended geometries, respectively. It is proposed that when pressure is applied to the inner surface of the balloon, part of the energy is used to promote a reduction of the thickness of its membrane and not only on radial expansion, remaining stored within the material.

It was anticipated that the balloon's thickness and sectional areas would fluctuate during inflation. Moreover, a more pronounced reduction of the membrane thickness was expected when the balloon established contact with the stent. Figure 5.6 shows the evolution of the transversal and longitudinal balloon areas during the simulation of the inflation process.

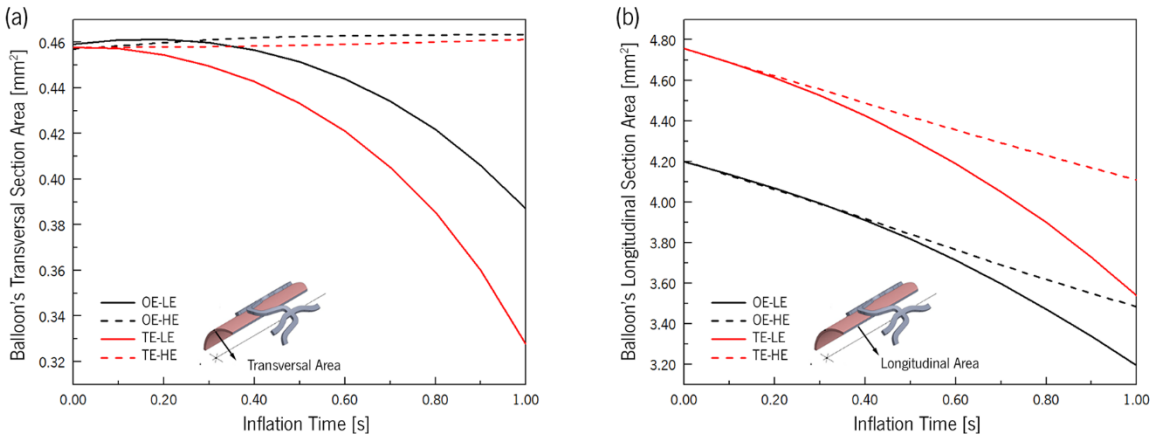

Figure 5.6 – Evolution of the (a) transversal area and (b) longitudinal area of the balloon during the inflation process.

During the inflation process, the transverse area of the hyperelastic balloons stayed rather constant, but that of the linear elastic model dropped (Figure 5.6 (a)).)). Once the linear elastic material is compressible, the thickness reduction is more pronounced than the increase of its perimeter, resulting in an overall decrease in volume.

Regardless of the material model used, a decrease in the balloon longitudinal section area was verified due to the thickness reduction and its fixed ends (Figure 5.6 (b)). In this sense, it is possible to conclude that the adopted material model directly influences the balloon deformation profile and hence the stent expansion process and final configuration.

B. VON MISES STRESS DISTRIBUTION

The stress distribution in the stent is presented in Figure 5.7. There were no significant discrepancies in the outcomes of the four evaluated models. For all cases studied, a stress concentration was located at

the curved crown segments of the stent cell, which act as hinges and thus underwent large plastic deformation during the expansion process, as presented in detail (1) and detail (2).

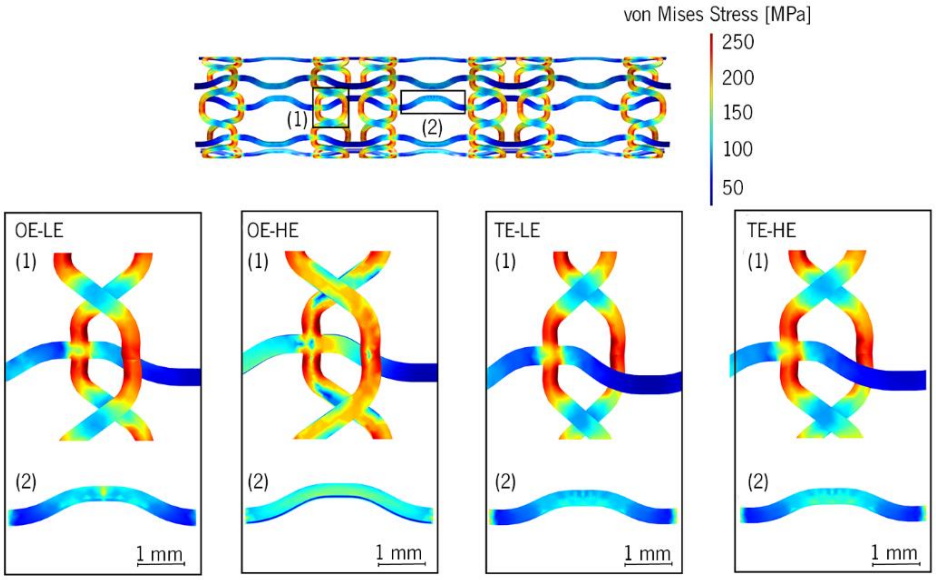

Figure 5.7 – von Mises stress distribution in the stent at the maximum expansion for the OE-LE model, where detail (1) and detail (2) represent the stress concentration within the curved struts of the stent for the four balloon models tested.

Figure 5.8 presents the evolution of the von Mises stress during the inflation process for the open- and taper-ended balloons. According to Figure 5.8 (b), (b), for the tapered balloon, the results of linear and hyperelastic models near overlapped, while in the open-ended balloon, there was a deviation of 25.8% in the first stage of expansion (Figure 5.8 (a Such behavior was associated with the faster increase of the stent radius of the OE-HE model at the beginning of the expansion compared to verified for the OE-LE model, as observed in Figure 5.3.

Table 5.3 presents the maximum and averaged von Mises stress values at the full expansion for all studied models. Considering the same balloon's geometry, it was possible to conclude that the maximum stress was lower when a hyperelastic model was used. The difference was about 2.7% higher for the taper-ended balloon and 2.0% for the open-ended balloon. On the other side, the open-ended balloon exhibited lower values than the taper-ended balloon when the linear elastic model was used, occurring the opposite for the hyperelastic model.

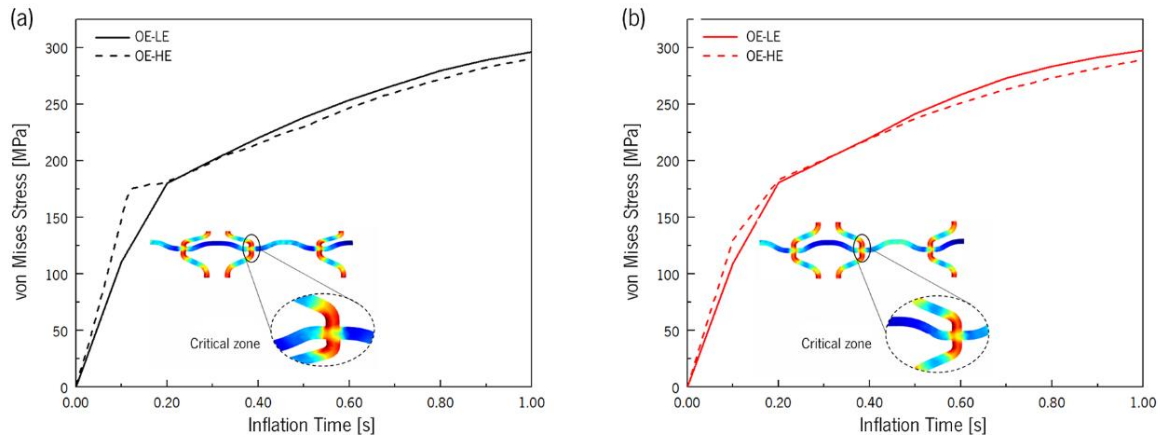

Figure 5.8 – Evolution of the von Mises stress during the inflation process (a) open-ended and (b) taper-ended balloons.

Table 5.3 – Maximum and averaged von Mises stress within the stent at the maximum expansion of OE-LE, OE-HE, TE-LE, and TE-HE balloons.

Balloon model	Maximum stress [MPa]	Average stress [MPa]
OE-LE	295	118
OE-HE	290	111
TE-LE	297	118
TE-HE	289	118

The results demonstrate that the ability of a stent to expand is insensitive to the balloon model when both the fully expanded diameter and von Mises stress are considered. Indeed, the maximum stress value occurred at the curved areas of the ring for all four models, underlying the conclusion that von Mises stress is not sensitive to balloon geometry or material model. The difference between the maximum value for the linear elastic and hyperelastic tapered balloon was close to zero. In the case of an open-ended balloon, the discrepancy found at the early stage of expansion may be due to the faster increase of the stent radius of the OE-HE model at the beginning compared to the OE-LE model, as observed in Figure 5.3. Such results agree with those reported by Schiavone *et al.* [132] and Chen *et al.* [133] and suggest that the four balloon models can be used interchangeably for stent stress analysis purposes.

5.2.3. Conclusions on the balloon modeling effect on stent deployment outcomes

This section presents the study of the influence of both balloon constitutive modeling and geometry on the outcomes of the numerical simulation of the stent deployment procedure. While stent expanded diameter and von Mises stress over the stent were found to be little sensitive to the balloon modeling strategy adopted, the choice of balloon geometry and material model has proven to influence balloon and stent expanding behavior. Indeed, the results suggest that balloon-type influences the stent expanded profile along its length and diameter due to different deformation behavior exhibited by the balloon. In

this regard, it was possible to conclude that the TE-HE balloon model was the one that showed the closest behavior to clinical and experimental results, namely concerning the development of balloon protrusions at stent cells. Such ability is of utmost importance since balloon-artery interaction has been pointed to as capable of promoting endothelium denudation and restenosis.

This work enhances understanding of the effect of balloon modeling on the simulated outcomes of stenting. The results presented here can be utilized in future research to optimize stent geometry and placement protocols to reduce balloon-induced arterial damage.

5.3. IMPACT OF THE STENT MATERIAL PROPERTIES ON THE DEPLOYMENT OUTCOMES

To ensure a suitable performance during and after the deployment procedure, the stent must meet a set of mechanical requirements, including high radial strength, low elastic radial and longitudinal recoil, and minimal dogboning and foreshortening [14,15]. Different approaches may be adopted to accomplish these characteristics once factors such as the deployment set used, which includes the expansion balloon, the stent design, and the applied materials, can significantly impact the outcomes of the process [13,16–18]. In this regard, it is virtually possible to resort to coatings, processing techniques, and functionally graded materials to tailor the stent properties as desirable and overcome the limitations due to the intrinsic mechanical properties of a given material.

The application of ultrasound treatment to AZ91D-1.0% Ca (wt.%) magnesium alloy melt has been proven to enhance the characteristics of the material concerning its yield and tensile strength, as well as elongation at break [19]. Such improvement may lead to a better performance of a stent built in this processed material in a way that makes it more suitable for that application.

To assess the effect of the material on stent deployment, FEA was conducted on two identical geometric stents built-in AZ91D-1% Ca (wt.%) from non- and ultrasound-treated ingots. For this purpose, the stress-strain curves from tensile tests of both materials were used.

5.3.1. METHODOLOGY FOLLOWED FOR STENT DEPLOYMENT MODELING

The assessment of the influence of the material characteristics resulting from the different processing techniques on the stenting outcomes was performed through the simulation of the stent deployment procedure, considering both the inflation and deflation stages of the process.

A non- and ultrasound-treated AZ91D-1.0% Ca (wt.%) alloy was used as the stent's material to study their properties' influence on the stent performance during the deployment procedure. Due to the manufacturing process, both materials were considered isotropic and elastoplastic. The different

processing conditions significantly affected stress-strain curves and elongation at break, yield, and tensile strength values. The mechanical properties used are presented in Chapter 3.

The plastic behavior of both materials was modeled using the von Mises yield criterion, while the nonlinear isotropic stress-strain hardening curve was modeled using a Voce-type law.

Considering the results of the study of the influence of balloon modeling on the outcomes of the deployment procedure, a taper-ended balloon modeled as a hyperelastic material was used. The adopted parameters are described in section 5.2 of this chapter.

A linear pressure was applied to the inner surface of the balloon, leading to its expansion in a process that mimics its real inflation during the stent deployment procedure. The expansion of the balloon imposed a radial deformation to the stent that also expanded. The pressure application ceased when the von Mises stress equaled the tensile strength; afterward, the balloon returned to its original diameter, allowing the stent to recoil slightly.

Considering the abovementioned symmetry of the stent and the balloon models, only one-tenth of the assembly balloon+stent was used in this numerical study, applying symmetry conditions to their lateral faces and central ends. The distal end of the balloon was fully constrained to represent its bond to the delivery catheter system.

The contact between the stent and the balloon was frictionless and modeled using an augmented Lagrange formulation.

5.3.2. Results and discussion

A. Expansion behavior of the stent

Figure 5.9 presents the demanded expansion pressure to be applied on the inner surface of the balloon as a function of the stent expanded radius for the non- and ultrasound-treated AZ91D-1.0% Ca (wt.%) alloy.

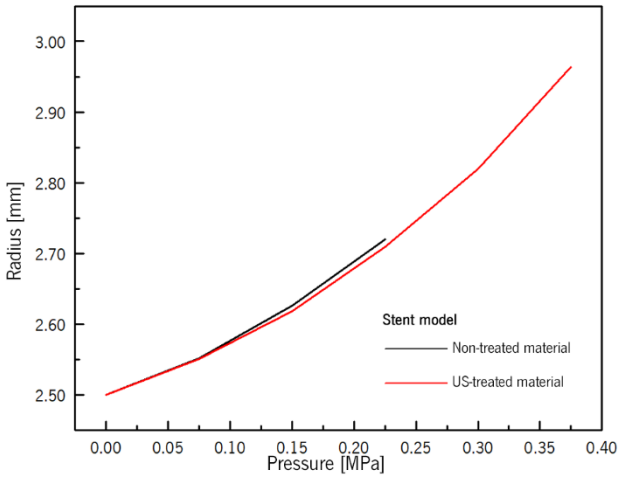

Figure 5.9 – Required expansion pressure as a function of the stent diameter.

The behavior of the stents built from the non- and ultrasound-treated materials was comparable mainly in the early stages of the expansion, during which the pressure-diameter curves overlapped. However, the stent manufactured using the ultrasound-treated alloy was revealed to achieve radial expansion of higher magnitude once the ultrasound treatment has been proven to enhance the tensile strength and elongation of the material, as previously concluded by Puga *et al.* [19].

Regarding the dogboning and foreshortening parameters, Figure 5.10 presents the results for the two considered materials

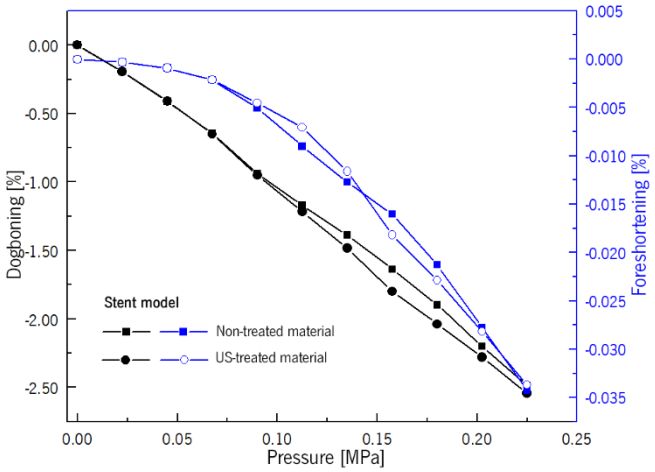

Figure 5.10 – Dogboning and foreshortening evolution during the expansion of the stent built-in non- and ultrasound-treated material.

For an applied pressure of about 0.23 MPa, which corresponds to approximately the same expanded diameter for both materials, the results suggest that dogboning and foreshortening were not sensitive to the material used.

Both materials presented approximately equal negative values of dogboning, which means that the expansion of the central region of the stent was greater than that of its ends, an effect also observed in a free stent expansion study carried out by Schiavone *et al.* [16]. In this regard, the authors claimed that negative values of dogboning were considered desirable once such behavior helps dilate the stenotic plaque, which is intended to be in direct contact with the middle section of the stent. The maximum value of dogboning was about -2.50%, suggesting that the stent expansion was nearly uniform, preventing artery injury during the procedure [13].

The foreshortening effect was also comparable for both materials. The negative values were associated with the longitudinal shrinkage of the stent as its diameter increased, which agrees with the results reported in the literature [13,14,16,20]. The foreshortening values obtained in the present study were very low, indicating that the length of the stent did not suffer significant changes during the deployment procedure. It is vital to keep this parameter as low as possible to ensure full coverage of the diseased part of the blood vessel and to prevent the friction between the stent and the blood vessel that may lead to its damage and consequent restenosis event [16,21].

The results presented for both parameters, dogboning and foreshortening, suggested that other factors may impact these metrics more significantly than the material used in the stent manufacturing. Indeed, some optimization studies focused on reducing these phenomena used design parameters as control variables to achieve it, which stresses the influence of the stent geometry on the device's performance regarding these phenomena [18,22,23].

B. VON MISES STRESS

The evolution of the average and maximum von Mises stress over the stent is presented in Figure 5.11. At the approximately same expanded diameter, corresponding to an applied pressure of 0.23 MPa, the stent made of ultrasound-treated alloy tended to exhibit higher stress levels than those of the non-treated one, in line with the difference observed between the materials' behavior and their properties.

For both materials, it is possible to notice that the average stress presented a much lower value than the maximum stress, which may have its origin in local stress concentrations.

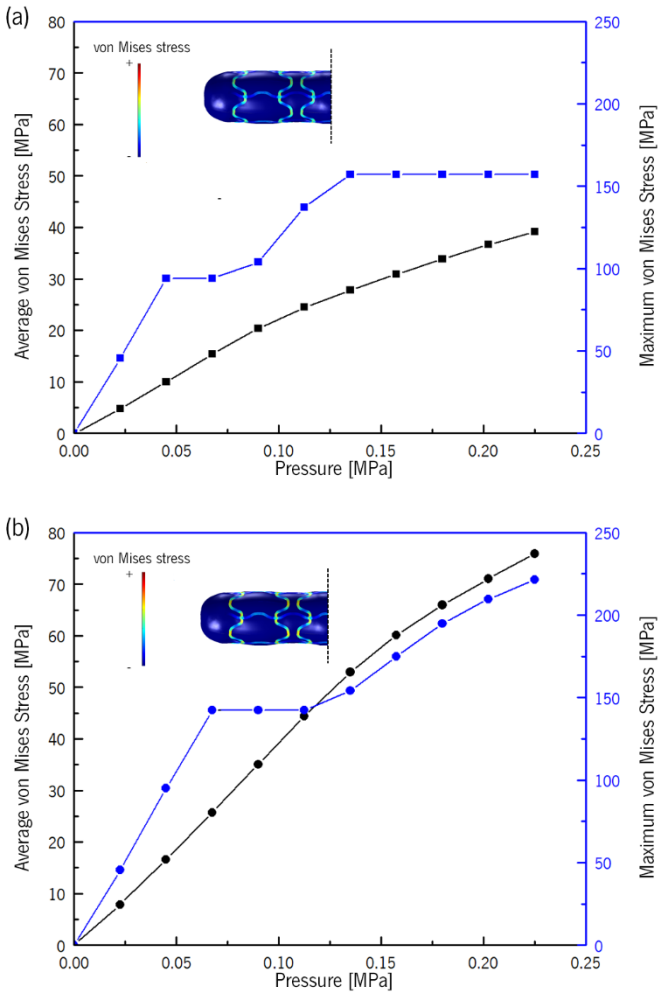

Figure 5.11 – Evolution of von Mises stress over the system during the expansion of the stent built-in (a) non- and (b) ultrasound-treated material.

By analysing Figure 5.12, , where the von Mises stress is plotted for the stent built-in ultrasound-treated AZ91D-1.0% Ca (wt.%), it is feasible to deduce that the stress distribution was fairly uniform, except for the corners of the struts, where stress concentration occurred due to the shape of the struts.

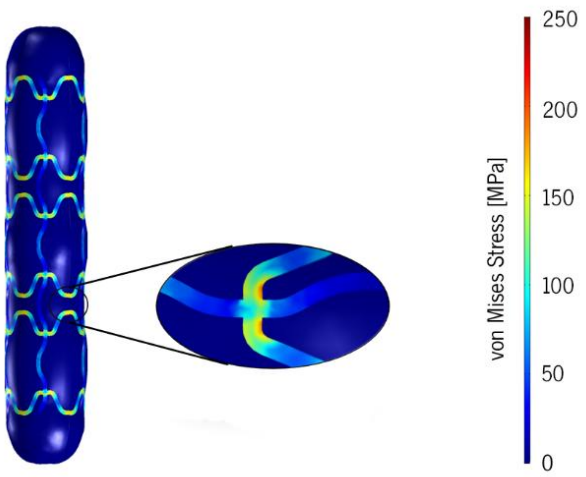

Figure 5.12 – von Mises stress distribution over the fully-expanded stent built-in ultrasound-treated material.

The location of the maximum stress for the stent built-in non-treated material was consistent with these results. Previous research [16,20] has determined that corner and link elements are the most likely to experience the largest deformations during expansion and, thus, to display the highest stress values.

The stent recoil after the balloon deflation is also a parameter that may be used to assess the stent's functional performance. As the balloon deflates, the pressure exerted in the stent decreases, which may lead to a slight recovery of the elastic part of the stent's deformation. It is critical for the stent's functional performance that it presents a sufficiently high plastic ductility combined with low longitudinal and radial elastic recoil [14,18].

Figure 5.13 presents the recoil evaluation of the stents made from non- and ultrasound-treated alloys.

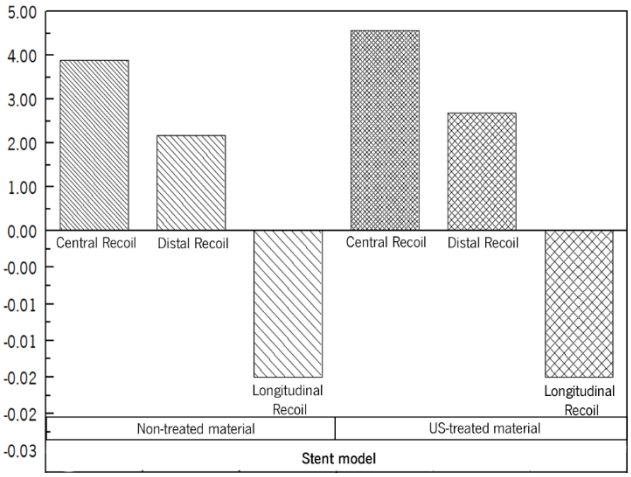

Figure 5.13 – Recoil evaluation for non- and Ultrasound-treated stents.

The results show that the effect ultrasound treatment of the AZ91D-1.0% Ca promoted on the material's tensile properties significantly impacted the stent recoil effect, leading to its increase, except for the

longitudinal recoil. As observed for the foreshortening, it is suggested that the length variation of the stent may be more sensitive to the geometry of the device than to the material applied, as previously referred to by Khosravi *et al.* [21]. The distal recoil, measured at the ends of the stent, was about 43.8% and 41.4% inferior to the central recoil, evaluated at its plane of symmetry for the stents made of non- and ultrasound-treated alloy, respectively. This situation agrees with the results observed in dogboning, which showed that the ends of the stent expanded less than its central section, suffering a smaller elastic recoil. Ultrasound-treated material led to the stent displaying a distal and central recoil of about 22.9% and 17.8% higher than the stent built-in non-treated one.

5.3.3. Conclusions on the stent's material properties impact on deployment outcomes

This study investigates the effect of the stent's material properties on its expansion behavior, considering metrics such as expanding pressure required, dogboning, foreshortening, and *von Mises* stress. It is suggested that the stent made of ultrasound-treated alloy achieved greater radial expansions than that fabricated from the non-treated one, given its superior material properties represented by the stress-strain curves used as input in the numerical model. Dogboning and foreshortening parameters showed similar results for both materials studied, indicating that they are more sensitive to other factors than the material used. The geometric parameters may be an example of such. The average and maximum stress values that the stent underwent at full expansion were significantly different for both cases presented. This situation suggests the existence of local stress concentrations, which was confirmed by the stress distribution plot. It was shown that the corner elements are subjected to higher stresses than the remaining structure.

Furthermore, it is suggested that using the ultrasound-treated material leads to the stent developing higher stress values than the non-treated one. The stent central and distal elastic recoil was influenced by the material used, whereas the longitudinal recoil presented the same value for both conditions. Higher values of radial recoil were found for the stent built-in ultrasound-treated material.

The results obtained highlight the potential of the application of ultrasound treatment to enhance the stent deployment procedure outcomes by meaningfully improving the material's mechanical properties. In fact, greater radial expansion could be achieved without compromising the integrity of the stent thanks to the higher mechanical properties, namely in terms of tensile strength. Such a feature can help improve the device's versatility, given that it can assume a wider range of diameters.

5.4. OPTIMIZATION OF A NEW STENT DESIGNED FOR MANUFACTURING THROUGH ULTRASONIC-MICROCASTING

Achieving better outcomes from deploying a stent in a stenosed artery may depend on several factors in which the applied material properties and the stent geometry are included.

Manufacturing a stent using the microcasting technique opens a wide set of new geometric possibilities [22]. The variation in the stent's cross-section thickness is an example. Indeed, the thickness of the stent struts is a key element of stent design, given its influence on the device deliverability and restenosis rate, as demonstrated in the ISAR-STEREO clinical trial [24,25]. The results showed that thinner struts lead to lower rates of restenosis when compared to thicker ones. However, it was also associated with a larger recoil following deployment, resulting in lower luminal gain and, thus, inferior results in rectifying vascular obstruction.

The dogboning and foreshortening phenomena have also been referred to as restenosis triggers due to the injury inflicted on blood vessels [14]. These effects may be minimized by controlling the stent design by resorting to shape optimization. An example is increasing the thickness of the regions prone to expand more. This way, the stent shape may assume a more uniform expanded configuration and present a lower dogboning value than the original design.

This section presents and discusses the results of shape optimization of a stent manufactured from ultrasound-treated AZ91D-1% Ca alloy to improve its functional performance, considering the unique and novel advantage of cross-section thickness variation granted by the microcasting process.

5.4.1. METHODOLOGY FOR STENT DESIGN OPTIMIZATION

In order to facilitate the iterative design process, an NG stent is created in parametric form for shape optimization. The architecture of the stent has open-cell and link elements: the former gives structural support to the artery, while the latter affords the device flexibility

To optimize the stent design, the hypothesis of non-uniform cross-section thickness of the stent struts is considered. Hence, the stent geometry is segmented so the cell and the link elements can present different thickness (t) values, as depicted in Figure 5.14.

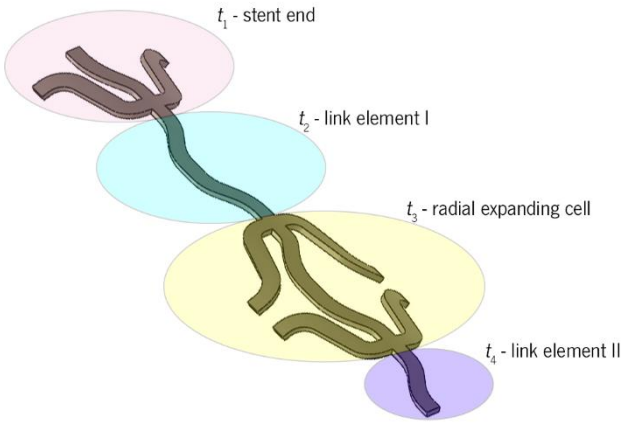

Figure 5.14 – Identification of the stent segments used as design variables.

A reference design with a uniform cross-section of 0.20 mm was used as the reference design.

A linear increasing pressure p is applied at the stent's inner surface to promote its expansion, mimicking the balloon inflation within the stent, and symmetry constraints are applied to lateral faces and the central end of the stent unit. Tetrahedral elements were used to mesh the stent model, ensuring a minimum value of the Average Quality Element parameter equal to 0.75 over 1.

The stationary study of the stent deployment was carried out using MUMPS solver, while the Constrained Optimization by Linear Approximations (COBYLA) algorithm was defined as the optimization method. COBYLA minimizes an objective function F(X) subject to M inequality constraints of the form g(X) >= 0 on X, where X is a vector of variables that has N components. This algorithm uses linear approximations to both objective and constraint functions by using linear interpolation at N+1 points of the variables' space. When calculating new variable values, each constraint is considered separately instead of combined into a single penalty function.

In this study, the objective function is defined as the sum of the maximum values of dogboning and foreshortening. Both metrics are of great importance concerning the stent performance once they are pointed to as possible triggers of restenosis events due to the injury inflicted on the blood vessel wall [13,16,26]. The constraints are design-related and imposed by the manufacturing *process, e.g., maximum* thickness ratio between two successive sections and minimum thickness allowed. The optimization problem is mathematically translated as follows:

$$\text{Objects: } \begin{cases} \min \textit{Dogboning} \\ \min \textit{Foreshortening} \end{cases}$$

$$\text{St.} \begin{cases} \frac{t_1}{t_2}, \frac{t_2}{t_3}, \frac{t_3}{t_4} \leq 0.3 \\ t_n \geq 0.20 (n = 1,2,3,4) \\ \sigma_{stent} \leq \sigma_{ult} \end{cases} \tag{5.10}$$

Where the thicknesses (t, i=1,2,3,4) are selected as design variables.

5.4.2. Results and Discussion

Figure 5.15. depicts the evolution of the stent's objective function and design control variables. The results suggest that the thickness of the link between the cell and the end ($t2$) does not significantly impact the objective function, which is demonstrated by its near-constant value across all the iterations. Regarding the link between cells ($t4$), it was found that a higher value was favorable to the minimization of the objective function since its value remained approximately constant from the fourth iteration on. A lower value of the thickness of the stent cell and end appeared to support the reduction of the objective function value.

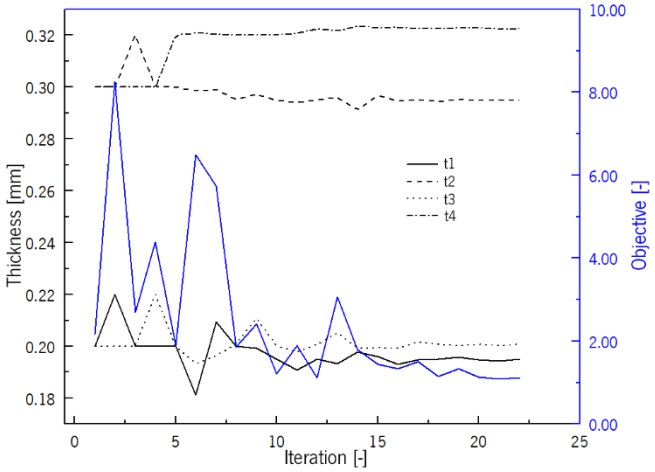

Figure 5.15 – Iterative process of stent design optimization: evolution of the design variables and objective function.

The values of the design control variables (thickness of the different stent sections) for the reference and optimized designs are presented in Table 5.4.

Table 5.4 – Thickness values of the different stent sections for reference and optimized designs.

	t_1 [mm]	t_2 [mm]	t_3 [mm]	t_4 [mm]
Reference design	0.200			
Optimized design	0.195	0.295	0.200	0.320

Figure 5.16 shows the stent radius as a function of the applied expanding pressure for both reference and optimized geometries. Comparing the two designs' performance, it is possible to observe that the optimized geometry required higher pressure than the reference one to achieve the same expanded radius (0.62 MPa vs. 0.38 MPa). It can be suggested that the higher value of t2 and t4 contributed to such an increase since thicker struts offer high resistance to deform. Despite high values of expanding pressure may be associated with higher rates of adverse events like restenosis, the optimized design demanded pressure was still within the desirable range [6].

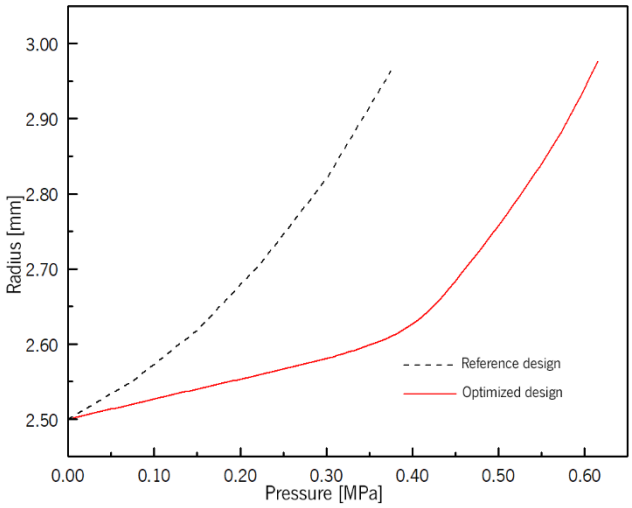

Figure 5.16 – Required expansion pressure as a function of the stent radius for both reference and optimized geometry.

Regarding the dogboning metric, the optimized geometry substantially improved over the reference one (see Figure 5.17). Indeed, the initial design led to some regions being likely to expand more than others, resulting in a non-uniform radial expansion of the stent. By modifying the thickness of each segment, it is possible to tailor their resistance to expansion, i.e., regions prone to expand more due to their configuration may see that effect counteracted by higher thickness. In this sense, the optimization method resulted mostly in (i) an increase in the thickness of the two link elements which used to exhibit a higher radius - t_2 and t_4 - and (ii) a reduction of the thickness of the stent end to ease its expansion – t_1. The optimized geometry allowed a maximum dogboning of about 1.0%, roughly 80.0% less than the initial design.

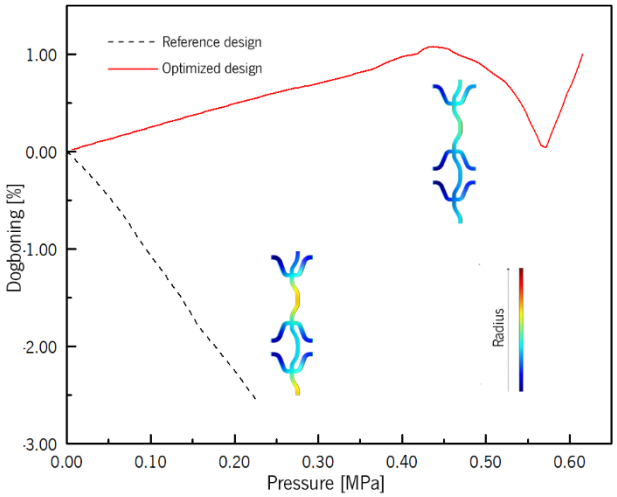

Figure 5.17 – Dogboning evolution during stent expansion for both reference and optimized geometry.

Figure 5.18 shows the evolution of the foreshortening in relation to the expanding pressure. Even though the foreshortening value of the reference geometry was already low (approximately 0.06%), the optimization process reduced this value to about -0.04%, meaning that the stent length varied about 0.01 mm, which can be neglected. However, it could be noticed that, differently from what was observed for the reference geometry, the stent length decreased. This shift in the stent behavior is promoted by the link elements being thicker in the optimized design, resisting better deformation, and, thus, do not fully compensate for the shrinkage. On the other hand, this reduction meant a difference of nearly 40.0% between the results, highlighting once again the significant influence and potential that the stent design, and in this case, the thickness of its struts, has on the device performance.

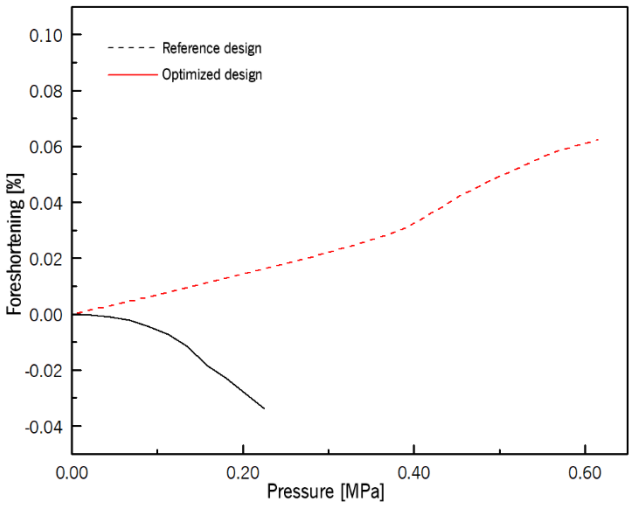

Figure 5.18 – Evolution of foreshortening during the stent expansion for both reference and optimized geometry.

5.4.3. CONCLUSIONS ON THE POTENTIAL OF STENT CROSS-SECTION THICKNESS VARIATION

This study's findings shed light on the unique potential that casting procedures may bring to the field of stent design, specifically the possibility of creating devices with variable cross-section thickness.

In fact, the cross-sectional thickness of the stent has been shown to significantly impact all of the investigated parameters: stent expanding ability, dogboning, and foreshortening. The optimized geometry was found to demand higher expansion pressure than the reference geometry; however, the required value remained within the acceptable range. Furthermore, the optimized design exhibited lower values of dogboning and foreshortening, achieving a reduction of about 80.0% and 40.0%, respectively, compared to the reference design. In this way, a more uniform stent expanded configuration could be achieved, directly associated with better treatment outcomes, as it reduces the likelihood of artery damage during the deployment procedure.

5.5. EFFECT OF MATERIAL DEGRADATION ON THE STENT MECHANICAL STRENGTH LOSS

The poor corrosion resistance of magnesium and its alloys is one of the major bottlenecks for their application in biomedical device manufacturing. In recent years, several researchers have concentrated their efforts on developing strategies that can slow the corrosion rate of these materials when exposed to body fluids. Indeed, in addition to the increased risk of bacterial infections due to hydrogen release, a fast loss in mechanical strength is observed, compromising the structural function of the device. In particular, the loss of mechanical integrity may lead to stent acute recoil and fracture and, hence, stent thrombosis.

In this way, due to the rapid and non-uniform degradation of the material, magnesium-based stents require high thickness to ensure radial support for a longer period. However, thicker struts bring serious problems, such as slower endothelialization, worse biocompatibility, and a considerably increased risk of late restenosis [27,28]. In fact, the Absorb BVS withdrawal from the market in 2017 by the Food and Drug Administration was driven by the high thickness (157 μm) and malposition of its struts.

Using FEA to optimize the stent's design may be one way to lower the strut's thickness while assuring adequate performance for crucial metrics such as mechanical support capacity. Several optimization-based strategies have already been documented in the literature. Gharleghi *et al.* [29] developed a multiobjective optimization based on hemodynamic indices commonly used to asses stents' clinical risk and mechanical performance. The authors considered seven design variables, including the strut cross-section and the connector shape, and set the percentage of vessel area exposed to harmfully high Wall Shear Stress (WSS) and the radial stiffness of the stent as the objective functions.

A different methodology was adopted by Chen *et al.* [30], who performed a shape optimization of a biodegradable magnesium stent to achieve a more uniform deformation during the crimping and expansion processes. Through design optimization, the mechanical performance of the stent was enhanced, and lower values of dogboning and foreshortening were attained while the radial strength was increased. Nonetheless, the struts were still too thick, stressing that enhancing the radial strength and reducing the residual stress is challenging for biodegradable devices such as magnesium-based ones [31]. Furthermore, the investigation of the effect of degradation on the mechanical performance of stents over time is still lacking in the literature.

This section presents a study of the impact of mechanical properties deterioration on the stent's radial strength through FEA resorting to tensile test results of AZ91D-1.0% Ca (wt.%) wires immersed in an EBSS flow from 48 h to 7 days (168 h). Additionally, a shape optimization study was carried out to reduce the stent strut thickness to make it suitable for clinical practice without compromising the integrity and performance of the device, addressed through residual stress and equivalent plastic strain minimization.

5.5.1. Methodology for simulation of stent radial strength evolution with the material degradation

Radial strength is a metric commonly used to assess the stent performance that is highly dependent on the material's mechanical properties. The degradation of the magnesium alloy under physiological conditions primarily results in a loss of mechanical properties and, consequently, a reduction in the radial support capacity of the stent.

The NG stent model was selected as the reference design in this study. A two-step model was developed, consisting of (i) the stent radial expansion and recoil followed by (ii) the simulation of the radial pressure exerted by the artery on the stent. In the first stage, the stent was subjected to a radial displacement that increased its internal radius from 2.50 mm to 3.15 mm, following which it was allowed to recoil. As the expansion behavior of the stent was not the focus of the present investigation, it was determined that the balloon's existence could be omitted, hence decreasing the computational cost of the simulation. In the second stage, an increasing force was linearly applied inwards until the von Mises stress reached the tensile strength of the material at each degradation time point. This way, the stent's radial strength evolution with the immersion time could be determined.

The stress-strain curves (Figure 5.19) from the tensile testing of the non- and ultrasound-treated AZ91D-1.0% Ca wires immersed in EBSS for 48, 72, and 168 h were used as input data to the numerical model

so the mechanical properties degradation influence on the radial strength of the stent could be evaluated. Stress-strain curves of the non-degraded materials were used to simulate the stent expansion.

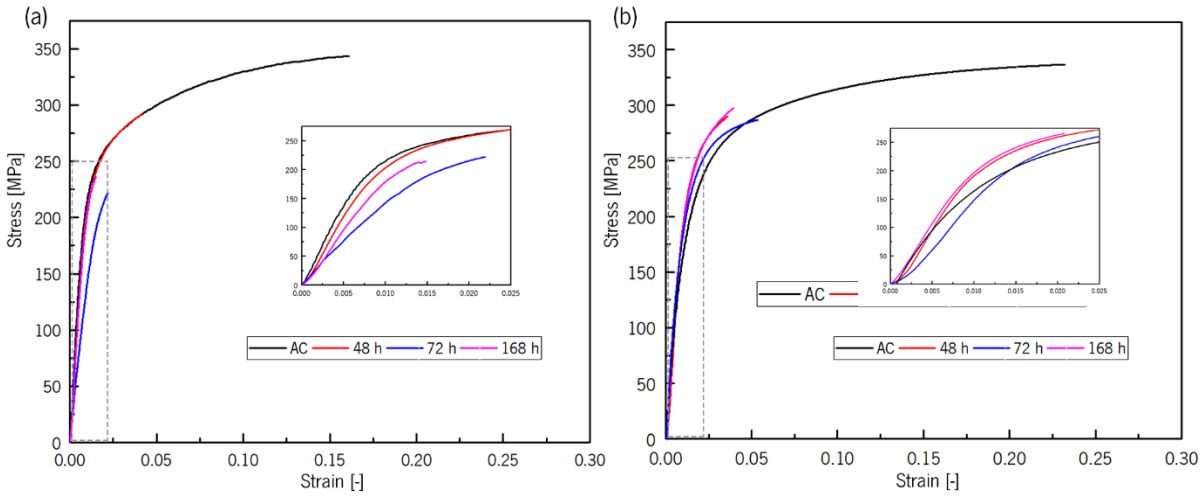

Figure 5.19 – Stress-strain curves from uniaxial tensile testing of (a) non- and (b) Ultrasound-treated AZ91D-1% after immersion in EBSS.

The stress-strain curve corresponding to 168 h of immersion time was used in the optimization study, so the design could be optimized considering the most demanding scenario studied. In this case, the application of a radial force in the stent's outer surface in the simulation's second stage was replaced by a radial pressure equal to 0.20 MPa to mimic the artery recoil effect [32]. The multiobjective optimization process was based on COBYLA numerical method. The optimization routine aimed to minimize the objective function, composed of three individual objectives, namely (i) strut thickness, (ii) average residual stress after stent recoiling, and (iii) average equivalent plastic strain at full stent expansion.

The width of horizontal and vertical struts (see Figure 5.20) was designated as design control variables, while a maximum von Mises stress over the tensile strength of 5.0% of the stent volume was set as a constraint.

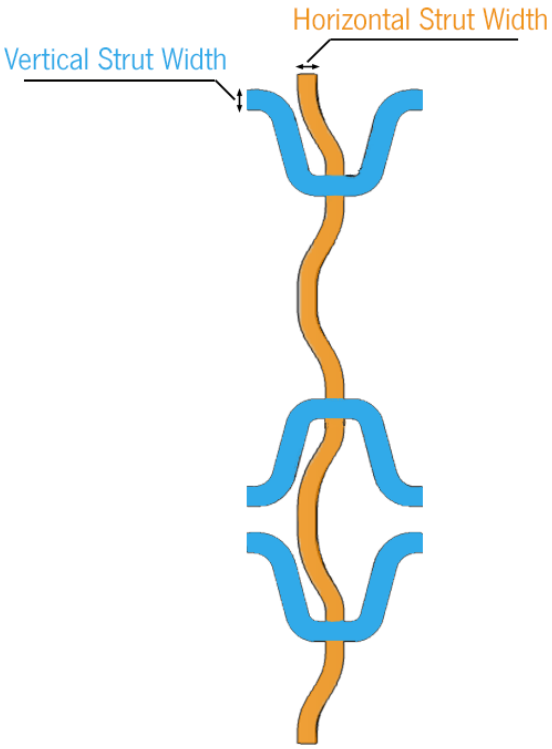

Figure 5.20 – Schematic representation of the design control variables used in the optimization process.

The process of optimization could be described as follows:

$$\text{Objective function: } \begin{cases} \min \ \textit{strut thickness} \\ \min \ \textit{residual stress} \\ \min \ \textit{equivalent plastic strain} \end{cases}$$

$$\text{St. } \left\{ \frac{V_{stent}(\sigma_{VM} \geq \sigma_{ult})}{V_{stent}} \leq 0.05 \right. \tag{5.11}$$

5.5.2. Results and Discussion

A. Expansion behavior of the stent

The evolution of the stent radius as a function of the expanding pressure applied to its inner surface is presented in Figure 5.21 (a).

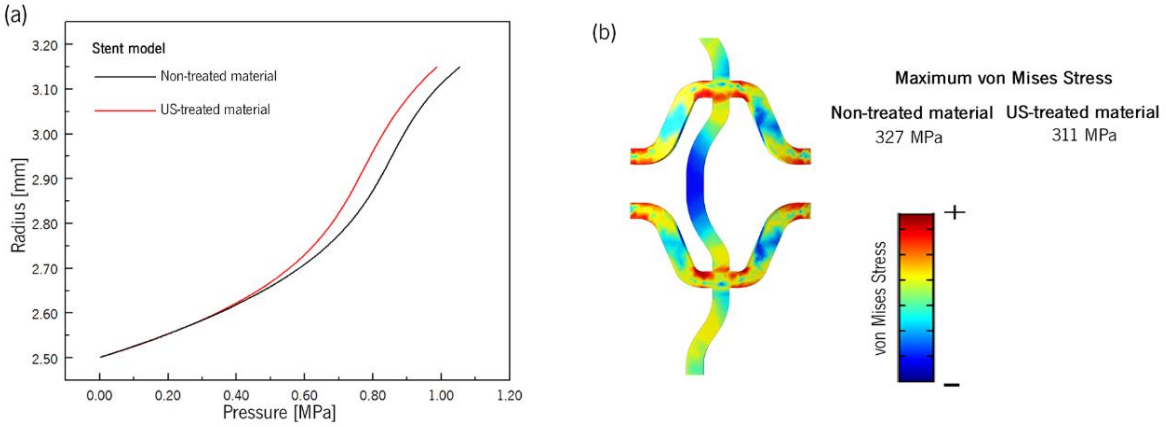

Figure 5.21 – Evolution of the stent radius as a function of the expanding pressure applied in its inner surface and (b) von Mises distribution over the stent unit.

It is observable that less pressure was necessary to expand the stent made from ultrasound-treated material compared to the one made from non-treated alloy. Such a difference is promoted by the higher ductility exhibited by the former, which grants higher deformation under lower pressure. These findings are consistent with the maximum von Mises stress over the stent unit (Figure 5.21 (b)), which was shown to be inferior for the ultrasound-treated material case (311 vs. 327 MPa). Nonetheless, the distribution of the von Mises stress was comparable for both conditions, with higher values found on the curved regions of the stent's struts due to the more significant deformation.

Figure 5.22. depicts the progression of the radial strength of stents made from non- and ultrasound-treated AZ91D-1.0% Ca wires.

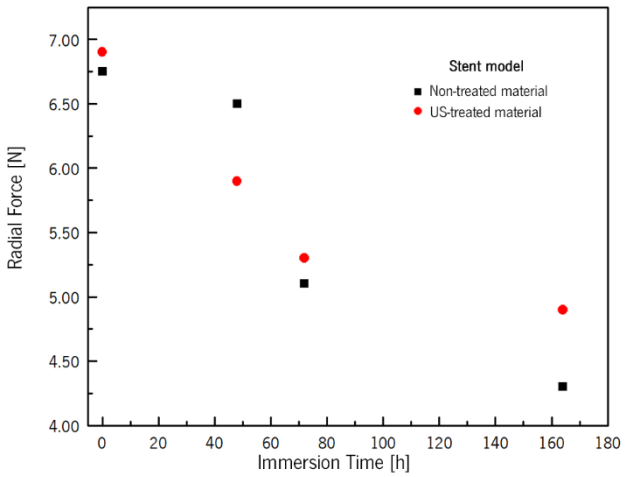

Figure 5.22 – Evolution of the radial strength of the stents built from non- and ultrasound-treated wires over immersion time.

The results showed that, at the initial stages of the degradation tests, the radial force supported by the stent built from non-treated material was higher than that of the ultrasound-treated one. This pattern

persisted for immersion for up to 48 hours, after which an inversion could be noticed. After immersion for 72 h, the radial strength of the stents made of ultrasound-treated material was about 4.0% higher than that of the stents built-in non-treated ones, a difference that increased to 14.0% after 168 h. These observations are consistent with the corrosion results reported in Chapter 4, as the corrosion rate of the ultrasound-treated material is significantly higher in the first hours of immersion, translating into an accelerated loss of mechanical properties, after which it significantly drops. In fact, for longer immersion times, the mechanical strength decreased at a remarkably slower pace for the ultrasound-treated material compared to the non-treated one, which is suggested to result from the different degradation behavior. Notwithstanding, it can be inferred that radial strength loss happened at a very high rate for both circumstances, indicating that additional modifications may be necessary to preserve the stent's integrity during the treatment term, typically set at six months.

B. OPTIMIZATION PROCESS RESULTS

Design optimization is a valuable tool that helps find the best structural architecture considering pre-established objectives. Optimizing the stent design can remarkably enhance the treatment outcomes, which is why there is an increasing number of scientific publications under this scope.

Nonetheless, this complex problem is characterized by many variables, ranging from geometrical parameters and material properties to physiological conditions [33]. In this regard, developing a comprehensive numerical model capable of addressing all the related issues is challenging, so most research on this topic usually focuses on a limited number of factors.

It has been found that the strut thickness of a stent has a significant impact on the outcomes of stenting treatments. It is usually associated with inflammation at the location of the lesion, and in extreme situations, it inhibits the struts of the stent from being covered with neo-intima [34,35]. Several studies indicate that thinner struts can assist reduce the restenosis rate, and a meta-regression analysis [36] indicated a substantial positive link with late lumen loss.

When developing a stent, residual stress is also an important metric that must be considered. High-stress values after the stent expansion can lead to stress corrosion, micro-cracks formation and fractures, seriously compromising the device's integrity and, thereby, patient safety [37]. On the other hand, the equivalent plastic strain minimization is a critical parameter in reducing high-stress areas, as stated by Li *et al.* [39], working to improve the stent's mechanical resistance by indirectly reducing the likelihood of stress corrosion occurrence.

Figure 5.23 also depicts the evolution of the objective function and design factors and Table 5.5 and Table 5.6, present, respectively, the matrix of the stent design iteration of the optimization process for the reduction of (i) strut thickness, (ii) average residual stress after stent recoiling, and (iii) average equivalent plastic strain at the fully expanded configuration of the stents made of non- and ultrasound-treated AZ91D-1.0% Ca.

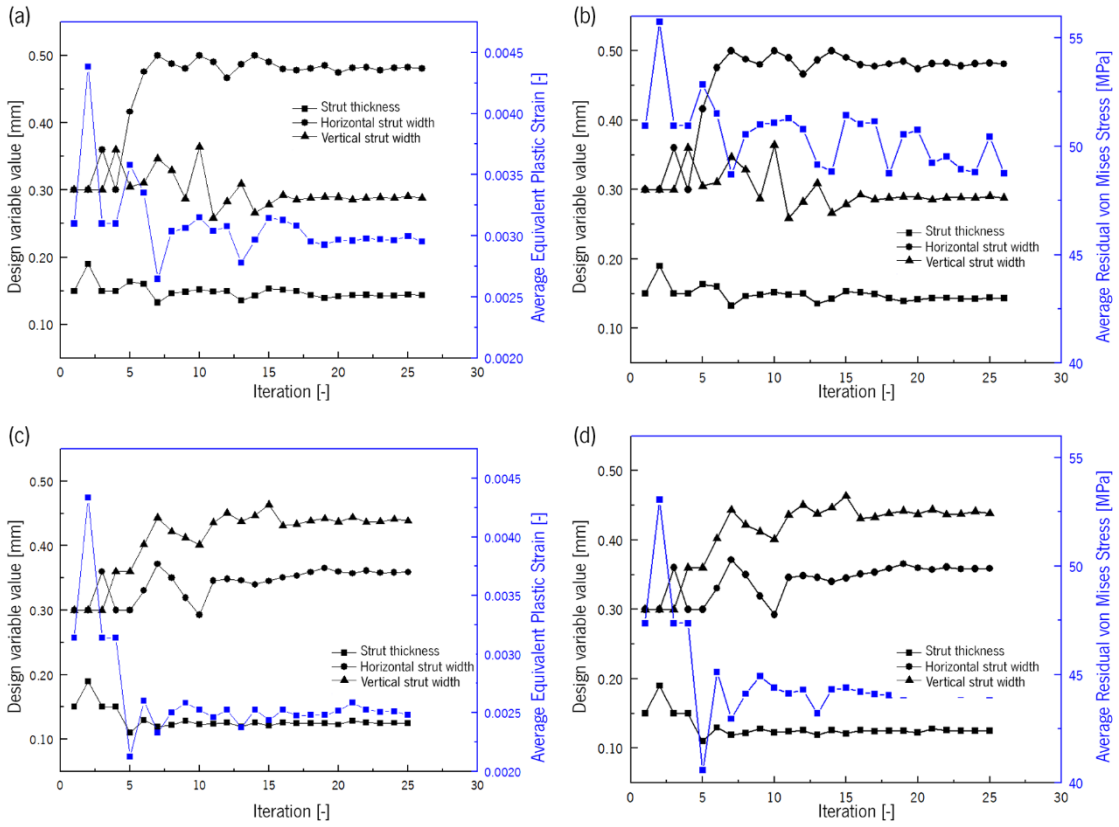

Figure 5.23 – Evolution of (a,c) plastic strain and (b,d) residual stress as function of the design control variables for (a,b) non- and (c,d) Ultrasound-treated stents.

Table 5.5 – Optimization iterative process of the stent built-in non-treated AZ91D-1%Ca.

Iteration	Horizontal Strut Width [mm]	Vertical Strut Width [mm]	Strut Thickness [mm]	Average Equivalent Plastic Strain [-]	Average Residual Stress [MPa]	Objective [-]
Reference	0.300	0.300	0.200	0.0047	56.02	-
1*	0.300	0.300	0.150	0.0031	50.95	81.9626
2	0.300	0.300	0.190	0.0044	55.74	99.5846
3*	0.360	0.300	0.150	0.0031	50.95	81.9626
4*	0.300	0.360	0.150	0.0031	50.95	81.9626
5	0.416	0.305	0.163	0.0036	52.85	88.6451
6**	0.476	0.311	0.160	0.0034	51.50	85.0375
7*	0.500	0.347	0.133	0.0026	48.70	NaN
8*	0.488	0.329	0.146	0.0030	50.55	80.9224
9*	0.480	0.287	0.148	0.0031	50.99	81.6527
10*	0.500	0.364	0.152	0.0031	51.09	82.6008
11*	0.490	0.259	0.149	0.0030	51.29	81.6939
12*	0.466	0.283	0.150	0.0031	50.79	81.6003
13*	0.487	0.309	0.135	0.0028	49.16	76.9642
14*	0.500	0.266	0.143	0.0030	48.84	78.5065
15*	0.490	0.279	0.153	0.0031	51.42	82.8892
16*	0.480	0.293	0.152	0.0031	51.03	82.3237
17*	0.478	0.285	0.149	0.0031	51.14	81.9962
18*	0.481	0.288	0.143	0.0030	48.75	78.3016
19*	0.485	0.290	0.139	0.0029	50.54	79.8190
20*	0.474	0.289	0.142	0.0030	50.76	80.4449
21*	0.481	0.285	0.144	0.0030	49.22	78.8224
22*	0.482	0.288	0.144	0.0030	49.52	79.3130
23*	0.478	0.289	0.143	0.0030	48.94	78.6634
24*	0.481	0.288	0.142	0.0030	48.80	78.4427
25*	0.482	0.290	0.144	0.0030	50.44	80.4262
26*	0.481	0.288	0.143	0.0030	48.75	78.3016

* The design did not obey to the problem constraint

** Optimal solution

Table 5.6 – Optimization iterative process of the stent built-in Ultrasound-treated AZ91D-1%Ca.

Iteration	Horizontal Strut Width [mm]	Vertical Strut Width [mm]	Strut Thickness [mm]	Average Equivalent Plastic Strain [-]	Average Residual Stress [MPa]	Objective [-]
Reference	0.300	0.300	0.200	0.0046	52.30	-
1	0.300	0.300	0.150	0.0031	47.36	78.7623
2	0.300	0.300	0.190	0.0043	53.06	96.4117
3	0.360	0.300	0.150	0.0031	47.36	78.7623
4	0.300	0.360	0.150	0.0031	47.36	78.7623
5*	0.300	0.360	0.110	0.0021	40.59	61.8671
6	0.330	0.402	0.130	0.0026	45.11	71.1572
7*	0.371	0.443	0.119	0.0023	42.96	66.2896
8*	0.350	0.422	0.122	0.0025	44.10	69.1510
9	0.319	0.412	0.128	0.0026	44.92	70.7781
10*	0.293	0.401	0.123	0.0025	44.39	69.6469
11*	0.346	0.436	0.124	0.0025	44.11	68.7373
12	0.349	0.451	0.126	0.0025	44.29	69.5657
13*	0.346	0.438	0.119	0.0024	43.21	66.9639
14	0.340	0.447	0.126	0.0025	44.30	69.5739
15*	0.345	0.463	0.121	0.0024	44.38	68.7686
16	0.351	0.431	0.126	0.0025	44.20	69.4615
17*	0.354	0.433	0.125	0.0025	44.10	68.8621
18	0.359	0.438	0.125	0.0025	44.03	68.8520
19*	0.365	0.442	0.125	0.0025	44.03	68.8480
20*	0.360	0.437	0.123	0.0025	44.36	69.5477
21	0.357	0.444	0.128	0.0026	44.93	70.8193
22	0.361	0.437	0.126	0.0025	44.29	69.5574
23*	0.358	0.437	0.125	0.0025	44.05	69.1436
24*	0.358	0.441	0.125	0.0025	44.15	69.2815
25**	0.359	0.438	0.125	0.0025	44.03	68.8520

* The design did not obey the problem constraint

** Optimal solution

The results presented indicate that the influence of the design control variables in the plastic strain and residual stress was similar for stents modeled using material data from non- and ultrasound-treated alloy. However, the enhanced mechanical properties exhibited by the ultrasound-treated material enabled the reduction of the strut thickness of the stent without compromising the individual objectives. Compared to the initial geometry, the strut thickness of stents modeled using non- and ultrasound-treated mechanical parameters was reduced by approximately 20.0% and 37.5%, resulting in strut thicknesses of 0.160 and 0.125 mm, respectively. Furthermore, it could be observed that the reduction of the strut thickness was compensated by the increase in the width of the horizontal and vertical struts, granting the minimization of the average residual stress and equivalent plastic strain without violating the constraint condition. The reduction of the strut thickness without loss of radial strength constitutes a significant advance in the field of biodegradable stents design. Indeed, most degradable devices resort to thick struts to ensure sufficient

radial support to the blood vessel during the remodeling process. However, as aforementioned, these high-thickness struts are frequently associated with an increased risk of late thrombotic events and impaired endothelialization [38].compares the performance of the optimized and reference stent designs numerically simulated considering non- and ultrasound-treated material.

Table 5.7 compares the performance of the optimized and reference stent designs numerically simulated considering non- and ultrasound-treated material.

Table 5.7 – Summary of the main results concerning the reference and optimized stents made from non- and ultrasound-treated material.

Material	**Thickness**		**Average Residual Stress [MPa]**		**Maximum Residual Stress [MPa]**		**Average Equivalent Plastic Strain [-]**		**Maximum Plastic Strain [-]**	
Non-treated	**Ref.**	**Opt.**	**Ref.**	**Opt.**	**Ref.**	**Opt.**	**Ref.**	**Opt.**	**Ref.**	**Opt.**
	0.200	0.160	56	51	339	335	0.0048	0.0031	0.1357	0.1050
Ultrasound-treated	**Ref.**	**Opt.**	**Ref.**	**Opt.**	**Ref.**	**Opt.**	**Ref.**	**Opt.**	**Ref.**	**Opt.**
	0.200	0.125	54	43	314	295	0.0049	0.0028	0.1248	0.0551

The optimized stent modeled with mechanical parameters acquired from non- and ultrasound-treated material achieved an average residual stress reduction of 8.1% and 15.5%, respectively, compared to the reference geometry. The drop in average equivalent plastic strain was more significant, decreasing by 28.4% and 46.0% for stents modeled using the mechanical parameters obtained from non- and ultrasound-treated material, respectively. Furthermore, the stent volume fraction subjected to high levels of von Mises residual stress (>100 MPa) was also reduced for both material conditions, despite the difference being negligible for the stent modeled with mechanical properties of non-treated material (15.4% vs. 14.9%). On the contrary, the stent modeled with mechanical properties of ultrasound-treated material exhibited a reduction of about 45.1%, from about 14.2% to 7.8%.

The distribution of the equivalent plastic strain at the fully expanded stent modeled with mechanical properties of non- and ultrasound-treated material is presented in Figure 5.24.

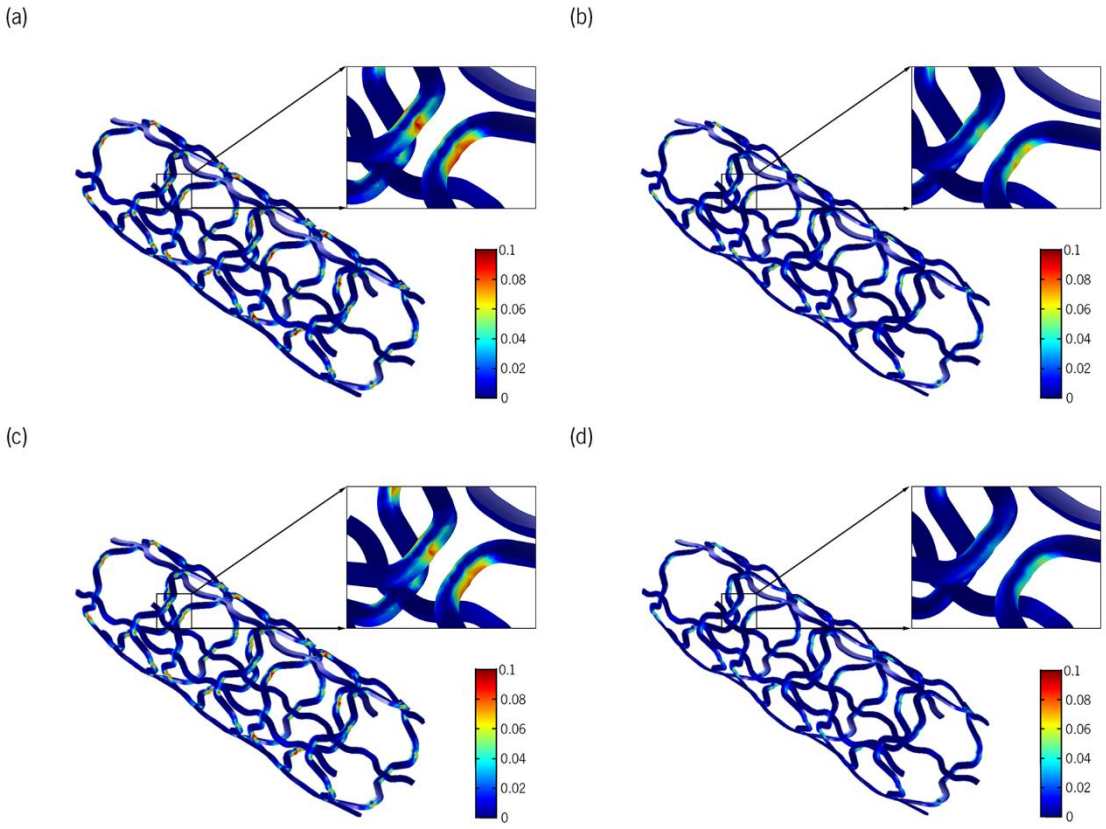

Figure 5.24 – Distribution of the equivalent plastic strain at the maximum expanded configuration of the (a,c) reference and (b,d) optimized stent geometry built-in non-(a,b) and ultrasound-treated (c,d) material.

It is possible to observe that the highest equivalent plastic strain values are found in high-curvature radius regions for both reference and optimized geometries, regardless of the processing condition. Nonetheless, the maximum equivalent plastic strain value and the volume subjected to it dropped significantly, the decrease more significant for the stent modeled with mechanical properties of ultrasound-treated material, as presented in Table 5.7.

As expected, the distribution of the von Mises stress after stent recoiling (Figure 5.25), the highest values were located in the same areas as the maximum equivalent plastic strain. The design optimization allowed diminishing the maximum von Mises stress for both stents modeled with mechanical properties of non- and ultrasound-treated material, which is known to help enhance the mechanical strength of the device when in service.

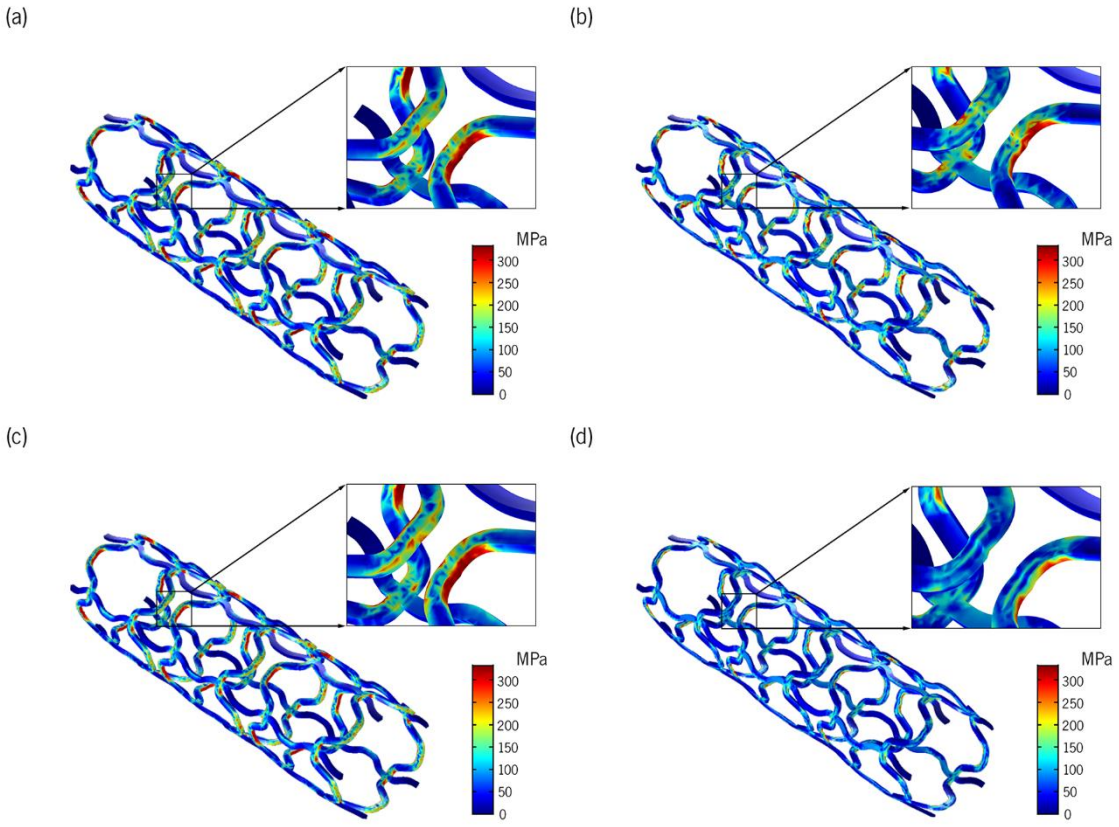

Figure 5.25 – Distribution of the von Mises stress after stent recoiling of the (a,c) reference and (b,d) optimized geometry using non-(a,b) and ultrasound-treated (c,d) material data.

By reducing the average equivalent plastic strain and the average residual stress, the optimization process provided a stent design that could exhibit superior functional performance. Indeed, the minimization of both parameters reduces stress corrosion and prevents early fracture, which may extend the period during which the stent can support the artery remodeling process [37]. On the other hand, the superior mechanical properties granted by the ultrasound treatment allowed a significant decrease in the strut thickness, which is advantageous from the biocompatibility and endothelialization perspective.

5.5.3. Conclusions on the impact of material degradation on the stent mechanical performance

This study assessed the effect of the AZ91D-1.0% Ca degradation due to exposure to an EBSS flow for 48h to 7 days (168 h) on the stent's mechanical strength. The results showed that the stent's mechanical resistance decreased remarkably as the immersion time increased. Radial force decreased from 6.7N and 6.9 N for stents modeled with mechanical properties of non- and ultrasound-treated materials before degradation to approximately 4.3 N and 4.9 N after immersion for 7 days (168 h), indicating progressive loss of radial support ability. Moreover, the trend observed concerning the evolution of the radial strength decrease suggests that the considered stent model will likely fail prematurely, which may compromise

the treatment outcomes. Despite these findings, the stent modeled using ultrasound-treated material properties has shown promising results as the mechanical resistance deterioration occurred slower than in the stent modeled using non-treated material data.

Additionally, a design optimization study was performed to find the most suitable stent geometry considering the minimization of the average residual stress and equivalent plastic strain, as well as the reduction of the strut thickness. The superior mechanical properties of the ultrasound-treated material allowed for obtaining an optimized stent geometry with a significantly lower thickness (0.125 mm) compared with the non-treated one (0.160 mm) without compromising the functional performance of the device. In fact, the average residual stress was reduced from 52.3 MPa to about 44.03 MPa, whilst the average equivalent plastic strain decreased by about 46.1%.

5.5.4. Summary and Conclusions

Several publications have proven the potential of FEA in predicting the outcomes of the stenting procedure. In this chapter, four different case studies resorted to this valuable tool to study the influence of several factors, from the impact of the strategy adopted for balloon modeling to the impact of the material's properties on the stent behavior before and after degradation, including its design optimization.

In the first case, two different balloon geometries – open- and taper-ended – and two material models – linear elastic and hyperelastic – were used to study the influence of the balloon modeling strategy on the outcomes of the stenting procedure. It was demonstrated that the balloon modeling choices little influenced the expandability of the stent and the maximum stent stress at a fully expanded radius. On the other hand, the stent expanded profile along its length and diameter was suggested to be affected by the different deformation behavior exhibited by the balloon due to the geometry and material model adopted. A hyperelastic balloon with tapered ends was found to be the one that showed the closest behavior to clinical and experimental results, as it was able to reproduce the balloon protrusion at the stent cells, which can induce arterial damage.

A different study investigated the effect of the material properties used to model the stent. In this scope, the stress-strain curves obtained from tensile testing of non- and ultrasound-treated AZ91D-1.0% Ca alloy were used, and the deployment procedure was simulated. The results showed that by presenting superior mechanical properties, the stent modeled using ultrasound-treated material properties could achieve a higher expanded radius than the non-treated one. On the other hand, dogboning and foreshortening parameters showed similar results for both materials studied, indicating that they are more sensitive to other factors than the material used. Such a hypothesis was confirmed in a third study, which was focused

on stent design optimization taking advantage of the unique capability of the microcasting technique of producing stents with non-uniform cross-section. It was found that by increasing the thickness of specific stent sections, a more uniform expanded profile could be achieved, which contributed to minimizing dogboning to values as low as 1.0%. By presenting thicker struts, the stent expansion required higher expansion pressure; however, the value was still within the acceptable range to prevent vessel injury.

The effect of the deterioration of the mechanical properties on the stent radial strength was evaluated using the stress-strain curves obtained through tensile tests of non and ultrasound-treated AZ91D-1.0% Ca after immersion for 48, 72 and 168 h. It was found that the radial strength dropped significantly with the immersion time, which is compatible with the loss of mechanical properties. This reduction was found to be more significant for the stent modeled using non-treated material data than that modeled using ultrasound-treated material properties (35.0 % vs. 28.8 %). These results agreed with the loss of mechanical properties observed in the tensile tests of the wires subjected to immersion tests.

Finally, an optimization study was performed to reduce the residual stent stress and equivalent plastic strain during the deployment and the stent strut thickness to improve the treatment outcomes. Also, a second step was included in the simulation to ensure the stent's ability to withstand the artery recoil pressure. The enhanced mechanical properties of the ultrasound-treated material enabled the reduction of the stent strut thickness without compromising the device's functionality. The average residual stress was reduced by about 15.9 %, while the average equivalent plastic strain decreased by about 46.1% for the stent modeled using ultrasound-treated properties.

Overall, FEA was confirmed as a unique tool capable of assisting the stent design process, allowing for the prediction of the stent deployment procedure and enabling its optimization. The results obtained stressed the potentiality of ultrasound treatment and microcasting techniques for obtaining stents with superior performance, which is why further efforts must be made to explore such routes.

CHAPTER REFERENCES

[1] V.Lopes, Development of a New Technique for Manufacturing Biodegradable Magnesium Stents. PhD, Guimarães, 2022.

[2] B.K. Keller, C.M. Amatruda, D.R. Hose, J. Gunn, P.V. Lawford, G. Dubini, F. Migliavacca, A.J. Narracott, Contribution of Mechanical and Fluid Stresses to the Magnitude of In-stent Restenosis at the Level of Individual Stent Struts, Cardiovasc Eng Tech 5 (2014) 164–175. https://doi.org/10.1007/s13239-014-0181-y.

[3] P.W. Serruys, H.E. Luijten, K.J. Beatt, R. Geuskens, P.J. de Feyter, M. van den Brand, J.H.C. Reiber, H.J. ten Katen, G.A. van Es, P.G. Hugenholtz, Incidence of restenosis after successful coronary angioplasty: a time-related phenomenon. A quantitative angiographic study in 342 consecutive patients at 1, 2, 3, and 4 months., Circulation 77 (1988) 361–371. https://doi.org/10.1161/01.CIR.77.2.361.

[4] A. Syaifudin, R. Takeda, K. Sasaki, Development of asymmetric stent for treatment of eccentric plaque, Bio-medical materials and engineering 29 (2018) 299–317. https://doi.org/10.3233/BME-181737.

[5] R. Hoffmann, G.S. Mintz, R. Mehran, K.M. Kent, A.D. Pichard, L.F. Satler, M.B. Leon, Tissue proliferation within and surrounding Palmaz-Schatz stents is dependent on the aggressiveness of stent implantation technique, The American journal of cardiology 83 (1999) 1170–1174. https://doi.org/10.1016/s0002-9149(99)00053-3.

[6] C. Rogers, D.Y. Tseng, J.C. Squire, E.R. Edelman, Balloon-artery interactions during stent placement: a finite element analysis approach to pressure, compliance, and stent design as contributors to vascular injury, Circulation research 84 (1999) 378–383. https://doi.org/10.1161/01.res.84.4.378.

[7] W.-Q. Wang, D.-K. Liang, D.-Z. Yang, M. Qi, Analysis of the transient expansion behavior and design optimization of coronary stents by finite element method, Journal of biomechanics 39 (2006) 21–32. https://doi.org/10.1016/j.jbiomech.2004.11.003.

[8] F. Gervaso, C. Capelli, L. Petrini, S. Lattanzio, L. Di Virgilio, F. Migliavacca, On the effects of different strategies in modeling balloon-expandable stenting by means of finite element method, Journal of biomechanics 41 (2008) 1206–1212. https://doi.org/10.1016/j.jbiomech.2008.01.027.

[9] P. Dong, H. Mozafari, J. Lee, Y. Gharaibeh, V.N. Zimin, L.A.P. Dallan, H.G. Bezerra, D.L. Wilson, L. Gu, Mechanical performances of balloon post-dilation for improving stent expansion in calcified coronary artery: Computational and experimental investigations, Journal of the mechanical behavior of biomedical materials 121 (2021) 104609. https://doi.org/10.1016/j.jmbbm.2021.104609.

[10] Ž. Donik, B. Nečemer, S. Glodež, J. Kramberger, Finite element analysis of the mechanical performance of a two-layer polymer composite stent structure, Engineering Failure Analysis 137 (2022) 106267. https://doi.org/10.1016/j.engfailanal.2022.106267.

[11] A. Schiavone, L.G. Zhao, A study of balloon type, system constraint and artery constitutive model used in finite element simulation of stent deployment, Mech Adv Mater Mod Process 1 (2015) 591. https://doi.org/10.1186/s40759-014-0002-x.

[12] S.N. David Chua, B.J. Mac Donald, M.S.J. Hashmi, Finite element simulation of stent and balloon interaction, Journal of Materials Processing Technology 143-144 (2003) 591–597. https://doi.org/10.1016/S0924-0136(03)00435-7.

[13] A. Khosravi, A. Akbari, H. Bahreinizad, M. Salimi Bani, A. Karimi, Optimizing through computational modeling to reduce dogboning of functionally graded coronary stent material, Journal of materials science. Materials in medicine 28 (2017) 142. https://doi.org/10.1007/s10856-017-5959-7.

[14] D. Lim, S.-K. Cho, W.-P. Park, A. Kristensson, J.-Y. Ko, S.T.S. Al-Hassani, H.-S. Kim, Suggestion of potential stent design parameters to reduce restenosis risk driven by foreshortening or dogboning due to non-uniform balloon-stent expansion, Annals of biomedical engineering 36 (2008) 1118–1129. https://doi.org/10.1007/s10439-008-9504-1.

[15] Q. Wang, G. Fang, Y.-H. Zhao, J. Zhou, Improvement of Mechanical Performance of Bioresorbable Magnesium Alloy Coronary Artery Stents through Stent Pattern Redesign, Applied Sciences 8 (2018) 2461. https://doi.org/10.3390/app8122461.

[16] A. Schiavone, L.G. Zhao, A.A. Abdel-Wahab, Dynamic simulation of stent deployment – effects of design, material and coating, J. Phys.: Conf. Ser. 451 (2013) 12032. https://doi.org/10.1088/1742-6596/451/1/012032.

[17] M. de Beule, P. Mortier, S.G. Carlier, B. Verhegghe, R. van Impe, P. Verdonck, Realistic finite element-based stent design: the impact of balloon folding, Journal of biomechanics 41 (2008) 383–389. https://doi.org/10.1016/j.jbiomech.2007.08.014.

[18] H. Li, J. Gu, M. Wang, D. Zhao, Z. Li, A. Qiao, B. Zhu, Multi-objective optimization of coronary stent using Kriging surrogate model, Biomedical engineering online 15 (2016) 148. https://doi.org/10.1186/s12938-016-0268-9.

[19] H. Puga, V. Carneiro, J. Barbosa, V. Vieira, Effect of Ultrasonic Treatment in the Static and Dynamic Mechanical Behavior of AZ91D Mg Alloy, Metals 5 (2015) 2210–2221. https://doi.org/10.3390/met5042210.

[20] J. Bukala, P. Kwiatkowski, J. Malachowski, Numerical analysis of crimping and inflation process of balloon-expandable coronary stent using implicit solution, International journal for numerical methods in biomedical engineering 33 (2017). https://doi.org/10.1002/cnm.2890.

[21] A. Khosravi, H. Bahreinizad, M.S. Bani, A. Karimi, A numerical study on the application of the functionally graded materials in the stent design, Materials science & engineering. C, Materials for biological applications 73 (2017) 182–188. https://doi.org/10.1016/j.msec.2016.12.034.

[22] I.V. Gomes, H. Puga, J.L. Alves, Shape and functional optimization of biodegradable magnesium stents for manufacturing by ultrasonic-microcasting technique, Int J Interact Des Manuf 12 (2018) 1059–1069. https://doi.org/10.1007/s12008-017-0442-8.

[23] H. Li, T. Liu, M. Wang, D. Zhao, A. Qiao, X. Wang, J. Gu, Z. Li, B. Zhu, Design optimization of stent and its dilatation balloon using kriging surrogate model, Biomedical engineering online 16 (2017) 13. https://doi.org/10.1186/s12938-016-0307-6.

[24] H. Zahedmanesh, C. Lally, Determination of the influence of stent strut thickness using the finite element method: implications for vascular injury and in-stent restenosis, Medical & biological engineering & computing 47 (2009) 385–393. https://doi.org/10.1007/s11517-009-0432-5.

[25] N. Filipovic, D. Nikolic, V. Isailovic, M. Milosevic, V. Geroski, G. Karanasiou, M. Fawdry, A. Flanagan, D. Fotiadis, M. Kojic, In vitro and in silico testing of partially and fully bioresorbable vascular scaffold, Journal of biomechanics 115 (2021) 110158. https://doi.org/10.1016/j.jbiomech.2020.110158.

[26] H. Bahreinizad, M. Salimi Bani, A. Khosravi, A. Karimi, A numerical study on the application of the functionally graded bioabsorbable materials in the stent design, Artery Research 24 (2018) 1–8. https://doi.org/10.1016/j.artres.2018.09.001.

[27] M. Iantorno, M.J. Lipinski, H.M. Garcia-Garcia, B.J. Forrestal, T. Rogers, D. Gajanana, K.D. Buchanan, R. Torguson, W.S. Weintraub, R. Waksman, Meta-Analysis of the Impact of Strut Thickness on Outcomes in Patients With Drug-Eluting Stents in a Coronary Artery, The American journal of cardiology 122 (2018) 1652–1660. https://doi.org/10.1016/j.amjcard.2018.07.040.

[28] S. Buccheri, D. Capodanno, Bioabsorbable stents: only bad news?, European heart journal supplements journal of the European Society of Cardiology 21 (2019) B28-B30. https://doi.org/10.1093/eurheartj/suz009.

[29] R. Gharleghi, H. Wright, V. Luvio, N. Jepson, Z. Luo, A. Senthurnathan, B. Babaei, B.G. Prusty, T. Ray, S. Beier, A multi-objective optimization of stent geometries, Journal of biomechanics 125 (2021) 110575. https://doi.org/10.1016/j.jbiomech.2021.110575.

[30] C. Chen, J. Chen, W. Wu, Y. Shi, L. Jin, L. Petrini, L. Shen, G. Yuan, W. Ding, J. Ge, E.R. Edelman, F. Migliavacca, In vivo and in vitro evaluation of a biodegradable magnesium vascular stent designed by shape optimization strategy, Biomaterials 221 (2019) 119414. https://doi.org/10.1016/j.biomaterials.2019.119414.

[31] P.-J. Wang, F.R. Nezami, M.B. Gorji, F. Berti, L. Petrini, T. Wierzbicki, F. Migliavacca, E.R. Edelman, Effect of working environment and procedural strategies on mechanical performance of bioresorbable vascular scaffolds, Acta biomaterialia 82 (2018) 34–43. https://doi.org/10.1016/j.actbio.2018.10.020.

[32] R. Rieu, P. Barragan, C. Masson, J. Fuseri, V. Garitey, M. Silvestri, P. Roquebert, Radial force of coronary stents: A comparative analysis, Cathet. Cardiovasc. Intervent. 46 (1999) 380–391. https://doi.org/10.1002/(SICI)1522-726X(199903)46:3<380:AID-CCD27>3.0.CO;2-J.

[33] C.D. Resor, D.L. Bhatt, Thin to Ultrathin, Circulation. Cardiovascular interventions 11 (2018) e007407. https://doi.org/10.1161/CIRCINTERVENTIONS.118.007407.

[34] F. Otsuka, M. Vorpahl, M. Nakano, J. Foerst, J.B. Newell, K. Sakakura, R. Kutys, E. Ladich, A.V. Finn, F.D. Kolodgie, R. Virmani, Pathology of second-generation everolimus-eluting stents versus first-generation sirolimus- and paclitaxel-eluting stents in humans, Circulation 129 (2014) 211–223. https://doi.org/10.1161/CIRCULATIONAHA.113.001790.

[35] A. Lupi, A. Rognoni, G.G. Secco, M. Lazzero, F. Nardi, R. Fattori, A.S. Bongo, P. Agostoni, I. Sheiban, Biodegradable versus durable polymer drug eluting stents in coronary artery disease: insights from a meta-analysis of 5,834 patients, European journal of preventive cardiology 21 (2014) 411–424. https://doi.org/10.1177/2047487312467745.

[36] A. Kastrati, J. Mehilli, J. Dirschinger, F. Dotzer, H. Schühlen, F.J. Neumann, M. Fleckenstein, C. Pfafferott, M. Seyfarth, A. Schömig, Intracoronary stenting and angiographic results: strut thickness effect on restenosis outcome (ISAR-STEREO) trial, Circulation 103 (2001) 2816–2821. https://doi.org/10.1161/01.cir.103.23.2816.

[37] Y. Li, J. Wang, K. Sheng, F. Miao, Y. Wang, Y. Zhang, R. Hou, Di Mei, Y. Sun, Y. Zheng, S. Guan, Optimizing structural design on biodegradable magnesium alloy vascular stent for reducing strut thickness and raising radial strength, Materials & Design 220 (2022) 110843. https://doi.org/10.1016/j.matdes.2022.110843.

[38] B. Chevalier, Stent Strut Thickness: Have We Reached the Minimum?, Cardiac Interventions Today 12 (2018).

CHAPTER 6 – CONCLUDING REMARKS

Today's world presents countless obstacles that can only be resolved through a holistic and multidisciplinary approach. Particularly in the engineering field, the knowledge acquired in the scope of a specific subject is frequently useful across several research areas, contributing to significant advances in a short time span. It is here that doctoral research may find its most significant contribution to science and, thereby, to society.

Magnesium and its alloys are a popular focus of study and industry. Due to a unique combination of physical, chemical, and mechanical properties, these materials are appropriate for a variety of applications, from biomedical devices to aeronautical and aerospace components. Nonetheless, the processing of magnesium alloys to enhance their properties further is still underexplored, allowing the potential for the development of procedures that can contribute to this area.

The research work presented in this thesis focused on studying the impact of applying ultrasound treatment to the AZ91D-1-1.5%Ca magnesium alloy casting, aiming to improve downstream processing outcomes, namely stent fabrication. Furthermore, finite element analysis was performed to evaluate the stent performance and to support the design process of a novel stent to be produced through microcasting, considering the promising potential of ultrasound processing for mechanical properties enhancement. In this way, a workflow was established between the numerical modeling of the stent deployment procedure and the processing and subsequent characterization of the material.

6.1. STUDY CONCLUSIONS

In this section, the main conclusions drawn from the development of this work are presented, seeking to clearly answer the **Research Objectives (ROs)** outlined in **Chapter 1**.

Despite displaying singular characteristics such as an excellent strength-to-weight ratio - especially interesting for automotive and aerospace applications - and good biocompatibility - a critical property for biomedical devices – magnesium and its alloys still pose significant challenges concerning their processing. These materials show high reactivity and flammability, which hinders the casting process. SF_6 protective atmospheres are widely used to overcome such disadvantages; however, alternatives must be discovered in the face of increasingly strict environmental regulations. The addition of calcium to magnesium alloys has been proven to contribute to a significant increase in the material's ignition temperature, making the casting process more straightforward and safer, the reason why an AZ91D-1-1.5%Ca was used in this work. On the other hand, the downstream processing of magnesium alloys is complex due to the combination of the hexagonal compact crystallographic structure with the microstructural features of these materials. This way, applying ultrasound treatment is a possible route to overcome such drawbacks by changing the material's microstructural characteristics.

Chapter 3 discloses the effect of ultrasound treatment's continuous application during the solidification stage of an AZ91D-1-1.5%Ca alloy. The results confirmed the ultrasound's ability to modify the material's microstructure, significantly refining α-Mg and β-$Mg_{17}Al_{12}$ and Al_2Ca intermetallic phases. To fully understand the effect of the as-cast microstructure on the dissolution kinetics of the β-$Mg_{17}Al_{12}$ phases, solution heat treatment was done under varying temperature and time conditions. It has been established that the initial microstructure, namely the intermetallic size and morphology, plays a crucial factor in heat treatment outcomes.

The results obtained showed that ultrasound treatment enabled full dissolution of the β-$Mg_{17}Al_{12}$ even when solution-treated at a lower temperature (385 °C), while coarse particles could still be found in the non-treated samples after solution treatment at 415 °C for 24h.

By refining the microstructure, the ultrasound treatment accelerated the intermetallic phase dissolution, contributing to reducing both the temperature and time required and, thereby, allowing energy- and money-saving. This achievement may be particularly meaningful for severe plastic deformation processes as previous heat treatment stages are commonly required to reduce the intermetallics, given its detrimental effect.

Following solution treatment, aging treatment at 175 °C was performed. The ultrasound-treated samples displayed enhanced precipitation kinetics, reaching the peak-aging condition after 16 h, while the non-treated material was suggested not to have reached the peak-aging material under the considered conditions. Nonetheless, no improvements were observed regarding the hardness and tensile properties of the material, which may be explained by the low available content of solute to promote precipitation hardening. This situation may be caused by most aluminum being used to form the highly thermal stable Al_2Ca compound during the alloy solidification, which does not dissolve under the adopted solution treatment conditions. Despite the poor aging response of the AZ91D-1% Ca (wt.%) alloy, tensile tests revealed remarkably superior properties of the ultrasound-treated material compared to the non-treated one. In the as-cast state, the difference in tensile strength was roughly 50.0%, while elongation at break results were even more impressive. Compared with the non-treated material, ultrasound-treated one could reach elongation values about 72.0% higher in the as-cast state (1.75 % vs. 3.02 %), and in the solution-treated condition, it more than doubled it (2.04 % vs. 4.31 %).

The effect of the ultrasound treatment on the corrosion behavior of the AZ91D-1-1.5%Ca alloy was explored in **Chapter 4**. Non- and ultrasound-treated ingots were extruded to produce 1 mm diameter wires which were then subjected to dynamic corrosion tests by immersion in a constant flow of EBSS up to 168 h. Microstructural analysis revealed that ultrasound treatment could promote microstructure refinement, an effect that remained noticeable after the extrusion process. In this sense, despite the tensile strength being comparable, tensile tests showed that wires manufactured from the ultrasound-treated ingot exhibited significantly higher elongation (21.0 % vs. 16.3 %), which was suggested to result from the finer microstructure, namely smaller and evenly distributed intermetallic particles. Furthermore, the tensile properties of the extruded material were remarkably higher than those obtained in the as-cast condition, although it must be taken into consideration that the alloy composition differed concerning the calcium amount.

It has been concluded that despite the US-treated samples exhibiting a higher degradation rate than the non-treated material during the first stages of the immersion tests, this trend shifted for immersion times from 48 h on. The results showed that microstructure differences underly such behavior. The refined β-$Mg_{17}Al_{12}$ intermetallic phase acted as a cathode and promoted galvanic corrosion that hastened the material's degradation. Consequently, a layer of corrosion products formed and acted as a barrier that delayed further corrosion, working for the superior corrosion resistance of the ultrasound-treated material. The results from the tensile tests of the degraded materials confirmed the suggested hypothesis, given

that the ultrasound-treated material's mechanical properties decreased at a lower rate than the non-treated one. Compared with the non-degraded condition, the tensile strength of the non- and ultrasound-treated material decreased by about 28.0 % and 14.0 % after immersion for 7 days, respectively. Such results support the hypothesis that ultrasound treatment was able to delay the degradation of the material by modifying its microstructure, especially the intermetallic phase morphology.

Finite element analysis was used to assess the stent performance during the deployment procedure. Four different case studies were presented in **Chapter 5**, aiming at (i) investigating the role of the modeling strategy adopted on the outcomes of the process, (ii) assessing the effect of the material properties on the performance of the stent, (iii) optimizing the stent design taking advantage of the unique potentialities of microcasting process, namely the possibility of producing non-uniform cross-section stents and (iii) studying the impact of the mechanical properties deterioration on the radial strength by using the stress-strain curves of the degraded materials immersed in EBSS for 48, 72 and 168 h as input data to the numerical model; in this case, an optimization study was also performed to minimize the average residual stress after stent recoiling and the equivalent plastic strain at maximum expansion, along with the reduction of the strut thickness, whose higher values imposed by the poorer mechanical properties of the biodegradable materials are associated with severe adverse effects. The superior mechanical properties of the ultrasound-treated material allowed for a more significant reduction of the strut thickness (from 0.200 to 0.125 mm) without compromising the stent's functional performance.

Overall, this thesis proposes a processing technique strategy based on the application of ultrasound treatment during the solidification of an AZ91D-1-1.5%Ca to further enhance the microstructural and mechanical properties of the material. By combining the numerical modeling of the stent deployment procedure, the potential of this technique for manufacturing biomedical devices was assessed, and its viability was confirmed.

6.2. FUTURE WORK

Although this work focused on developing knowledge to be applied in the stents' manufacturing domain, the results obtained may be valuable for applications beyond this scope. Given the increasingly strict environmental and energetic policies, magnesium and its alloys will gain even more relevance, especially in the energy-demanding applications paradigm, due to their outstanding specific strength. The results presented herein may constitute a starting point for outlining processing strategies to overcome the main drawbacks of these materials, namely their poor formability at low temperatures and high corrosion rates. Indeed, the mechanical processing of these alloys frequently demands a previous heat treatment stage to dissolve the intermetallic phases, which are deleterious for the material's ductility. However, this previous step leads to a remarkable increase in the time and energy consumed, turning the process unattractive from an economic and environmental point of view. According to the results reported, ultrasound treatment can tune the as-cast microstructure and, this way, shorten the heat treatment duration. Furthermore, the corrosion-resistance properties of these materials also appear to be sensitive to the effect of the ultrasound, which may be considered encouraging for pursuing further research.

This study suggests that ultrasound treatment may revolutionize the manufacturing framework of magnesium alloy-based components. Nonetheless, further investigation must be carried on to understand the potentialities and limitations of such a technique thoroughly.

Optimizing the solution treatment to dissolve the thermally stable Al_2Ca intermetallic phase may help improve the aging response of these materials and their mechanical properties. This modification can be advantageous for structural applications in the automotive and aerospace industries.

Also, despite the promising results concerning the corrosion-resistance improvement through ultrasound treatment, further investigation must be pursued to make the most of this ability. In fact, ultrasound-treated samples displayed a lower corrosion rate. However, it was still too high to be suitable for manufacturing biodegradable devices.

6.3. SCIENTIFIC OUTCOMES

The scientific dissemination of the work developed in the scope of the doctoral research is fundamental and constitutes the recognition of the investigated topic's relevance.

As a result of the investigation pursued, scientific contributions were made in the form of papers published in international peer-reviewed journals, books, and conference papers. Table 6.1 presents a compilation of the referred contributions.

Additionally, the main advances were communicated in scientific events, which are summarized in Table 6.2.

Table 6.1 – Scientific outputs in written documents.

	Title	Type	Publication
[1]	Shape and functional optimization of biodegradable magnesium stents for manufacturing by ultrasonic-microcasting technique (2018)	Journal Paper	International Journal on Interactive Design and Manufacturing
[2]	Effect of the ultrasonic melt treatment on the deployment outcomes of a magnesium stent manufactured by microcasting: a finite element analysis (2019)	Conference Paper	*IEEE 6th Portuguese Meeting on Bioengineering (ENBENG)*
[3]	Numerical Simulation of the Deployment Process of a New Stent Produced by Ultrasonic-Microcasting: The Role of the Balloon's Constitutive Modeling (2019)	Book Chapter	*New Developments on Computational Methods and Imaging in Biomechanics and Biomedical Engineering*
[4]	Influence of the Adopted Balloon Modeling Strategies in the Stent Deployment Procedure: An In-Silico Analysis (2020)	Journal Paper	*Cardiovascular Engineering and Technology*
[5]	Ultrasonic Treatment as the Route for Grain Refinement of Mg-Al Alloys: A Systematic Review (2021)	Journal Paper	*Metals*
[6]	Ultrasound-assisted casting of AZ91D-1.5%Ca – Shifting T4 paradigm for downstream processing (2022)	Journal Paper	*Materials Letters*

Table 6.2 Dissemination of results in scientific events.

	Presentation Title	Type	Scientific Event
[1]	Numerical optimization of the deployment procedure of a new magnesium stent manufactured by ultrasound-microcasting: an approach to the role of balloon's geometry on the outcomes of the process	Poster	8th World Congress of Biomechanics (2018)
[2]	Numerical simulation of the deployment process of a new stent produced by ultrasound-microcasting: The role of the balloon's constitutive modeling	Oral	15th International Symposium on Computer Methods in Biomechanics and Biomedical Engineering CMBBE (2018)
[3]	Effect of the ultrasonic melt treatment on the deployment outcomes of a magnesium stent manufactured by microcasting: a finite element analysis	Oral	*IEEE 6th Portuguese Meeting on Bioengineering (ENBENG) (2019)*